THE UNIVERSITY *of* EDINBURGH

This thesis has been submitted in fulfilment of the requirements for a postgraduate degree (e.g. PhD, MPhil, DClinPsychol) at the University of Edinburgh. Please note the following terms and conditions of use:

- This work is protected by copyright and other intellectual property rights, which are retained by the thesis author, unless otherwise stated.
- A copy can be downloaded for personal non-commercial research or study, without prior permission or charge.
- This thesis cannot be reproduced or quoted extensively from without first obtaining permission in writing from the author.
- The content must not be changed in any way or sold commercially in any format or medium without the formal permission of the author.
- When referring to this work, full bibliographic details including the author, title, awarding institution and date of the thesis must be given.

Optimal cosmology from gravitational lensing: Utilising the magnification and shear signals

Christopher Duncan

A thesis submitted in fulfilment of the requirements
for the degree of Doctor of Philosophy
to the
University of Edinburgh
August 2014

Abstract

Gravitational lensing studies the distortions of a distant galaxy's observed size, shape or flux due to the tidal bending of photons by matter between the source and observer. Such distortions can be used to infer knowledge on the mass distribution of the intervening matter, such as the dark matter halos in which clusters of individual galaxies may reside, or on cosmology through the statistics of the matter density of large scale structure and geometrical factors. In particular, gravitational lensing has the advantage that it is insensitive to the nature of the lensing matter. However, contamination of the signal by correlations between galaxy shape or size and local environment complicate a lensing analysis. Further, measurement of traditional lensing estimators is made more difficult by limitations on observations, in the form of atmospheric distortions or optical limits of the telescope itself. As a result, there has been a large effort within the lensing community to develop methods to either reduce or remove these contaminants, motivated largely by stringent science requirements for current and forthcoming surveys such as CFHTLenS, DES, LSST, HSC, Euclid and others.

With the wealth of data from these wide-field surveys, it is more important than ever to understand the full range of independent probes of cosmology at our disposal. In particular, it is desirable to understand how each probe may be used, individually and in conjunction, to maximise the information of a lensing analysis and minimise or mitigate the systematics of each. With this in mind, I investigate the use of galaxy clustering measurements using photometric redshift information, including a contribution from flux magnification, as a probe of cosmology. I present cosmological forecasts when clustering data alone are used, and when clustering is combined with a cosmic shear analysis. I consider two types of clustering analysis: firstly, clustering with only redshift auto-correlations in tomographic redshift bins; secondly, clustering using all available redshift bin correlations. Finally, I consider

how inferred cosmological parameters may be biased using each analysis when flux magnification is neglected. Results are presented for a Stage–III ground-based survey, and a Stage–IV space-based survey modelled with photometric redshift errors, and values for the slope of the luminosity function inferred from CFHTLenS catalogues. I find that combining clustering information with shear gives significant improvement on cosmological parameter constraints, with the largest improvement found when all redshift bins are included in the analysis. The addition of galaxy-galaxy lensing gives further improvement, with a full combined analysis improving constraints on dark energy parameters by a factor of > 3. The presence of flux magnification in a clustering analysis does not significantly affect the precision of cosmological constraints when combined with cosmic shear and galaxy-galaxy lensing. However if magnification is neglected, inferred cosmological parameter values are biased, with biases in some cosmological parameters found to be larger than statistical errors. We find that a combination of clustering, cosmic shear and galaxy-galaxy lensing can provide a significant reduction in statistical errors from each analysis individually, however care must be taken to measure and model flux magnification.

Finally, I consider how measurements of galaxy size and flux may be used to constrain the dark matter profile of a foreground lens, such as galaxy- or galaxy-cluster-dark matter halos. I present a method of constructing probability distributions for halo profile free parameters using Bayes' Theorem, provided the intrinsic size-magnitude distribution may be measured from data. I investigate the use of this method on mock clusters, with an aim of investigating the precision and accuracy of returned parameter constraints under certain conditions. As part of this analysis, I quantify the size and significance of inaccuracies in the dark matter reconstruction as a result of limitations in the data from which the sample and size-magnitude distribution is obtained. This method is applied to public data from the Space Telescope A901/902 Galaxy Evolution Survey (STAGES), and results are presented for the four STAGES clusters using measurements of source galaxy size and magnitude, and a combination of both. I find consistent results with existing shear measurements using measurements of galaxy magnitudes, but interesting inconsistent results when galaxy size measurements are used. The simplifying assumptions and limitations of the analysis are discussed, and extensions to the method presented.

Lay Summary

The area of cosmology is rapidly becoming data-rich, with a host of large data-sets from current and future large-scale surveys such as Euclid, HST, LSST and others. The scale of these surveys and the number of observed astronomical bodies in each means that current theories of cosmology can be tested to unprecedented levels, with an expected substantial increase in the precision of measurements of standard-cosmology parameters and challenges to the currently held cosmological paradigm.

Current cosmological theory contains a large number of possible analyses with which to undertake these measurements. Whilst these are too numerous to list here, of particular note are recent measurements of temperature fluctuations in remnant radiation from the Big Bang taken by the Planck satellite, as well as detailed measurements of the clustering of galaxies in large-scale surveys such as SDSS, sensitive to the distribution of matter in the Universe and statistical early-Universe imprints on this distribution. A promising area of study concerns the observed changes in the observations of distant galaxies by the action of the gravitational force by intervening matter. In such a scenario, the light from distant sources is bent by the action of gravity according to the distribution of matter between the source and the solar system, causing a change in the observed shape (shear) and size and flux (magnification) of the source. Knowledge of the Universe can therefore be inferred from statistical measurements of these effects, and constraints on cosmological models can be deduced through the sensitivity of the gravitational lensing signal on geometry and the large-scale distribution of matter. Traditionally, measurements of the gravitational lensing signal are taken using the shear effect due to its advantageous statistical properties over the magnification effect, and recent measurements using CFHTLenS have provided competitive constraints on cosmological parameters.

The decrease in the size of statistical errors on cosmological measurements, a direct result of the consequent large increase in the size of the available data

sample, motivates the necessity to understand any residual systematics in the current techniques of cosmological parameter estimation. For example, recent measurements of the early Universe using Planck are known to be in tension with a number of other independent measurements including the most precise measurements using the signatures of gravitational lensing with CFHTLenS: such discrepancy could result in unaccounted for systematics in the analysis or observations or, more interestingly, new physics. The effects of such systematics could be mitigated by the combination of measurements through different analysis and data-sets, as each may be expected to be affected by a different, idiosyncratic set of systematic effects. Further, such a combination may be expected to give a substantial increase in the accuracy and precision with which the cosmological model can be constrained.

In this thesis I consider how the combination of probes can be used to infer knowledge about the Universe in an optimal way, by internally calibrating systematics and reducing statistical errors. I place particular emphasis on the signature of the magnification due to gravitational lensing, and motivate its use as a probe of cosmology and large-scale structure. Such measurements are currently taken as part of traditional clustering and lensing analyses, and therefore may be expected to provide a valuable source of new information for relatively little allocation of resources. I investigate the use of number counts of galaxies as a probe of cosmology with theoretical models, and detail the importance of the magnification signature in such an analysis. I make quantitative predictions on the improvement to cosmological measurements when such measurements are combined with shear measurements, and detail the sensitivity to such a combination to incorrect assumptions in the modelling of the magnification signal. This work is intended as a guide to the application of these methods to large-scale surveys, with the intent of providing the means to increase the accuracy and precision of cosmological measurements using signatures that would traditionally be ignored, but give valuable information at little expense.

Finally, I consider the use of the magnification in determining the mass of large clusters of galaxies. I present a method of constraining mass profiles using measurements of galaxy size and magnitude, both affected by the magnification effect. The accuracy and precision of this method is tested and applied to observations using the Hubble Space Telescope, for which a shear analysis has already been undertaken. Results are presented for different measurements of the magnification, and compared to shear measurements. This work is intended to determine the

use of such measurements in the determination of the mass of large astronomical bodies, to evaluate its competiveness with traditional techniques and quantify how the combination of these measurements can improve our knowledge of such bodies.

Declaration

Except where otherwise stated, the research undertaken in this thesis was the unaided work of the author. Where the work was done in collaboration with others, a significant contribution was made by the author.

C. Duncan
Aug 2014

Acknowledgements

The production of this thesis is the result of hard work and perseverance by more than just myself. Of the people I would like to thank, chief of these are the people who have supervised and guided this work over the years, all of whom I would like to thank for their guidance and insight, without which this would not have been possible. I would therefore thank Catherine Heymans, Alan Heavens and Benjamin Joachimi for their time and interest, the opportunity that they have afforded me and the answers to my numerous questions. I would extend particular thanks to Catherine for her continued positivity, support and patience, and Alan and Benjamin for the effort they have expended in supporting me even when they have moved across the country.

I would like to acknowledge the influence of my family, who provided the direction which lead me here and the support to continue to this stage. I am truly thankful to the close friends I have met during my time at the ROE, who have enriched not only my time here, but also myself. Of these I give special thanks to Rebecca Bowler and Sandy Rogers for encouraging me to push myself physically as well as mentally, and ensuring the final years far surpassed the preceding; as well as Alex Mead and David Harvey.

Contents

List of Figures

List of Tables

Chapter 1

An Introduction to Cosmology

The subject of cosmology, that is the discussion of the structure and content of the Universe that we live in, has concerned humans for centuries. It is within the last century that the subject has truly seen a renaissance, with the formulation and acceptance of many of the principles that now form the 'standard model' of cosmology, so named to draw similarities to the successes seen in the standard model of particle physics. The central tenets of modern cosmology have been in place since the early 20th century, with the pioneering work of Friedmann, Lemaitre, Einstein and Hubble, as well as others too numerous to mention in passing. Within the first few decades of the previous century, the foundations for the Big Bang theory of the Universe was set, with the introduction of Einstein's General Relativity, solved under the simplifying assumption of the cosmological principle, and the discovery that observed 'nebulae' existed outside the Milky Way that led to the well-known Hubble law, a fit to observations which showed for the first time an expanding Universe.

This early version of the standard model of cosmology was not without its problems. In particular, the hot big bang theory failed to provide a mechanism for the creation of the initial seeds for structure formation, and seemed to predict singular initial conditions. Additionally, the model failed to explain the observed flatness and large-scale isotropy of the Universe (termed the flatness and horizon problems). The introduction of inflationary cosmology in the early 1980's, where an initial period of rapid exponential growth is postulated in place of the hot, dense singularity of the hot big bang theory, went some way to alleviating this, in particular providing natural solutions to the horizon and flatness problems, and providing a mechanism for the formation of local inhomogeneities and structure in the Universe. Further, the use of

the inflationary paradigm mitigates the problem of the initial singularity, by effectively 'pushing' the singularity back indefinitely. For these reasons, the modern standard model often implicitly contains the inflationary paradigm, although it has never been verified observationally.

Towards the end of the 20th century, Schmidt et al. (1998) showed that the Universe was undergoing a period of accelerating expansion, contradicting the expected deceleration in a Universe containing only matter. This led to the postulation of a new form of matter, frequently referred to as Dark Energy, with fluid properties and negative pressure which counteracts gravity on cosmological scales. The nature of dark energy is one of the most fundamental outstanding questions of modern cosmology.

The history of the Universe as predicted by the standard model then proceeds thus: an early period of inflation causes the rapid exponential growth of small causally connected areas, simultaneously causing the growth of small quantum fluctuations in the matter density field which seed early structure formation. The early, hot Universe contains both ionised baryonic matter, dark matter[1] and radiation, relics of big bang nucleosynthesis during the inflationary period, which are tightly coupled resulting in an opaque Universe. Upon recombination, when ionised nucleii combined with free electrons, the Universe became transparent, allowing the propagation of radiation in all directions and forming the last scattering surface seen today as the cosmic microwave background (CMB). During this period radiation is the dominant energy component in the Universe, suppressing structure formation on scales smaller than the particle horizon until matter-radiation equality, after which the matter content of the Universe dominates. During this time only the radiation remnant from the Big Bang is present until the first stars and galaxies are formed in over-dense regions. Radiation from these structures then re-ionises the surrounding neutral atoms, however by this point the expansion has proceeded to the point that the coupling of radiation to the ionised gas no longer causes the Universe to be opaque. Finally, dark energy becomes dominant and the Universe begins accelerating expansion, up to the present day.

In the following chapter I will describe some of the main tenets of modern cosmology, building from a homogeneous and isotropic world model to the formation of structure which is observed with modern surveys. I discuss cosmology as a modern science, with a brief overview of some of the most promising probes of cosmology, and argue that whilst we are in an era of precision cosmology, tensions in the most

[1]Non-luminous, weakly- or non-interacting mass that cannot be observed directly

recent measurements require more detailed study.

1.1 A featureless Universe

On large scales the Universe appears to be isotropic. By invoking the cosmological principle, which states that we do not expect to occupy a special place in the Universe, we expect the same large scale isotropy to be observed everywhere. As a result, the cosmological principle dictates that the Universe is not only isotropic, but also homogeneous. Under these simplifying assumptions, the geometry of an expanding Universe can be described by the Friedmann-Robertson-Walker metric

$$ds^2 = c^2dt^2 - a^2(t)[d\chi^2 + f_K^2(\chi)(d\theta^2 + \sin^2\theta d\phi^2)] \tag{1.1}$$

where ds is the space-time interval between two events measured by fundamental observers, who move in free-fall or equivalently are at rest with respect to their local matter distribution, and we have defined the cosmic time t to be that measured by these fundamental observers. By definition, fundamental observers move with the global expansion of the Universe, parameterised here through the scale factor $a(t)$. The scale factor is spatially independent due to homogeneity, and satisfies $a(t_0) = 1$ with subscript 0 hereon in representing the present time. The spatial part of the metric is described using the spherical polar coordinates χ, θ and ϕ, with χ the co-moving radial distance and f_K the angular diameter distance, defined for three geometries as

$$f_K(\chi) = \begin{cases} K^{-1/2}\sin\left[K^{-1/2}\chi\right] & K > 0 \\ \chi & K = 0 \\ (-K)^{-1/2}\sinh\left[(-K)^{-1/2}\chi\right] & K < 0 \end{cases} \tag{1.2}$$

where K describes the global curvature. The three geometries include the flat ($K = 0$) case, where co-ordinates are Euclidean; the open, spherical ($K > 0$) case, where co-ordinates correspond to ordinary spherical polar co-ordinates; and the closed, saddle-like ($K < 0$) case.

On cosmological scales, we expect that dynamics are governed by gravity, and therefore well described by Einstein's field equations

$$G_{\mu\nu} + g_{\mu\nu}\Lambda = -\frac{8\pi G}{c^4}T_{\mu\nu} \tag{1.3}$$

where subscripts run over one temporal and three spatial coordinates, and the distinction has been made between the geometrical properties of space-time and the properties of matter on either side of the equation. On the left hand side, the $G_{\mu\nu}$ term, geometric information enters through contractions over the Ricci Tensor, which describes the curvature of space-time using the metric and its derivatives up to second order via the affine connection. The second term on the left is the cosmological constant, originally introduced by Einstein in a misguided attempt to enforce a static Universe which is now more frequently invoked as an explanation for modern-day accelerated expansion. The stress-energy-momentum tensor, $T_{\mu\nu}$ describes the local matter content. We consider here matter at rest which does not experience shear stress, meaning the energy-momentum tensor $T_{\mu\nu}$ is diagonal. For a fluid which is fully described by its matter density ρ and pressure p, we define

$$T_{\mu\nu} = \left(\rho + \frac{p}{c^2}\right) U_\mu U_\nu - p g_{\mu\nu} \tag{1.4}$$

where U is the four-velocity, which for a particle at rest in co-moving co-ordinates satisfies $U = (c, \mathbf{0})$. If defined locally in cartesian co-ordinates the energy-momentum tensor gives $T_{00} = \rho c^2$ and $T_{ii} = p$ (no summation). Conservation of mass and energy are contained in the 4-divergence of this tensor $T_{\mu\nu;\nu} = 0$, where notation $_{;\nu}$ denotes covariant differentiation on space-time co-ordinate ν, and summation convention is assumed.

By applying this energy-momentum tensor to the field equations given in (1.3) we obtain two equations governing the evolution of the scale factor with the matter content of the Universe. The Friedmann equation in its first form is

$$\left(\frac{\dot{a}}{a}\right)^2 = H^2(a) = \frac{8\pi G}{3}\rho(a) - \frac{Kc^2}{a^2} \tag{1.5}$$

where we have identified the Hubble parameter as $H(a) = \dot{a}/a$. To see this, consider a proper distance which is related to a co-moving distance through the scale factor, $x = a(t)r$. Differentiating with respect to time, we find that $\dot{x} = \dot{a}r = (\dot{a}/a)x$, provided the co-moving distance is constant with time. Comparison with the Hubble Law then allows us to identify the Hubble parameter. Frequently, the Hubble parameter is recast in dimensionless form, $h = H/100\ \mathrm{kms}^{-1}\mathrm{Mpc}^{-1}$. Further, we obtain an

equation of motion for the scale factor

$$\frac{\ddot{a}}{a} = -\frac{4\pi G}{3}\left(\rho(a) + \frac{3p}{c^2}\right). \tag{1.6}$$

Both equations contain contributions from either the matter density or pressure, therefore we see that the expansion history of the Universe depends on the dominant contribution to the energy density at a given time. The energy density contains contributions from three different types of matter: radiation, a matter component which contains dark matter and ordinary baryonic matter, and a dark energy contribution

$$\rho(a) = \rho_r(a) + \rho_m(a) + \rho_\Lambda(a) \tag{1.7}$$

which vary with the scale factor in different ways.

For an adiabatic system under a pressure p the first law of thermodynamics states that $dE = -pdV$, where E is the internal energy of the system with volume dV. For a system undergoing expansion with the scale factor $V \propto a^3$, and noting $E = \rho c^2 V$ it follows that

$$\rho(a) = \rho_0 \exp\left\{-3\int_1^a [1 + w(a)]\mathrm{d}\ln(\mathrm{a}')\right\} \tag{1.8}$$

where we have defined the time-varying equation of state parameter

$$w = \frac{p}{u} = \frac{p}{\rho c^2} \tag{1.9}$$

where u is the energy density. Radiation with energy density equal to $u = 3p$ therefore has $w = 1/3$, pressure-less matter has $w = 0$, and the cosmological constant description of dark energy has $w = -1$. The time evolution for each contribution to the total energy budget of the Universe follows, with

$$\rho_r(a) \propto a^{-4} \tag{1.10}$$

$$\rho_m(a) \propto a^{-3} \tag{1.11}$$

$$\rho_\Lambda(a) = \text{constant}. \tag{1.12}$$

It is interesting to note that these dependencies are expected from purely physical arguments: the matter contribution should just scale as the change in volume as the matter becomes diluted due to the expansion of the Universe, whilst the radiation gains an extra contribution from the scale-factor as the energy density of relativistic particles

are redshifted. The final relation, that for the dark energy component, assumes the cosmological constant explanation.

By defining a critical density $\rho_{\rm Crit}$ to be the mass density which gives an exactly flat Universe, the Friedmann equation gives

$$\rho_{\rm Crit}(a) = \frac{3H^2(a)}{8\pi G}. \tag{1.13}$$

With the dimensionless mass density defined as $\Omega = \rho/\rho_{Crit}$, the Friedmann equation can then be recast as

$$\begin{aligned} H^2(a) &= H_0^2\left(\Omega_m(a) + \Omega_r(a) + \Omega_\Lambda(a) - \frac{Kc^2}{a^2}\right) && (1.14)\\ &= H_0^2(\Omega_{m0}a^{-3} + \Omega_{r0}a^{-4} + \Omega_{\Lambda 0} + (1-\Omega_0)a^{-2}) && (1.15) \end{aligned}$$

where the curvature term has been recast in terms of the total mass density Ω, and the time dependence of each density parameter has been detailed explicitly, with the dark energy cast as a cosmological constant. Solutions to the Friedmann equation for various choices of $\Omega_{\rm m0}$ and $\Omega_{\Lambda 0}$ are shown in Figure 1.1.

1.2 Dark Energy

Observations using Type 1a supernova first revealed that the present day Universe is undergoing a period of accelerated expansion (Schmidt et al., 1998; Perlmutter et al., 1999), eventually leading to the postulation of dark energy. Friedmann's equation in its second form, given in equation 1.6, explicitly determines the acceleration of the expansion, through the scale factor a, according to the matter content of the Universe. Accelerated expansion, corresponding to $\ddot{a} > 0$, requires $(\rho + 3p/c^2) = (1+3w)/c^2 < 0$ or equivalently $w < -1/3$, which cannot be accounted for either through pressureless dark matter($w = 0$) or radiation ($w = 1/3$). A solution is provided with the postulation of a new form of matter, particularly a fluid with negative pressure, which can be attributed to the vacuum energy and is commonly referred to as dark energy.

Whilst the postulation of a new, exotic form of matter attributed to the energy density of the vacuum provides a mechanism for the observed accelerated expansion, an alternative route is to instead consider the modification not to the mass-energy content of the Universe, but equivalently a modification to the Einstein field equations,

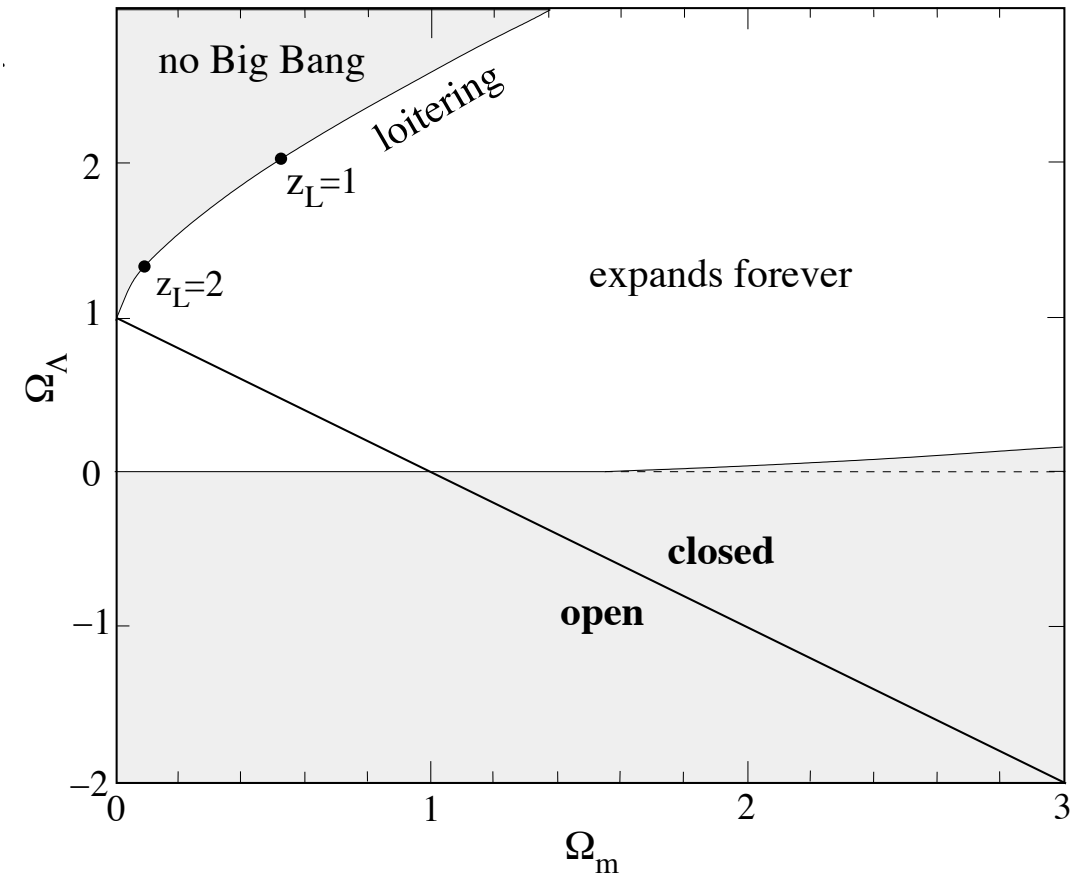

Figure 1.1: The geometry and expansion history of the Universe for various present day values of the matter and dark energy density. The lower shaded area shows cosmologies with eventual recollapse, whilst the upper shaded area shows cosmologies with a large contribution from dark energy which doesn't exhibit a big bang. The unshaded area defines cosmologies which continue to expand, whilst in between there exist loitering solutions with an infinite age and a maximum redshift, denoted with $z_{\rm L}$. Cosmologies with $\Omega > 1$ are closed, whilst $\Omega < 1$ give open solutions. Current measurements place us in a flat Universe, with $\Omega_{m0} \sim 0.3$ and $\Omega_{\Lambda 0} \sim 0.7$ (see Section1.6). From J.A.Peacock (1999).

given in equation 1.3. The simplest modification is the "cosmological constant" famously proposed by Einstein to achieve a static Universe from the unstable field equations. The cosmological constant (Λ) is a scalar solution to the field equations, and can be related to the dark energy density ρ_v under the assumption that $w = -1$ as

$$\Lambda = \frac{8\pi G}{c^2}\rho_v. \tag{1.16}$$

The cosmological constant therefore provides a solution to the accelerated expansion, equivalent to a non-time varying equation of state that can be associated with a negative pressure fluid formally known as dark energy. Current measurements using supernovae measurements in combination with other probes, such as Sullivan et al. (2011) which combines 3-year data from the Supernova Legacy Survey with WMAP7 and SDSS, give a dark energy equation of state consistent with a cosmological constant.

Under the cosmological constant explanation for the dark energy phenomenon, the far-future Universe is one where the dominant contribution to the mass-energy budget is the dark energy density. In this case, the Hubble factor becomes a constant, and the Friedmann equation of the first form admits a de-Sitter solution of the form

$$a(t) \propto \exp(Ht). \tag{1.17}$$

The far-future Universe is therefore one where the scale factor increases exponentially, much like an early-time inflationary period. In this scenario, the dark energy continues to be the dominant contribution to the mass-energy, as it is the only contribution that doesn't decay with increasing scale factor. Whilst the cosmological constant presents a succinct explanation for the dark energy phenomenon, it therefore raises the so-called 'coincidence problem', which questions why the present-day matter density and dark energy density are the same order of magnitude (see Figure 1.2). Further to this, quantum field theories predict a vacuum energy approximately 120 orders of magnitude larger than that required in the cosmological constant explanation. Anthropic arguments are often invoked as a solution: as Dark Energy suppresses growth, a larger dark energy component that became dominant earlier in the Universe's history would suppress galaxy formation and reduce the probabilistic chance of life. Alternatively, scalar field solutions such as quintessence can provide a solution by predicting a time-varying dark-energy density that tracks the dominant contribution to the mass-energy budget until late times. Another explanation for dark energy could

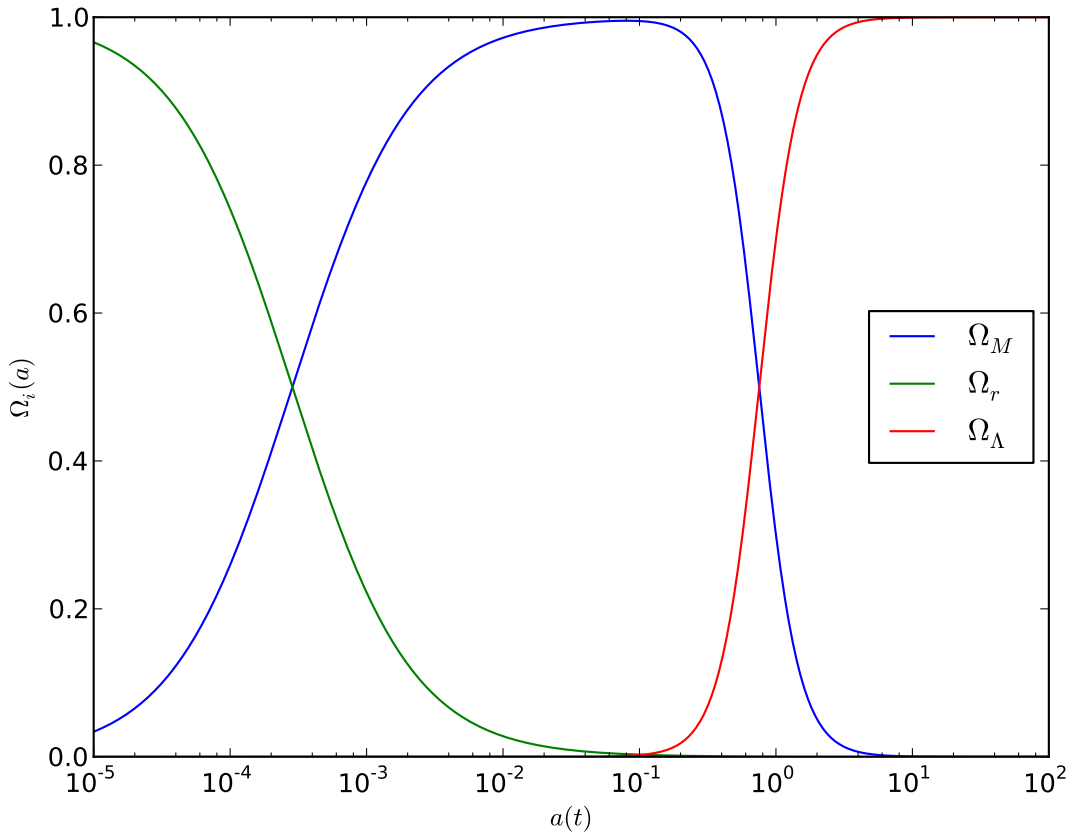

Figure 1.2: Contributions to the mass-energy budget of the Universe as a function of time. Scale Factor $a = 1$ corresponds to the present day, with $\sim 70\%$ dark energy and $\sim 30\%$ matter, and a largely sub-dominant radiation contribution. Early-time matter-radiation equality is evident at $z \sim 10^3$, whilst dark energy becomes dominant at $z \sim 1$. Here dark energy is modelled using as a cosmological constant, and stays dominant into the far-future, $a > 1$.

be provided by more elaborate modifications to gravity, often through extensions to the Einstein-Hilbert action of Einstein gravity such as $f(R)$ theories. Extensions to Einstein gravity must be able to produce the observed large scale structure of the Universe, and reproduce the success of Einstein gravity on Solar System scales (for example in describing the advance of the perihelion of mercury, or observed light bending around the Sun). In the case of the latter, many modified gravity models invoke a chameleon mechanism, where the strength of the modifications are linked to the matter density at that point, ensuring that Einstein gravity is effectively recovered in the high density environment of the Solar System.

1.3 Distance Measures

Light propagates along null geodesics. Starting from the metric, defined in equation (1.1), the radial distance of light propagation between two measurements of cosmic time t_0 and t_1 is given as

$$\chi = \int_{t_0}^{t_1} \frac{c\mathrm{dt}'}{a(t')}. \tag{1.18}$$

Consider the emission and consequent observation of photons in a homogeneous and isotropic Universe as described. As the radial distance χ is a co-moving quantity, then provided the point of emission and observer are not moving relative to each other (other than according to the expansion of the Universe) then χ should be independent of time. Therefore, if δt_0 and δt_1 denote an increment in measured emission and observation time

$$\chi = \int_{t_0}^{t_1} \frac{c\mathrm{dt}'}{a(t')} = \int_{t_0+\delta t_0}^{t_1+\delta t_1} \frac{c\mathrm{dt}'}{a(t')}. \tag{1.19}$$

Expanding and rearranging, this implies that

$$\frac{\delta t_0}{a(t_0)} = \frac{\delta t_1}{a(t_1)} \tag{1.20}$$

where it has been assumed that the scale factor does not vary appreciably over the incremental times δt_0 and δt_1. Choosing the time co-ordinate such that $\delta t \propto 1/\nu$, where ν is a measured frequency shift in spectral lines, then this implies that

$$\frac{\nu_1}{\nu_0} = \frac{a(t_0)}{a(t_1)} = (1+z) \tag{1.21}$$

where z is the measured redshift. Taking the observation to be present day, then this reduces to the relation $a(z) = (1+z)^{-1}$. Equations 1.18 and 1.21 indicate that one can infer knowledge of the expansion history of the Universe by measuring the observed shift in spectral lines from and distance measures to distant galaxies.

When defined such that t_1 is taken as the present day, and t_0 some time that adequately describes the beginning of the Universe, equation (1.18) describes the maximum radial distance that a particle can travel in the age of the Universe. If the integrand converges over the age of Universe such that χ is finite, photons would only have been able to propagate over a finite distance, and it is therefore referred to as a particle horizon χ_{hor}. The particle horizon therefore describes the distance over which

regions of space may be in causal contact.

In defining the particle horizon, we have made the assumption that there exists a well-defined beginning of the Universe, commonly referred to as the 'Big Bang'. This assumption is well motivated for the most common solutions to the Friedmann Equation, with solutions where the scale factor is monotonically increasing. Whilst other more exotic cosmologies can be postulated, such as cyclical 'bouncing' cosmologies, which would violate these assumptions, these models are currently strongly disfavoured with current measurements of cosmological parameters.

As discussed previously, the standard model of cosmology states that the Universe is currently in a period of close-to-exponential expansion in the present era, and the dark energy component of the total mass-energy budget dominates. Further into the past, the Universe was successively matter-dominated and then radiation dominated. At last scattering, where the Universe first becomes transparent and the CMB is free to propagate, the solution to the particle horizon predicts that only areas within approximately one degree of the observed CMB should be in causal contact, provided this period of radiation domination continues to the Big Bang. However, current measurements show that the CMB is isotropic to one part in 10^5 over the whole sky. This is a statement of the horizon problem, which exists provided the particle horizon is finite towards the Big Bang. A solution is provided by the existence of a period of rapid exponential expansion in the early Universe, postulated as the result of an early Inflationary period.

Using the chain rule, the cosmic time can be directly related to the scale factor as

$$t = \int \frac{\mathrm{d}a}{aH(a)}. \tag{1.22}$$

Consequently, the particle horizon may also be recast in terms of the Hubble parameter as

$$\chi_{hor} = \int_0^a \frac{c\mathrm{d}a'}{a'^2 H(a)}. \tag{1.23}$$

1.4 Structure formation

In preceding sections we have described the FRW Universe, one which is completely homogeneous and isotropic. In such a Universe, there could be no formation of structure, as the matter density is equal at all points. However, a direct consequence of

inflationary Big Bang cosmology is that quantum fluctuations in the primordial matter density field expand with the Universe, eventually seeding the formation of structure. Fluctuations in the matter field at position $\mathbf{x}$ and time t are quantified using

$$\delta(\mathbf{x},t) = \frac{\rho(\mathbf{x},t) - \bar{\rho}(\mathbf{x},t)}{\bar{\rho}(\mathbf{x},t)} \tag{1.24}$$

where $\bar{\rho}$ is the global mean density. As previously, the position vector $\mathbf{x}$ is defined in terms of a co-moving distance measure $\mathbf{r}$ and time-dependant scale factor $a(t)$. Taking the time derivative of $\mathbf{x}$

$$\ddot{\mathbf{x}} = \frac{\ddot{a}}{a}\mathbf{x} + \dot{\mathbf{u}} + 2H\mathbf{u} = \frac{\mathbf{g} + \mathbf{g_0}}{a} \tag{1.25}$$

where $\mathbf{u}$ defines the co-moving peculiar velocity, and the acceleration has been split into two terms: g_0 which describes the acceleration due to the global expansion (with $\dot{\mathbf{u}} = \mathbf{u} = 0$); and the peculiar acceleration g. The global acceleration is readily identified as $\mathbf{g_0} = \ddot{\mathbf{a}}\mathbf{x}$, so that the peculiar acceleration is described by

$$\dot{\mathbf{u}} + 2H\mathbf{u} = \frac{\mathbf{g}}{a} = -\frac{\bigtriangledown\phi}{a} \tag{1.26}$$

where ϕ denotes the gravitational potential that sources the acceleration. So far this is an exact solution, however to simplify the solution we continue to linearise the solution from here on out, assuming both $\mathbf{u} \ll 1$ and $\delta \ll 1$. Under the linear assumption, $d/dt = \partial/\partial t + \mathbf{u}\cdot\bigtriangledown\mathbf{u} \rightarrow \partial/\partial t$, so from hereon in, a dotted symbol denotes the partial derivative with respect to time. Locally solving the $\mu = 0$ case of the 4-divergence of the stress-energy tensor $T_{\mu\nu;\nu} = 0$, for the case of a non-relativistic fluid with comoving 4-velocity $U = (c, \mathbf{u})$, the conservation of energy for a fluid with pressure follows

$$\dot{\rho} = -(1+w)\bigtriangledown\cdot(\rho\mathbf{u}) \tag{1.27}$$

$$\rightarrow \dot{\delta} = -(1+w)\bigtriangledown\cdot\mathbf{u} \tag{1.28}$$

where the equation of state has been assumed to be time- and space-independent, and the final approximation takes the linear order perturbation in the density field. Poisson's Equation takes the form

$$\bigtriangledown^2\phi = \frac{3\Omega H^2}{2}(1+3w)\delta. \tag{1.29}$$

Taking the divergence of Equation (1.26), and applying the linearised conservation of energy and Poisson's equations, the matter density fluctuation satisfies

$$\ddot{\delta}(\mathbf{x},t) + 2H\dot{\delta}(\mathbf{x},t) = \frac{3\Omega H^2}{2a}(1+w)(1+3w)\delta(\mathbf{x},t) \tag{1.30}$$

to linear order. Solutions to this equation can then be sought for different values of w, where we consider the separation of the time and spatial dependancies in the density fluctuation through the use of a linear growth factor $\delta(\mathbf{x},t) = D(t)\Delta(\mathbf{x})$. When pressure-less matter (with $w = 0$) dominates, the growing solution[2] satisfies $D(t) = a(t)$, whilst for radiation domination the growing mode satisfies $D(t) = a^2(t)$. Defining the scale factor at radiation-matter cross-over as $a_{\rm eq}$, the growing mode then satisfies

$$D(t) = \begin{cases} a^2(t) & a < a_{\rm eq} \\ a(t) & a > a_{\rm eq} \end{cases} \tag{1.31}$$

1.4.1 Statistics of the field

The matter density field is often described by its statistical properties. By definition, the matter density fluctuation δ has zero mean, so that the field can only be described by second-order or higher moments.

Consider for generality a complex random field, which is isotropic and homogeneous, defined at spatial position x, and denoted by $f(x)$. The two-point correlation function (2PCF) for this field is defined as

$$\xi_f(|y|) = \langle (f(\boldsymbol{x}) - \mu(\boldsymbol{x}))(f(\boldsymbol{x}+\boldsymbol{y}) - \mu(\boldsymbol{x}+\boldsymbol{y}))^* \rangle,$$

where $\langle\rangle$ represents an ensemble average, y the vector connecting the field points where the 2PCF is evaluated, μ the expectation value of the field at that position, and f^* the complex conjugate of the field. To simplify calculations, from here on in we take the random field to be such that the mean is zero everywhere. This means that the ensemble average over many realisations of the field will vanish, and that $\langle f(x) \rangle = 0$. This will not prove to be too restrictive an assumption, and to retrieve a result for a field with non-zero mean simply requires the substitution $f(x) \to f(x) - \mu(x)$. In this case the correlation function reduces to

[2]For each case, there also exists a decaying mode, where the density fluctuations decay with time. For the purposes of describing the structure formation, we consider here only the growing solution.

$$\xi_f(|\boldsymbol{y}|) = \langle f(\boldsymbol{x}) f^*(\boldsymbol{x}+\boldsymbol{y})\rangle \tag{1.32}$$

In this the correlation function is a function only of the distance vector connecting the points where the field is being correlated, enforced as a result of the restriction to homogenous, isotropic random fields. The requirement of isotropy and homogeneity is of particular interest in cosmology, as we frequently invoke the cosmological principle in describing the properties of the Universe, and requires that the statistical properties of observations at any point in the Universe, and in any direction, are indistinguishable.

The field $f(\boldsymbol{x})$ can be expanded in terms of Fourier components $f(\boldsymbol{k})$ as

$$\hat{f}(\boldsymbol{k}) = \int d^n x e^{i\boldsymbol{k}\cdot\boldsymbol{x}} f(\boldsymbol{x}). \tag{1.33}$$

In Fourier space the correlation function can therefore be written as

$$\langle \hat{f}(k)\hat{f}^*(k')\rangle = \int d^n x e^{i\boldsymbol{k}.\boldsymbol{x}} \int d^n x' e^{-i\boldsymbol{k'}.\boldsymbol{x'}} \langle f(\boldsymbol{x}) f^*(\boldsymbol{x'})\rangle \tag{1.34}$$

Using the definition of the correlation function in real space (1.32), and defining $x' \equiv x + y$ this becomes

$$\begin{aligned} \langle \hat{f}(\boldsymbol{k})\hat{f}^*(\boldsymbol{k'})\rangle &= \int d^n x e^{i\boldsymbol{x}.(\boldsymbol{k}-\boldsymbol{k'})} \int d^n y e^{-i\boldsymbol{k'}.\boldsymbol{y}} \xi_f(|\boldsymbol{y}|) \\ &= (2\pi)^n \delta_D(\boldsymbol{k}-\boldsymbol{k'}) \int d^n y e^{-i\boldsymbol{k'}.\boldsymbol{y}} \xi_f(|\boldsymbol{y}|) \\ &= (2\pi)^n \delta_D(\boldsymbol{k}-\boldsymbol{k'}) P_f(|\boldsymbol{k}|) \end{aligned} \tag{1.35}$$

where we have defined the **Power Spectrum** P_f as the Fourier transform of the correlation function

$$P_f(|\boldsymbol{k}|) = \int d^n y e^{-i\boldsymbol{k'}.\boldsymbol{y}} \xi_f(|\boldsymbol{y}|).$$

Homogeneity is enforced by the presence of the Dirac Delta function, which ensures no mixing of modes. Further, isotropy of the random field requires that the power spectrum depend only on $|\boldsymbol{k}'|$.

As discussed in the previous section, the seeds for structure formation in the standard model are provided by the expansion of random quantum fluctuations to cosmological scales. A slow-rolling, single-field inflation predicts matter over-densities which form a Gaussian random field, and are therefore fully described by

two-point statistics such as the power spectrum. Applying the above prescription to the matter density field fluctuations δ, the matter power spectrum is given by P_δ, with total variance, given by summing the contributions from all scales, given as

$$\sigma^2 = \int \mathrm{d}\,(\ln k)\Delta^2(k) \tag{1.36}$$

at a given redshift, where the matter power spectrum has been recast into dimensionless form, $\Delta^2(k) = k^3 P_\delta(k)/2\pi^2$. The contribution to the variance of the field within a certain radius R at a given redshift is given by

$$\sigma^2(R, z) = \int \mathrm{d}\,(\ln k)\Delta^2(k, z)W^2(kR). \tag{1.37}$$

with $W(y) = [\sin(y) - y\cos(y)]/y^3$ a window function which is the Fourier transform of a spherical top-hat in real space. The variance is related to the amplitude of the power spectrum, and is frequently quoted as the contribution to the variance from linear growth within a radius $R = 8h^{-1}\mathrm{Mpc}$, denoted with σ_8.

In setting out the previous prescription, the ensemble average is used, requiring the average to be taken over many different realisations of the field. In reality however, the observer has access only to one realisation, the observable Universe. As it is not possible to formally average over many different ensembles, averages in cosmology are therefore taken under the Ergodic Hypothesis by taking averages over a large volume of the observable Universe, which is expected to contain a large number of statistically independent patches of sky, made possible observationally by large-volume surveys. For the remainder of this work, the ergodic hypothesis is assumed, and averages should be assumed to be taken over large volumes.

1.4.2 Physical Imprints on the field

On super-horizon scales, density fluctuations in both radiation and matter can grow together. However, if a matter density perturbation on a given scale enters the horizon before matter radiation equality, the growth of that perturbation is suppressed due to the rapid radiation driven expansion. This process starts on the smallest scales, and as the horizon size increases with time, larger scale perturbations that fall into the horizon are subsequently suppressed. This continues up until matter radiation equality, after which the matter contribution to the energy budget becomes dominant and matter

density fluctuations are free to grow on all scales. This effect, known as the Mészáros Effect leaves an imprint in the statistics of the matter density field: As the smallest scales enter the horizon first, the matter power spectrum shows the greatest suppression on the smallest scales, and the turnover in the power spectrum preserves information on the size of the horizon at matter-radiation equality, after which modes entering the horizon are no longer suppressed.

Radiation perturbations which enter the sound horizon[3] do not experience a suppression of growth in the same way that collisionless matter does. Instead, sub-horizon radiation perturbations oscillate due to radiation pressure which counteracts the force of gravity. After matter-radiation equality, ionised baryons continue to be tightly coupled to the radiation field through Compton scattering until recombination, $a_{\rm rec}$. Therefore, between $a_{\rm eq}$ and $a_{\rm rec}$, the tightly coupled photon-baryon fluid continues to oscillate. After recombination, the baryon component is no longer coupled to the photon fluid, and is then free to fall into the gravitational wells produced by the growth of matter perturbations in the intervening time. Similarly, the gravitational pull of the displaced baryonic component acts on the underlying cold dark matter distribution, leaving an imprint on the dark matter power spectrum in the form of baryonic acoustic oscillations (BAO), a series of ripples in the power spectrum whose maxima and minima correspond to the number of oscillations the baryon-photon fluid has managed to undertake on a given scale before recombination. The presence of BAO's can therefore give a measure of the sound horizon at recombination.

With these points in mind, a picture of the standard model of 'bottom-up' structure formation is formed. In this picture, structure is formed earliest on the smallest scales, which then in turn can merge to form larger structures as the horizon grows and larger areas become causally connected. This is true only for dark matter candidates for which the dark matter particle is expected to be non-relativistic when it enters the horizon, such as the cold dark matter used in the standard model. In contrast, dark matter candidates which are relativistic when they have entered the horizon suppress structure formation due to the free-streaming of particles moving with a high velocity. For hot dark matter, which postulates light relativistic particles, structure on small scales would then be suppressed up to the time that the particles become non-relativistic, and structure formation then proceeds via a 'top-down' mechanism where the largest structures form first. A measurement of the dark matter power on small

[3]The distance that a relativistic particle can travel in a given time.

scales can then give information on the type of dark matter candidate.

These points give examples of the modifications to the primordial matter power spectrum which occur due to complicated scale-dependent physical processes such as the Mészáros effect and photon-baryon oscillations described above. These modifications are encoded into the transfer function, $T(k)$, defined such that

$$P_\delta(k,a) = T^2(k)D^2(a)P_\delta^{\rm primordial}(k) \tag{1.38}$$

where D is the linear growth factor. The primordial power spectrum is predicted to be scale-invariant and takes the form $P_\delta^{\rm primordial} = Ak^n$, where the spectral index $n \approx 1$ is predicted from inflation and measured from the CMB (see Section 1.6), and A sets the amplitude of fluctuations, typically quoted in terms of σ_8 at $z = 0$. Formally, there exists an independent transfer function for each constituent of the Universe which are scale-factor-dependent, however the combinations of all constituents at late times are well described by a single transfer function which is invariant with time J.A.Peacock (1999).

In particular, the shape of the cold dark matter transfer function is frequently parameterised using the shape parameter Γ, given for curved cosmologies with matter and baryon content as (Sugiyama, 1995)

$$\Gamma = \Omega_{\rm M} h \exp\{-\Omega_B(1+\sqrt{2h}/\Omega_{\rm M})\}, \tag{1.39}$$

which describes the position of the turnover in the power spectrum due to the Mészáros Effect. Several fitting formula are commonly used for the cold dark matter transfer function, (Bardeen et al., 1986; Bond & Efstathiou, 1984; Eisenstein & Hu, 1998). For the remainder of this work, I use the Eisenstein & Hu CDM transfer function, given in Eisenstein & Hu (1998).

1.5 Non-linear structure formation

The results of the previous section are dependent on the validity of the linear approximation, assuming fluctuations in the matter field are small so that higher-than-linear-order terms can be safely ignored. For large scales this approximation is valid, as the root-mean-square fluctuation, defined as in equation 1.37, is much smaller than unity. For small scales, characterised by large k the linear approximation becomes

invalid as the fluctuations in the matter field approach unity and non-linear terms become non-negligible.

The solution to evaluating non-linear structure formation lends itself well to numerical simulations where, provided the dark matter particles are expected to be very weakly interacting, an N-Body simulation need only model the gravitational force on all particles. As modelling a sufficiently large number of bodies at high resolution is computationally expensive, fitting formulae are proposed using fits to simulations, such as that detailed in Peacock & Dodds (1996), to allow accurate modelling of the non-linear matter power spectrum without the computational expense of full N-Body simulations.

Dark matter collapse models, such as spherical collapse, predict the formation of virialised dark matter haloes once the matter fluctuation exceeds a critical value for collapse. The halofit formula (Smith et al., 2003) proposes a method of estimating the non-linear matter power using the halo model formalism of Peacock & Smith (2000); Seljak (2000), in which the total matter power is split into a one-halo and two-halo term

$$\Delta^2_{\rm NL}(k) = \Delta^2_{\rm 2h}(k) + \Delta^2_{\rm 1h}(k) \tag{1.40}$$

which describe the contribution to power from the large scale placement of dark matter haloes, and the contribution to power from the self-correlation of haloes respectively. The two-halo (2h) term is the quasi-linear term, which depends on the distribution of massive dark matter haloes and their bias with respect to the underlying dark matter density field, and the one-halo term corresponds to the fully non-linear contribution. For the remainder of this text, I use Smith et al. (2003) non-linear corrections to the matter power spectrum.

Figure 1.3 shows the dimensionless non-linear matter power using Smith et. al. non-linear corrections against the fully linear power spectrum, for a ΛCDM cosmology. From this figure the turnover of the power spectrum due to the Mészáros effect is evident at $k \sim 0.1h\mathrm{Mpc}^{-1}$, as well as increased small scale power due to non-linear effects for $k > 0.1h\mathrm{Mpc}^{-1}$.

1.6 Discordant Cosmology?

Modern cosmological measurements can be well explained with the single framework of concordance (or ΛCDM) cosmology, which postulates a present-day Universe

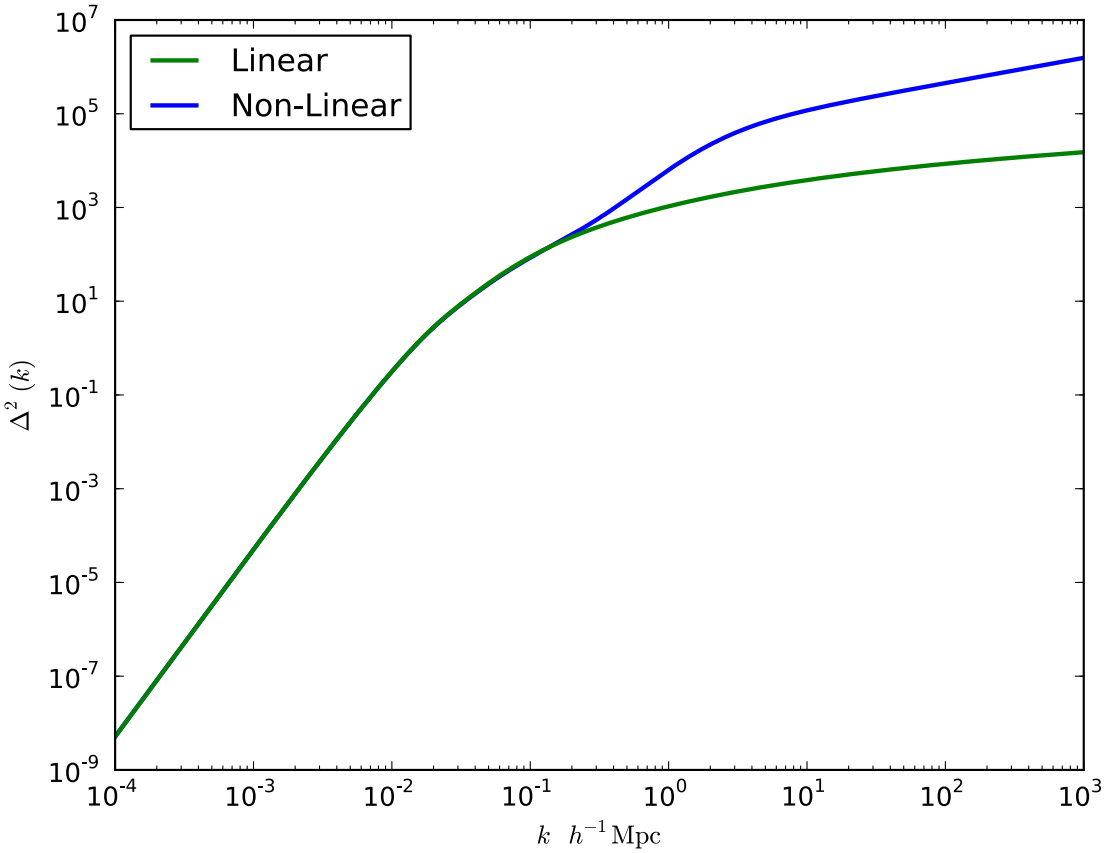

Figure 1.3: The matter power spectrum, in dimensionless form, in the linear approximation using Eisenstein & Hu transfer functions, and with non-linear corrections as given by Smith et al. (2003)

dominated by a non-dynamical dark energy and dark matter, and whose background geometry is well-described by the homogenous and isotropic FRW metric defined in Section 1.1. The concordance framework can be described by a small number of cosmological parameters, which are accurately measured with current observations. In this Section, I summarise cosmological measurements of an important subsection of this parameter space.

The cosmic microwave background (CMB) is a background of relic radiation left over from the last scattering surface at $z \approx 1100$, when the recombination of the ionised particles produced during Big Bang Nucleosynthesis caused the Universe to first become neutral, and transparent to radiation. Observations of the CMB, such as those by Planck (Collaboration et al., 2013a,c) and its predecessors, show that this relic radiation field is described by a thermal Planck spectrum across the sky. At the moment of last scattering, matter domination had already begun, and structure formation on sub-horizon scales left an imprint of order 10^{-5} in the form of a temperature shift in the radiation, primarily the result of temperature shifts as the radiation climbed out of gravitational potential wells on large scales, and damped fluctuations due to matter-radiation coupling on small scales. The measurement of the temperature power spectrum of the CMB takes the form of a series of peaks (see Figure 1.4), and the measurement of the position and amplitude of these peaks gives cosmological information such as information on the curvature, spectral index and matter density. Primary fluctuations in the CMB power spectrum are only weakly dependent on dark energy, however secondary effects, such as the Integrated-Sachs-Wolfe effect and lensing of the CMB by large scale structure, give some dark energy dependance. Further information can be added with low-redshift probes such as Supernova 1a (SN1a), weak gravitational lensing, and Baryonic Acoustic Oscillations (BAO).

BAOs originate from oscillations in the photon-radiation field up to the point of recombination, after which dark- and baryonic- matter fall into each others gravitational potential wells, leaving a small imprint on the matter power spectrum close the horizon size at matter radiation equality (see Figure 1.5). The position of the first BAO peak is related to the sound horizon at the time of recombination, much like the acoustic peak in the CMB, and therefore measurements of the BAO peaks in the matter power spectrum can be used to infer cosmology through angular diameter distances. Measurements in redshift space are also affected by redshift space distortions (RSD), which originate from the fact that the observed redshift of a galaxy is

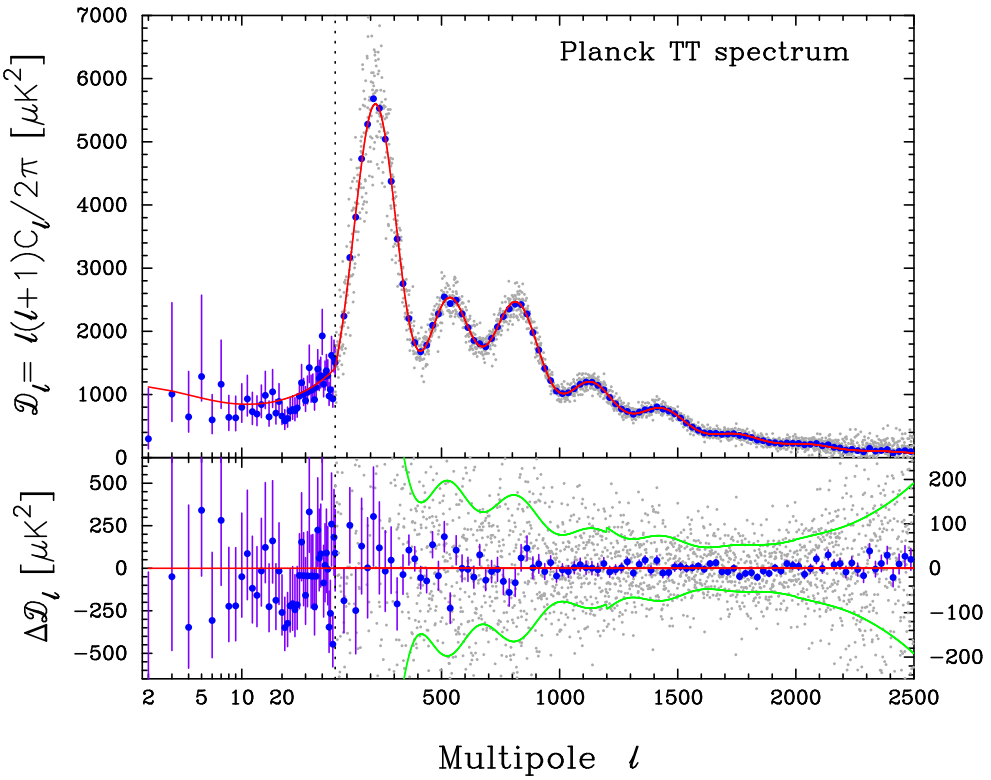

Figure 1.4: The measured CMB temperature power spectrum from Planck, from Collaboration et al. (2013b). The lower panel shows the ratio of the measured power to the fit ΛCDM model.

dependant not only on the redshift due to the Hubble flow, but also peculiar velocities due to galaxy infall or random motion near the centre of local over-densities. The dark matter power spectrum can only be inferred indirectly through galaxy surveys, though under the assumption that baryonic matter closely follows the underlying dark matter field the galaxy density field can be related to the dark matter density through a galaxy bias term, which is usually assumed to be linear and scale invariant on large scales. Measurements of the galaxy power spectrum from large-scale surveys can given constraints on cosmology through BAOs, RSDs or a direct measure of the power spectrum under assumptions on the galaxy bias. Such measurements have been undertaken with a variety of modern surveys, such as WiggleZ (Blake et al., 2010, 2011), GAMA (Blake et al., 2013), 6dFGRS (Beutler et al., 2011) and BOSS (Anderson et al., 2012; Percival et al., 2010).

Supernova Type 1a are extremely luminous standardisable candles, and can be used to infer luminosity distances to large redshift. Comparison of the inferred luminosity distance with observed redshift then gives a measure of the expansion history, and provided the first compelling evidence for a present-day accelerating Universe (see Section 1.2), and measurements using supernovae can provide a precise measurement of the present-day Hubble parameter, H_0 (Riess et al., 2011).

Finally, cosmology can be inferred from gravitational lensing, through the measurement of distortions in the observed shape of galaxies using cosmic shear, changes in the observed size of a population of lensed sources, or fluctuations in number counts in a flux-limited survey using the cosmic magnification effect. A fuller discussion of these techniques is left until Chapter 2, however cosmological parameter estimation has been carried out using the CFHTLenS survey in Heymans et al. (2013); Kilbinger et al. (2013); Kitching et al. (2014), whilst Simpson et al. (2013) constrains a general modified gravity parameterisation. Figure 1.6 shows constraints on the matter density and amplitude of the matter power spectrum for CFHTLenS, in combination with BAO measurements from BOSS and CMB measurements from WMAP7, taken from Heymans et al. (2013).

Recent results from Planck (Collaboration et al., 2013b) probe the CMB to unprecedented accuracy, allowing for the precision measurement of many cosmological parameters, a subsection of which I present in Table 1.1. Further to those values listed in Table 1.1, Planck with CMB lensing measurements infers a spatially flat cosmology, with the total matter density differing from one by less than approximately a tenth of

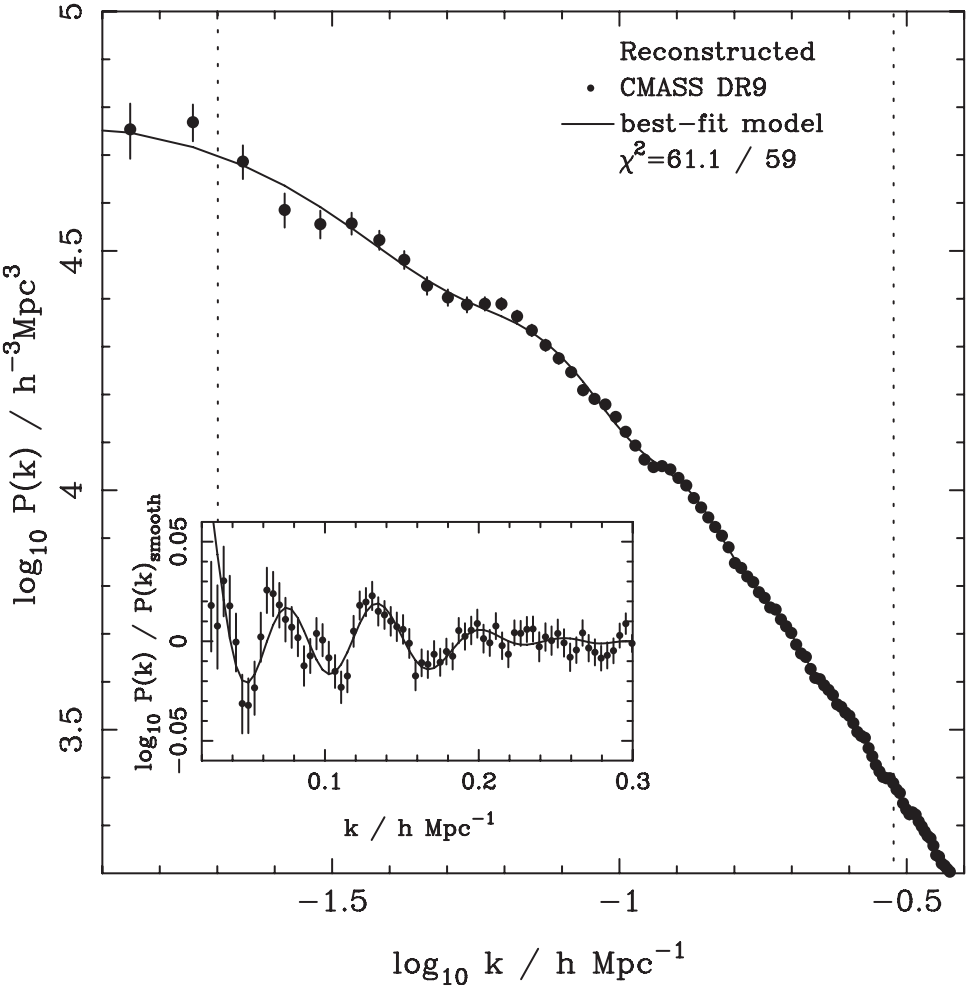

Figure 1.5: The measured matter power spectrum, using BOSS DR9 Anderson et al. (2012). Inset shows the BAO features.

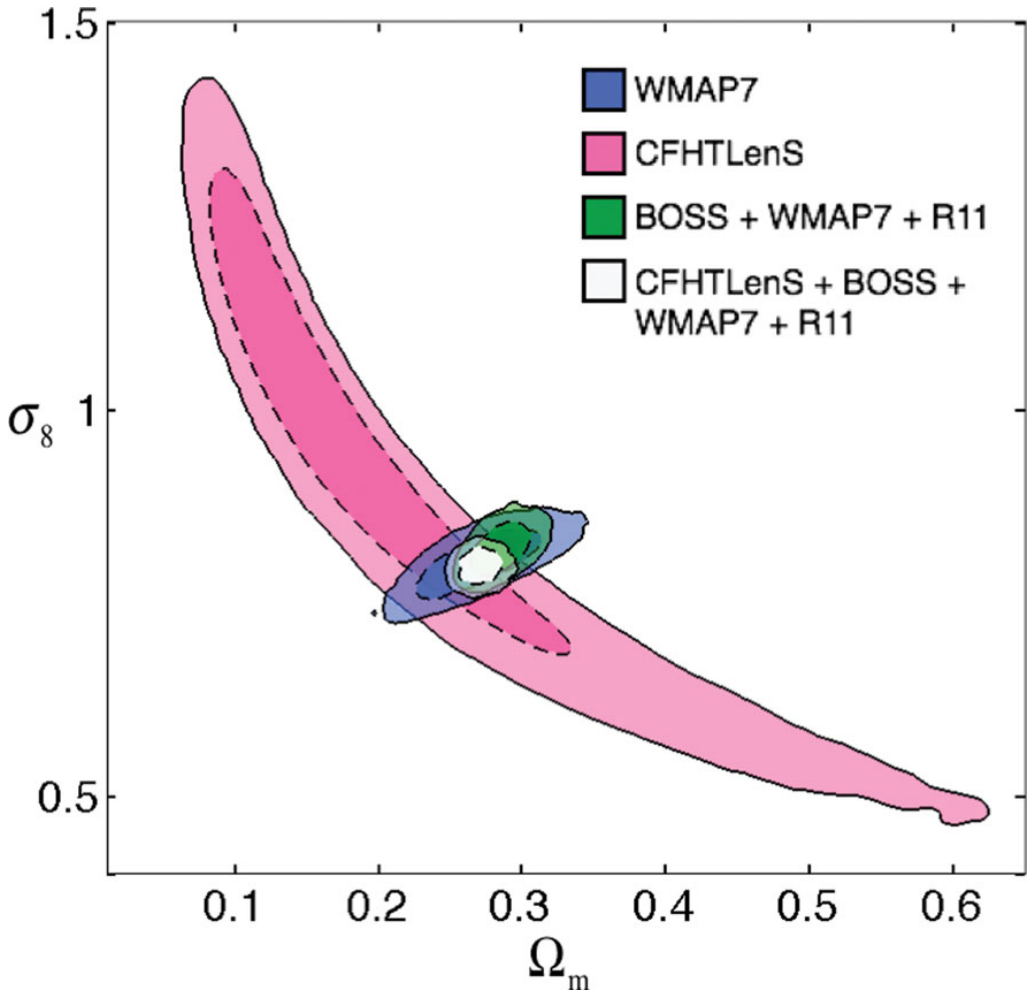

Figure 1.6: Constraints on Ω_M and σ_8 from a six-bin tomographic analysis (pink), for WMAP7 (blue), the combination of WMAP7, BOSS and Supernova with Cepheids (Riess et al., 2011) (R11), and the full combination of all of these (white). Taken from Heymans et al. (2013).

Table 1.1: Cosmological parameter constraints from the Planck analysis, as given in Collaboration et al. (2013b) . All results are best fit values taken from Planck alone, except for the dark energy equation of state w which is the value quoted for a combined Planck+BAO measurement.

Parameter	Value	Error
H_0	67.3	± 1.2
w_0	-1.13	$^{+0.24}_{-0.25}$
Ω_Λ	0.685	$^{+0.017}_{-0.016}$
Ω_M	0.315	± 0.016
σ_8	0.828	± 0.012
n_s	0.9585	± 0.007

a percent. It is clear that those cosmological parameters listed are measured to great accuracy using Planck data, however there exists some tension between the Planck results listed, and those found from other cosmological probes. Of particular note, the inferred value of H_0 from Planck data is noticeably lower than direct measurements from supernovae and lensing time delays, and previous measurements of the CMB from WMAP. For example, Riess et al. (2011) measure $H_0 = 73.8 \pm 2.4\ \mathrm{kms^{-1}Mpc^{-1}}$ using a combination of Type 1a supernovae and cepheids, approximately 2σ off the quoted Planck value. Similarly, measurements of the combination of σ_8 and Ω_M from Planck differ from those presented in Heymans et al. (2013) by approximately 2σ, and also with a 3σ discrepancy with an analysis of rich cluster counts using Planck data itself.

Whilst we are clearly in an era of precision cosmology, these discrepancies are concerning. On top of this, whilst current measurements suggest no deviation from standard ΛCDM cosmology, the model still leaves outstanding questions regarding the nature of the dark sector. Further observations can help to address these issues, and motivate a drive to produce accurate measurements of cosmology through a wide range of techniques, in part by reducing systematic errors as much as possible, as well as attempting to reduce statistical errors and mitigate systematics using a combination of various probes. By maximising the output of various current and forthcoming surveys, we can obtain a firmer grasp on the properties of the Universe in which we live.

Chapter 2

Gravitational Lensing

2.1 Introduction

In the previous chapter, I have detailed a selection of the most promising probes of cosmology. Included in this list was gravitational lensing, and it is on this topic that I focus the current chapter.

As light propagates through the Universe, its trajectory can be bent due to the presence of intervening matter. This phenomenon is predicted in Newtonian gravity, but gains a more solid basis from general relativistic arguments: indeed, the measurement of gravitational lensing by the mass of the Sun was one of the major indicators that led to the general acceptance of general relativity as the current theory of gravity. This effect is known as gravitational lensing, the etymology of which can be explained due to the similarity with classical optics, and the fact that it is induced by the effect of the gravitational potential of the foreground "lensing" matter. Tidal forces due to the gravitational potential of the foreground matter (the lens) induce observed changes in the shape, size and received flux from lensed background galaxies (the source), measurements of which can be used as a probe of the local lensing matter, and cosmology with lensing by large scale structure.

The total lensing effect on a source image is the sum of lensing on a macro-scale, where the lensing body is typically of galactic size or larger, and micro-lensing, where the lensing body is typically small compact bodies such as a star or brown dwarf. Due to the small lens mass typically associated with micro-lensing effects, such measurements usually require the close alignment of the source and lens. Where the lens shows observable movement with time against a luminous source background,

such as with bodies within the local group, the change in flux of the source due to the lens can be measured as a function of time via a measurement of the light-curve of the source, as is in this case a dynamical measure.

The lensing effect can be further sub-divided into two categories. Strong-lensing considers the lensing effect of bodies which are massive or sufficiently compact such that the Einstein radius of the lens is larger than the angular size of the lensing body itself: strong-lensing features such as giant arcs (fragments of Einstein rings) and multiple source images are observable for sources lying within the Einstein radius of the lens, but far enough from the source centre so as not to be obscured, and are therefore detectable. Due to the typically massive nature of the lens, strong-lensing events are the most striking of the three categories. For this reason, and the requirement that source, observer and lens be well-aligned, strong lensing events are rare, limiting its use as a cosmological probe. However, it can be used as a probe of the dark matter distribution of the lens, as well as a method of determining the Hubble parameter using the time delay of multiply imaged sources (e.g. Suyu et al. (2013)).

In contrast, weak lensing occurs when the source-lens geometry is such that distortions on the source are small, and therefore the signal must be extracted through the use of statistics on an acceptably large source sample. The use of intermediate mass lenses without the requirement for strict alignment allows for the use of a much larger sample of galaxies. It is this that makes weak-lensing particularly appropriate for the study of the large-scale structure of the Universe, and consequently the use of weak (macro-) gravitational lensing as a probe of cosmology has developed tremendously in recent years. It can be considered one of the most promising probes of the Universe due to the clean nature of the underlying theory, relying as it does only on well-understood geometry in the absence of contaminants. Furthermore, it is indifferent to the nature of the lensing matter. The use of traditional lensing techniques is complicated by difficulties in measurements of galaxy shapes and sizes, particularly for the smallest source galaxies, and complex astrophysical contaminants. Further, the accurate interpretation of weak lensing measurements requires the accurate modelling of the distribution of matter in the Universe as a function of cosmological parameters, which is particularly difficult on small scales where non-linear structure formation and baryonic physics become important. As a result, much of the work done by the weak lensing community since its inception has focussed on understanding and mitigating the source of systematics in weak lensing measurements and statistics, with

the result that recently weak lensing analyses have produced cosmological constraints that are competitive with other probes, such as the lensing analysis carried out with CFHTLenS (Heymans et al., 2013; Kitching et al., 2014; Kilbinger et al., 2013). This is a situation that will only improve with time, with the large wealth of data coming from forthcoming large-scale surveys such as KiDS (de Jong et al., 2013), Euclid (Laureijs et al., 2011), LSST [1], DES (Melchior et al., 2014), and HSC [2], and with the investment in the community that the requirements of these surveys bring, in particular with precision requirements in cosmological parameter estimation.

The layout of this Chapter is as follows: first, I detail the theory behind gravitational lensing, starting from deviations to the path of propagation for a photon passing a point mass and extended mass distributions, and considering the mapping of a source from the source plane to the observed plane, with special attention to the distortion in images from the shear and magnification effect. This framework is extended to lensing by large-scale structure, which forms the basis of cosmic shear and cosmic magnification analyses. Finally, I detail the use of shear and magnification analyses, their use in determining cosmological parameters or probing the lensing matter distribution, and notable successes and challenges in the field. I pay special attention to the flux- and size-magnification, and how these measurements are being used in recent literature, with a comparison between the relative strengths of a shear and magnification analysis.

2.2 Gravitational Lensing Theory

2.2.1 Light Deflection

Figure 2.1 shows the deflection of light form a distant source due to an intervening mass, with the deflection angle for a photon by a point mass M given as

$$\hat{\alpha} = \frac{4GM}{c^2\xi} = \frac{2R_S}{\xi} \tag{2.1}$$

where ξ is the impact parameter, denoting the closet point of approach of the photon to the lensing mass, and R_S is the Schwarzchild radius. If the photon passes far from the event horizon of the mass, $\xi \gg R_S$, the deflection angle is small, $\hat{\alpha} \ll 1$. Under the assumption that the weak field limit holds along the photon's path, this can be

[1] http://www.lsst.org/lsst/

[2] http://www.naoj.org/Projects/HSC/

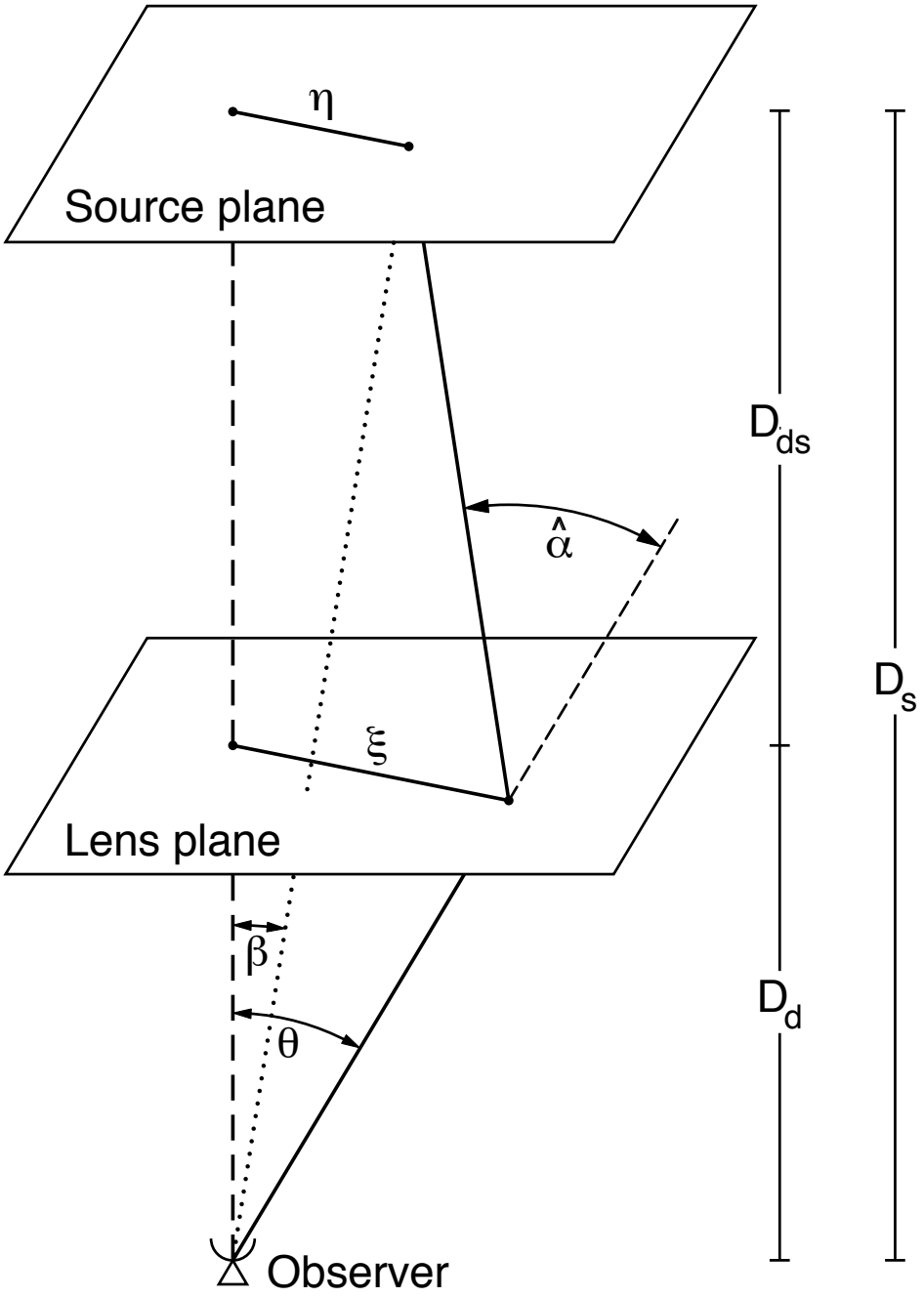

Figure 2.1: Diagram showing the cross-section of a lensing system: the light emitted by a source at lensed angular position β is bent through a deflection angle $\hat{\alpha}$ by the presence of an intervening mass source, here assumed to be thin and well-defined on a lens plane. As a result, the observer sees the source at angular position θ. Angles quoted here are two dimensional vectors denoting their position on the sky, and the angular diameter distance is denoted D, with subscripts s, d, ds denoting distance to the source, to the deflector (lens), and between the lens and source respectively. Taken from Bartelmann & Schneider (2001).

generalised to an extended source by summing the linearised deflections along the line of sight. The deflecting mass with a infinitesimal volume element is given by

$$dM = \rho(\boldsymbol{\xi}, \chi)\mathrm{d}^2\xi\mathrm{d}\chi, \tag{2.2}$$

where $\boldsymbol{\xi}$ defines the two-dimensional lens plane, and χ is the radial distance as defined in the metric (Equation 1.1). The generalised deflection angle for an extended source is then

$$\hat{\boldsymbol{\alpha}}(\boldsymbol{\xi}) = \frac{4G}{c^2}\int \mathrm{d}^2\xi' \int \mathrm{d}\chi'\ \rho(\boldsymbol{\xi}', \chi')\frac{\boldsymbol{\xi} - \boldsymbol{\xi}'}{|\boldsymbol{\xi} - \boldsymbol{\xi}'|^2}, \tag{2.3}$$

$$= \frac{4G}{c^2}\int \mathrm{d}^2\xi'\ \Sigma(\boldsymbol{\xi}')\frac{\boldsymbol{\xi} - \boldsymbol{\xi}'}{|\boldsymbol{\xi} - \boldsymbol{\xi}'|^2}, \tag{2.4}$$

where $\Sigma(\boldsymbol{\xi}) = \int d\chi\rho(\boldsymbol{\xi}', \chi)$ is the radially projected surface mass density. This result assumes the Born- and thin-lens-approximations, which require that the deflection angle over each infinitesimal line-of-sight-segment is small on the scale over which the lensing mass distribution changes, so that the photon's path of propagation is well-approximated by a straight line in the vicinity of the lensing mass, and the impact parameter to the mass in an infinitesimal volume $\mathrm{d}^3r = \mathrm{d}^2\xi'\mathrm{d}\chi'$ is approximately $\boldsymbol{\xi} - \boldsymbol{\xi}'$. Whilst this approximation holds for a large number of astrophysical situations such as lensing by individual galaxies and clusters, this prescription must be generalised when the lensing mass extends from the source to the observer, such as lensing by large-scale-structure. In this case, the cosmological expansion means that a 'straight' fiducial ray of light is ill-defined, and so the separation between two closely neighbouring photons must be used. I consider this situation in Section 2.2.6.

The observed angular position of the source on the sky $\boldsymbol{\theta}$, its undeflected angular position $\boldsymbol{\beta}$, and the deflection angle $\hat{\boldsymbol{\alpha}}$ can all be related with the lens equation

$$D_s\boldsymbol{\theta} = D_s\boldsymbol{\beta} + D_{ds}\hat{\boldsymbol{\alpha}} \tag{2.5}$$

using the angular diameter distances D_s, D_d and D_{ds} as defined in Figure 2.1 and assuming small angles. This can be recast into the simpler form

$$\boldsymbol{\theta} = \boldsymbol{\beta} + \boldsymbol{\alpha}; \qquad \boldsymbol{\alpha} = \frac{D_{ds}}{D_s}\hat{\boldsymbol{\alpha}}, \tag{2.6}$$

with $\boldsymbol{\alpha}$ the *reduced deflection angle*. Under the small angle approximation, the impact

parameter may also be recast as $\boldsymbol{\xi} = D_l\boldsymbol{\theta}$, so that the reduced deflection angle can be recast in terms of the surface mass density using Equation (2.3) as

$$\boldsymbol{\alpha}(\boldsymbol{\theta}) = \frac{4D_dD_{ds}G}{D_sc^2}\int \mathrm{d}^2\theta'\ \Sigma(\boldsymbol{\theta'})\frac{\boldsymbol{\theta}-\boldsymbol{\theta'}}{|\boldsymbol{\theta}-\boldsymbol{\theta'}|^2}, \tag{2.7}$$

$$= \frac{1}{\pi}\int \mathrm{d}^2\theta'\kappa(\boldsymbol{\theta'})\frac{\boldsymbol{\theta}-\boldsymbol{\theta'}}{|\boldsymbol{\theta}-\boldsymbol{\theta'}|^2}, \tag{2.8}$$

where I have defined the weak lensing *convergence* κ as

$$\kappa(\boldsymbol{\theta}) = \frac{\Sigma(\boldsymbol{\theta})}{\Sigma_{cr}}; \quad \Sigma_{cr} = \frac{c^2D_s}{4\pi GD_{ds}D_d}. \tag{2.9}$$

Defining the *weak lensing potential*, ϕ, as

$$\phi(\boldsymbol{\theta}) = \frac{1}{\pi}\int \mathrm{d}^2\theta'\kappa(\boldsymbol{\theta'})\ln|\boldsymbol{\theta}-\boldsymbol{\theta'}| \tag{2.10}$$

the reduced deflection angle can be recast as

$$\boldsymbol{\alpha} = 2\nabla_\theta\phi. \tag{2.11}$$

The reduced deflection which satisfies the lens equation is then sourced by the lensing potential ϕ, which satisfies the Poisson equation

$$\nabla^2_\theta\phi(\boldsymbol{\theta}) = 2\kappa(\boldsymbol{\theta}). \tag{2.12}$$

2.2.2 Image Distortions

The framework of the previous section can be extended to describe the alteration in the observed image of an extended source as it is lensed by a massive foreground, as photons emitted by the source are deflected differentially. If the distortion of the image is small compared to the scale over which the lens properties change, so that the lensing convergence does not change across the image, the linear distortion can be described by the Jacobian

$$\mathcal{A} = \frac{\partial\boldsymbol{\beta}}{\partial\boldsymbol{\theta}} = \delta^{ij}_K + \frac{\partial^2\phi}{\partial\theta_i\partial\theta_j}, \tag{2.13}$$

where I have used Equations (2.6) and (2.11). Defining the complex shear as $\gamma \equiv \gamma_1 + i\gamma_2 = |\gamma|e^{2i\psi}$, which satisfies

$$\begin{aligned} \gamma_1 = \ & \tfrac{1}{2}(\phi_{11} - \phi_{22}) \ & = |\gamma|\cos(2\psi), \\ \gamma_2 = \ & \phi_{12} = \phi_{21} \ & = |\gamma|\sin(2\psi), \end{aligned} \tag{2.14}$$

where subscripts denote differentiation with respect to the angular component, and ψ denotes the polar angle of the source, this can be simplified to

$$\mathcal{A} = \begin{pmatrix} 1-\kappa-\gamma_1 & -\gamma_2 \\ -\gamma_2 & 1-\kappa+\gamma_1 \end{pmatrix} \tag{2.15}$$

$$= (1-\kappa)\begin{pmatrix} 1-g_1 & -g_2 \\ -g_2 & 1+g_1 \end{pmatrix}, \tag{2.16}$$

where I have used Equation (2.12), and defined the reduced shear $g = (1-\kappa)^{-1}\gamma$.

The convergence causes an equal distortion along both basis angles; $\gamma_1 > (<)\ 0$ causes a contraction (expansion) along the θ_1 direction, with a simultaneous expansion (contraction) in the θ_2 direction; whilst a non-zero γ_2 causes a contraction/expansion along $|\beta| = \pm\gamma_2|\theta|$, in the $\theta_1 = \theta_2$ and $\theta_1 = -\theta_2$ direction. This can also be seen through the definition of the complex shear given above, where ψ describes the orientation of the source: an elliptical source would be expected to be invariant under a rotation of π radians, which is accounted for in the phase; similarly, γ_1 is equal to γ_2 under a phase change of $\pi/4$. Thus γ_1 measures the distortion along a given axis in the image plane, whilst γ_2 measures distortions at 45^o to this axis. The convergence then describes an isotropic expansion or contraction of the source with no distortion in its shape, whilst the shear describes the change in observed shape of the source due to the lens.

As gravitational lensing contains no mechanism for the emission or absorption of photons, a consequence of Liouville's theorem (Appendix A.1) is that the surface brightness of the source is conserved locally, so that $I(\beta) = I(\theta)$. The magnification of the source, defined as the ratio of the observed intensity to the intensity of the unlensed source, is then determined only by its change in area, and determined by the inverse of the localised Jacobian mapping:

$$\mu = [\det(\mathcal{A})]^{-1} = [(1-\kappa)^2 - \gamma^2]^{-1}. \tag{2.17}$$

In the weak lensing regime, which corresponds to $\kappa, |\gamma| \ll 1$, the linearised magnification reduces to

$$\mu \approx 1 + 2\kappa. \tag{2.18}$$

As the observed intensity of the source is given by the source surface brightness profile integrated over its surface area, an induced increase in the size of the source also corresponds to an *amplification* in its total observed flux or magnitude, an effect which can be used as a probe of the lensing matter in an analysis using the magnification effect.

In the special case of an axially-symmetric lens mass profile, the projected surface mass distribution and convergence vary symmetrically with transverse separation about a given origin, and satisfy $\Sigma(\boldsymbol{\xi}) = \Sigma(|\boldsymbol{\xi}|)$ and $\kappa(\boldsymbol{\theta}) = \kappa(|\boldsymbol{\theta}|)$. For this distribution, the reduced deflection angle, as defined in Equation (2.7), can be recast as

$$\begin{aligned} \boldsymbol{\alpha} &= 2\frac{\boldsymbol{\theta}}{|\boldsymbol{\theta}|^2}\int_0^{|\boldsymbol{\theta}|} \mathrm{d}\theta'\ \theta'\kappa(\theta'), & (2.19)\\ &= \boldsymbol{\theta}\bar{\kappa}(|\boldsymbol{\theta}|) & (2.20) \end{aligned}$$

provided that the origin is defined such that $\boldsymbol{\theta}$ and $\boldsymbol{\theta'}$ are measured from the centre of the mass distribution, and where in the final step I have defined the average convergence within a sphere of radius $|\boldsymbol{\theta}|$,

$$\begin{aligned} \bar{\kappa}(|\boldsymbol{\theta}|) &= \frac{2\pi\int_0^{|\boldsymbol{\theta}|}\mathrm{d}\theta'\ \theta'\kappa(\theta')}{\pi|\boldsymbol{\theta}|^2}, & (2.21)\\ &= \frac{m(|\boldsymbol{\theta}|)}{|\boldsymbol{\theta}|^2}, & (2.22) \end{aligned}$$

and $m(|\boldsymbol{\theta}|) = 2\int_0^{|\boldsymbol{\theta}|}\mathrm{d}\theta'\ \theta'\kappa(\theta')$ is a dimensionless mass contained in that sphere. Using the definition of the critical surface mass density, Σ_{crit} and the small angle formula to relate angles to a physical size via the angular diameter distance, the deflection angle in this case can be reduced to

$$\hat{\boldsymbol{\alpha}} = \frac{4GM(|\boldsymbol{\xi}|)}{c^2}\frac{\boldsymbol{\xi}}{|\boldsymbol{\xi}|^2}; \quad M(|\boldsymbol{\xi}|) = 2\pi\int_0^{\xi}\mathrm{d}\xi'\ \xi'\Sigma(\xi') \tag{2.23}$$

We see then that the deflection angle induced by the lensing of an axially-symmetric foreground mass distribution is the same as that for a point lens, with mass equal to the

mass contained within a sphere defined by the impact parameter of the lensed photon $\boldsymbol{\xi}$. This states that the deflection caused by the mass of the lens outside the sphere bounded by the impact parameter of the passing photon exactly cancels to zero, and thus has no effect on the observed position of the source, a result which is a direct analogy to Birkhoff's Theorem.

Using Equation 2.20, the lens equation can be rewritten as

$$\boldsymbol{\beta} = [1 - \bar{\kappa}(|\boldsymbol{\theta}|)]\boldsymbol{\theta}, \tag{2.24}$$

so that the lensing Jacobian which describes the mapping from the observed position on the lens plane to the intrinsic position on the source plane is given by

$$\mathcal{A} = [1 - \bar{\kappa}]\mathbb{I} - \frac{\kappa'}{|\boldsymbol{\theta}|}\begin{pmatrix} \theta_1^2 & \theta_1\theta_2 \\ \theta_1\theta_2 & \theta_2^2 \end{pmatrix}, \tag{2.25}$$

where $\kappa' = \partial\kappa/\partial\theta = 2[\kappa - \bar{\kappa}]/\theta$.[3] Defining $\theta_1 = |\boldsymbol{\theta}|\cos\psi$, $\theta_2 = |\boldsymbol{\theta}|\sin\psi$, this can be rearranged into

$$\mathcal{A} = [1 - \kappa]\mathbb{I} - 2[\kappa - \bar{\kappa}]\begin{pmatrix} \cos^2(\psi) + \frac{1}{2} & \cos(\psi)\sin(\psi) \\ \cos(\psi)\sin(\psi) & \sin^2(\psi) + \frac{1}{2} \end{pmatrix}, \tag{2.26}$$

so that by comparison with Equation (2.16) the shear can be identified as

$$\gamma = [\kappa - \bar{\kappa}]e^{2i\psi}, \tag{2.27}$$

and

$$\kappa \propto \Sigma;\ \gamma \propto \Sigma - \bar{\Sigma}, \tag{2.28}$$

follows. Thus, the shear and convergence of a source probe the lensing mass distribution in two different ways: the convergence at a given position such as that measured directly with magnification probes the surface mass density at that position, whilst the measured shear probes the difference between the surface mass density at that position minus the mean within a sphere bounded by that position.

[3]To see this result, one may use $\frac{\partial m(|\boldsymbol{\theta}|)}{\partial\theta_i} = 2\boldsymbol{\theta}_i\kappa(|\boldsymbol{\theta}|)$ and $\frac{\partial m(|\boldsymbol{\theta}|)}{\partial\theta_i} = -2\frac{\boldsymbol{\theta}_i}{|\boldsymbol{\theta}|^3}$, where the former is found by defining X such that $\frac{\partial X}{\partial\theta} = \theta\kappa(\theta)$ so that $m(|\boldsymbol{\theta}|) = 2[X(\theta) - X(0)]$.

Tangential Shear

The shear components γ_1, γ_2 are defined in a Cartesian reference co-ordinate frame, however it is often more convenient to define the measurement of shear and ellipticity in a reference frame which is defined from the centre of a mass density, as a foreground over-density tends to shear a source image tangentially to the centre of the mass distribution. Defining the angular position of a source with respect to some origin as $\boldsymbol{\theta} = \theta(\cos(\varphi), \sin(\varphi))$, where φ measures a direction as the orientation of the angular position of the source from some line projecting radially from the origin, the tangential- and cross- component of the shear, which denote the component of the shear in a co-ordinate system orientated radially from the lens, and at 45^o to this axis respectively, can be defined as

$$\gamma_{\rm t} = -\Re[\gamma e^{-2i\varphi}]; \;\; \gamma_{\times} = -\Im[\gamma e^{-2i\varphi}]$$

For a circularly symmetric mass distribution the complex shear in cartesian co-ordinates satisfies Equation 2.27, and the tangential shear satisfies

$$\gamma_{\rm t} = \bar{\kappa} - \kappa; \;\; \gamma_{\times} = 0,$$

showing that weak lensing induces shears tangential to the mass distribution, as can be seen in the massive arcs which can be observed around galaxy clusters. In general, it can be shown that for any mass distribution the tangential shear satisfies

$$\langle \gamma_{\rm t} \rangle = \bar{\kappa} - \langle \kappa \rangle$$

where $\langle \kappa(\boldsymbol{\theta}) \rangle$ denotes the mean surface mass density on a circle of radius $\boldsymbol{\theta}$ (Bartelmann & Schneider, 2001). Thus, a measurement of the tangential shear, such as that provided by galaxy-galaxy lensing, averaged over concentric circles defined about some origin can measure the azimuthally-averaged mass profile of the lens, independently of its underlying symmetry.

2.2.3 Mass Profiles

Singular Isothermal Sphere

A singular isothermal sphere profile describes a dark matter mass profile of the form

$$\rho(r) = \frac{\sigma_v^2}{2\pi G}\frac{1}{r^2}. \tag{2.29}$$

By integrating along the line of sight, using the transformation $\psi = \tan^{-1}(z/\xi)$ between limits $\psi_{\pm\infty} = \pm\pi/2$, where z denotes the line of sight direction, it can be shown that the surface mass density satisfies

$$\Sigma(\xi) = \frac{\sigma_v^2}{2G}\frac{1}{\xi}, \tag{2.30}$$

and the mass contained within a radius R is then given by

$$M(< R) = \int_0^R \xi\, d\xi \int_0^{2\pi} d\psi\, \Sigma(\xi) \tag{2.31}$$

$$= \frac{\pi\sigma_v^2 R}{G}. \tag{2.32}$$

From the form of the surface mass density, Equation (2.30), it can be seen that the SIS profile is divergent at $\xi = 0$, giving a singular surface mass density at the centre of the halo. As well as this, the mass contained within a profile of the form given in Equation (2.31) is unbounded from above[4]. As a result, the SIS profile is frequently defined as

$$\Sigma(\xi) = \frac{\sigma_v^2}{2G}\left[\frac{1}{\sqrt{\xi^2 + \xi_{\rm core}^2}} - \frac{1}{\sqrt{\xi^2 + \xi_{\rm t}^2}}\right], \tag{2.33}$$

with a core radius, $\xi_{\rm core}$, and truncation radius, $\xi_{\rm t}$. Using this definition, the surface mass density is approximately constant within the core radius, tends to zero outside the truncation radius and declines as approximately inverse radius within these limits,

[4]From this, it is also noticeable that the mass contained in a sphere of radius R is never divergent when the upper limit is finite, despite the singularity at the centre of the halo.

as required from its definition

$$\Sigma(\xi) \approx \begin{cases} \frac{\sigma_v^2}{2G}\frac{1}{\xi_{\rm core}} & (\xi \ll \xi_{\rm core}) \\ \frac{\sigma_v^2}{2G}\frac{1}{\xi} & (\xi_{\rm core} \ll \xi \ll \xi_{\rm t}) \\ 0 & (\xi_{\rm t} \ll \xi) \end{cases} \tag{2.34}$$

The universal profile

The mass profile presented in Navarro, Frenk & White (1997), commonly referred to by the acronym NFW or as the 'universal' profile, describes a dark matter mass profile with density given as

$$\rho(r) = \frac{\delta_c \rho_c}{(r/r_s)\,(1 + r/r_s)^2}, \tag{2.35}$$

where $\rho_c = \frac{3H^2(z_{\rm halo})}{8\pi G}$ is the critical density for closure of the universe at the redshift of the halo, and

$$\delta_c = \frac{200\Omega_{\rm M}(z_{\rm halo})}{3}\frac{c^3}{\ln(1+c) - c/(1+c)}, \tag{2.36}$$

where the concentration parameter, $c = r_{200}/r_s$ is a dimensionless parameter which relates the scale radius to the virial radius r_{200}, defined as the radius at which the matter density is 200 times larger than the matter density at that redshift. The mass contained within the radius r_{200} of the centre of the halo is

$$M_{200} \equiv M(r_{200}) = \frac{800\pi}{3}\rho_c \Omega_{\rm M}(z_{\rm halo}) r_{200}^3 = \frac{800\pi}{3}\overline{\rho}_{\rm M}(z) r_{200}^3 \tag{2.37}$$

The surface mass density of such a profile can be derived by integrating equation (2.35) along the line of sight (Wright & Brainerd, 1999)

$$\Sigma_{\rm nfw}(x) = \begin{cases} \frac{2r_s\delta_c\rho_c}{(x^2-1)}\left[1 - \frac{2}{\sqrt{1-x^2}}\operatorname{arctanh}\sqrt{\frac{1-x}{1+x}}\right] & (x < 1) \\ \frac{2r_s\delta_c\rho_c}{3} & (x = 1) \\ \frac{2r_s\delta_c\rho_c}{(x^2-1)}\left[1 - \frac{2}{\sqrt{x^2-1}}\arctan\sqrt{\frac{x-1}{1+x}}\right] & (x > 1) \end{cases} \tag{2.38}$$

where $x(R)$ denotes a dimensionless radial distance, $x = R/r_s$, so that $x(r_{200}) = c$,

and the mass enclosed within a radius R is given by

$$M(\leq R) = 4\pi\delta_c\rho_c(z)r_s^3\left[\ln\left(1+\frac{R}{r_s}\right) - \frac{R/r_s}{1+R/r_s}\right] \tag{2.39}$$

which can be seen to reduce to the virial mass, M_{200} ,when evaluated at $R = r_{200}$. The weak lensing convergence is then related using $\kappa = \Sigma_{\rm nfw}/\Sigma_{\rm crit}$, and as the NFW profile is axi-symmetric, the magnitude of the shear can be calculated using Equation (2.27), where $\bar{\kappa} = \bar{\Sigma}_{\rm nfw}/\Sigma_{\rm crit}$ and (Wright & Brainerd, 1999)

$$\overline{\Sigma}_{\rm nfw}(x) = \frac{2}{x^2}\int_0^x x'\Sigma_{\rm nfw}(x')dx' = \begin{cases} \frac{4}{x^2}r_s\delta_c\rho_c\left[\frac{2}{\sqrt{1-x^2}}\text{arctanh}\sqrt{\frac{1-x}{1+x}} + \ln\left(\frac{x}{2}\right)\right] & (x<1) \\ 4r_s\delta_c\rho_c\left[1+\ln\left(\frac{1}{2}\right)\right] & (x=1) \\ \frac{4}{x^2}r_s\delta_c\rho_c\left[\frac{2}{\sqrt{x^2-1}}\arctan\sqrt{\frac{x-1}{1+x}} + \ln\left(\frac{x}{2}\right)\right] & (x>1) \end{cases} \tag{2.40}$$

Figure 2.2 shows the projected surface mass density for an NFW profile for various choices of virial radius, r_{200}, and scale radius, r_s. As either is varied, the other is held fixed. For fixed scale radius, varying the virial radius causes an increase in the virial halo mass, causing an increase in the projected surface mass density. This can be seen in the analytic solution given in Equation (2.38): a variation in r_{200} only induces a change in δ_c, which sets the amplitude of the projected surface mass density, whilst the region in which each solution is valid is invariant. The scale radius sets the turnover in the profile, and defines the radius between the solutions for the surface mass density given in Equation (2.38). Increasing r_s, whilst keeping the virial mass constant, pushes the turnover to larger radii and thus decreases the mass at lower radii, whilst increasing the mass at larger radii. For a halo of given mass (fixed r_{200}), an increase in the concentration is equivalent to a decrease in r_s, pushing more of the mass towards the centre of the halo and making it more 'cuspy' at the centre.

2.2.4 Caustics and Einstein Rings

If the Jacobian mapping between the lens and source plane is singular, so that $\det(A) = 0$, there exists no unique solution for the mapping from the source plane to the lens, corresponding to the case where the magnification is infinite, as can be seen from Equation (2.17). In practice, no source experiences infinite magnification

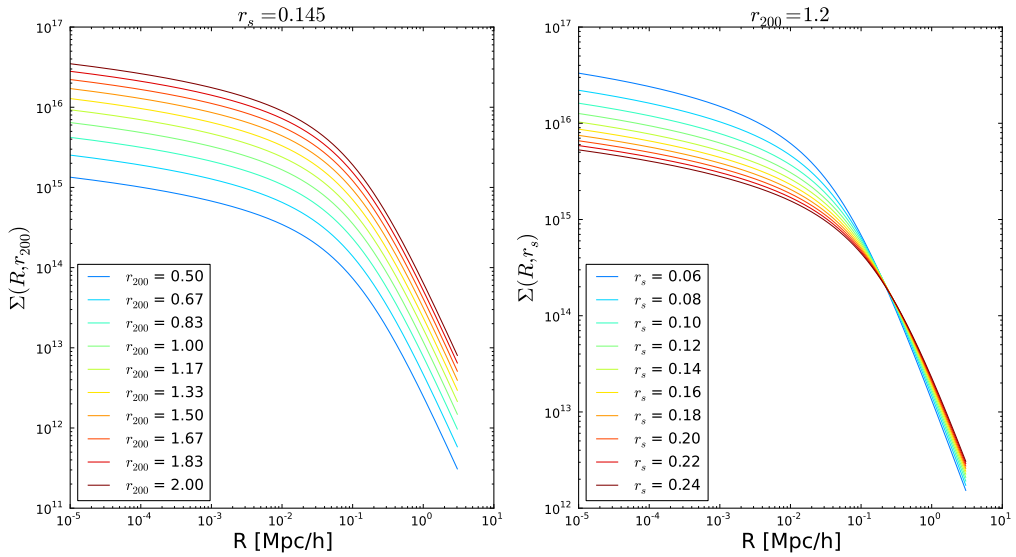

Figure 2.2: Projected surface mass density for an NFW profile, *left*: varying virial radius with fixed scale radius, *right*: varying scale radius with fixed virial radius

as for extended sources the magnification at any point is the surface-brightness weighted point-source magnification, and for point sources the geometrical-optics approximation breaks down near critical curves (Bartelmann & Schneider, 2001), however in the case of strong lensing large magnifications are commonplace. These *critical curves* in the source plane where the source is so largely distorted are referred to as *caustics* in the lens plane.

Combining Equations (2.1) and (2.6), for a point mass the lens equation can be written as

$$\theta = \beta + \frac{\theta_E^2}{\theta}, \tag{2.41}$$

$$\rightarrow \quad \theta^2 - \beta\theta - \theta_E^2 = 0, \tag{2.42}$$

where the *Einstein Angle* is defined as

$$\theta_E^2 = \frac{4GM}{c^2}\frac{D_{ds}}{D_d D_s}, \tag{2.43}$$

with the solution given by

$$\theta = \frac{1}{2}\left[\beta \pm \sqrt{\beta^2 + 4\theta_E^2}\right]. \tag{2.44}$$

This gives a general solution for the observed position of a source which has been lensed by a foreground point mass. In general, there always exists two solutions for a point mass system. When the source lies far from the Einstein Angle of the lens, $\beta \gg \theta_E$, this result, expanded to lowest order, gives the solutions:

$$\theta = \beta + \frac{\theta_E^2}{\beta};\ \theta = \frac{\theta_E^2}{\beta} \tag{2.45}$$

with the next highest order terms of the order θ_E^4/β^3. The first solution corresponds to a solution where the source has only been deflected slightly by the lens, and is observed close to its un-deflected position β. The second image, whose position is given by the second solution, lies close to the lens, is much fainter than the first solution and thus obscured by the lens. In this limit, the gravitational lensing of the source is weak as it lies far from the lens on the sky, and one would expect to only observe one image.

In the case where the lens and source are in perfect alignment, corresponding to $\beta = 0$, the two solutions are:

$$\theta = \pm\theta_E. \tag{2.46}$$

In this case, as the lens is circularly symmetric, the image is expanded into a ring around the source, called an *Einstein Ring*. The caustic for a point source therefore corresponds to the position of the lens, giving a critical curve at $\theta = \theta_E$. This corresponds to the case where the source is maximally magnified, and is one of the most visually apparent distortions caused by gravitational lensing by a foreground object. As the observation of such large distortions to the image of the source require precise alignment between the source and lens, Einstein rings are a rare occurrence in nature, however particularly spectacular examples of partial Einstein rings have been observed around the large over densities found around galaxy clusters, an example of which is shown in Figure 2.3.

dep Both limits presented here give an indication of the expected effect on the source image due to lensing in two very different examples: in the first, the source is far from the lens where only a minimal deflection is observed; in the second, the source and lens are nearly perfectly aligned and large distortions to the image are observed.

Figure 2.3: A Hubble Space Telescope image of the Abell 383 cluster. Arcs are visible as background galaxies experience large distortions caused by the strong lensing of the cluster. Available at: http://www.spacetelescope.org/images/heic1106a/. Image Credit: NASA, ESA, J. Richard (CRAL) and J.-P. Kneib (LAM). Acknowledgement: Marc Postman (STScI)

Thus, the Einstein angle of a lens-source couple is a useful proxy for the strength of the lensing effect: sources which lie close to or within the caustic in the lens plane are expected to be highly magnified with large, visible distortions and multiply imaged, whilst sources which lie far from the caustic will only show small distortions with a second image close to the lens and too faint to be observable. It should be noted, however that the definition of the Einstein Radius depends not only on the mass of the lens itself, but also on the lens-source geometry, therefore knowledge of the lens only is not sufficient to gain knowledge of a unique Einstein Radius for that lens. However, for a widely separated lens-source pair in redshift, the geometric factor tends to a constant (Figure 2.4), meaning some generalisations on the Einstein Radius for a given mass lens can be made to within a few percent in this case: for a strong lensing cluster of mass $M \sim 10^{14} M_{\rm Sun}/h$, $\theta_E \sim 10''$; a weak lensing large galaxy with $M \sim 10^{12} M_{\rm Sun}/h$, $\theta_E \sim 1''$; and for a micro-lensing local star with $M \sim M_{\rm Sun}/h$, $\theta_E \sim 10^{-6''}$.

Consider a mass profile with an inverse radial dependence

$$\Sigma \propto \frac{1}{\xi}; \quad \kappa \propto \frac{1}{|\boldsymbol{\theta}|}, \tag{2.47}$$

such as that expected from a singular isothermal model. Denoting the constant of proportionality by A, so that $\kappa = A/|\boldsymbol{\theta}|$, it can be shown by direct integration that the mean convergence within a sphere of radius $|\boldsymbol{\theta}|$, Equation 2.21, is given by

$$\bar{\kappa}(|\boldsymbol{\theta}|) = \frac{2A}{|\boldsymbol{\theta}|}. \tag{2.48}$$

As this profile is axi-symmetric, the magnitude of the complex shear satisfies:

$$|\gamma| = -\kappa = -\frac{A}{|\boldsymbol{\theta}|}, \tag{2.49}$$

as can be seen from Equation 2.28, and magnification satisfies

$$\mu = [1 - 2\kappa]^{-1} = \frac{|\boldsymbol{\theta}|}{|\boldsymbol{\theta}| - 2A}. \tag{2.50}$$

By inspection, we can then identify the Einstein radius as $\theta_{\rm E} = 2A$. Singular isothermal spheres (introduced in Section 2.2.3) are an example of a mass profile with

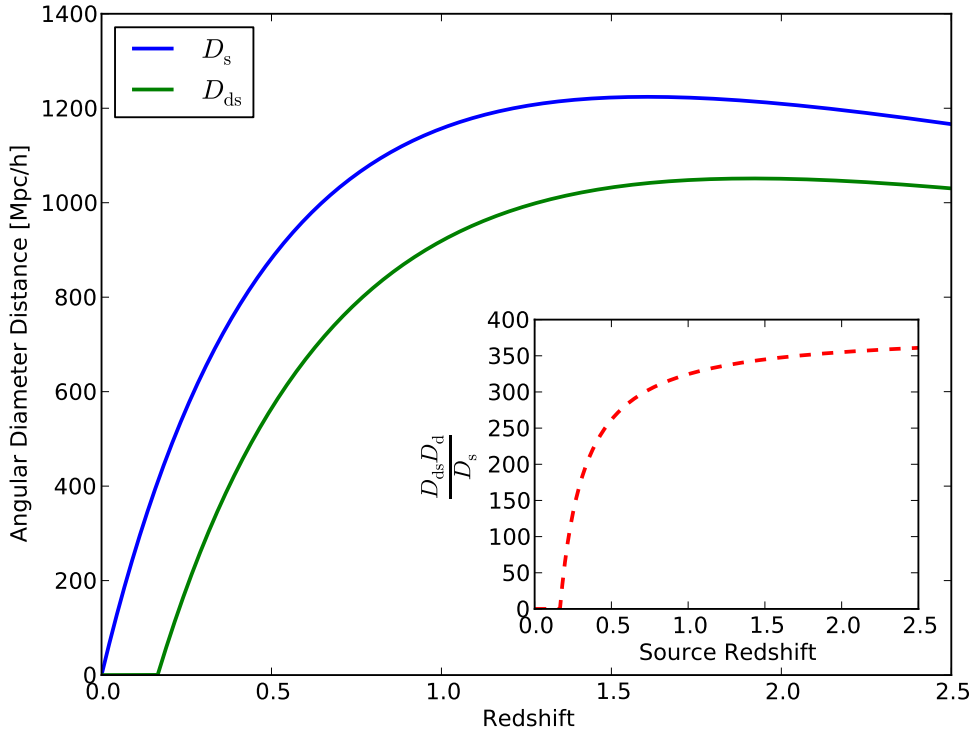

Figure 2.4: Proper angular diameter distances for a source, D_s, and between a source and lens at $z = 0.165$ as a function of the source's redshift, D_{ds}. Inset shows the lensing geometrical factor, $D_{\rm ds}/D_{\rm d}D_{\rm s}$, for a lens at z = 0.165 as a function of the source redshift. For a source at $z > 1$, the geometrical factor changes only by a few percent with increasing source redshift.

an inverse radial dependence, for whom

$$|\boldsymbol{\theta_E}| = \frac{4\pi D_{\rm ds}}{D_{\rm s}} \left(\frac{\sigma_v}{c}\right)^2 . \tag{2.51}$$

Such a critical curve maps onto the source plane as a highly degenerate point caustic, $\boldsymbol{\beta} = 0$, however any perturbation to the symmetry of the mass profile of the lens will in general expand this caustic onto a caustic curve. (Schneider, Ehlers & Falco, 1992)

2.2.5 Connecting Shear and Convergence

Starting from the definition of the shear and convergence in terms of the lensing potential, the Fourier transformed shear and convergence satisfy

$$\hat{\kappa}(\boldsymbol{\ell}) = \frac{1}{2}(\ell_1^2 + \ell_2^2)\hat{\phi}(\boldsymbol{\ell}) \tag{2.52}$$

$$\hat{\gamma}_1(\boldsymbol{\ell}) = \frac{1}{2}(\ell_1^2 - \ell_2^2)\hat{\phi}(\boldsymbol{\ell}); \quad \hat{\gamma}_2 = (\ell_1\ell_2)\hat{\phi}(\boldsymbol{\ell}), \tag{2.53}$$

so that it can be seen that $\langle|\hat{\kappa}^2|\rangle = \langle|\hat{\gamma}^2|\rangle$, and consequently

$$P_\kappa(\boldsymbol{\ell}) = P_\gamma(\boldsymbol{\ell}). \tag{2.54}$$

Thus, the shear and convergence field share equivalent statistics at second order.

To first order, the relation of the shear and convergence field is slightly more complicated. Differentiating the lensing potential as given in Equation (2.10) twice, the shear can be related to the convergence in real space as (Bartelmann & Schneider, 2001)

$$\gamma(\boldsymbol{\theta}) = \frac{1}{\pi}\int \mathrm{d}^2\theta'\, \mathcal{D}(\boldsymbol{\theta} - \boldsymbol{\theta}')\kappa(\boldsymbol{\theta}') = \frac{1}{\pi}[\kappa * \mathcal{D}](\boldsymbol{\theta}) \tag{2.55}$$

$$\rightarrow \quad D(\boldsymbol{\theta}) = \frac{\theta_2^2 - \theta_1^2 - 2i\theta_1\theta_2}{|\theta|^4} = -\frac{1}{(\theta_1 - i\theta_2)^2} \tag{2.56}$$

where $[\kappa * \mathcal{D}]$ denotes a convolution. Using the convolution theorem

$$\hat{\gamma}(\boldsymbol{\ell}) = \frac{1}{\pi}\hat{\kappa}(\boldsymbol{\ell})\hat{\mathcal{D}}(\boldsymbol{\ell}) \tag{2.57}$$

for $\ell \neq 0$, so that

$$\kappa(\ell) = \frac{1}{\pi}\hat{\mathcal{D}}^*(\boldsymbol{\ell})\hat{\gamma}(\boldsymbol{\ell}) \quad \ell \neq 0 \tag{2.58}$$

giving

$$\kappa(\theta) - \kappa_0 = \frac{1}{\pi}\int \mathrm{d}^2\theta' \mathcal{D}^*(\theta - \theta')\gamma(\theta'), \tag{2.59}$$

where I have used $\hat{\mathcal{D}}^*\hat{\mathcal{D}} = \pi^2$ (Bartelmann & Schneider, 2001), and taken the inverse Fourier transform in the final line. Thus, one can see that the convergence field can be recovered from a measurement of the shear field, up to an additive constant equivalent to the $\ell = 0$ term, which corresponds to the fact that a constant surface mass density

does not induce a shear, and is therefore unconstrained by γ. This is a statement of the Kaiser & Squires (1993) (KS) inversion technique. Measurements of the shear field can then be used to determine the convergence field directly, providing an alternative method to map the mass of foreground structure than the more direct probes of the convergence field provided by magnification measurements.

In practice, the application of the KS technique is complicated by the limitations of the data. In particular, the integral required for the inversion extends over all space, leading to boundary artefacts towards the edge of the field, beyond which the shear field must be assumed to be zero. The use of Fourier transforms in practice requires periodic boundary conditions, and so care must be taken to pad the edges of the image appropriately to avoid contamination. As the shear field is sampled discretely at the positions of background sources, the shear field must be constructed as the average over a series of grid points, or the convergence at a position can be calculated as Equation (2.59) with the integral replaced by a discrete sum over all galaxies: in this case, this estimate of the convergence has infinite noise (Bartelmann & Schneider, 2001) and so the data must be smoothed, thus changing the window function $\mathcal{D}$. Further, the use of Fourier transforms means that masked regions (such as the masking of bright stars or un-imaged patches of the sky) must be correctly accounted for in the process of taking the Fourier transform. Finally, only in the case of weak lensing is the shear itself a direct observable: in general, only the reduced shear is observable, and thus in high density areas such as the centre of clusters, the estimate of the mass from this technique may be biased low. The technique can be modified to alleviate some of these problems, such as the finite-field inversion and non-linear generalisations summarised in Bartelmann & Schneider (2001), but I do not present them here.

Equation (2.59) shows that the inversion techniques can only infer the convergence field up to an additive constant; in actuality, observations of galaxy shapes can only infer the convergence field up to an additive constant as a result of a general invariance transformation known as the *Mass Sheet Degeneracy*. Consider a transformation of the lensing Jacobian under the form

$$\mathcal{A}_\lambda = \lambda \mathcal{A}.$$

Through consideration of the form of the Jacobian, either using the reduced shear or the normal definition of the shears, it can be discerned that the convergence and

shear transform as

$$(1-\kappa_\lambda) = \lambda(1-\kappa); \quad \kappa_\lambda = (1-\lambda)+\lambda\kappa \tag{2.60}$$

$$\gamma_\lambda = \lambda\gamma, \tag{2.61}$$

corresponding to a global rescaling of the mass profile, κ, and the addition of a constant mass, $1-\lambda$. Under this transformation, the reduced shear is therefore invariant, meaning that observations of galaxy ellipticities cannot distinguish between different values of λ, without additional information which can set the unlensed size or luminosity of the source (in the absence of statistic methods), or the mass of the lens (such as stellar dynamics or X-ray measures). As an alternative viewpoint, it is worth noting that the rescaling of the Jacobian corresponds to a rescaling of the mapping between the observed position in the lens plane and the intrinsic position in the source plane; in one spatial dimension, this implies that it is impossible to distinguish between a shift in the intrinsic position of a point in the source plane with a shift in the lensing strength; in two dimensions, the transformation corresponds to an isotropic distortion in both directions, much like the convergence term itself, so that shape information cannot distinguish between values of λ. Under the above invariance transformation (2.60), the magnification scales as

$$\mu_\lambda = \lambda^{-2}\mu.$$

Thus, a direct measurement of the magnification, or equivalently convergence, such as that provided by the flux- or size-magnification techniques, can distinguish between mass profiles and break the degeneracy. With a direct probe, one may directly measure the constant, $(1-\lambda)$ by considering a region of space far from a foreground lens, or in a blank field.

2.2.6 Lensing by Large-Scale-Structure

When the mass distribution which causes the lensing of a background image extends the length of the distance between the observer and the source, as is the case when the lensing is caused by the large-scale structure (LSS) of the Universe, the formalism presented in Section 2.2.1 no longer applies and must be generalised to include the background expansion of the Universe, and non-local curvature. In this case, a

'straight' fiducial ray is poorly defined, and we must instead consider the separation between two fiducial light rays. In perturbed FRW space, the propagation equation for a pair of light rays is given as

$$\frac{\mathrm{d}^2\boldsymbol{x}}{\mathrm{d}\chi^2} + K\boldsymbol{x} = -\frac{2}{c^2}\nabla_\perp\Phi \tag{2.62}$$

where $\boldsymbol{x}$ defines the separation between both light rays, Kdenotes the global curvature of the universe as defined in the FRW metric, and any change in separation between the neighbouring light rays is sourced by gradients in the perturbation transverse to the light of sight, $\nabla_\perp = \partial/\partial\theta$. A solution can be sought using Green's functions, and takes the form (Bartelmann & Schneider, 2001)

$$\boldsymbol{x} = f_K(\chi)\boldsymbol{\theta} - \frac{2}{c^2}\int_0^\chi \mathrm{d}\chi'\ f_K(\chi-\chi')\nabla_\perp\Phi[\boldsymbol{x}(\boldsymbol{\theta},\chi'),\chi']. \tag{2.63}$$

The first term here contains the solution in the absence of inhomogeneities, and corresponds to the deflection from a homogeneous and isotropic background. For the purposes of this re-derivation, we are concerned with the solution due to local inhomogeneities, and therefore ignore this solution in the following. In this case, the change in the separation of light rays is sourced by the local Newtonian perturbation to the FRW metric, which satisfies Poisson's Equation of the form

$$\nabla^2\Phi = \frac{3}{2}\frac{H_0^2\Omega_M}{a}\delta, \tag{2.64}$$

where δ is the fractional matter over-density. The deflection angle is then given by [5]

$$\alpha(\boldsymbol{\theta},\chi) = \frac{2}{c^2}\int_0^\chi \mathrm{d}\chi'\ \frac{f_K(\chi-\chi')}{f_K(\chi)}\nabla_\perp\Phi[f_K(\chi')\boldsymbol{\theta},\chi'], \tag{2.65}$$

where I have used the small angle formula to relate the transverse separation $\boldsymbol{x}$ to the deflection angle through $f_K(\chi)\boldsymbol{\alpha} = f_K(\chi)\boldsymbol{\theta} - \boldsymbol{x}$. Following the same method as before, and noting that the convergence is related to the deflection angle as $\kappa =$

[5]One can verify that this reduces to the deflection angle for a point mass, equation 2.1, by considering a locally defined Newtonian potential $\Phi \to \delta_D(\chi'-\chi_d)\Phi$, where χ_d labels the co-moving radial distance of the lens, and identifying $D_d = f_K(\chi_d)$, $D_{ds} = f_K(\chi-\chi_d)$ and $D_s = f_K(\chi)$. In this case, the deflecting mass is a thin sheet, and the acceleration of the deflected photon is sourced by mass contained within a sphere bounded by its impact parameter, a consequence of Birkhoff's theorem.

$\nabla_\theta \boldsymbol{\alpha}/2$, an effective convergence can be written as

$$\kappa_{\rm eff}(\boldsymbol{\theta},\chi) = \frac{1}{c^2}\int_0^\chi \mathrm{d}\chi' \, \frac{f_K(\chi-\chi')f_K(\chi')}{f_K(\chi)}\nabla_\perp^2\Phi[f_K(\chi')\boldsymbol{\theta},\chi']. \tag{2.66}$$

Combining equation 2.66 with the matter over density Poisson's equation (equation 1.29 with $w=0$), the lensing convergence can be related to the fractional matter over-density along the line of sight as

$$\kappa_{\rm eff}(\boldsymbol{\theta},\chi) = \frac{3H_0^2\Omega_M}{2c^2}\int_0^\chi \mathrm{d}\chi' \, \frac{f_K(\chi-\chi')f_K(\chi')}{f_K(\chi)}\frac{\delta(\boldsymbol{\theta},\chi')}{a(\chi')}. \tag{2.67}$$

Note that the convergence, as defined in 2.66, contains the two-dimensional Laplacian $\nabla_\perp$, whereas the matter Poisson's equation contains an extra radial term. As this term is expected to average to zero to the order to which the result is presented, this term is neglected.

This gives the convergence due to the LSS for a source at χ. The convergence averaged over a distribution of sources with probability distribution function $p(\chi)$, satisfies

$$\begin{aligned}\kappa_{\rm eff}(\boldsymbol{\theta}) &= \frac{3H_0^2\Omega_m}{2c^2}\int_0^{\chi_H}\mathrm{d}\chi\, W(\chi)\frac{\delta(\boldsymbol{\theta},\chi)}{a(\chi)} \\ &\leftarrow \; W(\chi) = \int_\chi^{\chi_H}\mathrm{d}\chi'\, p(\chi')\frac{f_K(\chi'-\chi)f_K(\chi)}{f_K(\chi')}.\end{aligned} \tag{2.68}$$

It is often more viable to work with galaxy redshift information rather than comoving distance, as redshift can be obtained directly from observations without the need to assume a particular cosmology. For sources with redshift distribution $n(z)$, such that $n(z)dz = p(\chi)d\chi$, the effective convergence becomes

$$\begin{aligned}\kappa_{\rm eff}(\boldsymbol{\theta}) &= \frac{3H_0^2\Omega_m}{2c^2}\int_0^{z_H}\mathrm{d}z\,\frac{\mathrm{d}r}{\mathrm{d}z}\bar{W}(r|_z)(1+z)\delta(\boldsymbol{\theta},z); \\ &\leftarrow \; \bar{W}(r|_z) = \int_z^{z_H}\mathrm{d}z'\, n(z')\frac{f_K(r|_{z'}-r|_z)f_K(r|_z)}{f_K(r|_{z'})}\end{aligned} \tag{2.69}$$

As the lensing kernal, $\bar{W(\chi)}$, integrates over the weighted galaxy redshift distribution from $z \to z_H$ it contains contributions only for sources which are behind the lens, and satisfies $z \to 0, z_H$; $\bar{W}(r|_z) \to 0$.

Equations 2.68 and 2.69 give the projected convergence for a sample of sources

which radial distributions given by $p(\chi)$ or $n(z)$. In doing this projection radial information on the sample is lost, reducing the constraining power of a lensing analysis which measures statistics of this quantity. Much of this information can be regained by splitting the sample according to the measured redshift of each galaxy. In this case, the effective convergence of each subsample of sources is given as above with a $p \rightarrow p^i$, where i labels the subsample of sources, and $p = \sum_i p^i$. Statistics can then be constructed on each subsample, and constraints placed on cosmological model free parameters with the combination of fits to each of these statistics. Each subdivision will add radial information to the analysis, and thus improve cosmological parameter constraints, particularly on those which are highly redshift dependent such as the dark energy parameters. A natural limit on such subdivisions is provided by the noise of the sample: when the sample is subdivided enough that the noise in each bin surpasses the signal, further subdivisions will no longer add information. Similarly, if the lensing efficiency does not change significantly across the redshift range of the sample, further subdivision will not add information as both samples will be highly degenerate in their information content. Thus, an increase in model parameter constraints can be expected for a lensing analysis as a small number of tomographic bins is added, which eventually levels out with the addition of more bins (Hu, 1999). Such a process is termed 'tomography'. In contrast, the 3D shear analysis of Castro, Heavens & Kitching (2005); Heavens, Kitching & Taylor (2006) does not consider projected quantities, but rather takes each galaxy individually. In this case, radial information is not lost, however this comes at the expense of increased complexity of the analysis.

2.3 Weak Lensing analyses

In this section I focus on the weak lensing regime, which satisfies $|\gamma| \ll 1; \kappa \ll 1$, where the distortions to the shapes and sizes of galaxies are too small to be easily discerned by a single source, and one must use statistics to extract a signal. I detail the use of the major weak lensing probes: namely shear; flux- and size- magnification; and galaxy-galaxy lensing as a probe of cosmology or dark matter environment. To do this, I will first revisit the second order statistics of a field, as set out in Section 1.4.1, in particular the relation between the statistics of projected quantities and their three-dimensional counterparts through the use of Limber's equation, and which can be used to connect projected lensing quantities to the three-dimensional matter power

spectrum for cosmological lensing analyses.

2.3.1 Limber's equation

In Section 2.2.6 I presented the projected convergence for a distribution of sources which are lensed by the large-scale structure along the line of sight. It is desirable to relate these projected quantities to the matter power spectrum in three dimensions, which describes the clustering of the lensing medium and is well-known in the linear regime. To aid the completeness of this thesis I here present a re-derivation of Limber's equation, which relates the power spectrum for a projected field to its underlying three-dimensional power under certain conditions, and will be used extensively for the remainder of this thesis. In doing so, I follow closely the derivation described in Bartelmann & Schneider (2001), and use the definitions of the correlation function and power spectrum set out in Section 1.4.1.

Consider an isotropic, homogenous field, projected along the line of sight and described by its angular position on the sky, $g(\boldsymbol{\theta})$, and which is related to a three-dimensional, isotropic and homogenous complex field, $\delta(\boldsymbol{\theta}, \chi)$ as

$$g_i(\boldsymbol{\theta}) = \int \mathrm{d}\chi \; q_i(\chi)\delta(f_K(\chi)\boldsymbol{\theta}, \chi)$$

where $q_i(\chi)$ describes the weighting kernel for a sub-set of the full source set (such as a tomographic redshift bin), marked with roman subscript.

The correlation function for g using two source sub-samples, denoted using i, j, can be related to the correlation function of the underlying three-dimensional field as

$$\begin{aligned}
\xi^{ij}_{gg}(|\boldsymbol{\Delta\theta}|) &= \langle g_i(\boldsymbol{\theta}) g^*_j(\boldsymbol{\theta}')\rangle, \\
&= \int \mathrm{d}\chi \; q_i(\chi) \int dr' \; q_j(\chi')\langle\delta(f_K(\chi)\boldsymbol{\theta}, \chi)\delta^*(f_K(\chi')\boldsymbol{\theta}', \chi')\rangle, \\
&= \int \mathrm{d}\chi \; q_i(\chi) \int \mathrm{d}\chi' \; q_j(\chi')\xi_{\delta\delta}(|\boldsymbol{r}|), \qquad (2.70)
\end{aligned}$$

where $\xi_{\delta\delta}$ labels the correlation function for the field δ, $\boldsymbol{\theta}' = \boldsymbol{\theta} + \boldsymbol{\Delta\theta}$, and $\boldsymbol{r}$ the three-dimensional vector connecting the field points. This can be related to the Fourier

coefficients of the field δ as

$$\begin{aligned}\xi_{gg}^{ij}(|\boldsymbol{\Delta\theta}|) &= \int \mathrm{d}\chi\; q_i(\chi) \int \mathrm{d}\chi'\; q_j(\chi') \int \frac{\mathrm{d}^3k}{(2\pi)^3} \int \frac{\mathrm{d}^3k'}{(2\pi)^3} \\ &\times\; e^{i(\boldsymbol{k}_\perp \cdot f_K(\chi)\boldsymbol{\theta} - \boldsymbol{k'}_\perp \cdot f_K(\chi')\boldsymbol{\theta'})} e^{i(k_3\chi - k'_3\chi')} \langle \delta(\boldsymbol{k},\chi)\delta^*(\boldsymbol{k'},\chi')\rangle \\ &= \int \mathrm{d}\chi\; q_i(\chi) \int \mathrm{d}\chi'\; q_j(\chi') \int \frac{\mathrm{d}^3k}{(2\pi)^3} \int \frac{\mathrm{d}^3k'}{(2\pi)^3} e^{i(k_3\chi - k'_3\chi')} \\ &\times\; e^{i(\boldsymbol{k}_\perp \cdot f_K(\chi)\boldsymbol{\theta} - \boldsymbol{k'}_\perp \cdot f_K(\chi')\boldsymbol{\theta'})} [(2\pi)^3 \delta_D^3(\boldsymbol{k} - \boldsymbol{k'}) P_\delta(|\boldsymbol{k}|,\chi)]. \end{aligned} \tag{2.71}$$

where in the final step I have used the definition of the power spectrum from Equation (1.35), and the χ dependence of the power spectrum labels time. The integration over the Fourier modes $\boldsymbol{k'}$ can be taken using the Dirac Delta function, giving

$$\begin{aligned}\xi_{gg}^{ij}(|\boldsymbol{\Delta\theta}|) &= \int \mathrm{d}\chi\; q_i(\chi) \int \mathrm{d}\chi'\; q_j(\chi') \int \frac{\mathrm{d}^3k}{(2\pi)^3} e^{i\boldsymbol{k}_\perp \cdot (f_K(\chi)\boldsymbol{\theta} - f_K(\chi')\boldsymbol{\theta'})} \\ &\times\; e^{ik_3(\chi-\chi')} P_\delta(|\boldsymbol{k}|,\chi). \end{aligned} \tag{2.72}$$

Under the assumption that

- There is negligible power in the correlations of δ on scales greater than the coherence scale of correlations, given by L_{coh}. This means that the only non-zero terms in $P_{\delta\delta}$ occur on scales such that $|\chi - \chi'| < L_{\mathrm{coh}}$.
- The field δ does not evolve appreciably over scales $|\chi - \chi'| < L_{\mathrm{coh}}$
- The weight functions q_i are wide and do not vary appreciably over the scale $|\chi - \chi'| < L_{\mathrm{coh}}$

over the scale where the power is non-zero, we can approximate $f_K(\chi') \approx f_K(\chi)$ and $q_i(\chi') \approx q_i(\chi)$. Under these conditions, the correlation for g becomes

$$\begin{aligned}\xi_{gg}^{ij}(|\boldsymbol{\Delta\theta}|) &= \int \mathrm{d}\chi\; q_i(\chi) q_j(\chi) \int \frac{\mathrm{d}^3k}{(2\pi)^3} P_\delta(|\boldsymbol{k}|,\chi) e^{ik_3\chi} e^{i\boldsymbol{k}_\perp \cdot f_K(\chi)(\boldsymbol{\theta}-\boldsymbol{\theta'})} \int \mathrm{d}\chi'\; e^{-ik_3\chi'} \\ &= \int \mathrm{d}\chi\; q_i(\chi) q_j(\chi) \int \frac{\mathrm{d}^3k}{(2\pi)^3} P_\delta(|\boldsymbol{k}|,\chi) e^{ik_3\chi} e^{i\boldsymbol{k}_\perp \cdot f_K(\chi)(\boldsymbol{\theta}-\boldsymbol{\theta'})} (2\pi)\delta_D(k_3) \\ &= \int \mathrm{d}\chi\; q_i(\chi) q_j(\chi) \int \frac{\mathrm{d}^2k_\perp}{(2\pi)^2} P_\delta(|\boldsymbol{k}_\perp|,\chi) e^{i\boldsymbol{k}_\perp \cdot f_K(\chi)(\boldsymbol{\Delta\theta})} \end{aligned} \tag{2.73}$$

where we have carried out the k_3 integration and used $\boldsymbol{\Delta\theta} = \boldsymbol{\theta} - \boldsymbol{\theta'}$. The presence of the $\delta_D(k_3)$ shows that only the k-modes that lie on the plane of the sky contribute to

the correlation function for g, thus all the power has effectively been placed in a thin two-dimensional slice across the sky.

Expanding this relation out in terms of Fourier coefficients described by angular wavenumber $\boldsymbol{\ell}$, the projected power spectrum can be given as

$$\begin{aligned} P_g^{ij}(\boldsymbol{\ell}) &= \int \mathrm{d}^2\Delta\theta e^{i\boldsymbol{\ell}\cdot\boldsymbol{\Delta\theta}}\xi_{gg}^{ij}(|\boldsymbol{\Delta\theta}|) \\ &= \int \mathrm{d}\chi\ q_i(\chi)q_j(\chi)\int\frac{\mathrm{d}^2k_\perp}{(2\pi)^2}\int\mathrm{d}^2\Delta\theta P_\delta(|\boldsymbol{k}_\perp|,\chi)e^{i\boldsymbol{\Delta\theta}\cdot(\ell-f_K(\chi)\boldsymbol{k}_\perp)} \\ &= \int \mathrm{d}\chi\ q_i(\chi)q_j(\chi)\int\frac{\mathrm{d}^2k_\perp}{(2\pi)^2}\frac{1}{f_K^2(\chi)}P_\delta(|\boldsymbol{k}_\perp|,\chi)(2\pi)^2\delta_D\left(\boldsymbol{k}_\perp-\frac{\boldsymbol{\ell}}{f_K(\chi)}\right) \\ &= \int \mathrm{d}\chi\ \frac{q_i(\chi)q_j(\chi)}{f_K^2(\chi)}P_\delta\left(|\boldsymbol{k}_\perp|=\frac{\boldsymbol{\ell}}{f_K(\chi)},\chi\right) \end{aligned} \tag{2.74}$$

This relation gives Limber's equation in Fourier space for angular wave numbers $\boldsymbol{\ell}$. Where δ is the matter over-density, as defined in Equation (1.24), P_δ labels the matter power spectrum, and this result relates the projected power spectrum of a field to the three-dimensional power spectrum: this is particularly useful in constructing the projected effective-convergence power spectrum used in cosmological lensing analyses. In deriving this relation, I have considered the Fourier components of the underlying fields, thus this relation can only hold in regions where the sky is approximately flat. For this reason, the results presented here can only be applied up to a certain angular scale over which the flat-sky approximation is no longer sufficiently precise. A fuller treatment which does not rely on this assumption may be sought by expanding the fields using spherical harmonics as a basis set, however I do not cover this here.

2.3.2 Shear

The use of galaxy shapes, as used in a shear analysis, has received a large amount of interested in the lensing community, owing in large part to its predicted signal-to-noise over other lensing observables (see Section 2.3.6). The use of shear has the further advantage that it is clean of many sources of astrophysical contamination and is insensitive to the nature of the lensing matter[6]: in comparison, galaxy clustering

[6]Whilst the deflection of light is insensitive to the nature to the deflecting mass, a shear analysis which considers second-order or higher statistics is sensitive to the nature of the matter power spectrum, which may deviate from the dark matter power spectrum on small scales where baryons dominate.

analyses (including the use of the magnification signal through number counts) must account for biased structure formation. However, the observational difficulties inherent in a shear analysis (detailed in Section 5.2) limits the measurement of shear on the smallest, faintest galaxies, potentially reducing the sample size over a galaxy clustering analysis where only the detection and accurate photometry of the source is required. Further to this, a shear analysis must account for intrinsic ellipticity of galaxies due to their local environment, and accurate modelling of the small scale matter distribution, where the effects of non-linear collapse and baryonic effects will be largest.

In the absence of measurement errors, the total ellipticity of a source can be described in three parts:

$$\epsilon = \gamma + \epsilon_I + \epsilon_{\rm rn} \tag{2.75}$$

where a random stochastic element, which is uncorrelated to the other terms and contributes only to the noise is given by $\epsilon_{\rm rn}$, and the shear due to lensing by the foreground is denoted with γ. The final constituent of the total ellipticity comes from the intrinsic, pre-lensed ellipticity of the source, ϵ_I, determined by the local dark matter environment in which the source resides: if galaxies are randomly orientated across the sky, this term will just add to the noise, however tidal fields in the local environment can cause the preferential alignment of galaxies towards the centre of the local matter over-density: this effect is summarised in Figure 2.5 which shows the preferential intrinsic alignment of a source close to a matter over density, and that on a background source caused by the lensing of the same foreground matter. From this estimate, the total power spectrum for the observed ellipticity of the source can be constructed from five terms:

$$P_{\epsilon\epsilon} = P_{\gamma\gamma} + P_{\gamma\epsilon_I} + P_{\epsilon_I\gamma} + P_{\epsilon_I\epsilon_I} + P_{\rm SN} \tag{2.76}$$

where the power spectra are understood to correlate Fourier components across a given scale (suppressed for notational convenience), the first of these terms can be related to the power spectrum of the convergence field, and the final term is the pure shot noise contribution to the power coming from the stochastic contribution to the ellipticity estimator. The remaining terms correspond to the overall power coming from the inclusion of a non-vanishing intrinsic alignment of the sources, caused by the tendency of galaxies to align due to their local dark matter environment.

The interpretation of the above power spectrum is aided if we consider the first subscript to label the foreground quantity, and the last the background source. In this notation, $P_{\epsilon_I\epsilon_I}$ gives the correlation (II) between the intrinsic ellipticity of the

foreground and that of the background: this is important for galaxy samples that are physically close, and are therefore correlated due to the tendency of the galaxies in the sample to align according to the same tidal forces in the local gravitational field during galaxy formation. Thus, this term can be measured either by correlating galaxy ellipticities at low redshift, where the cosmic shear is subdominant (as in Brown et al., 2002), or correlating close galaxy pairs (Mandelbaum et al., 2006; Hirata et al., 2007). The cross-correlation, $P_{\epsilon_I\gamma}$, denotes the shear of the background with the ellipticity of the foreground, and is commonly referred to as the gravitational-shear-intrinsic-alignment (GI) term in the literature: the local dark matter environment in which the foreground sample resides is responsible for both the preferential radial alignment of the foreground galaxies and the tangential alignment of the background galaxies by gravitational lensing (Figure 2.5), inducing anti-correlations with can reduce the expected positive correlation coming from the lensing correlations alone ($P_{\gamma\gamma}$ or GG terms). The effect of the GI contribution is to thus damp the expected GG-only power. In the case where a non-negligible GI term is ignored as part of a shear analysis, the resulting cosmological parameter constraints may be biased (Bridle & King, 2007): however the size of this effect can be minimised by 'nulling' the intrinsic alignment signal (Joachimi & Schneider, 2008, 2009), or by introducing a flexible parameterisation of the signal as part of the analysis (Bernstein, 2009; Joachimi & Bridle, 2010), both at the expense of a loss of information through the reduction of the lensing signal or an increase in error bars on cosmological parameters through the marginalisation over free parameters in the intrinsic alignment (IA) model. Following a similar interpretation, in this notation $P_{\gamma\epsilon_I}$ will denote the correlations between the intrinsic alignment of the background and the lensing of the foreground: as the intrinsic alignment is a result of galaxy formation processes, it should show no correlation to the lensing of the matter distribution foreward of the lens samples, is thus expected to be zero for samples with large spatial separation. However, in the presence of redshift errors, this term may be interpreted as another GI term.

The contribution to the overall power from each term thus shows a complicated dependence on both the redshift of the lens sample and the source sample, and the angular separation between them: on large angular scales, the source and lens intrinsic alignment are correlated only by large scale structure whilst samples separated by small angular scales should feel the increasingly similar tidal forces due to the local environment, and so the contribution due to the intrinsic alignment terms will fall as

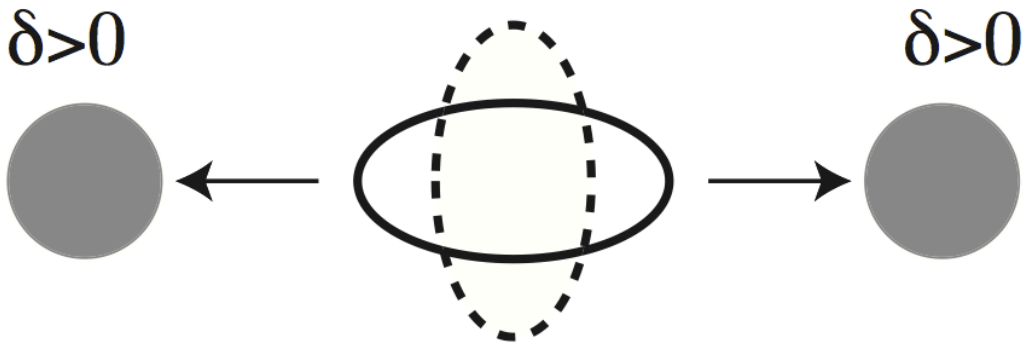

Figure 2.5: Diagrammatic representation of the preferential alignment due to a dark matter over density, for a local galaxy (radially aligned, solid), and a gravitationally lensed background (tangentially aligned, dashed). The presence of a density fluctuation induces non-zero anti-correlations between local foreground galaxies and lensed background galaxies, as the preferential alignment of both is sourced by the same matter distribution. From Hirata & Seljak (2004)

Table 2.1: Cosmological Parameter constraints for various analysis types with CFHTLenS. Kilbinger et al. (2013) and Heymans et al. (2013) figures include information from WMAP7 with BAO and H_0 distance measures. Kitching et al. (2014) combines with WMAP7.

Publication	$\Omega_{\rm M}$	σ_8	w	Probe
Kilbinger et al. (2013)	0.283 ± 0.01	0.813 ± 0.012	-1.1 ± 0.15	2D Correlations
Heymans et al. (2013)	0.271 ± 0.01	0.799 ± 0.015	-1.02 ± 0.09	6-Bin Tomography
Kitching et al. (2014)	0.252 ± 0.079	0.88 ± 0.23	-1.16 ± 0.38	3D Power Spectrum

a function of angular scale. The GG correlation will increase with the simultaneous increase in the redshift of the source and lens sample, as both will be lensed by the matter distribution foreground to both samples, and will fall of with angular scale. The II term will increase in amplitude as the redshift separation of the lens and source samples is reduced, and vice-versa, whilst the GI term may be expected to be roughly constant with lens-source separation. Whilst trends like this may be expected from heuristic reasoning, the relative size of each contribution to the theoretical power and its behaviour will depend on the intrinsic alignment, or galaxy formation model used. These trends can be seen in the theoretical predictions in Hirata & Seljak (2004); Joachimi & Bridle (2010).

In spite of the challenges that one must overcome in the use of shear, the use of such a probe is rapidly maturing and producing promising and interesting results. Recently, the use of the CFHTLenS survey (Heymans et al., 2013; Kitching et al., 2014; Kilbinger et al., 2013) has provided the best lensing constraints to date on the cosmological parameters, shown here in Table 2.1. The methods used in each of these analyses are fundamentally different: Kilbinger et al. (2013) presents constraints from a projected 2D shear analysis for a variety of shear correlation probes; Heymans et al. (2013) considers a tomographic shear analysis using correlation functions whilst Kitching et al. (2014) presents a 3D shear analysis using a pseudo-Cl power spectrum, each with their own advantages and disadvantages. In Heymans et al. (2013) the intrinsic alignment contribution is accounted for with a non-linear intrinsic alignment model with one free parameter. Using this method allows the authors to constrain the intrinsic alignment model at the expense of cosmological parameter constraints, and find an IA signal which is dependent on galaxy type: with non-zero intrinsic alignment signal in early-type galaxies to 2σ level, and an intrinsic alignment measurement consistent with zero for late type galaxies, consistent with the measurement of a zero IA signal using blue galaxies with WiggleZ in Mandelbaum et al. (2011) and a non-zero intrinsic alignment measurement using Mega-Z LRGs in Joachimi et al. (2011). This result is used in the sample selection for the 3D shear analysis of Kitching et al. (2014), where the authors choose a sample of blue galaxies to minimise the affects of IAs in the analysis. In contrast, the projected 2D analysis of Kilbinger et al. (2013) ignores the IA signal: in this case the II and GI contributions are diluted in the large sample of galaxies taken over a broad redshift range, and thus expected to give a bias subdominant to statistical errors (e.g. Kirk, Bridle & Schneider, 2010).

Further differences between these analyses result from the ability of each to use information on different scales. In all three, small scale cuts are used to minimise the impact of small-scale uncertainties such as non-linear structure formation and baryonic effects. Whilst the correlation function methods of Heymans et al. (2013) and Kilbinger et al. (2013) implement cuts on angular scale in the correlation function, the 3D shear analysis of Kitching et al. (2014) allows for the separation of angular and radial cuts: in this case, cuts on the wavenumber are used to limit the impact of small scale physical effects whilst cuts on the angular wavenumber can be used to limit the inclusion of power on large scales near the limit of the survey. Further, limitations on the modelling of the large-scale covariance matrix in the tomographic analysis of

Heymans et al. (2013) limit the use of larger scales. Together with the reduction in statistical power resulting from the necessity to account for IA in such a tomographic analysis, this removes much of the extra constraining power gained from the use of tomographic bins.

The analyses discussed above both use the cosmic shear as the signal, and therefore correlate the shear induced on sources due to the large scale structure of the Universe. In this case, the signal is constructed from the correlations of the ellipticity of a large sample of foreground galaxies with the ellipticities of background galaxies: since galaxies which are closely separated on the sky are lensed by the same local matter density between the observer and the foreground galaxy, correlations will be expected as a function of the angular separation between pairs of galaxies. In contrast, one may consider the lensing due to a particular lensing matter distribution, such as a large cluster. In such cases, a convergence map of the lensing matter may be determined through Kaiser-Squires Inversion (Section 2.2.5). From this, one may obtain the surface mass density on the plane of the lens, allowing a parameter-free mass map of the lensing mass, or a measurement of the cluster mass contained within a given radius. Such mass maps have been produced for large scale structure using CFHTLenS (**?**), and may be used to map the mass of large over-densities, such as clusters. Such Cluster-Galaxy lensing does not make assumptions on the nature of the lensing matter, does not require the virialisation of the halo and does not rely on luminous tracers residing in the cluster potential. Further, the use of mass maps constructed from lensing can be complementary to those from traditional methods such as X-ray emission due to the difference in the dependence of the signal on the nature of the matter in the cluster: in fact, the separation in the peaks of the lensing mass map and the mass map from X-ray emission in the Bullet Cluster provides compelling evidence for the existence of a large unseen, and weakly interacting matter component to the mass content of the merging clusters, and can be used to constrain modified gravity theories as alternatives to dark matter, where no separation between the lensing mass map and X-ray mass map would be observed (Clowe et al., 2006). Further, the offsets between the baryonic matter, dark matter mass maps and stellar positions can be used to probe the cross section of dark matter with a sample of merging clusters (for the Bullet Cluster:Markevitch et al. (2004), and others: Bradač et al. (2008)) or in-falling substructure (Harvey et al., 2013, 2014).

2.3.3 Size Magnification

Isotropic tidal stretching of photons emitted from a distant source by a foreground lensing mass can cause a change in the observed size of the source, so that the observed area covered by the source is related to its unlensed value (A_0) by the local magnification factor: $A = \mu A_0$. The definition of galaxy size can be ambiguous, however Heavens, Alsing & Jaffe (2013) show that a measure of source size proportional to the square root of the area is minimally correlated to galaxy ellipticity measures, suggesting such a definition would maximise the information gain in the combination of size and shear measurements. Taking this definition of the source size, a measured value for the observed galaxy size can be related to its intrinsic, unlensed value with knowledge of the local convergence field

$$R = \mu^{\frac{1}{2}}(\boldsymbol{\theta}) R_0 \tag{2.77}$$

$$\sim (1 + \kappa(\boldsymbol{\theta})) R_0 \tag{2.78}$$

where in the last step the linear value in the weak lensing limit, $\kappa, |\gamma| \ll 1$, has been used. Equations (2.77) and (2.78) suggest that the local convergence acting on a source can be estimated by

$$\hat{\kappa} \approx \ln\left(\frac{R}{R_0}\right) \tag{2.79}$$

$$\approx \frac{R}{R_0} - 1 \tag{2.80}$$

where the linear approximation has been used in both cases. Knowledge of the change in observed size of a source gives a direct measurement of the local convergence. As only the lensed size is observable, the convergence cannot be measured on a single source without other means of determining its intrinsic size, [7] however the local convergence field can be measured statistically using a local sample of lensed sources by measuring the shift in the mean of the distribution of sizes over the mean of the full

[7] Another recent technique to use the magnification part of the lensing signal uses the fundamental plane to relate the effective radius of a galaxy, which is altered by magnification, to the galaxy's surface brightness and stellar velocity dispersion, both of which remain unaltered (Bertin & Lombardi, 2006; Huff & Graves, 2011)

global sample across the field. In this case, the above relation becomes

$$\hat{\kappa} \approx \ln\left(\frac{\langle R\rangle}{\langle R\rangle_{\rm field}}\right) \tag{2.81}$$

$$\approx \frac{\langle R\rangle}{\langle R\rangle_{\rm field}} - 1. \tag{2.82}$$

where $\langle R\rangle$ is the mean of the lensed sample, and $\langle R\rangle_{\rm field}$ is an estimate of the mean of the unlensed distribution: thus to ensure this convergence estimator is unbiased the field mean size should be calculated on a field where mean convergence across the field is zero, usually requiring either a blank field or a large survey area. Further, the lensed sample should be chosen such that the convergence field does not change appreciably across the sample. Direct observations of the induced change in size of a sample of lensed galaxies is the most obvious measure of the magnification effect, and magnification has been successfully detected using a combination of the change in sizes of a lensed population of galaxies and a change in their magnitudes in Schmidt et al. (2012). However, due to the nature of the measurements required to detect size change due to magnification, it suffers from many of the same systematics listed for cosmic shear, and as a result much of the work using the cosmic magnification effect has focused on using the flux magnification signal with number counts. In Casaponsa et al. (2013) it was shown that these systematics may limit the use of size change for ground–based surveys where the size of the PSF is significant compared to the average galaxy size. However for space–based surveys with smaller PSF and higher signal–to–noise ratio, the statistical power of size magnification can rival cosmic shear, and may be an excellent complement to shear analyses (Heavens, Alsing & Jaffe, 2013; Eifler et al., 2013).

Intrinsic-Size-Luminosity relations

As shown above, the action of gravitational lensing by a foreground mass on a source galaxy can have measurable affects on the size distribution of a set of lensed sources, provided the unlensed size distribution is known for that set of sources. However, as detailed in Section 2.2.2, this increase in size corresponds to an increase in the observed flux of the source. As a result, the existence of a non-constant flux-size relation will lead to a bias in a measured convergence estimator using size alone for a sample of

sources limited in flux. Consider a power-law flux-size relation of the form

$$R(S) = AS^{\beta}, \tag{2.83}$$

where A denotes a constant of proportionality, and $\beta > 0$ corresponds to the case where larger galaxies are typically brighter. Under a convergence field, with a local value of κ, the flux transforms according to $S = \mu(\boldsymbol{\theta})S_0$, so that the observed size, due only to the flux magnification of the source, is given by

$$\begin{aligned} R(S_{\rm obs}) &= \mu^{\beta} R(S_0) & (2.84)\\ &\approx (1 + 2\beta\kappa)R(S_0), & (2.85) \end{aligned}$$

where S_0 denotes the un-lensed flux of the source, and magnification factor μ has been expanded to linear order in the final step. Using the estimator given in equation (2.79) with $R_0 = R(S_0)$

$$\hat{\kappa} = \ln\left(\frac{R}{R_0}\right) = \ln\left(\frac{(1 + 2\beta\hat{\kappa})R(S_0)}{R_0(S_0)}\right), \tag{2.86}$$

giving

$$(1 - 2\beta)\hat{\kappa} = \ln\left(\frac{R(S_0)}{R(S_0)}\right), \tag{2.87}$$

where the right-hand-side of equation 2.86 has been Taylor expanded around $\kappa = 0$. Thus, a measurement of the convergence using a size ratio which does not account for the change in flux of the source will return an estimator which is biased by the factor $1 - 2\beta$, and an unbiased estimator can be formed as

$$\hat{\kappa} = \frac{\ln\left(\frac{R}{R_0}\right)}{(1 - 2\beta)}. \tag{2.88}$$

The above relation would be directly applicable to single galaxy measurements if the unlensed size of the galaxy is known, and the size-luminosity relation is exact. Figure 2.6 details the origin of this bias in the case where the convergence is calculated as the shift in the mean value of the size distribution. In this case, the bias is a result of measuring the field mean within the same flux range as the lensed sample: the action of the convergence field also causes a brightening of the sample with the result that the field average within this flux range is no longer representative of the unlensed

distribution for that same body of galaxies. If the field mean is calculated across the field using a sample within a de-lensed flux range, the convergence estimate will be unbiased: thus the mean field size should be calculated using a fainter, typically smaller set of galaxies, or the convergence estimate should account for the intrinsic size-luminosity relation using equation (2.88). The left plot of Figure 2.6 shows an unlensed distribution (blue-crosses), and the magnitude limit (black-solid) on which the sample of lensed galaxies is taken, and from which $\langle R \rangle$ is calculated. Lensed sources which lie within these magnitude limits and form this sample are shown by red crosses. Green solid vertical lines show these magnitude limits when corrected for the constant convergence field across the sample: the blue crosses between these green lines constitute the same body of sources as the lensed bodies in red: thus an unbiased estimator for the convergence field on this sample would compare the mean size of the red crosses with the field mean of the blue crosses within the green lines. Size distributions are shown in the two plots to the right: the top shows the shift between the lensed bodies (red crosses) which constitute the data and the *same* unlensed bodies (blue crosses between green magnitude limits), thus the convergence measured from this shift will not be biased by any intrinsic size-luminosity relation. The bottom panel shows the distribution for the lensed data against the size distribution for the unlensed source which has not taken the size-luminosity relation into account: in this case, the field mean (black-dashed) is taken by averaging the body of sources between the black magnitude limits across the whole sky. As this body of sources experienced flux lensing, they are typically larger than the same sources in the absence of lensing, shifting the field mean to larger values (compare black-dashed to green-dashed), and inducing a systematically low bias in the recovered convergence value. This bias can be corrected for if the correlation of the size-magnitude distribution is understood using Equation (2.88).

2.3.4 Flux Magnification

As a direct consequence of the application of Liouville's theorem (as detailed in Appendix A.1), and as the process of gravitational lensing provides no mechanism for the absorption or emission of photons, the surface brightness of a given patch of sky is conserved, but remapped on the source plane as described by the lensing Jacobian. Denoting the surface brightness in angular co-ordinates as $I_\nu(\theta)$, the surface brightness

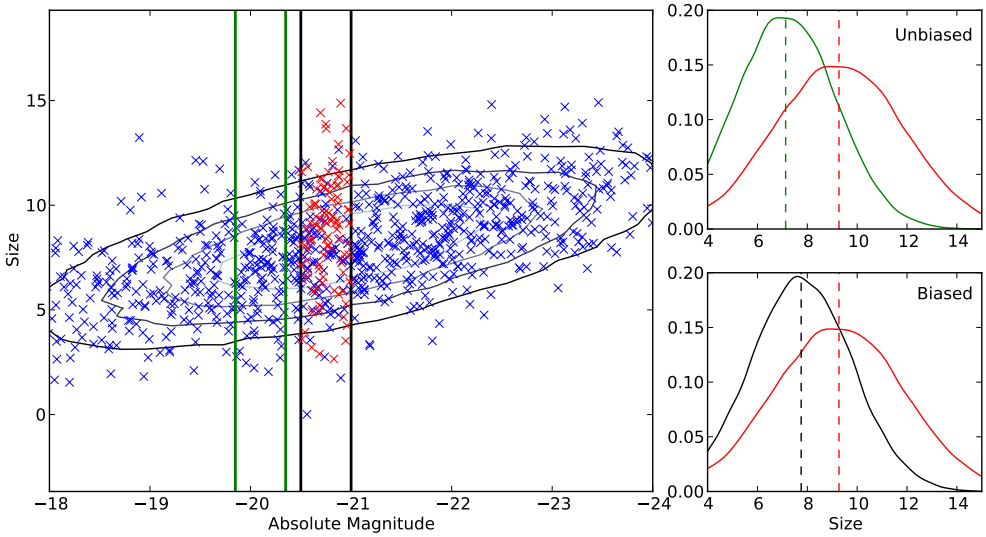

Figure 2.6: An illustrative example of the bias in convergence from using the shift in sizes as an estimator, without proper correction for the intrinsic size-luminosity relation. *Left* shows an illustrative size-absolute-magnitude distribution, with a positive correlation between luminosity and size. Blue crosses show the distribution from unlensed sources, whilst red crosses show lensed sources, under a relatively strong constant convergence field of $\kappa = 0.3$, within a fixed observed magnitude range, shown by black vertical lines. Green vertical lines show the magnitude range of the red crosses in the absence of lensing. *Right* shows size distributions for two cases: *top* shows the size distribution of the unlensed distribution between the unlensed magnitude limits (green solid), with the associated mean value (green-dashed); *bottom* shows the size distribution for the unlensed distribution between the lensed magnitude limits (black-solid), and its associated mean (black-dashed). Both show the size distribution for the lensed data (red-crosses) within this magnitude range (red-solid) and its associated mean (red-dashed). Estimating the convergence using the ratio of red-dashed to black-dashed would give biased results, if the slope of the size-luminosity relation was not corrected for.

profile of the source therefore satisfies

$$I_\nu(\theta) = I^s_\nu(\beta(\theta)) \tag{2.89}$$

where I^s_ν describes the surface brightness of the source in the source plane, and I_ν the surface brightness as mapped onto position θ in the lens plane. The flux emitted by a source with angular area described by solid angle $d\Omega_0$ satisfies $S^0_\nu = I_\nu d\Omega_0$; in the presence of a foreground lensing field, this becomes $S_\nu = I_\nu d\Omega$, where in general the area subtended by the solid angle $d\Omega$ is no longer equal to $d\Omega_0$. From this it can be seen that whilst the surface brightness profile of the source is preserved by gravitational lensing, the subsequent change in its observed size described by the mapping of solid angle $d\Omega_0$ on the source plane to the observed solid angle $d\Omega$ in the lens plane causes a change in the observed flux of the source, described by $S_\nu = \mu S^0_\nu$, where μ is the magnification factor given by the lensing Jacobian describing the mapping between the source and lens planes in a gravitational lensing system, Equation (2.17). Using the relationship between flux and magnitude, the magnitude equivalently transforms according to

$$m = m_0 - 2.5\log_{10}(\mu(\boldsymbol{\theta})). \tag{2.90}$$

Taking the linear limit in κ, and Taylor expanding $\ln(\mu)$ around $\kappa = 0$, the magnitude transforms in the weak lensing limit according to

$$\begin{aligned} m &\sim m_0 - \frac{5}{\ln(10)}\kappa(\boldsymbol{\theta}), & (2.91)\\ &\sim m_0 - 2.17\kappa(\boldsymbol{\theta}). & (2.92) \end{aligned}$$

Thus the action of a magnification field with $\mu > 1$ is to cause a brightening (or *amplification*) of the source, whilst $\mu < 1$ causes a de-amplification and $\mu = 1$ leaves the source unchanged. A measurement of the shift in magnitude under lensing thus gives information on the underlying magnification field, or convergence field in the weak lensing limit. Whilst in practice one can only observe the lensed magnitude of a given source, the local convergence field can be determined statistically by measuring the shift in the mean of the magnitude distribution of the sources in a given patch of sky, over the mean of the distribution across the field. This requires that the field mean is an accurate measure of the mean of the unlensed distribution. As a result, the field mean should ideally be taken on a sample of field galaxies, devoid of large over- or

under-densities that would cause a significant sample of the field to be lensed. If this is not possible, this consideration may hold if the survey area is large enough that the number of samples that experience a brightening due to magnification is balanced by the number that experience a dimming (such as those that reside behind a void) or vice-versa. Further, the sample should be chosen so that the convergence does not vary appreciably over the patch of sky in which the sources reside (otherwise a mean convergence in that patch is measured).

Apart from direct measurements of the magnitude distribution of the sample of sources, the combination of the change in position and change in flux of the source can cause a change in the observed number density of sources in a local lensing potential: the former is sourced directly from the deflection of lensed photons as they propagate between the source and observer, causing a dilution of sources as the solid angle behind the lens is stretched, and the latter the result of observations being limited by flux and the (de–)amplification of sources as their fluxes are (de–)magnified (below) above the survey flux limit, equivalent to a local effective change in the flux limit of the survey. Figure 2.7 provides an illustrative example of this concept, and shows the action of a constant convergence field on a sample of sources. Red points show the position of a body of lensed sources in the size-magnitude plane after the action of this convergence field, blue points show the intrinsic size-magnitude distribution for that sample, and horizontal an vertical lines show the limits on size and magnitude for a given survey or analysis, which may result from limitations in the detection or measurement of galaxies outwith these values. The action of the convergence field serves to increase the brightness and size of the source galaxies, as can be seen in the translation across the size-magnitude plane between the blue and red points. As a result, galaxies whose intrinsic size and magnitude lay outside the survey limits will have been moved into the sample, increasing the size of the background sample after lensing. Similarly, some galaxies whose unlensed values lay within the survey limits will have moved outside this limits, reducing the size of the sample. The combination of both these effects is the origin of the ‘lensing bias’ discussed in Schmidt et al. (2009a,b). The right hand side of Figure 2.7 shows the equivalent change in the survey limits in the presence of a convergence field: shaded regions show the change in each survey limit, where bodies in the green area will be lensed into the sample, whilst bodies in the red areas will be lensed out of the sample.

Lensing can therefore induce non–vanishing number density contrast correlations

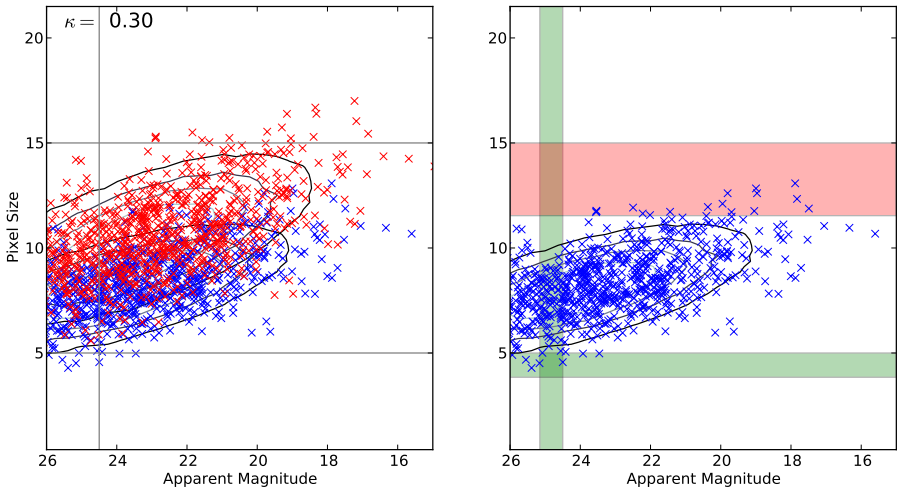

Figure 2.7: Scatter in points randomly sampled from a joint size-magnitude distribution, here modelled for illustration as a multivariate Gaussian. *Left*: red points and contours show the size-magnitude distribution for the blue sample after lensing by a uniform convergence $\kappa = 0.3$, which shifts the measured sizes to larger values, and measured magnitude to brighter values, as well as increasing the variance of the distribution. The vertical line illustrates a faint cut in apparent magnitude whilst the horizontal line illustrates size cuts. *Right*: The unlensed distribution of galaxies plotted in the *left* plot. Filled horizontal and vertical regions show the equivalent change in survey limits in magnitude and size for a sample of source galaxies in this convergence field.

between a background distribution of sources and foreground large scale structure, which are sensitive to cosmology through the distribution of matter and its evolution, and distance measures. The presence of a lensing foreground modifies the observed number density of sources at position $\boldsymbol{\theta}, \chi$ as

$$n(> f, \boldsymbol{\theta}, \chi) = \frac{n_0(> f/\mu(\boldsymbol{\theta}, \chi), \boldsymbol{\theta})}{\mu(\boldsymbol{\theta})}, \tag{2.93}$$

where the μ^{-1} pre-factor accounts for the dilution of sources, and f/μ, the amplification of sources through an equivalent change in the flux limit of the observation.

Considering a probability distribution in magnifications for the source sample, this can be written as

$$n(> f, \boldsymbol{\theta}, \chi) = \frac{\int \mathrm{d}\mu \; p(\mu) n_0(> f/\mu(\boldsymbol{\theta}, \chi), \boldsymbol{\theta})}{\langle \mu(\boldsymbol{\theta}) \rangle}, \tag{2.94}$$

from which the former result can be determined if the magnifications of the source sample are close to single-valued, and are therefore well-approximated by a Dirac delta function around this value. Source counts taken randomly across the field should have $\langle\mu\rangle = 1$, whilst a source sample which resides behind a foreground over-density will have $\langle\mu\rangle > 1$, and behind a foreground under-density $\langle\mu\rangle < 1$. Approximating the unlensed number counts as following a power law at the faint end, $n_0(> f) \propto f^{\alpha}$, the observed number counts are given by

$$\begin{aligned} n(> f, \boldsymbol{\theta}, \chi) &= \mu^{\alpha(f)-1} n_0(> f, \boldsymbol{\theta}, \chi) \\ &\approx \{1 + 2[\alpha(f) - 1]\kappa(\boldsymbol{\theta})\} n_0(> f, \boldsymbol{\theta}, \chi), \end{aligned} \tag{2.95}$$

where the weak lensing approximation $\mu \approx 1+2\kappa$ has been used and the result Taylor–expanded around $\kappa = 0$.

From Equation (2.95) it is clear that when $\alpha = 1$ the overall magnification effect does not cause a change in the observed number density of sources, as the dilution of sources is perfectly balanced by the increased number of galaxies caused by the amplification of sources over the flux limit of the survey. Alternatively, when $\alpha \neq 1$ there will be an overall increase/reduction in the observed number of sources. In terms of magnitudes,

$$\alpha(i_{\rm AB}) = 2.5 \frac{\mathrm{d} \log_{10}\, n(> i_{\rm AB})}{\mathrm{d}i_{\rm AB}}. \tag{2.96}$$

where we have quoted an i–band, AB magnitude $i_{\rm AB}$, chosen here as we will use this passband when analysing CFHTLenS data in Chapter 3. Defining the number density contrast as $\delta n = (n - n_0)/n_0$, equation (2.95) gives the fluctuation in observed number density due to magnification:

$$\delta n_m(\boldsymbol{\theta}) = 2(\alpha - 1)\kappa(\boldsymbol{\theta}). \tag{2.97}$$

The observed number density contrast is then

$$\delta n(\boldsymbol{\theta}) = \delta n_m(\boldsymbol{\theta}) + \delta n_g(\boldsymbol{\theta}) + \delta n_{rn}(\boldsymbol{\theta}), \tag{2.98}$$

with δn_g the contribution from the intrinsic clustering of the sources, and δn_{rn} a random stochastic element which is uncorrelated with the other terms.

From equation (2.98) a clustering number-density-contrast power spectrum can be

constructed from five components:

$$P_{nn} = P_{n_m n_m} + P_{n_g n_m} + P_{n_m n_g} + P_{n_g n_g} + P_{\rm SN}, \tag{2.99}$$

where $P_{\rm SN}$ denotes a pure shot-noise term that originates from the stochastic contribution to the observed number density contrast. Here the first subscript labels the foreground sample: for example, $P_{n_m n_m}$ (mm) denotes the correlation in the number density between the foreground and background samples due to the lensing of both by the same matter distribution forward of the foreground. The final non-noise term, $P_{n_g n_g}$, corresponds to the intrinsic clustering contribution, sourced from the clustering of sources due to their local dark matter environment. As such, this term is largest when the foreground and background are spatially close, and decreases with increasing angular difference of redshift difference between the samples. The cross terms, $P_{n_g n_m}$ (gm) and $P_{n_m n_g}$ (mg) give the correlation between the intrinsic clustering and lensing of the foreground and background: where the first subscript is the foreground, the gm term gives the correlation that arises as the dark matter environment local to the foreground sample is simultaneously responsible for part of the lensing of the background, whilst the mg term is be expected to be zero for samples separated by a large redshift as the clustering of the background is not determined in any way by the mass distribution along the line of sight of the foreground[8]. The contribution to the overall power over a range or redshift bin combinations is shown in Figure 2.8, where the power spectrum contributions have been calculated using the theory detailed in Chapter 3.

The reader is encouraged to note the similarity between the extra clustering terms from intrinsic clustering, and the intrinsic alignment contribution to the power in Section 2.3.2, however it should be noted that the intrinsic clustering terms contribute a much larger fraction of the total clustering power than the intrinsic alignment contribution to the ellipticity power respectively. In practice, the gg term dominates for all but the most widely separated samples, and the gm term dominates the mm term on all scales and redshifts. As a result, analyses which aim to measure the change in number density due to lensing will measure the gm power spectrum, sensitive to both lensing and biased galaxy formation, using cleanly separated galaxy samples

[8]As noted for the GI term in the ellipticity power spectrum, this interpretation is complicated in the presence of uncertainty in the redshift of the foreground and background samples, in which case a small non-zero mg term maybe measured for the small number of galaxies in the background sample which in reality lie forward of the foreground sample.

with little or no overlap in redshift distributions. The domination of the intrinsic clustering contribution subtly changes its interpretation in the context of an analysis using galaxy number densities in comparison to the shear result: whilst one may expect cosmological information in the intrinsic alignment terms due to the process of galaxy formation, its contribution to the shear power is in nearly all cases subdominant and therefore it exists mainly as a contaminant to the analysis; in a number density analysis, the intrinsic clustering contains valuable cosmological information through structure formation and the statistics of the matter field, and thus frequently the lensing contribution exists as a contaminant of the traditional clustering analysis.

The use of observed changes in number density is commonly referred to as 'flux magnification' or 'magnification bias', and it is the former moniker that I will be adopting for the remainder of this text. To date, flux magnification remains the most commonly used probe of the cosmic magnification effect, a fact due not only to its relatively easier measurement [9] but also due to its origins as an unexplained contaminant of early angular clustering measurements. Early measurements of flux magnification using a background set of quasars due to foreground large scale structure were commonly in disagreement, and with measurements that gave amplitudes of correlations far larger than theoretical predictions (Scranton et al. (2005) provides a concise summary of early literature). However, the successful measurement of number density contrast correlations between background quasars and foreground galaxies using the Sloan Digital Sky Survey (Scranton et al., 2005) and the 2dF (Myers et al., 2003), and later using high redshift Lyman break galaxies as sources in CARS (Hildebrandt, Waerbeke & Erben, 2009), laid the basis for the use of magnification as a probe of cosmology and large scale structure.

In contrast to cosmic shear analysis, flux magnification as a probe of cosmology is less mature. For a given sample of galaxies the signal–to–noise ratio for flux magnification is expected to be smaller, as the shot noise in the shear case is reduced by factor of the square of the intrinsic ellipticity dispersion for each ellipticity component. However it should be noted that in the case of ground–based surveys we expect to be

[9] To first order, flux magnification using number counts requires only the counting of galaxies, and is unaffected by the observational difficulties of a direct measurement of galaxy shape or size, such as the PSF or pixelisation. However, since the intrinsic clustering, which constitutes a noise term in a flux magnification analysis, dominates the flux magnification signal except when source and lens are widely separated in radial distance, and the flux magnification signal can be mimicked by dust extinction due to the foreground, a flux magnification measurement requires accurate photometry and tight control over the sample of galaxies used in the analysis.

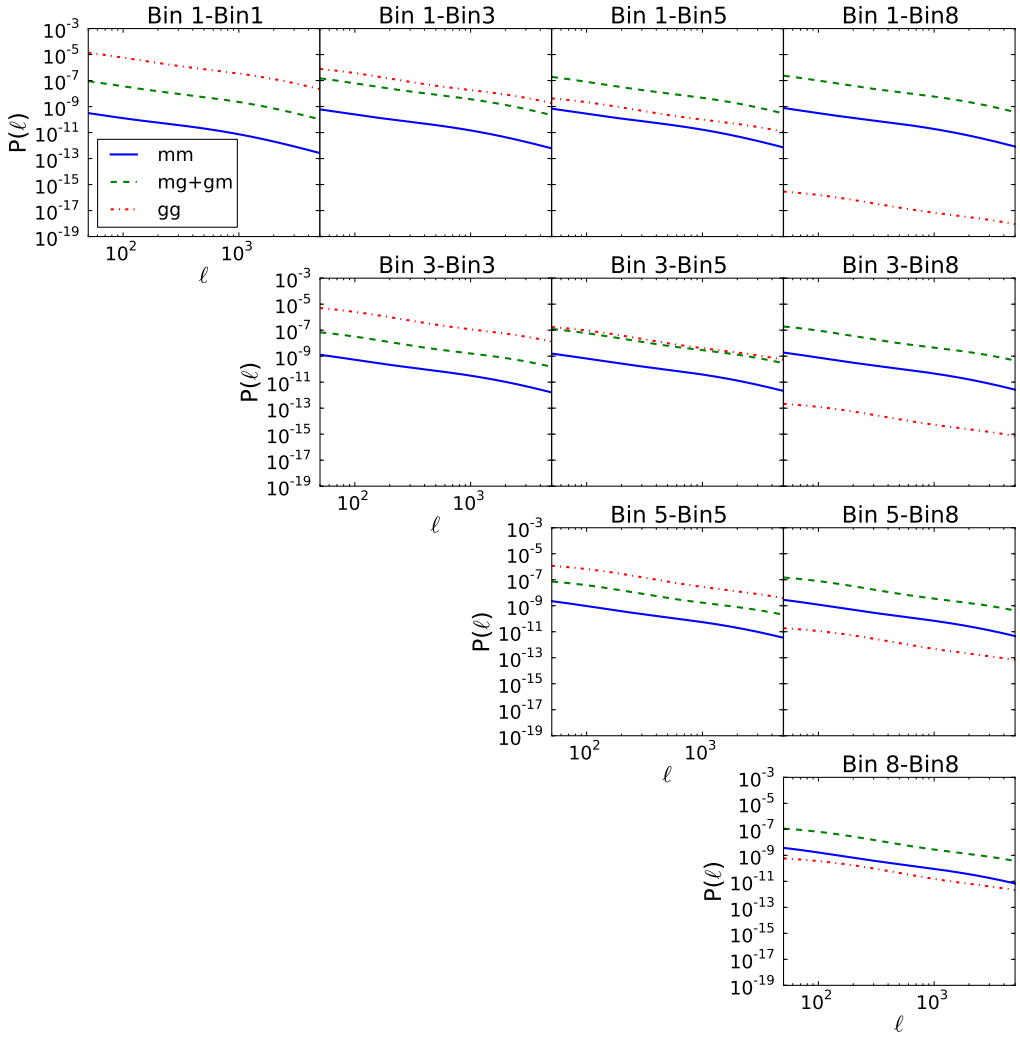

Figure 2.8: Contributions to the number density contrast power spectrum for a combination of background redshift bins, using the survey modelling of Chapter 3. It can be seen that for foreground and background that are spatially close in redshift, the overlap in redshift distribution due to redshift errors can easily cause the magnification terms (mg or mm) to be swamped by the intrinsic clustering term (gg). As we increase the separation in redshift between foreground and background, the amplitude of the gg term decreases whilst the cross (mg + gm) and mm terms increase.

able to use a greater number of galaxies in a flux magnification analysis (provided accurate photometry is determined for these galaxies) than for cosmic shear, as the measurement itself is easier and does not require accurate shape information. This will go some way to offsetting the discrepancy in signal–to–noise ratio between shear and flux magnification.

The use of flux magnification as a probe of cosmology is mainly limited by errors in determining the photometric redshift of sources. In particular, the amplitude of the number density contrast correlation from magnification is smaller than that induced by the intrinsic clustering of galaxies due to their dark matter environment, making it difficult to disentangle these signals in the presence of photometric scatter, causing the intrinsic clustering of spatially close populations to be mis–interpreted as a magnification signal, and giving spurious results. Previous analyses have attempted to remove most of this contamination by choosing carefully selected foreground and background populations which are spatially disjoint (such as Hildebrandt, Waerbeke & Erben, 2009; van Waerbeke, 2010), or using the nulling technique (Heavens & Joachimi, 2011; Schneider, 2014). In 'nulling' the intrinsic clustering signal, the aim is to choose a suitable weighting for projected number density correlation functions to down-weight the unwanted signal, in this case the intrinsic clustering signal. In turn, motivation in the use of this technique is provided by the desire to construct a further lensing signal that is independent of complex astrophysical processes (as for cosmic shear in the absence of intrinsic alignments), such as the efficiency of galaxy formation usually encoded in a galaxy bias factor, which in turn describes the intrinsic clustering signal. In Heavens & Joachimi (2011) the authors attempt to not only null the intrinsic clustering contribution to the number density contrast power spectrum using the redshift dependence of the intrinsic clustering signal, but to also down weight the intrinsic-clustering-flux-magnification cross power and isolate the flux-magnification induced number density correlations only, in an attempt to leave a clean lensing signal. The results show that whilst the remaining signal picks out cosmological parameter values in a less biased way under incorrect assumptions about the galaxy bias, much of the statistical power in the analysis is lost as cosmological information in the cross terms is discarded. The authors note that whilst the nulling technique presented successfully down weights the intrinsic clustering power spectrum to negligible levels, the remaining cross terms are sufficiently large to require accurate modelling of these terms in a flux magnification analysis. The aims of Schneider

(2014) are subtly different: in this, the authors only aim to remove the intrinsic-clustering power whilst *boosting* the cross power. Doing this, the authors show that isolating the cross power gives marginally better constraining power with reduced dependence on inaccuracies of galaxy bias modelling.

In requiring only the use of disjoint redshift distributions to construct the flux magnification signal, one must be aware that one is discarding a large fraction of the information available to a clustering analysis. Similarly, nulling the intrinsic clustering signal will also remove the cosmological information held in that signal, thus both methods may be expected to reduce the statistical power of the analysis over one where all galaxies spanning the whole redshift range of the sample are used to infer cosmology. Even so, the use of an isolated cosmic flux magnification may still be a promising probe: in van Waerbeke (2010) it is shown that the flux magnification between two spatially distinct galaxy populations can give improvement to the shear-only constraints in the $\Omega_{\rm M}, \sigma_8$ plane due to degeneracy breaking between the two signals, whilst in Eifler et al. (2013) the improvement to a larger set of cosmological parameters is shown when magnification information is added to a non-binned, projected shear and clustering analysis[10].In Chapter 3, I investigate further the impact of a cosmic flux magnification contribution to a photometric clustering analysis, and quantify the gains in adding number density information to shear measurements and the contribution of the flux magnification to the accuracy and bias of a series of combined shear-number density experiments.

Beyond the cosmic magnification signal, the flux magnification effect can be used to probe the dark matter distributions for foreground lenses in a similar way to the shear signal. The flux magnification, as with size magnification, is a direct probe of the convergence field, and therefore provides a direct measurement of the mass profile of the lens and not the differential mass profile of shear measurements, nor does it require the complicated conversion between shear measurements and convergence (such as Kaiser-Squires inversion), and is not affected by the mass sheet degeneracy. For this reason, one may expect that the flux magnification can also

[10]In this example, the authors consider the magnification as a separate probe which can be measured independently of the shear and clustering. In an analysis which does not separate the lens and source samples, the flux magnification cannot be easily disentangled from the intrinsic clustering measurement, which will dominate the signal: thus, this result is more easily applied to the cases where the magnification comes from a separate probe, such as size measurements. Even so, the analysis does give an indication of the information gain in combining magnification, shear and clustering, which can be interpreted in the context of a flux magnification analysis.

give complementary information on a local lensing mass distribution to that given by shear measurements alone: this is borne out in Rozo & Schmidt (2010), where the authors show a 50% improvement to mass estimates with the combination of galaxy size and number density information with shear measurements. Further, since flux magnification through number density measures can use a larger sample of unresolved sources which cannot be used for a shear or size analysis, it can be used to probe matter distributions to higher redshift (van Waerbeke, 2010). The measurement of the flux magnification signal has been used to probe the stacked mass profiles of galaxy clusters in SDSS DR3 (Bauer et al., 2013) and CFHTLenS (Ford et al., 2014), galaxy mass profiles in the Deep Lens Survey (Morrison et al., 2012), and measurements of mass density profiles for a selection of CLASH clusters using a joint flux-magnification-shear analysis (Umetsu et al., 2014). The mass of high-redshift sub-millimeter galaxies in HerMES (Hildebrandt et al., 2013) has also been measured, for which traditional shear-based techniques cannot be used due to the unresolved nature of the source galaxies in such a high-redshift sample.

Further potential contaminants in a flux magnification analysis can come from dust extinction by foreground galaxies, and fluctuations in the magnitude zero point of the survey, both of which remain relatively unexplored in the context of a cosmic magnification analysis. The former is caused by the absorption of light from source galaxies by dust in the foreground, causing a reddening of the source , and reducing the observed flux. If dust follows mass, this effect can be problematic for the use of a magnification analysis, as the presence of dust can cause anti-correlations in the observed number of foreground galaxies and background sources that can mimic the magnification signal. Since the flux magnification signal is achromatic, whilst the dust reddening effect is not, the two signals may be separated with knowledge of the colour of the sources. The measurement of, and correction for, the dust extinction effect has been undertaken in the process of obtaining dark matter profile constraints: in (Ménard et al., 2010), the mean dust profile is measured an a sample of foreground SDSS galaxies with high-redshift quasars as a background using the cross-correlation between quasar colour and foreground density, from which dust-corrected flux-magnification galaxy mass profiles are constructed; in Bauer et al. (2013) stacked dust-corrected cluster mass profiles are constructed for both the magnification signal through number counts, and magnitudes. Where the foreground and background sample have been chosen to be spatially disjoint to isolate the flux

magnification signal, care must also be taken to account for errors in the photometry of the background sample due to the reddening by foreground dust, which can cause contamination of the source sample by low redshift galaxies. Contamination of the source sample by reddened background sources can then cause a non-zero intrinsic clustering contribution which may be misinterpreted as a flux magnification signal (Morrison et al., 2012).

2.3.5 Galaxy-Galaxy Lensing

Galaxy-Galaxy lensing (hereafter GGL), denotes the process of cross-correlating the lensing observables (normally tangential shear) of background sources around a sample of foreground lenses. Whilst traditionally galaxy-galaxy lensing analyses measure the shear of the background source sample, similar measurements could be constructed with measurements of the convergence or magnification using galaxy sizes or magnitudes.

As the foreground galaxy sample is biased with respect to the dark matter distribution, and the relation of the lensing of a background galaxy to the foreground matter distribution and geometry is well-known, the GGL cross-correlation function and power spectrum can give useful information on cosmology through the dark matter power spectrum and distance measures (see, for example Mandelbaum et al. (2013) which presents constraints on $\Omega_{\rm M}, \sigma_8$ from a joint clustering and GGL analysis). A consequence of the change in observed number density due to the flux magnification, detailed in Equation (2.98), is that the GGL correlation will contain an extra term resulting from the correlation of the foreground and background sample due to the lensing of both by the same matter distribution forward of the foreground sample. The importance of this extra contribution is detailed in Chapter 3.

Galaxy-galaxy lensing lends itself particularly well to the mass reconstruction of galaxy dark matter halos, with the GGL cross-correlation function constructed to give the correlation between the tangential shear of a sample of background galaxies, around a sample of foreground galaxies which trace the lensing dark matter distribution. Since the tangential shear measures the differential surface mass density of the lens (Section 2.2.2), correlating the position of foreground galaxies with the tangential shear of the background within a given annulus gives a statistical measure of the averaged differential surface mass density of the dark matter halo on a given scale: on small ($\sim$ kpc) scales the GGL signal probes the surface mass density of

the halo in which the galaxy resides, and on larger ($\sim$ Mpc) scales the signal is sensitive to neighbouring halos and large scale structure. Thus GGL can be used to statistically trace the dark matter distribution of galaxy host halos to larger radii than techniques with rely on luminous matter alone (such as through the measurement of rotation curves). It is important to note that in the case of weak lensing, the shear induced in an individual galaxy is too small to be measured directly, and thus the use of a GGL analysis usually requires the correlation around a large sample of foreground galaxies to obtain a statistically significant signal.

The first detection of the GGL signal was reported in Brainerd, Blandford & Smail (1996), and has been detected more recently in several surveys such as Hoekstra et al. (2003); Choi et al. (2012); Velander et al. (2014).

2.3.6 Relative Strengths of Weak Lensing Analyses

In the preceding discussion in this section, I have, so far without qualification, made the point that the weak lensing community has favoured the use of shear over magnification as an observable due to the reduced statistical noise inherent in a cosmic shear analysis. Here I will show this by comparing the relative signal–to–noise for the shear and magnification analyses under some simplifying assumptions. In the interests of brevity, I postpone the more detailed discussion of the construction of each covariance matrix to that undertaken in Chapter 3, instead detailing the simplifications entering each analysis. In each case, the signal–to–noise is constructed as

$$\left(\frac{S}{N}\right) = \left[\sum_{i,j} d_i [\mathrm{Cov}(d)]^{-1} d_j\right]^{\frac{1}{2}} \tag{2.100}$$

where d signifies the data vector used in each analysis, and Cov the covariance of the data. In all cases, I consider the variance across all scales as the data and do not assume the data has been binned in any way.

For the cosmic shear case signal-to-noise is estimated as

$$\left(\frac{S}{N}\right)_{\mathrm{shear}} \propto \frac{2\sigma_{\kappa\kappa} n}{\sigma_\epsilon^2} \tag{2.101}$$

where the covariance is assumed to be shot-noise dominated, $\sigma_{\kappa\kappa}$ is the total variance from all scales, the equality of shear and convergence second-order statistics has been

used, σ_ϵ is the total intrinsic ellipticity dispersion, and n the number density of the sample.

Similarly for an idealised flux magnification analysis using source number counts the signal-to-noise is approximately

$$\left(\frac{S}{N}\right)_{\rm flux} \propto 4|\alpha - 1|^2 \sigma_{\kappa\kappa} n, \tag{2.102}$$

where the covariance is again assumed to be shot–noise dominated, and where α is the slope of the luminosity function which sets the strength of the magnification signal.

Finally, the size magnification has signal–to–noise approximately

$$\left(\frac{S}{N}\right)_{\rm Size} \propto \frac{\sigma_{\kappa\kappa} n}{\sigma^2_{\ln R}}. \tag{2.103}$$

Here again, the covariance is assumed to be shot noise dominated, and the convergence is measured using the shift in galaxy sizes from a distribution of unlensed sizes with width $\sigma_{\ln R}$, where the full range of galaxy fluxes has been measured without limit so the intrinsic size-luminosity relation is unimportant.

From Equations (2.101), (2.102) and (2.103), the relative signal-to-noise can be estimated for each probe as

$$\frac{(S/N)_{\rm shear}}{(S/N)_{\rm flux}} = [2(\alpha - 1)^2 \sigma_\epsilon^2]^{-1}; \quad \frac{(S/N)_{\rm shear}}{(S/N)_{\rm size}} = \frac{2\sigma^2_{\ln R}}{\sigma^2_\epsilon}. \tag{2.104}$$

Taking typical values for the ellipticity and size dispersions as $\sigma_\epsilon \sim 0.4$ (Laureijs et al., 2011) and $\sigma_R \sim 0.5$ (Shen et al., 2003), as well as $|\alpha - 1| \sim 0.5$ (see Chapter 3), we see that the signal-to-noise for the shear analysis is larger than the flux magnification by a factor of approximately 10, and the size analysis by a factor of approximately 3. In both cases, the improvement for the shear analysis is a result of the reduction in statistical noise as a result of the tighter distribution in galaxy ellipticities over sizes or number counts.

We therefore get a clear indication of the relative strength of the shear signal to either the size or flux magnification, however the analysis presented above has been necessarily simplified for illustrative purposes. As well as assuming that the noise in each case is shot-noise dominated, I have assumed that the number of sources in each analysis is roughly the same: whilst this would be approximately true for the comparison between size and shear analyses, it is likely an over-simplification

for the flux magnification case. In actuality, the signal-to-noise estimated for the flux magnification above makes the most assumptions, the largest of which is the assumption that the magnification signal, which can be directly related to the convergence, is accessible: this is not the case in the absence of advanced statistical techniques such as nulling, and instead this contribution to the clustering signal is dominated by a few orders of magnitude by the intrinsic clustering if the foreground and background samples are radially close, and the intrinsic-clustering-flux-magnification cross correlation if the foreground and background are adequately separated. Methods to minimise the intrinsic clustering contamination such as nulling and foreground-background separation must discard cosmological information to do so, increasing statistical errors. This can be avoided if the full clustering signal, including the intrinsic clustering contribution, is used at the expense of increased complexity of the modelling and measurement: the comparison of relative signal-to-noise in this case is complicated by the need to then understand the ratio of the convergence to dark-matter-density correlation to the dark matter power, and will not be presented here; instead, this situation is investigated in detail using a Fisher matrix analysis in Chapter 3.

The discussion presented here focusses on the relative signal-to-noise for each probe individually, and taken on its own this brief analysis would seem to suggest that the use of shear will be much more powerful than either magnification analyses. However, this discussion has relied on some simplifying discussions, and comparing the signal-to-noise for each probe does not allow for much insight into the different information that either analysis contains. A typical lensing survey will have access to more than each probe individually, and so one would like to consider the combination of multiple lensing probes to reduce the statistical errors and provide a form of self-calibration of systematics of each probe individually. It is therefore important to fully understand the relative merits of each analysis, in detail greater than that presented here. In particular, one may wish to understand possible model parameter degeneracy breaking with the combination of multiple lensing probes. The gain from the combination of magnification, shear and clustering analyses looks promising, with expected improvement in cosmological parameter constraints demonstrated with the combination of projected clustering, magnification and shear in Eifler et al. (2013), size-magnification and shear in Heavens, Alsing & Jaffe (2013), and number-counts flux-magnification and shear van Waerbeke (2010). In Chapter 3 I go beyond some

of the simplifying assumptions in these analyses and consider the effect of a flux-magnification signal in the precision and accuracy of a combined clustering, galaxy-galaxy lensing and shear analysis.

Chapter 3

The complementarity of galaxy clustering with cosmic shear and flux magnification

3.1 Introduction

With many current and forthcoming large scale surveys such as the Canada-France-Hawaii Lensing Survey (CFHTLenS)[1], the Dark Energy Survey (DES)[2], the Kilo-Degree Survey (KiDS)[3], Hyper Suprime-Cam (HSC)[4] and Euclid[5](Laureijs et al., 2011), it is becoming more important than ever to understand what gains there are to be made going beyond shear measurements, and in exploiting the other half of the lensing signal through the use of flux magnification.

In this chapter I consider the use of induced correlations in number density between tomographically binned samples of galaxies as a probe of cosmology using a Fisher matrix analysis. I critically focus on what potential gains are to be made when combining a shear and magnification analysis, and then turn to what biases to inferred cosmological parameters would be introduced if magnification was incorrectly neglected in a clustering analysis. The theoretical predictions for the number density power spectra are set out in Section 3.2. In Section 3.3 I detail the modelling of

[1]http://http://www.cfhtlens.org
[2]http://www.darkenergysurvey.org
[3]http://www.astro-wise.org/projects/KIDS
[4]http://www.naoj.org/Projects/HSC/index.html
[5]http://www.euclid-ec.org

galaxy bias and galaxy distributions with photometric redshift errors, and information on number counts taken from public CFHTLenS catalogues (**?**Erben et al., 2012) are used to motivate physical ranges for the slope of the luminosity function. Results are presented in Section 3.4, detailing forecasts using a Fisher matrix formalism for two types of current and future survey, and work investigating how inferred cosmological parameters are biased in a clustering analysis if the flux magnification contribution to number density fluctuations is incorrectly assumed to be zero. Concluding remarks are presented in Section 3.6.

3.2 Theory

3.2.1 Number density and cosmic shear statistics

I consider the observed projected ellipticity of sources using equation 2.75 with $\epsilon_I = 0$, and the projected number density contrast using equation 2.98, where each component is calculated on a sample binned by redshift. The convergence κ, is defined as

$$\kappa_y^{(i)}(\boldsymbol{\theta}) = \int_0^{\chi_H} d\chi \; q_y^{(i)}(\chi)\delta(\boldsymbol{\theta}, \chi) \tag{3.1}$$

with the dark matter over–density denoted by δ, and the weight given as (Bartelmann & Schneider, 2001)

$$q_y^{(i)}(\chi) = \frac{3H_0^2\Omega_m}{2c^2}\frac{f_K(\chi)}{a(\chi)}\int_\chi^{\chi_H} d\chi' \; p_y^{(i)}(\chi')\frac{f_K(\chi'-\chi)}{f_k(\chi')}. \tag{3.2}$$

where a is the dimensionless scale factor, and χ_H the co–moving particle horizon, and superscripts in brackets label the redshift bin of tomographically binned sources. The convergence has identical two–point statistics in Fourier space to the gravitational shear γ, and I therefore use it as the shear observable. Here I have used subscript $y = \{\mathrm{s}, \mathrm{M}\}$ to differentiate between convergence measured from shape and photometry samples. The galaxy comoving distance probability distribution for tomographic redshift bin i is denoted by $p^{(i)}(\chi)$ normalised such that $\int d\chi \; p^{(i)}(\chi) = 1$ for all redshift bins.

The projected number density contrast due to intrinsic clustering is related to the

three–dimensional number density fluctuations δ_g by

$$\delta n_g(\boldsymbol{\theta}) = \int_0^{\chi_H} d\chi \; p_M^{(i)}(\chi)\delta_g(\boldsymbol{\theta}, \chi). \tag{3.3}$$

As number density fluctuations and source ellipticity vanishes when averaged over large scales, I consider two–point correlations of these quantities. In particular, I consider the two–point correlation of the Fourier coefficients of the convergence and number density contrast, related to the power spectrum P by (equation 1.35):

$$\langle x^{(i)}(\boldsymbol{\ell}) y^{(j)}(\boldsymbol{\ell'})\rangle = (2\pi)^2 \delta_D(\boldsymbol{\ell} - \boldsymbol{\ell'}) P_{xy}^{(ij)}(\boldsymbol{\ell}), \tag{3.4}$$

for variables $x, y = \{\delta n, \kappa_s\}$. The two–dimensional Dirac delta function $\delta_D(\boldsymbol{\ell} - \boldsymbol{\ell'})$ illustrates the non–mixing of angular wavenumber (ℓ) modes due to homogeneity on the sky, and I make a flat sky approximation. I construct three observables: Firstly, the 'galaxy clustering' power spectra, constructed from position–position correlations including flux magnification contributions:

$$\begin{aligned} P_{\delta n \delta n}^{(ij)}(\boldsymbol{\ell}) &= P_{mm}^{(ij)}(\boldsymbol{\ell}) + P_{gg}^{(ij)}(\boldsymbol{\ell}) + P_{mg}^{(ij)}(\boldsymbol{\ell}) + P_{gm}^{(ij)}(\boldsymbol{\ell}) \\ &\quad + \delta_K^{ij} P_{\delta n}^{SN}. \end{aligned} \tag{3.5}$$

Secondly, 'cosmic shear' power using ellipticity–ellipticity correlations:

$$P_{\epsilon\epsilon}^{(ij)}(\boldsymbol{\ell}) = P_{\kappa_S \kappa_S}^{(ij)}(\boldsymbol{\ell}) + \delta_K^{ij} P_{\epsilon}^{SN}. \tag{3.6}$$

Thirdly, 'galaxy–galaxy lensing' power spectra, using position–ellipticity correlations:

$$P_{\epsilon \delta n}^{(ij)}(\boldsymbol{\ell}) = P_{\kappa_S g}^{(ij)}(\boldsymbol{\ell}) + P_{\kappa_S m}^{(ij)}(\boldsymbol{\ell}), \tag{3.7}$$

where δ_K^{ij} is the Kronecker symbol. For notational convenience, I have altered subscripts so that subscript 'm' denotes the fluctuation in number density due to flux magnification (formally δn_m) and subscript 'g' the fluctuation due to intrinsic clustering (formally δn_g). The stochastic term for the number density contrast and shear are uncorrelated with the other quantities and only contribute to the shot noise (P^{SN}) in the autocorrelation term. Readers should note that the presence of flux magnification modifies not only the clustering power spectra, but also adds an additional term to the galaxy–galaxy lensing power spectra.

The fluctuation due to intrinsic clustering is related to the matter over–density via a bias term (b) that can be scale– or distance– dependent so that the intrinsic clustering contribution to the power spectrum is given by

$$P_{\delta_g\delta_g}(\boldsymbol{k}, z) = b^2(\boldsymbol{k}, z) P_{\delta\delta}(\boldsymbol{k}, z), \tag{3.8}$$

$$P_{\delta_g\delta}(\boldsymbol{k}, z) = b(\boldsymbol{k}, z) r(\boldsymbol{k}, z) P_{\delta\delta}(\boldsymbol{k}, z), \tag{3.9}$$

where $r(k, z)$ is a stochastic bias which I take to be unity for the remainder of this chapter. Here, $P_{\delta\delta}$ denotes the three–dimensional matter density power spectrum, and $P_{\delta_g\delta_g}$ the three–dimensional intrinsic clustering number density contrast power spectrum. In this work, the matter power spectrum is modelled using Eisenstein & Hu (1998) transfer functions with Smith et al. (2003) non–linear corrections.

All power spectra terms for projected quantities are related to the three–dimensional dark matter power spectra using the Limber approximation in the flat sky limit. The contributions to the number density contrast power spectra in Equation (3.5) are then

$$P^{(ij)}_{mm}(\boldsymbol{\ell}) = 4(\alpha^{(i)} - 1)(\alpha^{(j)} - 1) P^{(ij)}_{\kappa_M\kappa_M}(\boldsymbol{\ell}), \tag{3.10}$$

$$P^{(ij)}_{\kappa_{\rm s} m}(\boldsymbol{\ell}) = 2(\alpha^{(j)} - 1) P^{(ij)}_{\kappa_{\rm s}\kappa_{\rm M}}(\boldsymbol{\ell}), \tag{3.11}$$

$$P^{(ij)}_{m\kappa_{\rm s}}(\boldsymbol{\ell}) = P^{(ji)}_{\kappa_{\rm s} m}(\boldsymbol{\ell}), \tag{3.12}$$

$$P^{(ij)}_{mg}(\boldsymbol{\ell}) = 4(\alpha^{(i)} - 1) \int_0^{\chi_H} d\chi \, \frac{q^{(i)}_{\rm M}(\chi) p^{(j)}_{\rm M}(\chi)}{f^2_K(\chi)} \times b\left(\frac{\boldsymbol{\ell}}{f_K(\chi)}, \chi\right) P_{\delta\delta}\left(\frac{\boldsymbol{\ell}}{f_K(\chi)}, \chi\right), \tag{3.13}$$

$$P^{(ij)}_{gm}(\boldsymbol{\ell}) = P^{(ji)}_{mg}(\boldsymbol{\ell}), \tag{3.14}$$

$$P^{(ij)}_{gg}(\boldsymbol{\ell}) = \int_0^{\chi_H} d\chi \, \frac{p^{(i)}_{\rm M}(\chi) p^{(j)}_{\rm M}(\chi)}{f^2_K(\chi)} \times b^2\left(\frac{\boldsymbol{\ell}}{f_K(\chi)}, \chi\right) P_{\delta\delta}\left(\frac{\boldsymbol{\ell}}{f_K(\chi)}, \chi\right), \tag{3.15}$$

$$P^{(ij)}_{\kappa_s g}(\boldsymbol{\ell}) = \int_0^{\chi_H} d\chi \, \frac{q^{(i)}_{\rm s}(\chi) p^{(j)}_{\rm M}(\chi)}{f^2_K(\chi)} \times b\left(\frac{\boldsymbol{\ell}}{f_K(\chi)}, \chi\right) P_{\delta\delta}\left(\frac{\boldsymbol{\ell}}{f_K(\chi)}, \chi\right), \tag{3.16}$$

where

$$P^{(ij)}_{\kappa_x\kappa_y}(\boldsymbol{\ell}) = \int_0^{\chi_H} d\chi \, \frac{q^{(i)}_x(\chi) q^{(j)}_y(\chi)}{f^2_K(\chi)} P_{\delta\delta}\left(\frac{\boldsymbol{\ell}}{f_K(\chi)}, \chi\right), \tag{3.17}$$

with $x, y = \{\mathrm{s}, \mathrm{M}\}$.

The final contribution to the observed number density contrast power spectrum comes from the shot noise term in Equation (3.5), which takes the form

$$P_{\delta n}^{SN} = \frac{1}{\langle n_{\delta n} \rangle^{(i)}}, \tag{3.18}$$

where $\langle n_{\delta n} \rangle$ is the mean number density of sources used for the clustering analysis.

For ellipticity measurements, the shot noise is given by

$$P_{\epsilon}^{SN} = \frac{\sigma_{\epsilon}^2}{2\langle n_{\epsilon} \rangle^{(i)}}, \tag{3.19}$$

where $\langle n_{\epsilon} \rangle$ is the mean number density of sources used in the shape analysis, and σ_{ϵ} is the total intrinsic ellipticity dispersion, taken here to be $\sigma_{\epsilon} = 0.4$.

Subscripts on the global mean number density $\langle n \rangle$ account for the fact that the global number density of sources used for a shear analysis may differ to that using galaxy clustering information, due to different source redshift distributions and differing source samples, as a result of different selection techniques for the shape and photometry samples (for example, size cuts applied to the shape sample of galaxies).

3.2.2 Parameter forecasts

To estimate parameter constraints I use a Fisher Matrix analysis (see Appendix A.3 for a discussion on the theory behind the use of the Fisher matrix). I consider constraints for the set of cosmological parameters $Q = \{\Omega_M, \Omega_{\mathrm{Baryon}}, \Omega_{\Lambda}, w_0, h, n_{\mathrm{s}}, \sigma_8\}$, which are the matter density, baryon density, dark energy density, dark energy equation of state, dimensionless Hubble parameter, spectral index giving the slope of the primordial power spectrum and the root–mean–square linear matter density fluctuations within a sphere of radius $8h^{-1}\mathrm{Mpc}^3$ respectively. These parameters are taken around fiducial values $\{0.3, 0.0456, 0.7, -1.0, 0.7, 1.0, 0.8\}$. I do not restrict this analysis to flat models, and the curvature is set by $\Omega_k = 1 - (\Omega_M + \Omega_{\Lambda})$. I choose $\ell_{\mathrm{min}} = 50$ to avoid inaccuracies in the Limber approximation, and let $\ell_{\mathrm{max}} = 5000$. However ℓ-mode cuts are implemented on the clustering data to remove scales where the bias is expected to be non–linear (see Section 3.3.1).

The covariance between two power spectra is (Joachimi & Bridle, 2010)

$$\mathrm{Cov}[P^{(ij)}_{\alpha\beta}(\ell), \quad P^{(rs)}_{\gamma\delta}(\ell')] = \delta^{\ell\ell'}_K \frac{2\pi}{\Delta\Omega\ell\Delta\ell} \times \tag{3.20}$$

$$\{P^{(ir)}_{\alpha\gamma}(\ell)P^{(js)}_{\beta\delta}(\ell) + P^{(is)}_{\alpha\delta}(\ell)P^{(jr)}_{\beta\gamma}(\ell)\}$$

$$= \mathrm{Cov}^{(ijrs)}_{\alpha\beta\gamma\delta}(\boldsymbol{\ell}), \tag{3.21}$$

where subscripts $\alpha, \beta, \gamma, \delta = \{\delta n, \epsilon\}$, $\Delta\ell$ is the width of the ℓ bin, and I have assumed that the fields are Gaussian, an assumption that would need to be modified in a more sophisticated analysis. The Kronecker delta symbol marks the non–mixing of angular wavenumber modes, and $\Delta\Omega$ denotes the sky coverage area of the survey.

As the mean of the power spectrum is non–zero, the Fisher matrix is dominated by variations in the mean and given by (Tegmark, Taylor & Heavens, 1997)

$$\boldsymbol{F}_{\eta\tau} = \sum_{\ell} \boldsymbol{D}_{,\eta}(\boldsymbol{\ell})\boldsymbol{C}^{-1}_{\mathrm{A}}(\boldsymbol{\ell})\boldsymbol{D}_{,\tau}(\boldsymbol{\ell}) \tag{3.22}$$

where $\boldsymbol{C}_{\mathrm{A}}(\boldsymbol{\ell})$ is the covariance matrix for data vector $\boldsymbol{D}(\boldsymbol{\ell})$ containing power spectra at angular wavenumber $\boldsymbol{\ell}_r$, with mean of zero, notation '$,\eta$' means the partial derivative with respect to parameter Q_η. Subscripts η and τ run over the set of cosmological parameters Q.

I consider various combinations of shear, clustering and galaxy–galaxy lensing analyses, listed in Table 3.1. For the remainder of this chapter, I use 'clustering–only' (AutoCl, AllCl) to refer to an analysis which takes the number density contrast power spectra (Equation 3.5) as data, 'shear–only' (Sh) to refer to an analysis which uses only the cosmic shear power spectra (Equation 3.6) as data, and 'galaxy–galaxy–lensing–only' (GGL) that which uses only the galaxy–galaxy lensing power spectra (Equation 3.7). For each analysis type, I construct a data vector:

1. For the shear–only case (Sh), the data vector takes the form $\boldsymbol{D}(\boldsymbol{\ell}) = \boldsymbol{D}_{\mathrm{s}}(\boldsymbol{\ell}) = \{P^{(11)}_{\epsilon\epsilon}(\boldsymbol{\ell}), P^{(12)}_{\epsilon\epsilon}(\boldsymbol{\ell}), \ldots, P^{(N_zN_z)}_{\epsilon\epsilon}(\boldsymbol{\ell})\}$ and contains $N_z(N_z+1)/2$ shear power spectra for each ℓ–mode, where N_z is the number of redshift bins used in a tomographic analysis. The covariance matrix is given as $\boldsymbol{C}^{(ij)(rs)}_{\mathrm{A}}(\boldsymbol{\ell}) = \mathrm{Cov}^{(ijrs)}_{\epsilon\epsilon\epsilon\epsilon}(\boldsymbol{\ell})$ for $i, j, r, s = [0, N_z]$.

2. When I consider the clustering–only case (AutoCl, AllCl), the data vector takes the form $\boldsymbol{D}(\boldsymbol{\ell}) = \boldsymbol{D}_{\mathrm{M}}(\boldsymbol{\ell}) = \{P^{(11)}_{\delta n\delta n}(\boldsymbol{\ell}), P^{(12)}_{\delta n\delta n}(\boldsymbol{\ell}), \ldots, P^{(N_zN_z)}_{\delta n\delta n}(\boldsymbol{\ell})\}$ when using

all redshift bin combinations, and $\boldsymbol{D}(\boldsymbol{\ell}) = \boldsymbol{D}_{\rm M}(\boldsymbol{\ell}) = \{P^{(11)}_{\delta n \delta n}(\boldsymbol{\ell}), P^{(22)}_{\delta n \delta n}(\boldsymbol{\ell}), \ldots, P^{(N_z N_z)}_{\delta n \delta n}(\boldsymbol{\ell})\}$ when considering only auto correlations. The data vector then contains N_z clustering power spectra for each ℓ–mode when only auto correlations are considered, and $N_z(N_z + 1)/2$ clustering power spectra when all redshift bin correlations are included. The covariance matrix then takes the form $\boldsymbol{C}^{(ij)(rs)}_{\rm A}(\boldsymbol{\ell}) = {\rm Cov}^{(ijrs)}_{\delta n \delta n \delta n \delta n}(\boldsymbol{\ell})$ for $i, j, r, s = [0, N_z]$.

3. For the galaxy–galaxy–lensing–only case (GGL), the data vector takes the form $\boldsymbol{D}(\boldsymbol{\ell}) = \boldsymbol{D}_{\rm GGL}(\boldsymbol{\ell}) = \{P^{(11)}_{\epsilon \delta n}(\boldsymbol{\ell}), P^{(12)}_{\epsilon \delta n}(\boldsymbol{\ell}), P^{(21)}_{\epsilon \delta n}(\boldsymbol{\ell}) \ldots, P^{(N_z N_z)}_{\epsilon \delta n}(\boldsymbol{\ell})\}$ and contains N_z^2 power spectra for each ℓ–mode. The covariance matrix is given as $\boldsymbol{C}^{(ij)(rs)}_{\rm A}(\boldsymbol{\ell}) = {\rm Cov}^{(ijrs)}_{\epsilon \delta n \epsilon \delta n}(\boldsymbol{\ell})$ for $i, j, r, s = [0, N_z]$.

4. For the combination of clustering with shear (Sh+AutoCl,Sh+AllCl), I define the data vector as $\boldsymbol{D}(\boldsymbol{\ell}) = \{\boldsymbol{D}_{\rm M}(\boldsymbol{\ell}), \boldsymbol{D}_{\rm s}(\boldsymbol{\ell})\}$. The covariance matrix then takes block form

$$\boldsymbol{C}_{\rm A}(\boldsymbol{\ell}) = \left(\begin{array}{c|c} {\rm Cov}^{(ijrs)}_{\delta n \delta n \delta n \delta n}(\boldsymbol{\ell}) & {\rm Cov}^{(ijrs)}_{\delta n \delta n \epsilon \epsilon}(\boldsymbol{\ell}) \\ \hline {\rm Cov}^{(ijrs)}_{\epsilon \epsilon \delta n \delta n}(\boldsymbol{\ell}) & {\rm Cov}^{(ijrs)}_{\epsilon \epsilon \epsilon \epsilon}(\boldsymbol{\ell}) \end{array} \right). \tag{3.23}$$

5. Finally for the combination of clustering with shear and galaxy–galaxy lensing (Sh+AutoCl+GGL,Sh+AllCl+GGL), I define the data vector as $\boldsymbol{D}(\boldsymbol{\ell}) = \{\boldsymbol{D}_{\rm M}(\boldsymbol{\ell}), \boldsymbol{D}_{\rm GGL}(\boldsymbol{\ell}), \boldsymbol{D}_{\rm s}(\boldsymbol{\ell})\}$. The covariance matrix then takes block form

$$\boldsymbol{C}_{\rm A}(\boldsymbol{\ell}) = \left(\begin{array}{c|c|c} {\rm Cov}^{(ijrs)}_{\delta n \delta n \delta n \delta n}(\boldsymbol{\ell}) & {\rm Cov}_{\delta n \delta n \delta n \epsilon}(\boldsymbol{\ell}) & {\rm Cov}^{(ijrs)}_{\delta n \delta n \epsilon \epsilon}(\boldsymbol{\ell}) \\ \hline {\rm Cov}^{(ijrs)}_{\delta n \epsilon \delta n \delta n}(\boldsymbol{\ell}) & {\rm Cov}^{(ijrs)}_{\delta n \epsilon \delta n \epsilon}(\boldsymbol{\ell}) & {\rm Cov}^{(ijrs)}_{\delta n \epsilon \epsilon \epsilon}(\boldsymbol{\ell}) \\ \hline {\rm Cov}^{(ijrs)}_{\epsilon \epsilon \delta n \delta n}(\boldsymbol{\ell}) & {\rm Cov}^{(ijrs)}_{\epsilon \epsilon \delta n \epsilon}(\boldsymbol{\ell}) & {\rm Cov}^{(ijrs)}_{\epsilon \epsilon \epsilon \epsilon}(\boldsymbol{\ell}) \end{array} \right). \tag{3.24}$$

Throughout this chapter I utilise a figure of merit (FoM) as a measure of the constraining power of either analysis considered above, defined as

$${\rm FoM} = \det([\boldsymbol{F}^{-1}]_q)^{-\frac{1}{n_q}}, \tag{3.25}$$

where q denotes the subset of parameter space I am interested in, and n_q the number of parameters in that subset, so that the figure of merit has been rescaled to one dimension. In this chapter I consider two types of FoM:

1. (${\rm FoM}_{\rm DE}$) A Dark Energy Task Force–like figure of merit (**?**), taking $q = \{\Omega_\Lambda, w\}$.

Table 3.1: List of all analyses considered here, with power spectra which enter the data vector, listed in Equations 3.5 through 3.7. Throughout, 'Sh' labels cosmic shear, 'GGL' labels galaxy–galaxy lensing, 'AllCl' labels a clustering analysis using all redshift bin combinations, whilst 'AutoCl' labels a clustering analysis using only auto–correlations in redshift.

Analysis Type	Data
AutoCl	$\delta_K^{ij} P_{\delta n \delta n}^{(ij)}$
AllCl	$P_{\delta n \delta n}^{(ij)}$
GGL	$P_{\epsilon \delta n}^{(ij)}$
AutoCl + GGL	$\delta_K^{ij} P_{\delta n \delta n}^{(ij)}$, $P_{\epsilon \delta n}^{(ij)}$
AllCl + GGL	$P_{\delta n \delta n}^{(ij)}$, $P_{\epsilon \delta n}^{(ij)}$
Sh	$P_{\epsilon \epsilon}^{(ij)}$
Sh + GGL	$P_{\epsilon \epsilon}^{(ij)}$, $P_{\epsilon \delta n}^{(ij)}$
Sh+ AutoCl	$P_{\epsilon \epsilon}^{(ij)}$, $\delta_K^{ij} P_{\delta n \delta n}^{(ij)}$
Sh + AllCl	$P_{\epsilon \epsilon}^{(ij)}$, $P_{\delta n \delta n}^{(ij)}$
Sh + AutoCl + GGL	$P_{\epsilon \epsilon}^{(ij)}$, $\delta_K^{ij} P_{\delta n \delta n}^{(ij)}$, $P_{\epsilon \delta n}^{(ij)}$
Sh + AllCl + GGL	$P_{\epsilon \epsilon}^{(ij)}$, $P_{\delta n \delta n}^{(ij)}$, $P_{\epsilon \delta n}^{(ij)}$

2. (FoM$_{\rm Cos}$) taking $q = Q$ to be the full cosmology parameter set, and thus containing information on the constraints on all parameters.

3.3 Modelling

3.3.1 Galaxy bias

In Section 3.2 I discussed briefly our parameterisation of the intrinsic clustering correlations using a galaxy bias parameter which can be both scale and redshift dependent, $b(k, z)$. I discard any information from the regime where the galaxy bias is expected to be non–linear, and least well–known. To do this I utilise a similar technique to that in Joachimi & Bridle (2010) and Rassat et al. (2008), and remove information at the Fisher matrix level by discarding any bias–dependent information above a certain ℓ–cut ($\ell_{\rm max}$), where

$$\ell_{\rm max}(z^{(i)}) = f_K[\chi(z^{(i)})]k_{\rm max}(z^{(i)}_{\rm max}). \tag{3.26}$$

I choose the median redshift as the characteristic redshift for bin (i), $z^{(i)}$. The maximum wavenumber is fit as $k_{\rm max} = 1.4\pi/R_{\rm max}$, where $R_{\rm max}$ is the radius beyond which the r.m.s. variations in the matter over–density fall below a certain value:

$$\sigma^2(R_{\rm max}, z) = \int d\ \ln(k)\Delta^2(k, z)W^2(kR) = \sigma^2_R, \tag{3.27}$$

using the Fourier transform of a spherical top–hat window function $W(y) = [\sin(y) - y\cos(y)]/y^3$, and $kR = 1.4\pi$ is the value at which this window function first crosses zero, and beyond which there is negligible contribution to the variance from the dark matter power. Hereafter I choose to take ℓ–cuts by fitting $k_{\rm max}$ such that the matter density variance with a sphere of radius R is $\sigma(R, z) \leq 0.5$ which gives $k_{\rm max} \approx 0.3\ h{\rm Mpc}^{-1}$ at $z = 0$, corresponding to $R \approx 14\ h^{-1}{\rm Mpc}$, within the quasi–linear regime. I investigate the implications of this choice of σ_R in Section 3.4.6.

For the number density contrast power spectra $P^{(ij)}_{\delta n\delta n}$, I take the ℓ–cut corresponding to the lowest redshift bin, and for the shear–number density contrast power spectra $P^{(ij)}_{\epsilon\delta n}$ I impose ℓ–cuts for the redshift bin from which number density information is obtained (in this example $\ell^{(j)}_{\rm max}$).

I assume the galaxy bias is scale–independent, and model the redshift dependence using one nuisance parameter per redshift bin, each varying independently and without

bound. I consider three scenarios: Firstly, all galaxy bias nuisance parameters are held fixed at their fiducial value, taken to be $b_{\rm fid}^{(i)} = 1$ for all redshift bins. This corresponds to the case where the linear galaxy bias is perfectly known. Secondly, all galaxy bias nuisance parameters are constrained by the data, with no prior.

In a third scenario I add a prior on the galaxy bias, where the covariance matrix of the galaxy bias parameters is modelled to take the form:

$$\boldsymbol{C}_{\rm Bias} = \sigma_\nu^2 \begin{pmatrix} 1 & \nu & \nu^2 & \cdots & \nu^{N_z-1} \\ \nu & 1 & \nu & \cdots & \nu^{N_z-2} \\ \vdots & & \ddots & & \vdots \\ \nu^{N_z-1} & \nu^{N_z-2} & \nu^{N_z-3} & \cdots & 1 \end{pmatrix}. \tag{3.28}$$

where ν gives the strength of the correlation between adjacent bins, and σ_ν is

$$\sigma_\nu = \sigma_0 \left[\frac{N_z - (N_z - 2)\nu}{N_z(1+\nu)} \right]^{\frac{1}{2}}. \tag{3.29}$$

to ensure 1–σ errors on each bias parameter along $b_1 = b_2 = \ldots = b_{N_z} \equiv b$ are independent of ν (see Appendix A.2), and where σ_0 is the uncertainty of each bias parameter. This prior is then added to the Fisher matrix as

$$\boldsymbol{F}_{\eta\tau} \rightarrow \boldsymbol{F}_{\eta\tau} + (\boldsymbol{C}_{\rm Bias}^{-1})_{\eta\tau} \tag{3.30}$$

where in this case η and τ run only over the bias parameters, $\eta, \tau = \{b^{(1)}, \cdots, b^{(N_z)}\}$, and all elements corresponding to all other parameters are left unchanged.

I therefore define a correlation length, equivalent to the redshift over which the adjacent galaxy bias parameters are significantly correlated. By increasing the strength of the correlation, I reduce the freedom each bias parameter has with respect to its neighbour, thus reducing the variance of the galaxy bias nuisance parameters across redshift bins and making the function of bias versus redshift smoother. I therefore expect that as we increase the correlation strength ($\nu \rightarrow 1$), we should improve cosmological constraints from clustering measurements as we retain more information from the clustering of sources, and increase the value of a FoM using cosmological parameters. As we expect galaxy bias to be a smooth function in redshift, we do not expect galaxy bias parameters between adjacent redshift bins to be negatively correlated, and I consider only $0 \leq \nu \leq 1$. It is worth noting that with the galaxy

bias prior defined in Equation (3.29), the prior becomes singular as $\nu \to 1$.

The parameter σ_0 gives the marginal error on each bias nuisance parameter when fully uncorrelated ($\nu = 0$). As such, σ_0 gives the scatter on the value of the bias in each redshift bin, and is assumed to be the same across all redshift bins considered. As σ_0 sets the level of uncertainty on each galaxy bias parameter, we expect that as we increase the uncertainty in galaxy bias, the constraining power from galaxy clustering will be reduced as less information from the clustering signal is accessible (conversely as $\sigma_0 \to 0$, we recover fully known galaxy bias).

3.3.2 The slope of the galaxy luminosity function

In choosing the values for the slope of the number counts (α) which sets the strength of the magnification effect, I first investigate what typical α values one would expect for an optical galaxy sample using public catalogues from the Canada–France–Hawaii Lensing Survey (CFHTLenS).

This survey covers 154 deg^2, ($\sim$ 125 deg^2 after masking) of the sky in the five $u^*g'r'i'z'$ filters. CFHTLenS combines weak lensing data processed with THELI (Erben et al., 2012), shear measurement using lensfit (Miller et al., 2007) and photometric redshift measurement using PSF–matched photometry (Hildebrandt et al., 2012), with full systematic error analysis of shear measurements and photometry in **?**, and further error analysis of photometric redshifts in Benjamin et al. (2013).

I construct the cumulative number densities of galaxies as a function of limiting magnitude, where sources have been separated into redshift bins, and take the slope of the cumulative number counts as set out in Equation (2.96) to calculate α. Fig. 3.1 shows α as a function of magnitude limit for six tomographic redshift bins as used in Heymans et al. (2013) for three sets of galaxy samples split by population type according to their spectral energy distribution (SED) template value (T): late–type galaxies characterised by $T \geq 2$, early–types taken to have $T \leq 2$, and a full sample (labelled "All"). Errors are taken from a bootstrap analysis, and agree with the estimated errors by taking the variance of α across all fields.

Whilst the value of α varies across the range of limiting magnitudes, all redshift bins converge to a similar value near the limiting magnitude of CFHTLenS at $i_{\rm AB} = 24.7$. The maximum value of α may occur at lower magnitudes. However by cutting at lower magnitudes one will reduce the number of galaxies in the sample thus increasing the shot noise contribution. This suggests that choosing a magnitude cut to maximise

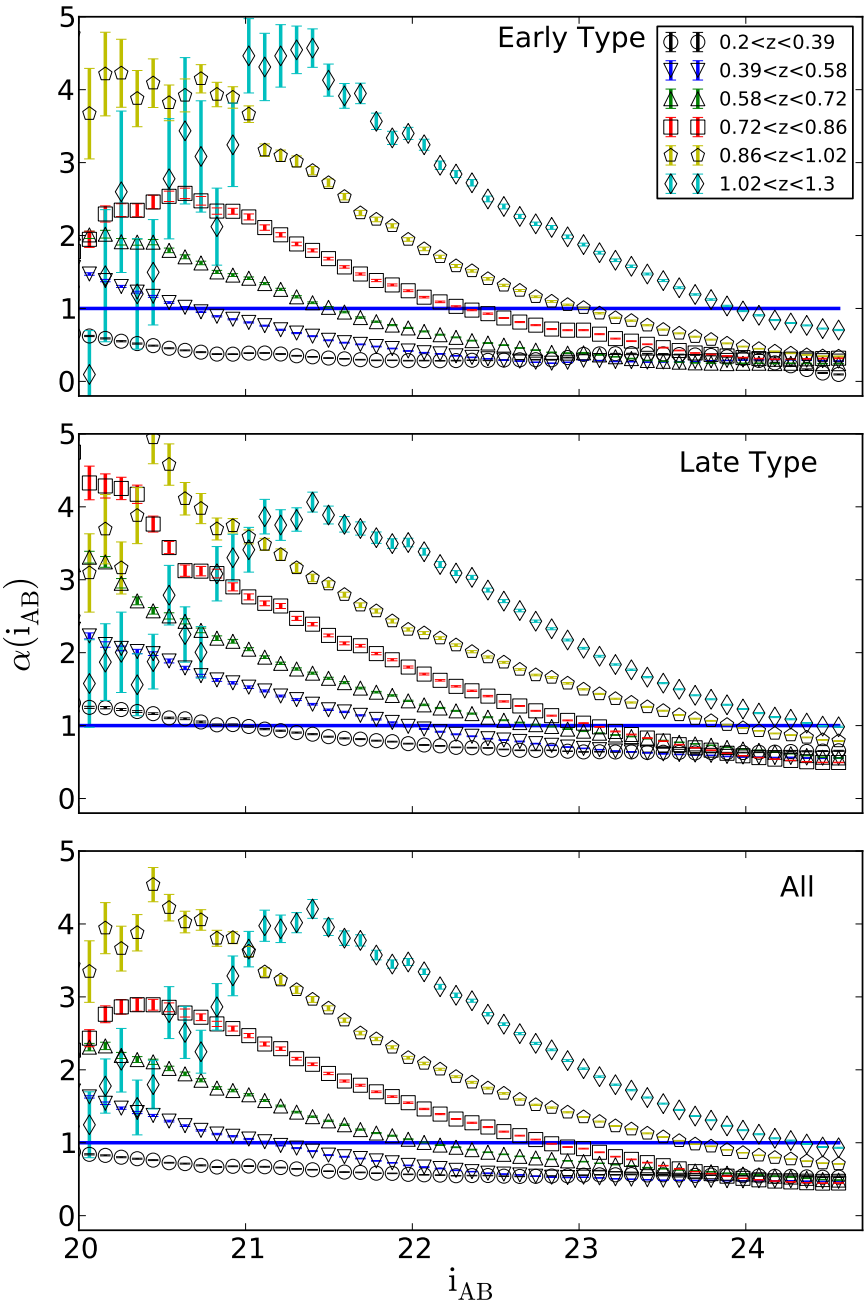

Figure 3.1: The slope of the cumulative galaxy number counts, α, as a function of magnitude for a sample of redshift bins, chosen to be the set of tomographic bins used in Heymans et al. (2013), for a population consisting of early–type galaxies (upper), late–type galaxies (middle) and the full combined sample (lower).

α (and consequently the strength of the contribution from cosmic magnification to the clustering signal) may not maximise the signal–to–noise ratio for a flux magnification analysis.

I therefore define a signal–to–noise ratio estimate for background redshift bin (j) lensed by foreground redshift bin (1) as

$$\hat{S}^{(j)}(i_{\rm AB}) = \langle n^{(1)} \rangle \langle n^{(j)}(i_{\rm AB}) \rangle [\alpha^{(j)}(i_{\rm AB}) - 1]^2, \tag{3.31}$$

where the magnitude limit for the foreground bin is chosen to be as deep as possible to maximise $\langle n^{(1)} \rangle$, and is proportional to the square of the true signal–to–noise ratio. To construct this signal–to–noise ratio estimator $\hat{S}$ I have considered the case where the magnification–intrinsic clustering power spectrum P_{gm} is the only contribution to the clustering signal, and cosmic variance has been assumed to be negligible. Fig. 3.2 shows how $\hat{S}$, rescaled by the maximum signal–to–noise ratio at the limiting magnitude of the survey, behaves as a function of limiting i magnitude, for early and late–type galaxy subsamples.

From Fig. 3.1 it is noticeable that the qualitative variation of α as a function of magnitude and redshift is similar for both samples of late– and early–type galaxies, however the value of α at a given magnitude and redshift is typically larger for the late–type sample. As the catalogues used contain predominantly late–type galaxies, the behaviour of α as a function of magnitude in the full sample is set mainly by the late–type galaxies, and similarly for the signal–to–noise ratio estimator. Whilst both samples show similar qualitative variation in α as a function of magnitude and redshift, the difference between the two samples is more marked in their respectively signal–to–noise plots. Typically, the signal–to–noise ratio for the late–type galaxies is larger than those for the early–type subsample, and this can be attributed to the fact that the late–type subsample contains more galaxies thus reducing the shot noise contribution.

For the late–type subsample, all redshift bins show an oscillation in signal–to–noise ratio as the magnitude is varied. For all redshift bins, we see an increase in the signal–to–noise ratio as the noise is reduced by increasing the size of the sample, followed by a reduction in signal–to–noise ratio as $\alpha \to 1$, the limit where there is no change in the number density of sources due to flux magnification. Finally, past this limit and for $\alpha < 1$ the reduction in noise from increased sample size causes an increase in the signal–to–noise ratio.

For the redshift bins encompassing $0.2 \leq z < 0.86$ the peak of the signal–to–

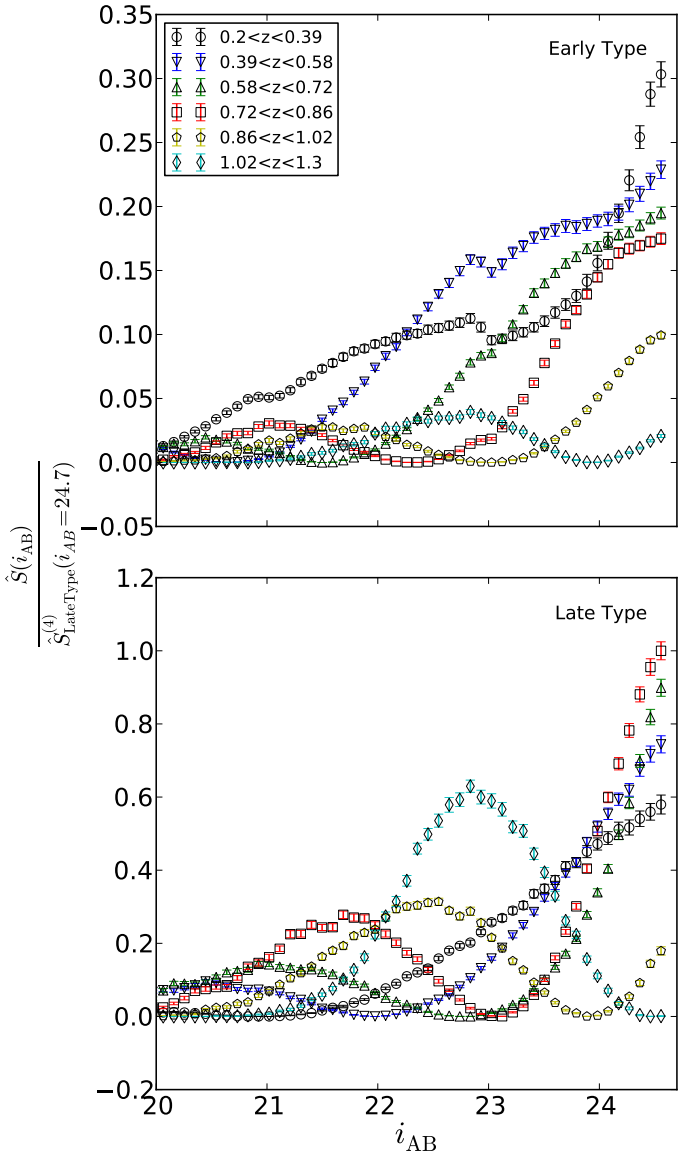

Figure 3.2: The signal–to–noise ratio estimate $\hat{S}$ as a function of magnitude for the set of tomographic bins used in Heymans et al. (2013), for a population consisting of early– and late–type galaxies. To aid comparison, signal–to–noise ratio values are rescaled to the maximum signal–to–noise ratio value at the magnitude limit of the survey, which occurs in redshift bin 4, $0.72 < z < 0.86$ in the late–type subsample. The signal–to–noise ratio for the late–type subsample is typically larger than the early–type subsample, which can be attributed to the smaller early–type population in the full catalogues. Note the different range of ordinates.

noise ratio estimator at the faint limit of the survey ($i_{\rm AB} = 24.7$) is larger than the peak of the oscillation for each respective redshift bin. However in the two largest redshifts bins, the peaks of these oscillations give a larger signal–to–noise ratio at a brighter magnitude than that obtained by naively cutting at the faint limit of the survey. This suggests an analysis chosen to optimise the strength of the magnification contribution to the measured clustering power spectrum should cut at lower magnitude limits for these redshift bins. However, peaks in the signal–to–noise estimator at magnitudes lower than the limit of the survey are limited to the highest redshift bins, where photometry is least accurate, and are nearly entirely absent in the early–type subsample.

In this analysis, I have chosen to consider the optimisation of the clustering signal as set out in Equation 3.5, however the signal–to–noise of the flux magnification contribution may also be optimised by weighting the sample according to $(\alpha - 1)$ (Menard & Bartelmann, 2002). I leave an analysis using this optimisation for future work.

As well as adding galaxies at the faint end of the luminosity function, magnification should also remove galaxies at the bright end of the luminosity function. Assuming that all galaxies in a redshift bin experience a change in magnitude Δm as a result of lensing by the foreground, then the change in the number of galaxies at the faint end is roughly $N(m_{\rm faint})\Delta m$, whilst the change at the bright end is $\sim N(m_{\rm bright})\Delta m$ [6]. Since $N(m_{\rm bright})/N(m_{\rm faint}) \ll 1$, we expect the effect of the removal of sources at the bright end to be subdominant, and ignore it. By choosing a magnitude cut close to the bright limit, this effect becomes more important.

For these reasons, I limit the choice of α values only to values close to the faint limit of the survey, and consider $0 < \alpha < 4$ as reasonable. Unless otherwise stated, results are shown assuming $\alpha = 0.7$ across all redshift bins, which is the value calculated for the full galaxy sample for $i_{\rm AB} \leq 24.7$ and $z \leq 0.86$.

3.3.3 Survey modelling

In this analysis, I consider two types of survey, following a Dark Energy Task Force–like classification of surveys (**?**) considering

[6] This ignores the second–order effect of the change in the cumulative number of sources brighter than the faint end by the removal of sources at the bright end

1. A Stage III ground–based survey (hereafter S3), covering $1500\ \mathrm{deg}^2$ to a depth of $i_{\mathrm{AB}} = 24$. Sources are measured between photometric redshift limits $z_{\mathrm{Phot}} = (0, 2)$ with photometric redshift errors $\sigma_{\mathrm{Phot}} = 0.05(1 + z_{\mathrm{Phot}})$

2. A Stage IV space–based survey (hereafter S4), which covers $15,000\ \mathrm{deg}^2$ of the sky, to a depth of 24.7 in the i–band, between photometric redshift limits $z_{\mathrm{Phot}} = (0, 2)$, and with photometric redshift errors $\sigma_{\mathrm{Phot}} = 0.05(1 + z_{\mathrm{Phot}})$. Unless otherwise stated, results hereafter are shown for an S4 survey.

Fig. 3.3 shows the median survey redshift, and effective number density of galaxies as a function of faint limiting i_{AB} magnitude taken from CFHTLenS catalogues for galaxies with valid shape measurement (**?**) as well as for all galaxies with photometry. As the galaxies broad size distributions are weakly redshift dependent, cuts on galaxy size such as those used in a shape analysis do not significantly affect the measured median redshift, but will cause a noticeable decrease in effective number density of galaxies used. From Fig. 3.3 I choose for the S3 survey a median redshift $z_{\mathrm{med}} = 0.66$, and galaxy number density of $\langle n \rangle = 8.5\ \mathrm{galaxies/arcminute}^2$ and $18\ \mathrm{gal/arcminute}^2$ for shear and clustering analyses respectively. Similarly, I consider for an S4 survey $z_{\mathrm{med}} = 0.7$, and assume shapes can be measured for every detected source. Therefore, I use the photometry line in deducing the number density of galaxies for S4, and take $n_{\mathrm{gal}} = 28\ \mathrm{galaxies/arcminute}^2$ for both shear and clustering analyses.

3.3.4 Galaxy redshift distributions

I model the distribution of galaxies with true redshift z_{t} as

$$p^{(i)}(z_{\mathrm{t}}) = \int_{z_l^{(i)}}^{z_h^{(i)}} dz_{\mathrm{ph}}\ p(z_{\mathrm{t}}|z_{\mathrm{ph}}) p(z_{\mathrm{ph}}), \tag{3.32}$$

where $p(z_{\mathrm{t}}|z_{\mathrm{ph}})$ is assumed to be a Gaussian with width $\sigma_z = 0.05(1+z_{\mathrm{ph}})$, and z_l and z_h denote the lower and higher bounds of the redshift bin in photometric redshift. I model the galaxy photometric redshift distribution, $p(z_{\mathrm{ph}})$, as (Smail, Ellis & Fitchett, 1994)

$$p(z_{\mathrm{ph}}) \propto \left(\frac{z_{\mathrm{ph}}}{z_0}\right)^2 e^{-\left(\frac{z_{\mathrm{ph}}}{z_0}\right)^{1.5}}, \tag{3.33}$$

with characteristic redshift $z_0 = z_{\mathrm{med}}/1.412$. The galaxy redshift distribution is subdivided into redshift bins with equal numbers of galaxies.

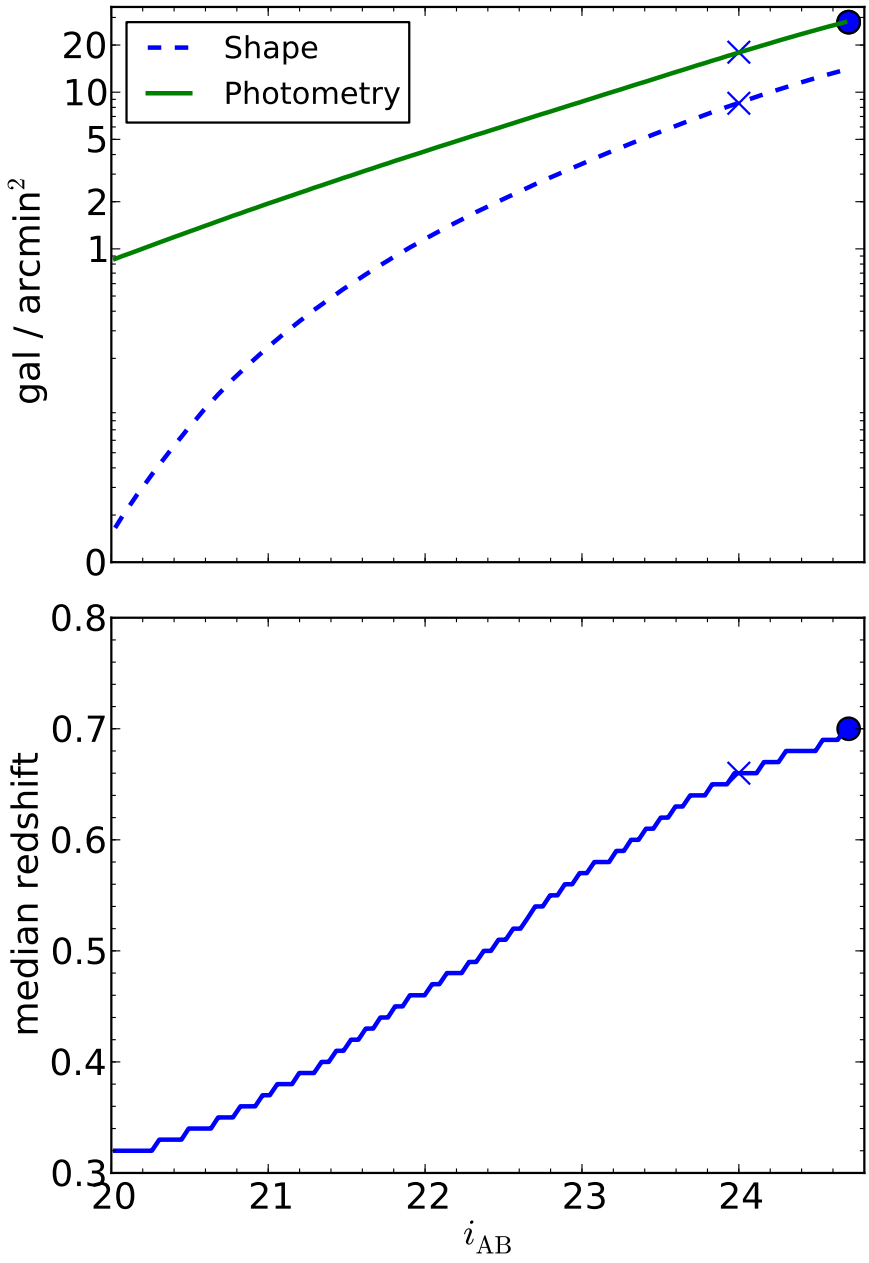

Figure 3.3: The top panel shows the effective number density of galaxies (in galaxies/arcminute^2) as a function of the faint limiting magnitude $i_{\rm AB}$ for sources with valid shape measurement (dashed), and for all galaxies with photometry (solid). The bottom panel shows the median redshift of sources as a function of the limiting magnitude. All data is taken from CFHTLenS catalogues. Crosses mark values taken for an S3 survey, whilst dots mark values taken for an S4 survey.

Fig. 3.4 shows the resultant galaxy distribution for 8 redshift bins for survey types S3 and S4, with the number density contrast power spectra given for three redshift bin combinations in Fig. 2.8, split by component. Noticeably, for closely–separated redshift bins, the intrinsic clustering term is non–vanishing due to the presence of photometric redshift errors which cause some galaxies to be incorrectly assigned to a given redshift bin, and causes overlap between the binned galaxy distributions. As we take redshift bins that are more widely separated, the power from intrinsic clustering decreases, so we see that for the most widely separated bins the total power is dominated by terms that include the magnification. It is for this reason that van Waerbeke (2010) and Hildebrandt, Waerbeke & Erben (2009) take spatially disjoint redshift bins to isolate the magnification contribution to the clustering power spectrum. As the cross power (mg+gm) is always dominant over the pure magnification (mm) power, frequently studies will ignore the pure magnification contribution to the overall clustering power, and instead just quote the cross contribution. In the situation where correlations are considered between distant foreground and backgrounds, the intrinsic clustering contribution is subdominant and may also be ignored. In this analysis, I consider all contributions to the power, as given in Equation 3.5.

3.4 Results

3.4.1 The effect of galaxy bias

In this section, I present forecasts for our S3 and S4 survey models, using the Fisher matrix formalism set out in Section 3.2.2. Throughout this section, I only consider a clustering analysis which includes all redshift bin correlations, and for which flux magnification is modelled (AllCl). Fig. 3.5 shows contours for the set of cosmological parameters laid out in Section 3.2.2, for the cases where we consider constraints coming from a shear–only (Sh), and clustering–only analysis using all redshift bin correlations (AllCl). Fig. 3.6 shows 1σ parameter constraints for a shear–only analysis (Sh), and a combined shear and clustering analysis including galaxy–galaxy lensing (Sh+AllCl+GGL). Both figures show constraints only for a S4 survey, however results for both S3 and S4 surveys are summarised in Tables 3.2 and 3.3. For analyses that contain number density contrast as a probe, ℓ–cuts are applied and galaxy bias is either marginalised over (labelled as unknown galaxy bias), or fixed to $b = 1$ (labelled as known galaxy bias).

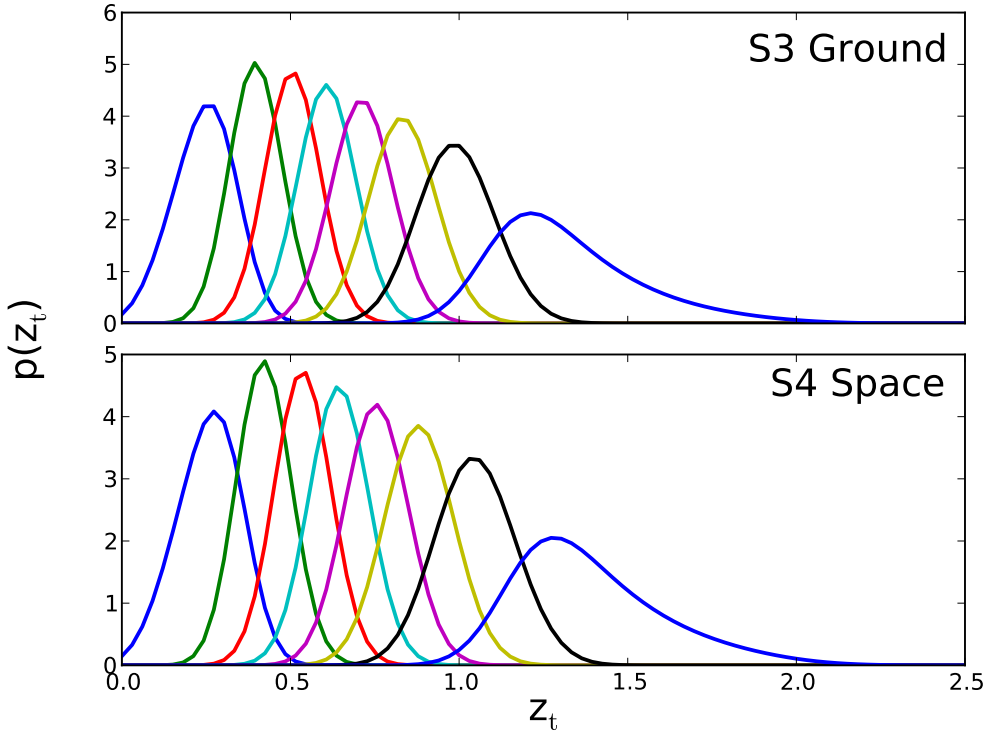

Figure 3.4: Galaxy redshift probability distribution functions as defined in Section 3.3.4, for an S3 ground–based (top) and S4 space–based (bottom) survey (defined in Section 3.3.3).

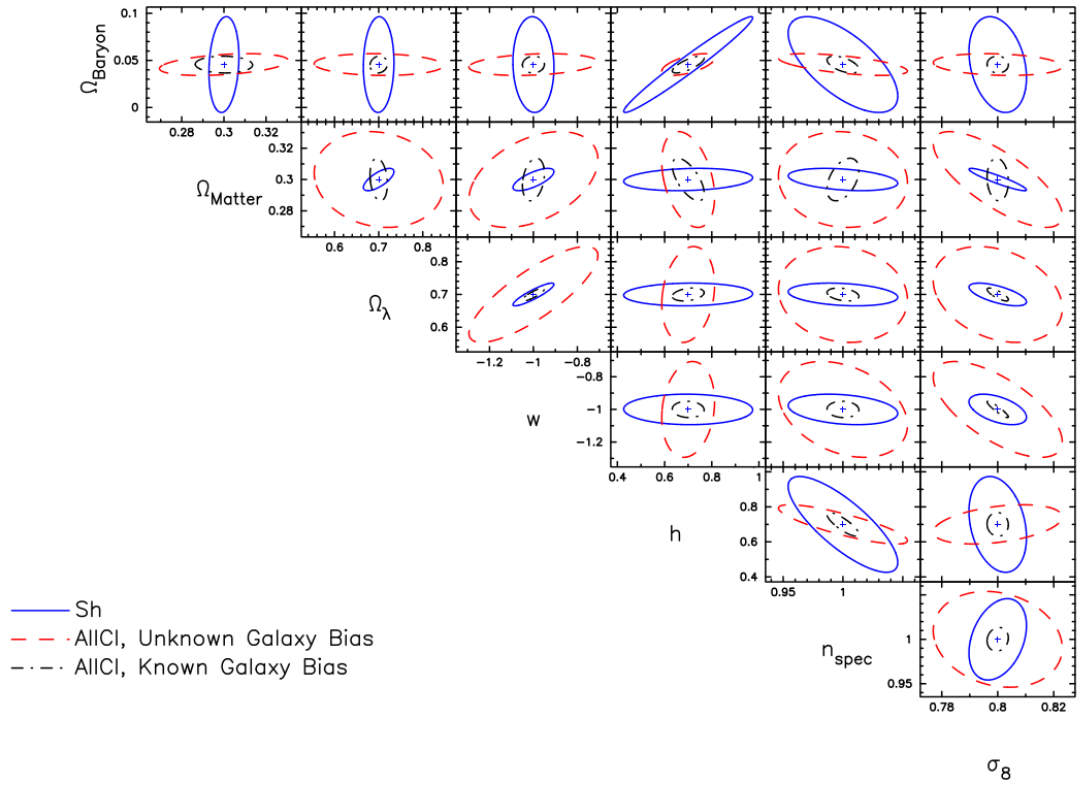

Figure 3.5: Fisher matrix forecast showing marginal two–parameter, 1σ constraints for an S4 space–based survey, considering measurements of galaxy ellipticities only ("shear only", solid blue line), and galaxy clustering including flux magnification. Fixed galaxy bias ($b = 1$) is shown in black (dot–dashed), and unknown galaxy bias (simultaneously constrained with the data) is shown in red (dashed). Constraints from clustering with flux magnification assume $\alpha = 0.7$, and only contain data from linear scales. Cuts on ℓ–modes are applied as detailed in Section 3.3.1, with $\sigma_R < 0.5$.

It is evident that in the case where galaxy bias is known, constraints from a clustering analysis are competitive with cosmic shear. However when galaxy bias is unknown and must also be constrained from the data the constraints from clustering alone are much weaker. This is expected, as when the linear galaxy bias is known the intrinsic clustering contribution to the power spectrum directly probes the matter power spectrum.

It is worth noting that constraints from clustering–only (AllCl) on Ω_B and h are better than those from ellipticity measurements, as the clustering data can better pick out the turnover in the matter power spectrum , since the kernel for projected number density fluctuations (Equation 3.3) is much narrower than that for cosmic

shear (Equation 3.1). Whilst seemingly promising, distance probes combined with CMB measurements will also constrain these parameters very well.

For the combined analysis (Sh+AllCl+GGL) there can be a significant improvement when adding clustering and galaxy–galaxy lensing to cosmic shear. However the improvement to constraints on cosmological parameters is dependent on whether galaxy bias is constrained using the data, or set to a fixed known value (Fig. 3.6). If galaxy bias is known there is a marked improvement in constraints, especially in the $\Omega_M - \sigma_8$ plane. This is in agreement with the results of van Waerbeke (2010), in which galaxy bias was assumed linear and fixed to $b = 1$. If galaxy bias is unknown some of the additional constraining power from clustering and galaxy–galaxy lensing is lost, with $\mathrm{FoM}_{\mathrm{DE}}$ approximately 3.4 times larger for the Sh+AllCl+GGL case if galaxy bias is fixed rather than free. I therefore conclude that the constraints presented in van Waerbeke (2010) will be too optimistic. In fact, in the Sh+AllCl+GGL analysis, much of the information on bias comes from galaxy–galaxy lensing, which allows internal calibration of galaxy bias. As a consequence, using both shear and number density to constrain both cosmology and galaxy bias simultaneously does not lead to much loss of information, provided the parameterisation of galaxy bias is realistic.

Even when the galaxy bias is unknown and simultaneously constrained with the clustering data, the improvement in parameter constraints from the addition of information from galaxy clustering and galaxy–galaxy lensing (Sh+AllCL+GGL) is significant, corresponding to an increase by a factor of 3.7 in $\mathrm{FoM}_{\mathrm{DE}}$ from its cosmic–shear–only value (Sh), for a S4 survey. I draw similar conclusions for the S3 model, with improvements in FoM value by a factor of 6.3 for Sh+AllCl+GGL over the shear–only value. The larger improvement from a combined analysis over shear–only in this case is due to decrease in shot noise in the clustering correlations, as the photometric sample is larger than the shape sample for the S3 model.

If galaxy bias can be constrained externally, the picture will be intermediate between the scenarios presented so far. Therefore, I consider how much information can be regained by correlating galaxy bias parameters across redshift bins, equivalent to making the galaxy bias a smoother function in redshift, or limiting its uncertainty using an external probe, by the addition of a prior on galaxy bias of the form detailed in Section 3.3.1. Fig. 3.7 shows $\mathrm{FoM}_{\mathrm{Cos}}$ for a range of correlation strengths and uncertainties. It is evident that the uncertainty in galaxy bias affects the recovery of information. However there is only a weak degradation of figure of merit when the

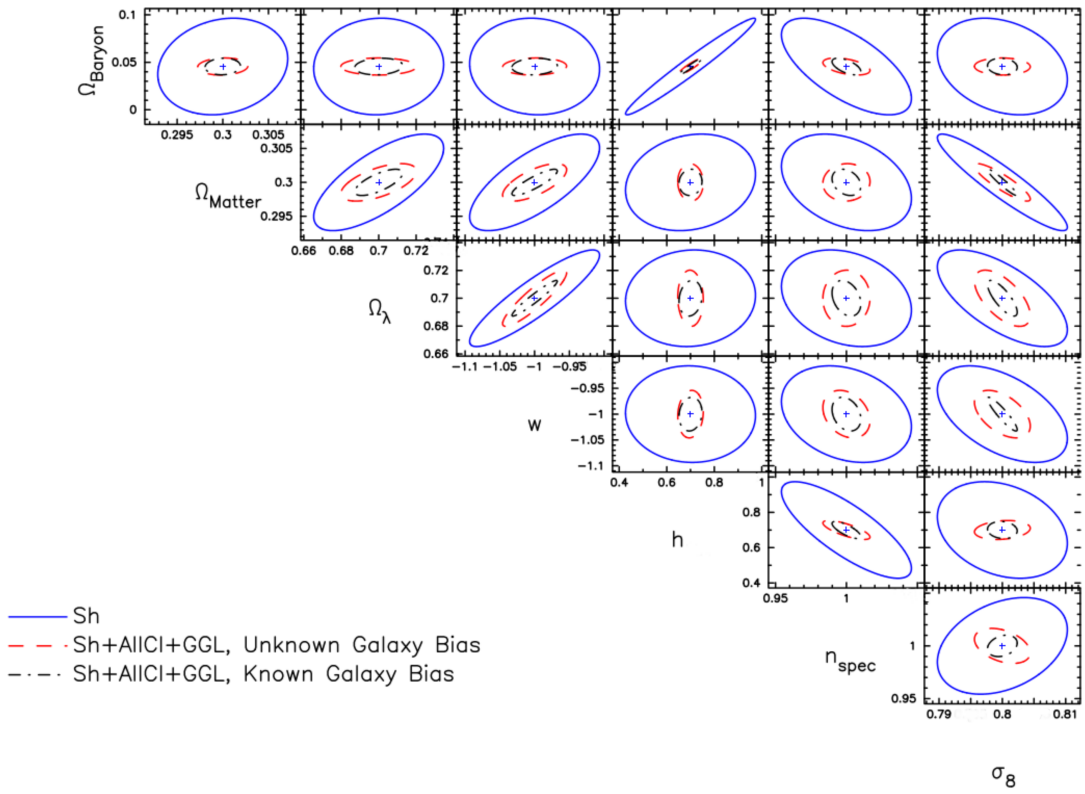

Figure 3.6: As Fig. 3.5, but instead comparing measurements from galaxy ellipticities only (“shear only”, solid), with a combination of shear and galaxy clustering measurements including galaxy–galaxy lensing, for known galaxy bias, $b = 1$, (dot–dashed), and unknown galaxy bias which is simultaneously constrained by the data (dashed).

correlation strength is decreased for a joint (Sh+AllCl+GGL) analysis.

Gaztañaga et al. (2012) concluded that magnification alone can produce better results than shear alone when the galaxy bias is known. However 'magnification' there corresponds with 'clustering' in this work, using all contributions to number density fluctuations. Accounting for the fact that we use different definitions for our figure of merits, our results are in broad agreement. It should be noted, however that they chose much more optimistic ℓ–cuts than those presented here, and applied these ℓ–cuts to all probes including their shear measurements. In addition, they assume linear theory when modelling the matter power spectrum, suggesting they under–estimate the constraining power of cosmic shear. Additionally, they modelled galaxy bias using four free parameters, whereas I assign a galaxy bias nuisance parameter to each redshift bin used. As a result, Gaztañaga et al. (2012) found that clustering (or magnification in their terminology) with unknown galaxy bias is much more competitive with cosmic shear than I find in this work. However the conclusion in both analyses is that when galaxy bias is known, galaxy clustering can be a competitive probe of cosmology to cosmic shear alone. Similarly, both analyses show that the combination of galaxy clustering, galaxy–galaxy lensing and cosmic shear gives a significant improvement in statistical errors on cosmological parameters over cosmic shear alone.

Eifler et al. (2013) consider a non–tomographic analysis which includes all cross–correlations between a intrinsic clustering, shear, galaxy–galaxy lensing, and magnification for a survey modelled on DES. The authors conclude that whilst the combination of all probes significantly improves the constraints over each individually, the inclusion of a magnification analysis does not substantially contribute to the information in joint shear, clustering and galaxy–galaxy lensing analysis, in agreement with the results I present here. However, the authors go beyond the assumption that the data are Gaussian distributed, and model a non–Gaussian contribution by summing tri–spectrum contributions using the halo model. The authors conclude that the change in forecasting cosmological parameter constraints for the full combined analysis due to incorrectly assuming Gaussianity is comparable to the change in constraints between taking known or free galaxy bias nuisance parameters. This change is largest for σ_8 and n_s, with the dark energy equation of state w insensitive to non–Gaussianity. However there is no cut on highly non–linear scales in the clustering signal, and as we expect that the effect would be reduced if highly non–linear scales are removed from the analysis, I therefore expect my results to be robust even under the Gaussian

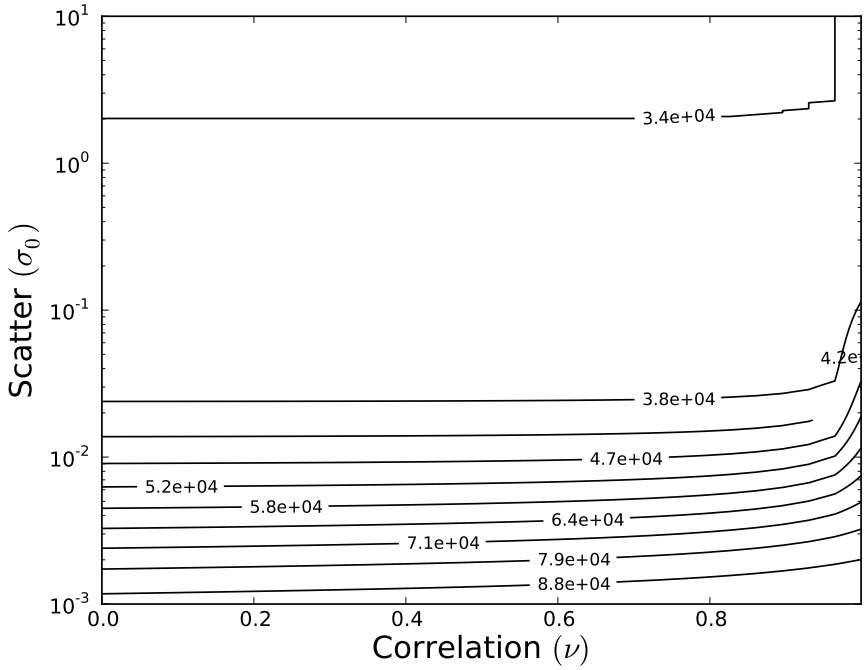

Figure 3.7: $\mathrm{FoM_{Cos}}$ as a function of σ_0 and ν (the uncertainty and correlation in the galaxy bias prior as detailed in Equation 3.28) for an S4 survey, using the Sh+AllCl+GGL analysis.

assumption, particularly for dark energy parameters.

3.4.2 The contribution from flux magnification

In this section, I investigate how much of the constraining power using galaxy clustering (AllCl) comes from the magnification terms ($P_{mm}, P_{mg} + P_{gm}$ in Equation 3.5), and how much comes from intrinsic clustering only (P_{gg}). If $\alpha = 1$, the terms which depend on the magnification are identically zero, so that number density fluctuations come from the intrinsic clustering only. In the limit of large α, the clustering power spectrum is dominated by the magnification contribution (P_{mm}) for all redshift bin combinations. By altering α, we can therefore alter the strength of the contribution from flux magnification, and therefore test the level of contribution to parameter constraints from the magnification effect.

Fig. 3.8 shows the figure of merit ($\mathrm{FoM_{Cos}}$) as a function of α from galaxy clustering–only (AllCl), and a combined clustering, cosmic shear and galaxy–galaxy lensing (Sh+AllCl+GGL) analysis. I note that the FoM increases with $\alpha > 1$ for

the AllCl case, as the contribution from flux magnification becomes larger, and the minimum in $\mathrm{FoM}_{\mathrm{Cos}}$ occurs at $\alpha = 1$ where the contribution to the clustering power spectrum from the magnification terms is zero. I therefore conclude that a non–zero measurement of $\alpha - 1$ will improve the total constraints on cosmological parameters provided no galaxies are removed from the sample. However, as discussed in Section 3.3.2, analyses that try to optimise for a clustering analysis by cutting at a magnitude limit which gives a large value of α may degrade the signal overall by removing sources from the sample and increasing noise.

Whilst similar behaviour is seen in the combined (Sh+AllCl+GGL) probe, I note that the relative improvement in the FoM as $|\alpha - 1| > 0$ is much smaller than the clustering–only (AllCl) case. As the constraints on cosmological parameters from clustering are much weaker that those from shear when galaxy bias is unknown, most of the improvement in FoM for the combined Sh+AllCl+GGL probe comes from degeneracy lifting between the clustering, shear and galaxy–galaxy lensing signals, and so, whilst a non–zero value of $\alpha - 1$ may greatly improve the constraining power of a clustering–only (AllCl) analysis, it does not change the constraining power of a combined (Sh+AllCl+GGL) analysis significantly. I note also that the minimum of the FoM for the combined analysis does not lie at $\alpha = 1$ as it does in the clustering–only case. For $\alpha > 1$, the clustering signal becomes more degenerate with the shear, and so we expect a shift in the minimum for the combined analysis. Over this minimum, the increase in α causes the FoM for the combined analysis to increase.

In this initial study, I have chosen to ignore intrinsic alignments, for improved clarity of the magnification effects. The analysis here would therefore be most applicable for blue samples, for which the intrinsic alignment is small (Heymans et al., 2013). For a sample of red galaxies, a more comprehensive analysis would need to take intrinsic alignments into account. However in Joachimi & Bridle (2010) it was shown that the best calibration for intrinsic alignments comes from the inclusion of galaxy–galaxy lensing with the shear information. Whilst the galaxy–galaxy lensing signal contains a contribution from flux magnification (Equation 3.7), we know that the sensitivity of the magnification–ellipticity contribution ($P_{\kappa_{\mathrm{S}}m}$) is sub–dominant to the intrinsic clustering–ellipticity correlations ($P_{\kappa_{\mathrm{S}}g}$) on all scales and for all redshift bin combinations. Therefore, while the inclusion of a flexible intrinsic alignment model will weaken the constraints for a shear only analysis, we expect that the flux magnification effect will only weakly affect the self–calibration when combining shear

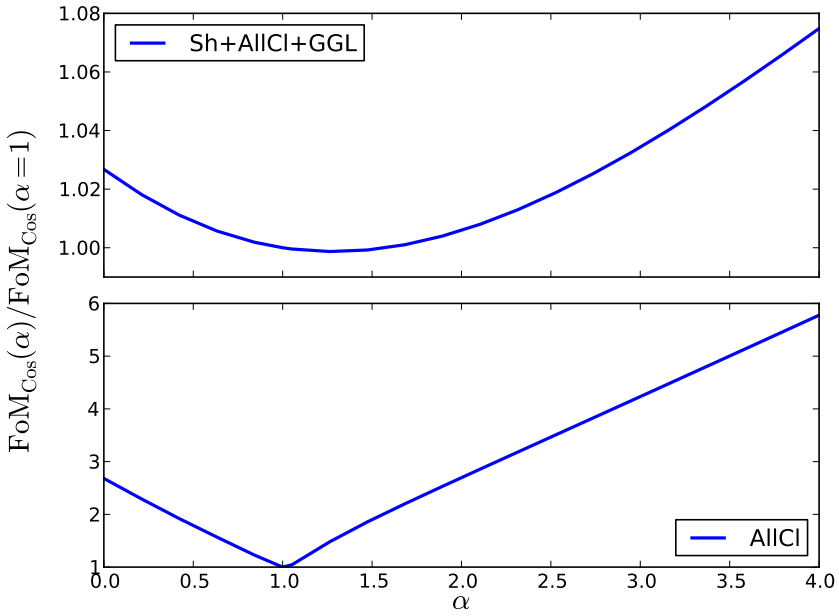

Figure 3.8: Figure of Merit ($\mathrm{FoM}_{\mathrm{Cos}}$) as a function of the slope of the cumulative number counts, α, for a clustering–only analysis (bottom), and combined shear and clustering analysis (top), for an S4 survey. All values are rescaled to the value of the Figure of Merit when $\alpha = 1$ corresponding to the case when fluctuations to the number density contrast come from the intrinsic clustering of galaxies only. Note the different range of the ordinate axes.

and clustering.

3.4.3 Tomography

Here, I consider how much information can be gained from increasing the number of redshift bins considered in the analysis. Fig. 3.9 shows $\mathrm{FoM}_{\mathrm{Cos}}$ as a function of N_z, the number of redshift bins, for shear–only (Sh), clustering–only (AllCl) and a combined shear, clustering and galaxy–galaxy lensing (Sh+AllCl+GGL) analysis. In all cases the clustering analysis uses all redshift bin correlations. For all N_z, the number of galaxies in each redshift bin is kept the same. We see that for all three cases, the information gain by adding redshift bins is large for small N_z, but quickly asymptotes to a constant. We note that for the shear–only case, there is little information gain in taking more than ~ 4 redshift bins, which agrees with results shown in Joachimi & Bridle (2010). However, the clustering analysis continues to improve constraints up to much higher numbers of redshift bins, and only starts to asymptote to its maximum

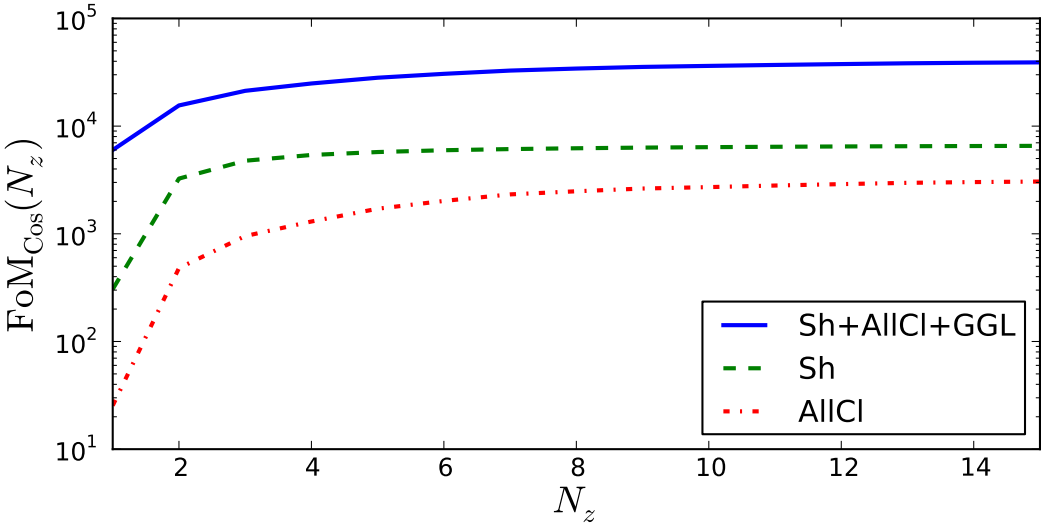

Figure 3.9: Figure of merit ($\mathrm{FoM}_{\mathrm{Cos}}$) as a function of number of redshift bins, for a S4 survey and for a shear–only (green, dashed), clustering–only (red dot–dashed) and combined (blue, solid) analysis.

around $N_z \sim 8$. This may be expected as the kernel of the fluctuations for number density due to intrinsic clustering, as defined in Equation 3.3, is much narrower than the lensing kernel, with less overlap between redshift bins, thus we may expect that we can continue to subdivide the galaxy distribution further for the clustering analysis before the clustering power spectra across different bin combinations become highly correlated.

For the combined case, we see that the improvement for a small number of tomographic bins is less than either the shear–only or clustering–only cases. However, constraints from the combined analysis continue to improve up to high N_z. By this point, the improvement from shear has asymptoted to its maximum, and the gain comes from continued information gain from the clustering and galaxy–galaxy lensing signals, as the galaxy distribution is further subdivided.

3.4.4 Forecasts for various combinations of clustering, cosmic shear and galaxy–galaxy lensing

Whilst results presented so far have focused on a clustering analysis which uses all available redshift bin correlations, one may be motivated to consider a clustering

analysis which only uses auto–correlations in redshift, as in the auto–correlation terms the intrinsic clustering signal is dominant to the largest magnification contribution, and for which it may be suggested that flux magnification can perhaps be ignored. In this section, I investigate what gains can be made to a photometric redshift clustering analysis when these cross correlations are also included, and whether there is a significant gain when combined with a cosmic shear analysis. Further, I investigate how well galaxy–galaxy lensing can probe cosmology, both as an independent probe or in combination with clustering and cosmic shear. In this section, I present forecast constraints on dark energy parameters for all analyses set out in Table 3.1, and using the Fisher matrix formalism of Section 3.2.2, I present forecasts for a S4 survey.

Fig. 3.10 shows marginal constraints in the dark energy parameter (Ω_Λ, w) plane, for two different values for α. The right column shows contours when $\alpha = 1$, the case when the clustering power spectrum contains no flux magnification contribution. In this case, any improvement in cosmological parameter constraints for a clustering analysis which includes redshift cross–correlations comes from the addition of the intrinsic clustering signal between separated redshift bins, which may be non–zero due to photometric redshift scatter. As well as probing cosmology, these cross–correlations of the intrinsic clustering signal can help constrain galaxy bias, as they are sensitive to cross–correlations between the galaxy bias in different redshift bins. However information from each cross–correlation contribution is expected to be less than the auto term, as in the absence of magnification the power from increasingly widely separated redshift bins rapidly decreases. Similarly, when $\alpha = 1$ the galaxy–galaxy lensing signal reduces to correlations between shear convergence and intrinsic clustering, and the magnification bias contribution vanishes. In the left column, I present contours for $\alpha = 0.7$, the value inferred from CFHTLenS data as described in Section 3.3.2. In this case, there is a contribution to the clustering power spectrum from the inclusion of flux magnification effects. Top panels show contours for both types clustering–only analysis (AutoCl, AllCl), middle panels the constraints coming from the addition of cosmic shear information to each clustering analysis (Sh+AutoCl, Sh+AllCl), and bottom panels with the further addition of galaxy–galaxy lensing (Sh+AutoCl+GGL,Sh+AllCl+GGL). In all panels, the cosmic shear contours are shown for reference.

From Fig. 3.10 we see that the use of cross–correlations in redshift bins gives considerable improvements in constraints from a clustering–only analysis. The

addition of clustering information to cosmic shear (Sh+AutoCl, Sh+AllCl) improves constraints over the shear–only case, with further significant improvement with the addition of galaxy–galaxy lensing.

These results are borne out by Tables 3.2 and 3.3, which show $\mathrm{FoM_{DE}}$ values, with 1σ errors on Ω_Λ and w for an S4 and S3 survey respectively. We see a significant improvement in parameter constraints with the addition of redshift cross–correlations in a clustering–only analysis (AutoCl to AllCl) for both survey types. For a S4 survey which takes galaxy bias as unknown and $\alpha = 0.7$, the use of clustering cross–correlations shows a decrease by a factor of ~ 2 in the statistical error of w, ~ 2.26 in Ω_Λ, and an increase in $\mathrm{FoM_{DE}}$ by a factor of 3.2 over the AutoCl case. When $\alpha = 1$, $\mathrm{FoM_{DE}}$ shows an increase by a factor of 2.4.

The combination of both clustering analyses with galaxy–galaxy lensing (AutoCl+GGL, AllCl+GGL) both outperform a cosmic shear only analysis (Sh), confirming that the combination of clustering with galaxy–galaxy lensing provides a competitive alternative to cosmic shear, as suggested by **?**.

The combination of clustering redshift auto–correlations with cosmic shear (Sh+AutoCl) show an improvement on parameter errors of $\sim 15\%$ for both dark energy parameters over the shear–only (Sh) case, corresponding to a 33% increase in $\mathrm{FoM_{DE}}$. The addition of redshift cross–correlations in the clustering analysis (Sh+AllCl) gives a further improvement of 14% in $\mathrm{FoM_{DE}}$.

For an analysis which combines cosmic shear, galaxy–galaxy lensing and clustering using all redshift bin correlations (Sh+AllCL+GGL), there is a significant improvement over parameter constraints when compared to the cosmic–shear–only case (Sh), with a decrease of ~ 2.0 and ~ 1.75 in statistical errors on w and Ω_Λ respectively, giving an improvement by a factor of 3.7 to $\mathrm{FoM_{DE}}$. This is a $\sim 30\%$ improvement to the case where only clustering auto–correlations in redshift are combined with cosmic shear and galaxy–galaxy lensing (Sh+AutoCl+GGL).

We note that there is little difference in statistical errors between both choices of α for the various combinations of shear with clustering (Sh+AllCl, Sh+AutoCl), and even if galaxy–galaxy lensing is also included (Sh+AllCl+GGL, Sh+AutoCl+GGL). For shear with clustering auto–correlations (Sh+AutoCl), there is no change to $\mathrm{FoM_{DE}}$ between both choices of α, as the clustering auto–correlation terms are dominated by the intrinsic clustering signal. With the inclusion of clustering cross–correlations in redshift (Sh+AllCl), the presence of flux magnification gives a sub–

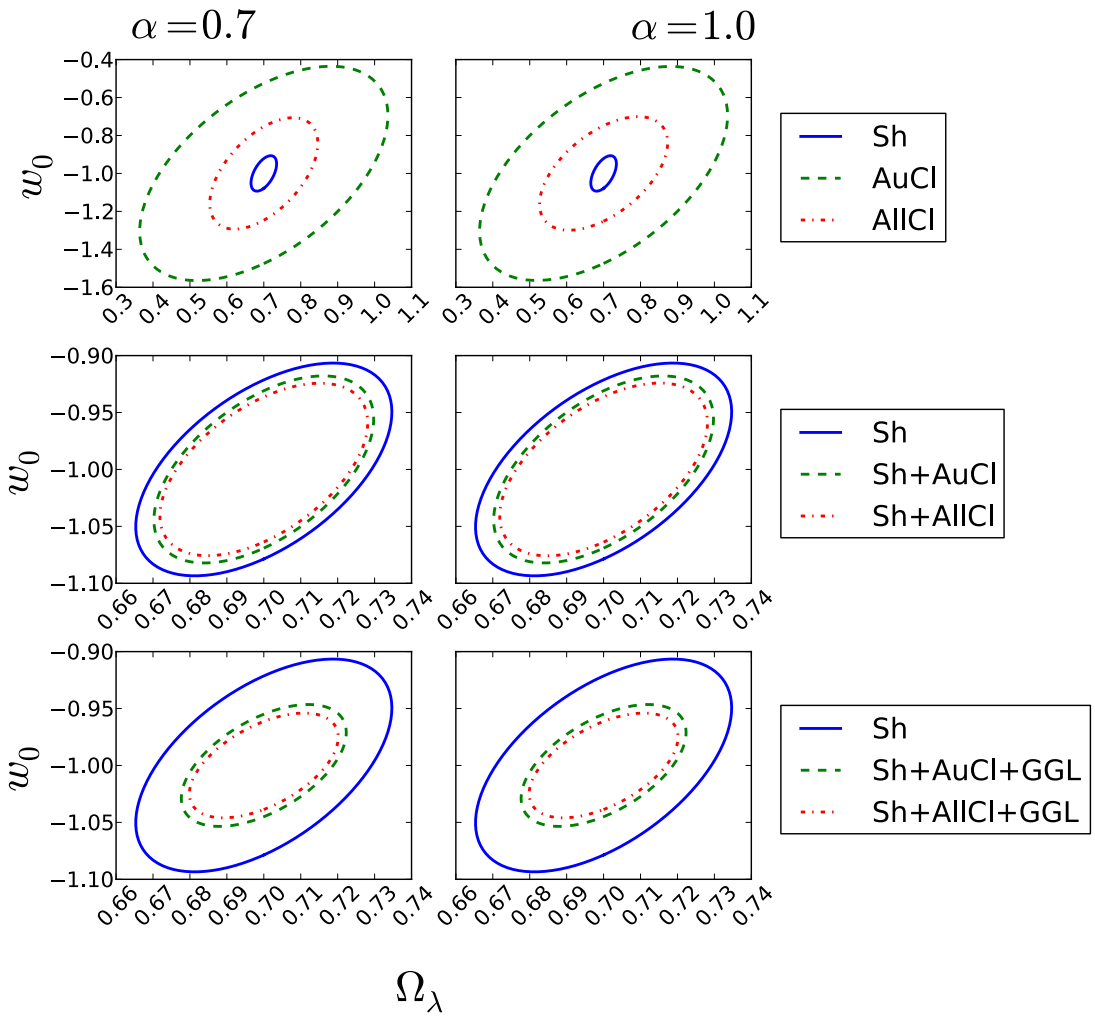

Figure 3.10: Fisher Matrix forecast showing marginal constraints in w, Ω_Λ for an S4 survey, comparing measurements using only the auto–correlation power for the clustering signal (green, dashed), to measurements using all redshift bin combinations in the clustering analysis (red, dot–dashed). All plots show shear–only constraints (blue, solid) for reference, and are the same in all panels. The right column shows contours when $\alpha = 1$, the case when there are no measured correlations in the number density contrast due to flux magnification, and only correlations due to intrinsic clustering. The left column shows contours when $\alpha = 0.7$, as inferred from CFHTLenS catalogues in Section 3.3.2. Top panels show contours using clustering only, middle panels show clustering combined with cosmic shear, and bottom panels show contours when clustering and galaxy–galaxy lensing information is added to a cosmic shear analysis. All panels take unknown galaxy bias, and cut information from clustering on non–linear scales.

percent change to the dark energy Figure of Merit, increasing to percent level for the case of shear combined with all clustering information and galaxy–galaxy lensing (Sh+AllCl+GGL). This agrees with the results detailed in Section 3.4.2.

I therefore conclude that there is significant gain in considering all redshift bin combinations in the clustering signal rather than the redshift auto–correlations only. The addition of clustering to cosmic shear gives noticeable improvement in parameter constraints, with further significant improvement with the addition of galaxy–galaxy lensing. In each case, the use of all redshift bin correlations in the clustering analysis gives modest improvement to constraints. I find that the flux magnification signal significantly reduces the error in clustering–only constraints, but it reduces statistical errors in a joint shear–clustering analysis only minimally.

Table 3.2: Table showing how constraints on Dark Energy parameters (through $\mathrm{FoM_{DE}}$) vary as galaxy bias is perfectly known (fixed) or constrained with the data (free) for an S4 survey,and with or with flux-magnification modelling in the clustering and GGL signals. Columns labelled with α values in the header show $\mathrm{FoM_{DE}}$ values. The last two columns show 1σ constraint for Ω_Λ and w when galaxy bias is free and taking $\alpha = 0.7$. Columns labelled Δ_{Ω_Λ} and Δ_w show bias on dark energy parameters, when flux magnification is neglected (when $\alpha = 1$ is incorrectly assumed). For each analysis considered in Table 3.1, results are presented for the case with no flux magnification ($\alpha = 1$) and using $\alpha = 0.7$ as measured from CFHTLenS catalogues (Section 3.3.2).

S4	b fixed		b free					
	$\alpha = 1$	$\alpha = 0.7$	$\alpha = 1$	$\alpha = 0.7$	σ_{Ω_Λ}	Δ_{Ω_Λ}	σ_w	Δ_w
AutoCl	582	621	12.4	12.4	0.34	0.026	0.56	0.045
AllCl	712	1965	30.1	39.5	0.15	0.69	0.29	0.77
GGL	161	260	49.0	84.0	0.11	-0.076	0.11	-0.044
AutoCl + GGL	5891	5976	719	736	0.033	-0.12	0.071	-0.50
AllCl + GGL	6964	7110	919	946	0.030	-0.2	0.062	-0.58
Sh	685	685	685	685	0.035	-	0.093	-
Sh + GGL	2134	2155	1324	1335	0.029	-0.12	0.067	-0.39
Sh + AutoCl	4896	5007	914	914	0.030	0.005	0.082	0.013
Sh + AllCl	5514	5634	1032	1040	0.028	-0.03	0.076	0.12
Sh + AutoCl + GGL	7046	7139	1927	1935	0.022	0.19	0.054	0.24
Sh + AllCl + GGL	8264	8426	2468	2505	0.020	0.11	0.046	0.13

Table 3.3: As Table 3.2, for an S3 survey.

S3	b fixed		b free					
	$\alpha = 1$	$\alpha = 0.7$	$\alpha = 1$	$\alpha = 0.7$	σ_{Ω_Λ}	Δ_{Ω_Λ}	σ_w	Δ_w
AutoCl	44.5	47	0.87	0.86	1.32	0.02	2.16	0.033
AllCl	54.0	144	2.2	2.8	0.57	0.72	1.10	0.77
GGL	5.5	8.9	1.47	2.3	0.66	-0.028	0.65	-0.1
AutoCl + GGL	330	338	32.0	32.2	0.17	0.1	0.4	-0.086
AllCl + GGL	375	386	39.0	39.6	0.15	-0.024	0.35	-0.24
Sh	10.4	10.4	10.4	10.4	0.3	-	0.8	-
Sh + GGL	42.6	43.3	24.4	24.7	0.21	-0.17	0.46	-0.52
Sh+ AutoCl	273	281	18.3	18.3	0.22	0.0066	0.56	0.022
Sh + AllCl	314	322	21.5	21.8	0.20	-0.038	0.50	0.32
Sh + AutoCl + GGL	349	357	52.8	53.1	0.14	0.28	0.32	0.36
Sh + AllCl + GGL	399	410	64.1	65.3	0.13	0.14	0.28	0.20

3.4.5 Biases in cosmological parameter estimates

In Section 3.4.4 I found that the *precision* of results for the various combinations of clustering information with cosmic shear and galaxy–galaxy lensing is not significantly improved by the presence of a magnification signal. In this section, I investigate how this flux magnification signal affects the *accuracy* of each analysis. I therefore turn our attention away from constraints on cosmological parameters, and instead consider possible shifts in the deduced maximum likelihood point when data are fitted using only the intrinsic clustering power spectrum, and where flux magnification has been neglected. To do this, I consider the linear shift in inferred parameters (Q) due to a bias in fixed model parameters (ψ) using the formalism of Taylor et al. (2007)

$$\boldsymbol{\delta Q}_i = -\sum_{k,j} [\boldsymbol{F}^{QQ}]^{-1}_{ik} \boldsymbol{F}^{Q\psi}_{kj} \boldsymbol{\delta\psi}_j, \tag{3.34}$$

where $\boldsymbol{F}^{QQ}$ is the Fisher matrix of measured cosmological parameters as set out in Section 3.2.2, and $\boldsymbol{F}^{Q\psi}$ is a pseudo–Fisher matrix between inferred and fixed model parameters using the same formalism. Our measured parameters consist of the cosmological parameter set described in Section 3.2.2 including N_z galaxy bias parameters (where N_z is the number of redshift bins). Our set of assumed parameters consists of one α value per redshift bin, so that $\delta\psi^i = \alpha^i_{\rm true} - 1$, where I have noted that setting $\alpha = 1$ sets the contribution to number density contrast fluctuations from magnification identically zero, thus equivalent to fitting only using the intrinsic clustering power spectrum. As previously, I choose $\alpha_{\rm true} = 0.7$. The same formalism calculates the bias in parameter estimates arising from an incorrect estimation of α.

The columns of Tables 3.2 and 3.3 labelled with Δ_{Ω_Λ} and Δ_w show the bias on each dark energy parameter introduced by incorrectly fitting to the clustering analysis ignoring the flux magnification contribution to the clustering power spectrum. We note that biases in cosmological parameters are reasonably robust to the survey type. However as the S4 survey gives better constraints to parameter values, biases in cosmological parameters are more significant for the S4 survey type than for the S3 case.

For a clustering analysis using only auto correlations in redshift, I find that biases in all cosmological parameters from incorrectly ignoring flux magnification are smaller than statistical errors. The inclusion of cross–correlations in a clustering analysis increases the size of bias on parameters, as the flux magnification contribution to the

power spectrum increases with more widely separated redshift bins (see Fig. 2.8). As the induced parameter biases can be at least as large as the statistical errors, particularly for the S4 survey, it is clear that whilst there is a significant increase in the figure of merit for a clustering analysis by including cross–correlations in redshift, this comes at the expense of increased complexity as flux magnification must be accurately measured and modelled to avoid large biases in inferred cosmological parameters.

Using the bias on $\Omega_{\rm M}$, chosen as the most significant case for AllCl and having a value of $\Delta_{\Omega_{\rm M}} = -0.39$, I find that α must be measured to within $\Delta\alpha = 0.085$ to ensure biases are smaller than statistical errors for all parameters for an S3 survey. For a S4 survey, this becomes $\Delta\alpha = 0.025$. The value of α measured from CFHTLenS data is known to within percent level precision at the faint limit of the survey. However this statistical uncertainty does not factor in expected systematic shifts in α due to selection bias, completeness or other observational effects.

Provided these effects are small, biases in inferred parameters should be smaller than statistical errors. However if these effects cause percent level shifts in the measured value of α, a photometric clustering analysis including redshift bin cross–correlations may be significantly biased even if the flux magnification effect is measured and modelled. This could be partially mitigated if statistical errors on α are propagated into cosmological parameter constraints, causing a decrease in figure of merit.

A combined shear and clustering analysis (Sh+AllCl, Sh+AutoCl) shows smaller biases than its clustering–only counterparts as the use of cosmic shear information, which is unaffected by flux magnification, helps to constrain parameter values. However, the further addition of galaxy–galaxy lensing, whose power spectrum includes a flux magnification contribution, causes a further increase to parameter biases to values larger than statistical errors for both the S3 and S4 survey types. I note that the bias on inferred parameters for the combination of clustering auto–correlations with cosmic shear and galaxy–galaxy lensing is of the same order of magnitude as the bias when combined with clustering using all redshift bin combinations (Sh+AllCl+GGL). Therefore, whilst there is an important improvement to the figure of merit when clustering and galaxy–galaxy lensing is added to shear (Sh+AutoCl+GGL, Sh+AllCl+GGL), as with the clustering–only case this comes at the expense of increased complexity as flux magnification must be accurately measured and modelled to avoid biasing inferred parameters for both analyses. This suggests that all available

information should be used to maximise the strength of parameter constraints, and Sh+AllCl+GGL should be used in preference to Sh+AutoCl+GGL as α would need to be accurately measured in either case. For the Sh+AllCl+GGL case, which shows the strongest constraining power, the bias on Ω_Λ is the most significant of all cosmological parameters, and using this value I find that α must be measured to within $\Delta\alpha = 0.13$ for an S3 survey, and $\Delta\alpha = 0.055$ for an S4 survey to keep biases smaller than statistical errors on each parameter.

3.4.6 The effect of cuts on non–linear scales

As detailed in Section 3.3.1, I impose cuts on ℓ–modes of the data vector where a significant part of the clustering signal is expected to come from regions where the galaxy bias is non–linear, thus allowing us to restrict our attention only the linear regime where galaxy bias can be modelled well. In the main body of this text, I have assumed that cuts following the method laid out in Section 3.3.1 with $\sigma_R = 0.5$ are adequate, as this gives a maximum k–mode within the quasi–linear regime (see for example **?**, which shows only a few percent deviation from linear theory on these scales). In this Section, I investigate how the results presented change with a change in σ_R, with particular emphasis on a more conservative cut using $\sigma_R = 0.2$, which gives $k_{\rm max} = 0.1\ h/{\rm Mpc}$ at z = 0.

Fig. 3.11 shows how the dark energy figure of merit, FoM$_{\rm DE}$, renormalised to its value when $\sigma_R = 0.5$, varies for a selection of analyses that include number density information, as a function of σ_R. Both clustering analyses, AutoCl and AllCl, depend strongly on the scale set for non–linear cuts, with the figure of merit an order of magnitude smaller when the more conservative $\sigma_R = 0.2$ is used. It is notable that the behaviour of the FoM for both the AutoCl and AllCl cases are very similar, suggesting that most of the improvement in FoM due to the inclusion of more non–linear scales comes from the auto–correlations in number density, and particularly the intrinsic clustering contribution. The information from a galaxy–galaxy lensing (GGL) analysis depends less strongly on the scale of non–linear cuts than either of the clustering–only analyses. Finally, the full combined probe, Sh+AllCl+GGL, shows the weakest dependence on cuts on non–linear scales, as no cuts are applied to the shear information. I note however that in all cases, more conservative cuts give a noticeable change in the cosmological constraints for each analysis, as more conservative cuts discard more information from which cosmology can be inferred.

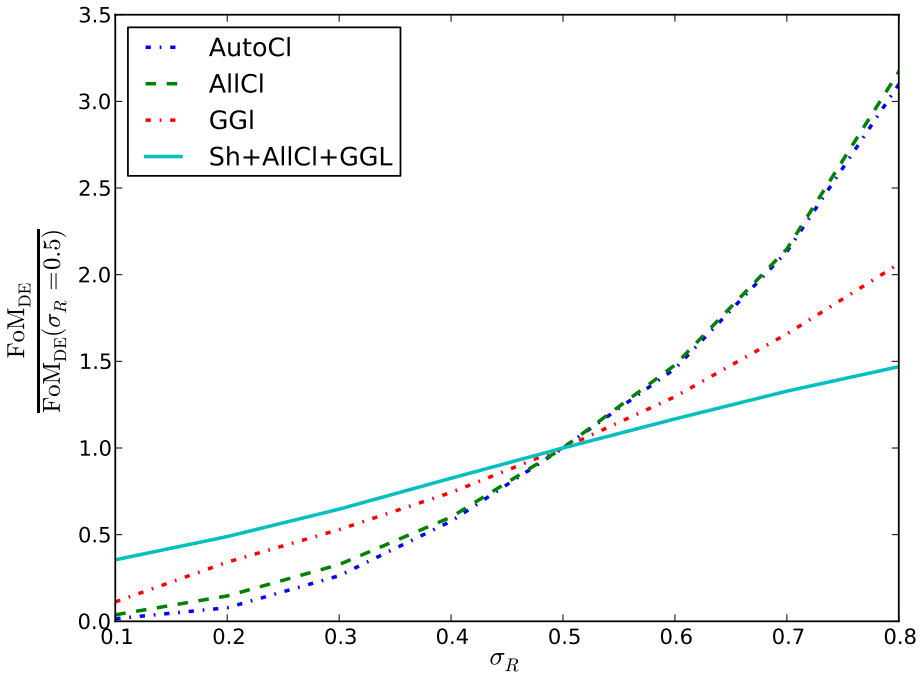

Figure 3.11: Figure showing how the dark energy figure of merit $\mathrm{FoM_{DE}}$ varies as a function of σ_R, which sets maximum ℓ–mode to be included in a clustering or galaxy–galaxy lensing analysis. The method used to apply these cuts are defined in Section 3.3.1. The ordinate axis has been renormalised to the figure of merit value when $\sigma_R = 0.5$, the value used in the main body of this text, for each analysis considered.

For the full combined probe, choosing $\sigma_R = 0.2$ gives a reduction by a factor of ≈ 2 in the figure of merit compared to the less conservative choice of $\sigma_R = 0.5$.

However, qualitatively the results presented in this text do not change with the choice of either $\sigma_R = 0.2$ or 0.5. In particular, with the more conservative ℓ–cuts the magnification contribution to a full combined analysis gives only sub–percent change to the figure of merit for realistic choices of α, in agreement with the discussion in Section 3.4.2. Further, conclusions on biases on inferred parameters (Section 3.4.5) remain unchanged with either choice, however it should be noted that biases on inferred parameters caused by neglecting the magnification signal tend to be smaller with more conservative cuts due to the reduced constraining power of the clustering and galaxy–galaxy lensing signal. Further, these biases are usually less significant due to the increased statistical error on each parameter when using more conservative ℓ–cuts.

Setting $\sigma_R = 0.5$, the maximum ℓ-modes which are included in the clustering and GGL analysis as a function of increasing tomographic bin are $\ell_{\mathrm{max}} =$

$(362, 608, 812, 1012, 1242, 1491, 1873, 2651)$. No information from correlations using number density information on scales smaller than these are included in the analysis. In contrast, I enforce a maximum ℓ-mode of $\ell_{\rm max} = 5000$ on the shear analysis, corresponding to $k_{\rm max} \sim 1 \rightarrow 4h/{\rm Mpc}$ for the eight tomographic redshift bins considered here. As such, ellipticity-ellipticity correlations contain information on much smaller scales than those assumed for clustering or GGL. Consequently, this work assumes that the non-linear matter power spectrum is sufficiently well known down to these scales, even if the non-linear galaxy bias is not. In Takahashi et al. (2012) a fit of the Halo Model to dark matter simulations recovers the non-linear matter power spectrum to $\leq 5\%$ on scales $k \leq 1h/{\rm Mpc}$ for $0 \leq z \leq 10$, and $\leq 5\%$ on scales $1 \leq k \leq 10h/{\rm Mpc}$ for $0 \leq z \leq 3$, suggesting that the non-linear power spectrum is adequately well known on the scales of the cuts applied here. However, the effect of baryonic physics on small scales is less clear, and in Semboloni et al. (2011) it is found that the inclusion of baryonic physics can lead to a deviation in the non-linear matter power spectrum as large as $\sim 10 - 20\%$ in the range $1 \lesssim k \lesssim 5$ in the worst case scenario they considered, suggesting baryonic physics may be the largest source of uncertainty on these scales. The accurate modelling of these effects is therefore of prime concern for future shear studies. If this is not possible, one may wish to impose stricter cuts on the shear analysis. If so, more information contained in the shear signal will be discarded and the forecast errors on cosmological parameters using shear-only can be expected to increase, whilst GGL and clustering-only contributions will not change. In such a case the relative improvement from the addition of GGL and clustering can be expected to increase, as well as parameter biases, over the results presented here, reinforcing the broad conclusions of this work.

3.5 Discussion on the application to data

In this chapter, I have motivated the use of number density information as complementary to a shear analysis using galaxy ellipticity measurements, with the caveat that knowledge of the flux magnification signal, although subdominant to the intrinsic clustering in its constraining power, is important to ensure the accuracy of the results.

As motivated in Chapter 1, cosmological parameter constraints from various cosmic shear analyses with CFHTLenS are discrepant with recent results using measurements of the temperature fluctuations in the cosmic microwave background

taken by Planck. Looking to the future, the arrival of the large data sets provided by KiDS, DES, HSC, LSST and Euclid should allow the measurement of cosmology to greater precision than ever with lensing and clustering techniques, providing complementary information to that provided through CMB measurements. The full utilisation of this information requires accurate knowledge of the data, and in particular the systematics inherent in a shear analysis which have been described elsewhere in this thesis, and also the methods to extract the maximum amount of information from the survey itself to improve the constraints on cosmology and to calibrate the systematics in each individual probe.

The work presented in this chapter can be used as a guide to the application of a combined analysis to data, by allowing the determination of the correct balance between the addition of information and the increased reliance on the accurate determination of the flux magnification signal. Whilst the statistical errors on the measurement of α using CFHTLenS are smaller than the requirements to ensure cosmological constraints using clustering with flux magnification are unbiased according to this analysis, one must note that the accurate knowledge in the flux magnification is not limited to the statistical uncertainty in its determination; further potential systematics to a magnification analysis include:

1. Error in the determination of α due to incompleteness of the sample near the magnitude limit,
2. Source obscuration and blending by a large, luminous foreground,
3. Unaccounted-for redshift overlap between source and lens sample due to redshift uncertainty,
4. Dust Extinction, in particular if dust correlates with mass,
5. Spatial variations in survey depth, and
6. Spatial variation in source magnitude determination.

Points 1 and 2 can change the inferred value of α by altering the number counts as a function of magnitude, away from the true, underlying form. The presence of a luminous foreground can obscure background objects, artificially lowering the observed number of sources and decreasing the inferred value of α, whilst blending with foreground objects can affect photometrically derived quantities such as source

redshift and magnitude. As well as the resultant error in magnitude determination, photometric errors can propagate to errors in the redshift determination for the galaxy sample, which can cause misinterpretation of the measured signal if a significant fraction of the signal comes from galaxy pairs which are closer to or further from each other than expected. If the photometric redshift errors for the galaxy sample are known, then the projected number density from the intrinsic clustering and magnification can be accurately modelled, so that biases can be avoided.

Extinction by dusty foregrounds (point 4) can cause anti-correlations in the observed number density, and can mimic a flux magnification anti-correlation if dust follows mass. As gravitational lensing is achromatic whilst dust extinction causes reddening of the background sources, the level of the dust contamination can be determined by correlating the shift in magnitudes in different wavebands correlated with the foreground over-density (Ménard et al., 2010). It is important to understand any spatial variation in the survey depth (point 5) to ensure that the luminosity function (and consequently number counts as a function of magnitude) from which α is determined is probed consistently across the field: for example, deeper observations in a patch of sky will increase the number density of sources in that patch as the underlying luminosity function is integrated to a fainter limit, which can mimic the flux amplification which may be observed around a foreground over-density. Spatially varying errors in magnitude determination (for example through variation in magnitude zero-point) can lead to misinterpretation of the magnification signal as a counterpart to the spatially varying survey depth: in this case, the inferred luminosity function is altered due to systematic offsets in the magnitude of the sources.

All of these effects will introduce uncertainty of systematic errors in the determination of α. If one or a combination of these effects changes the inferred α to a significant extent, one may introduce significant biases to inferred parameters. Thus an analysis using a combination of number density and ellipticity information for a given survey may need to account for these systematics, particularly in the analyses which show large bias in the case of an incorrectly-modelled flux magnification (Tables 3.3 and 3.2). Before this method can be applied to data, further investigation into the spatial dependence of the magnitude estimates, depth, photometric errors and dust and their effects on the measured clustering signal would need to be carried out, and accurate measurements of each of these effects may be required to ensure accurate parameter estimation, particularly in the cases which show the largest dependence on the flux

magnification signal. The increase in parameter constraints that may be expected to result from such a combined analysis and its applicability to a large number of large-scale surveys which aim to undertake precise cosmological measurements such as DES, HSC, KiDS, CFHTLenS and Euclid, motivates the need for this investigation. Figure 3.12 shows the predicted dark energy constraints for the combination of shear and photometric clustering information against a shear-only analysis for the DES, KiDS and Euclid surveys. The combination of shear and photometric clustering using the auto-power-spectra in redshift bins is expected to be most insensitive to the flux magnification, and provides a simpler first step before the addition of further information and complexity.

In Gaztañaga et al. (2012); Cai & Bernstein (2012); Kirk et al. (2013) it was demonstrated that the addition of a bright, shallow spectroscopic sample of galaxies to a faint, deep photometric sample could further improve constraints on cosmology and modified gravity, through the addition of redshift space distortions and baryonic acoustic oscillation measurements with the spectroscopic clustering, and improved constraints on galaxy bias. Further, the combination of two differently-biased samples could reduce the sample variance, improving constraints on large scales (McDonald & Seljak, 2009), and the combination of weak lensing with redshift space distortions (RSD) can lift the degeneracy between the galaxy bias and the growth rate ($\beta = f/b$) inherent in a RSD-only analysis, improving constraints on the growth of structure (Bernstein & Cai, 2011). In both Gaztañaga et al. (2012); Cai & Bernstein (2012), it was found that the improvement was greatest when combining samples which overlap[7], thus the combination of an overlapping bright spectroscopic and faint photometric sample, such as that provided by the overlapping footprints provided by surveys such as KiDS with GAMA, or HSC and the Prime Focus Spectrograph (PFS), show particular promise in probing cosmology.

The discussion presented so far has focussed on optical data, however the use of current and future radio data for gravitational lensing studies deserves particular mention. The use of radio data to construct a lensing analysis opens an entirely new avenue of study as deep and wide radio imaging provided by the next generation of radio surveys such as eMERLIN, LOFAR, SKA and its precursors, start to produce

[7]Gaztañaga et al. (2012) find that the addition of RSD measurements to the combined weak lensing signal (WL, consisting of the combination of galaxy clustering, galaxy-galaxy lensing and shear) lead to a further increase in the dark energy figure of merit (w_0, w_a) by 72% against the WL-only measurement when the photometric and spectroscopic samples are taken over independent patches of the sky, and by 770% when the spectroscopic measurements are taken on a subsample of the photometric sample.

images with high-resolution imaging needed to produce reliable shape and size measurement, the wide survey area to reduce sample variance and a high number density (comparable to optical surveys) needed to reduce the statistical noise in a lensing analysis. Further, for radio images the PSF is in principle known precisely, and can be determined predictably from knowledge of the antennae positions, and the position of the source, and precise redshifts are available from the H1 emission of a subset of galaxies (Blake et al., 2014). In Brown & Battye (2011), it was demonstrated that measurement of the polarisation of radio data could be used to measure intrinsic alignments, and thus effectively negate much of the systematic effects of an intrinsic alignment signal, and its consequent bias, in a shear analysis. This results from the fact that whilst lensing will alter the observed morphological orientation of source galaxies, it has been shown that it will not affect the observed polarisation Kronberg et al. (1991); Surpi & Harari (1999), meaning that polarisation observations should trace the original morphological orientation of the source, provided there exists a tight relation between the intrinsic morphological orientation and polarisation of galaxies. This has been shown in the local Universe (Stil et al., 2009), but remains unknown at higher redshifts. In addition, many of the systematics that are expected to affect a flux magnification analysis, such as dust extinction (see above), will not be present in an analysis using radio data. Thus, the use of radio data is particularly attractive for a combined analysis of the sort described here. Furthermore, combinations of radio data with optical, such as the overlapping data-sets provided by eMERLIN and Suburu as part of the SuperCLASS survey, could be expected to provide a means to self-calibrate the systematics inherent in either.

3.6 Conclusions

In this chapter I made forecasts for statistical errors on cosmological parameters from a cosmic shear analysis, and two types of clustering analysis using photometric redshift information, including flux magnification effects: one which contains information only from correlating all redshift bins with themselves (auto); and one where all redshift bin combinations are included, both in the presence of scatter due to photometric redshift errors. I considered the gain from combining either clustering analysis with a cosmic shear and/or galaxy–galaxy lensing, and investigated how inferred cosmological parameters are biased when the flux magnification effect is neglected.

The full list of experiments considered is given in Table 3.1.

Using public CFHTLenS catalogues, I inferred a value for the slope of the cumulative number counts, α, at the faint limit of the survey to be $\alpha \approx 0.7$. Although cuts at brighter magnitude limits can give a larger value of α, I find that the subsequent removal of sources from our sample causes a decrease in signal–to–noise ratio in all but the highest redshift bins where photometry is least accurate.

For a Stage–IV type survey, the inclusion of all redshift correlations in a clustering–only analysis can give significant improvement to cosmological constraints, improving $\mathrm{FoM}_{\mathrm{DE}}$ by a factor of 3.2 over a clustering analysis which uses only auto–correlations in redshift. When combined with a shear analysis, clustering using only the auto–correlations in tomographic redshift bins improves the figure of merit for dark energy parameters Ω_Λ,w_0 ($\mathrm{FoM}_{\mathrm{DE}}$) by a factor of 1.33 over the shear–only case. Including cross–correlations improves $\mathrm{FoM}_{\mathrm{DE}}$ by a factor of 1.51 over a shear–only analysis. However if galaxy–galaxy lensing is also included this increases to 3.7 when galaxy bias is unknown. In contrast, when galaxy bias is well known, the addition of clustering information using all redshift bin correlations and galaxy–galaxy lensing improves $\mathrm{FoM}_{\mathrm{DE}}$ by a factor of 12.3 over a shear–only analysis.

Whilst a non–zero flux magnification can cause a significant improvement in constraints from a clustering–only analysis when galaxy bias is free (giving an increase in figure of merit by a factor of ~ 1.3 for clustering using all redshift bin combinations, when $\alpha = 0.7$ compared to $\alpha = 1$), the presence of a magnification signal in the clustering data causes only a few percentage change in parameter constraints from a joint clustering, shear and galaxy–galaxy lensing analysis and does not significantly alter the precision of results. However, if clustering cross–correlations in redshift or galaxy–galaxy lensing are used as part of an analysis, the flux magnification effect must be modelled and included to avoid inferred parameter constraints being largely biased and inaccurate.

If flux magnification is incorrectly neglected, biases in inferred cosmological parameters from clustering–only analysis which includes cross–correlations in redshift can be many times larger than statistical uncertainties for an S4 survey. For a combined clustering, cosmic shear and galaxy–galaxy lensing analysis, parameter biases can be larger than statistical uncertainties for an S4 survey, and there is little improvement in these biases when clustering redshift cross–correlations are discarded. As there is significant improvement in the statistical errors when clustering redshift cross–

correlations are used in this type of analysis, I suggest that these are included. This comprises the case where all available information is used from number density contrast and ellipticity measurements.

As the use of all available information in this way outperforms all other analyses (see Table 3.2) I suggest that given number density information and ellipticity measurements, the full combined analysis which includes cosmic shear, galaxy–galaxy lensing and clustering using all redshift bin combinations should be used (Sh+AllCl+GGL in Table 3.2). When compared to a cosmic shear–only analysis, this comes at the expense of increased complexity due to the necessity to accurately measure and model flux magnification to avoid causing these parameters to be biased. Alternatively, the combination of cosmic shear and number density contrast redshift auto–correlations (Sh+AutoCl) shows the smallest bias in inferred parameters when flux magnification is neglected, and thus may reduce the complexity of the analysis at the expense of weaker parameter constraints.

As well as the improvement in statistical errors that comes from adding clustering measurements and galaxy–galaxy lensing to cosmic shear, number density information gives an important consistency check by allowing independent verification of inferred parameter values using either number density contrast correlations, or galaxy–galaxy lensing. As the information required for a photometric clustering analysis is already taken as part of a shear survey, this information is obtained without the need for further data, provided α can be accurately measured.

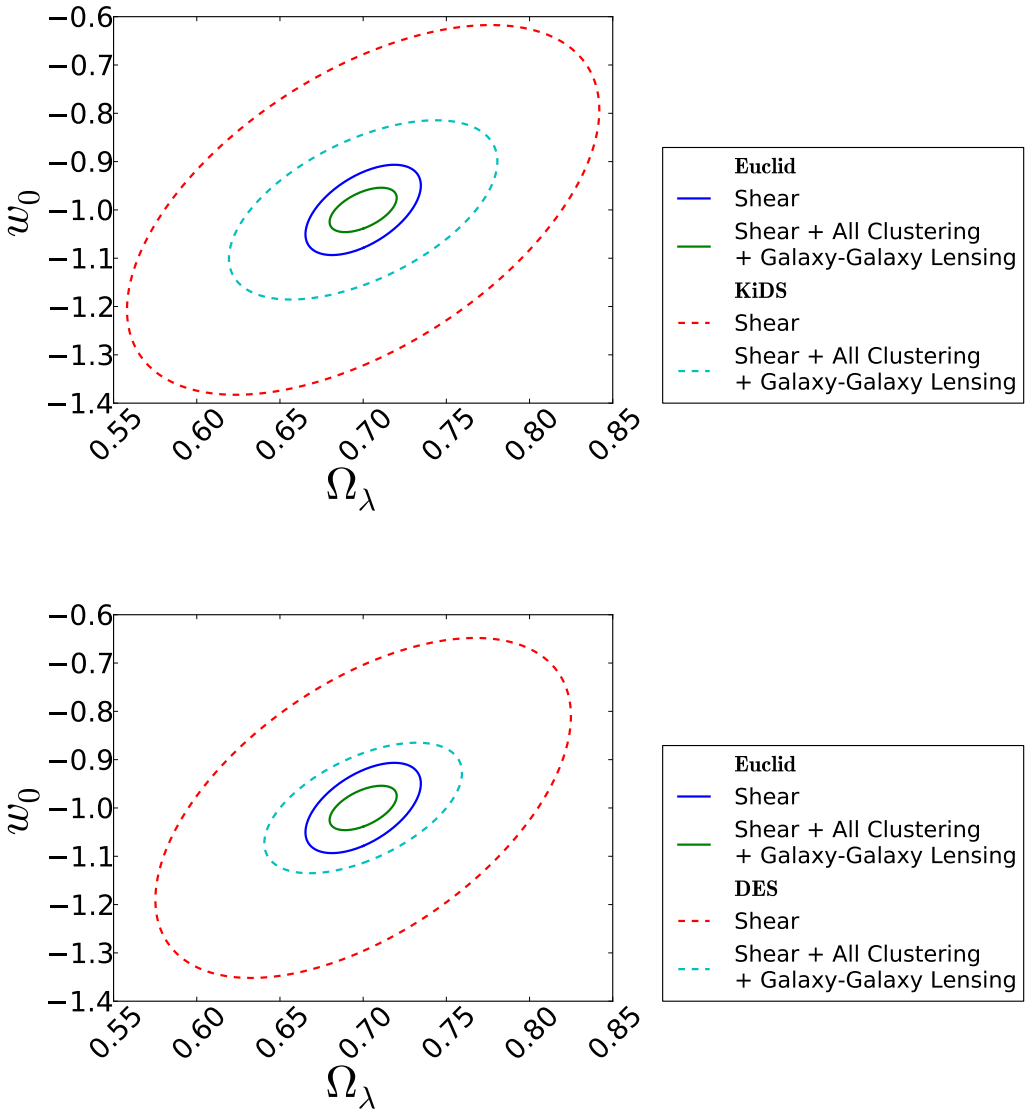

Figure 3.12: Fisher matrix predictions for dark energy parameter constraints for the Kilo Degree Survey (*top*), the Dark Energy Survey (*bottom*) and Euclid. For each case, constraints are shown for a shear-only analysis, as well as the most constraining combination of shear, photometric clustering and galaxy-galaxy lensing. For each survey, the latter analysis is expected to the biased if the flux magnification signal is not modelled to an accuracy of $\sim 3\%$.

Chapter 4

A method of dark matter mass reconstruction using galaxy sizes and magnitudes

4.1 Introduction

Galaxy clusters, comprising the largest mass gravitationally-bound bodies in the Universe, represent the apex of hierarchical structure formation as the largest objects the have been produced within the Hubble time. For these objects the dynamics and distributions are well described within the linear regime of structure formation, where the distribution of mass and the correlation of mass and light is relatively simple and well understood by models using gravitational collapse only using Gaussian statistics. The cluster mass function[1] probes the amplitude of the linear power spectrum (Fedeli et al., 2008; Reiprich & Böhringer, 2002), and it's evolution can provide constraints on dark matter and dark energy densities through the growth of linear density perturbations (e.g. Mantz et al., 2008). Of particular note, the recent results of Collaboration et al. (2014), which provides constraints on the product of the matter density and amplitude of the power spectrum using cluster counts detected through the Sunyaev-Zeldovich effect, give constraints which are discrepant with the constraints from primary CMB temperature fluctuations. Such discrepancy between probes could result from unaccounted or systematics in the determination of the cluster mass function, such as completeness, or in the determination of the X-ray cluster

[1] A measure of the number of objects of a certain mass.

mass; however, the discrepancy could also be indicative of new physics: in particular, the inclusion of processes that suppress power on small scales, such as the free-streaming of massive neutrinos, may reconcile both probes (e.g. Wyman, Rudd & Vanderveld, 2013). The distribution of massive clusters, measured through statistics such as the correlation function or power-spectrum, provides a measure of the matter distribution whose evolution is also sensitive to the cosmological model through the growth of density perturbations (e.g. Balaguera-Antolínez et al., 2011). A measure of the gas fraction of large clusters can be expected to be a good estimator of the ratio of the baryonic to dark matter densities of the background cosmological model for the Universe (e.g. Ettori & Fabian, 1999; Ettori et al., 2009; Grego et al., 2001). Further, the dependence of cluster mass with properties of the cluster and its members can provide information on the physics of galaxy formation and its dependence on environment (see Voit, 2005, for a summary). As all these probes are dependent on the cluster mass, it is clear that robust measurements of cluster mass are a valuable astrophysical tool, and may often be a determinant factor in one's ability to constrain cosmology from a cluster sample.

Weak gravitational lensing analyses provide a robust way of mapping the total matter distribution of a lens beyond the radius in which methods relying on the use of luminous tracers or the cluster gas can probe, and has been successfully applied to the study of cluster dark matter environments (**?**Hildebrandt et al., 2011) and galaxy halos (Choi et al., 2012; Morrison et al., 2012). Until recently, the measurement of cluster mass with weak gravitational lensing has focused on the use of the shear (Hoekstra, Franx & Kuijken, 2000; **?**; Heymans et al., 2008), however the use of shear as a probe of the lens dark matter halo does not directly measure the mass of the lens: rather, the tangential shear is a probe of the differential surface mass density, or requires the use of inversion methods such as Kaiser & Squires (1993) to relate the shear to the convergence from which the projected mass of the lens can be directly extracted. As such inversion methods require care when applied to data (see section 2.2.5), one may be motivated to look for more direct probes of the convergence field. In the linear regime, the magnification of sources by a foreground lens depends only on the local convergence field across the source. As a result, measurements using galaxy sizes, magnitudes or counts can provide a direct probe of the projected lensing mass, which is not affected by the mass sheet degeneracy. Whilst such measurements of the magnification signal are expected to exhibit larger statistical noise properties than a

shear analysis (section 2.3.6), the combination of such measures may provide results which are competitive to that using shear measurements alone. Further, a magnification analysis provides information which is complementary to shear analyses alone, and a combination of both measures may be expected to improve the accuracy and precision of either analysis (Rozo & Schmidt, 2010), whilst simultaneously breaking the mass sheet degeneracy and self-calibrating either analysis.

Measurements of the lensing matter using magnification have already been successfully undertaken: using galaxy counts in Bauer et al. (2013); Ford et al. (2014); Hildebrandt et al. (2013); Morrison et al. (2012), and the combination of galaxy sizes and magnitudes in Schmidt et al. (2012). The latter presents the surface mass density for a sample of 211 X-ray selected galaxy groups in the COSMOS field and find that the best fit NFW profile for the stacked surface mass density using source size and magnitude gives a mass estimate within scales of 1 Mpc consistent with and with a signal-to-noise of $\sim 40\%$ of a shear analysis on the same field. The analysis does make a few simplifying assumptions in the intrinsic size-magnitude distributions: the source magnitude and size are modelled as Gaussian and log-normal respectively, with Gaussian covariance. Measurements of the distribution of log-sizes and magnitude in the STAGES field, undertaken in chapter 5 suggest that these distributions show non-Gaussianity, suggesting that such an assumption may introduce a bias in the inferred group mass. Further, whilst the analysis contains a correction on the lensing efficiencies for the lensing bias which results from the existence of magnitude and size limits in the analysis, the effect of such magnification-dependent cuts on the renormalisation of the likelihood is not taken into consideration, potentially causing a systematically low bias in the recovered surface mass density.

In this chapter I propose a Bayesian method for the determination of the surface mass density profile of a foreground lens using measurements of source size and magnitude, which does not rely on the simplifying assumptions of Schmidt et al. (2012). In particular, the method proposed herein does not make any assumption on the form of the intrinsic size-magnitude distribution of the sources, which can instead be measured from the data, or from a separate blank field. Further, this method does not require the availability of redshifts for the source sample, but instead includes the flexibility to marginalise over a defined redshift distribution when individual galaxy redshifts are unknown. The method can naturally account for the intrinsic size-luminosity relation through the measured size-magnitude distribution,

and includes a magnification-dependent renormalisation of the likelihood in the presence of magnitude and size cuts.

I investigate the accuracy and precision of this method using mock catalogues, where the method is used with some simplifying assumptions, or in situations where the analysis is limited by the data. In doing so, I quantify the expected signal–to–noise of the analysis for different data-sets, quantifying the importance of the number of samples and redshift information, as well as providing a comparison between the use of galaxy-sizes only, magnitudes only, or a combination of both. Limitations of the analysis are discussed, and the results presented here are used to motivate the application to the size and magnitude measurements from HST images on the Space Telescope A901/902 Galaxy Evolution Survey (STAGES) field, taken over a patch of sky containing the A901a, A901b and A902 clusters and the South-West group. The application to the STAGES field will be undertaken in Chapter 5.

4.2 Bayesian dark matter profiles fitting using source size and magnitude information

4.2.1 Determination of cluster dark matter profile using galaxy sizes and magnitudes

In this section I develop a Bayesian method for constraining model parameters for a given dark matter mass profile model. Consider a lensing foreground, fit by mass profiles such as the SIS or NFW models detailed in Section 2.2.3. For a given lens redshift, the magnification acting on a background source is a function of four free parameters, namely the physical transverse distance between the source and profile centre (ξ), the redshift of the source (z) and a model-dependent free parameter which sets the virial mass of the lens α[2]. In the case of a lens well described by an SIS profile $\alpha = \sigma_v^2$, whilst for an NFW profile $\alpha = r_{200}$ provided one has a known mass-concentration relation (see Section 2.2.3 for a definition of these terms).

[2]In general, one may wish to consider the set of parameters which fully describes the mass profile of the lens. For an SIS profile, only the total mass of the profile is allowed to vary, however for an NFW profile one may vary the total mass and concentration of the halo. In this analysis, I consider the virial mass as the only model-dependent free parameter, and assume that the concentration can be adequately set using the mass-concentration relation of Dolag et al. (2004), measured from simulations. The analysis is easily extended to constrain the concentration also, by taking α to describe the set containing the virial mass and concentration.

From this, we wish to calculate the probability, $p(\alpha|\theta, m)$, that the foreground dark matter halo is fitted by one of the above models with free parameter α, given the measured size θ and magnitude m of a sample of galaxies. From Bayes' Theorem, the posterior for each galaxy can be related to the likelihood as

$$p(\alpha|\theta, m) = \frac{p(\theta, m|\alpha)p(\alpha)}{p(\theta, m)} \propto p(\theta, m|\alpha). \tag{4.1}$$

In Bayesian nomenclature, $p(\alpha|\theta, m)$ is the posterior probability for the model free parameter, and $p(\theta, m|\alpha)$ is the likelihood of obtaining a measurement of θ, m for a given model free parameter. In the last step, a flat prior on the surface mass density free parameter was assumed. It should be noted that in the following analysis, results will frequently be presented for the virial mass rather than the virial radius: since the virial mass is non-linear in its dependence on the virial radius, a flat prior on the virial radius does not correspond to a flat prior on the virial mass. This can be seen through the conservation of probability: the probability density function of the virial mass can related to that of the virial radius as

$$p(M_{200})dM_{200} = p(r_{200})dr_{200} \tag{4.2}$$

so that

$$p(M_{200}) \propto \frac{p(r_{200})}{r_{200}^2} \propto \frac{p(r_{200})}{M_{200}^{\frac{2}{3}}}, \tag{4.3}$$

where $M_{200} \propto r_{200}^3$ was assumed. Thus, a flat prior on r_{200} will down-weight large mass clusters, however this shift should be small given adequate data. A further consequence of the above relation is the fact that the posterior on the virial mass is divergent as $r_{200} \to 0$, where $p(r_{200} = 0) \neq 0$. Where posteriors are given on the virial mass, they will be calculated using a flat prior on r_{200} and converted using this equation. Future work will extend this idea to produce cluster-mass-posteriors with a prior set from a halo mass function, to correctly account for the reduced probability for the existence of large clusters, however I note that the above power-law prior on the mass will also down-weight large clusters.

Taking each galaxy as an independent measure, the likelihood for the complete sample of galaxies is the product of the likelihood, or equivalently the sum of the log-

likelihoods, for each galaxy in the sample:

$$p(\theta, m|\alpha) = \prod_g p(\theta_g, m_g|\alpha) \tag{4.4}$$

$$\ln p(\theta, m|\alpha) = \sum_g \ln p(\theta_g, m_g|\alpha), \tag{4.5}$$

where g labels the galaxies in the sample. In the presence of magnitude- or size-cuts as part of the source selection, the likelihood should be normalised in a way that accounts for the change in size-magnitude parameter space in the presence of a local magnification field. This concept will be detailed in section 4.2.2.

The likelihood for a given source is known provided the intrinsic size (θ_0), intrinsic magnitude (m_0) and redshift of that source are also known. Marginalising over these intrinsic properties for the galaxy, the likelihood can be written as

$$p(\theta, m|\alpha) = \int dm_0 \; d\theta_0 \; dz \; p(\theta, m|\alpha, \theta_0, m_0, z) p(\theta_0, m_0, z|\alpha). \tag{4.6}$$

The final term here relates the joint distribution of intrinsic size, magnitude and measured redshift to a realisation of the lensing foreground. The intrinsic size and magnitude are intrinsic to the galaxy being observed, and are therefore taken to be independent of the lensing foreground so $p(\theta_0, m_0, z|\alpha) \rightarrow p(\theta_0, m_0, z)$. By carrying out this final simplification, I make the assumption that there are no intrinsic size-density nor magnitude-density correlations which could cause a general change in size or magnitude of a population of sources physically close to the lens. This assumption should give accurate results if the source sample is selected to be radially distant from the lens so that the lensing effect dominates, however such separation is not always possible, particularly if the redshift is unknown for a large fraction of the source sample. In such a case, given a suitable model for this relation, one can naturally incorporate this model into the intrinsic size-magnitude relation, keeping the α dependence explicit. The investigation of such correlations is left to future work.

The final term can then be expanded as

$$p(\theta_0, m_0, z|\alpha) = p(\theta_0, m_0, z) = p(\theta_0, m_0|z) p(z|m_0). \tag{4.7}$$

Re-substitution of this term into the likelihood gives

$$p(\theta, m|\alpha) = \int dm_0 \; d\theta_0 \; dz \; p(\theta, m|\alpha, \theta_0, m_0, z) p(\theta_0, m_0|z) p(z|m_0). \tag{4.8}$$

The second term contains information on the intrinsic size-luminosity relation, and the lensing relations are contained solely in the first term. In the absence of measurement noise, knowledge of the redshift of the source and α allows for the determination of the lensing convergence, so that the first term can be determined exactly and takes the form:

$$p(\theta, m|\alpha, \theta_0, m_0, z) = \delta_D(\theta - \theta_0 \mu^{\frac{1}{2}}[\alpha, \xi, z]) \delta_D(m - m_0 + 2.5 \log_{10}\{\mu[\alpha, \xi, z]\}). \tag{4.9}$$

The Dirac delta relationships imply a deterministic relation between the observed size and magnitude to the intrinsic size and magnitude through lensing only. Measurement noise may be included here by changing these to a more general probability density such as a bivariate Gaussian distribution centered around the lensed size and magnitude with width given by the measurement error, $\sigma_{\rm meas}$. For this analysis we assume that the dispersion in measured sizes and magnitudes due to measurement effects is subdominant to the intrinsic variations in both, and so the joint distribution given above is well approximated by the product of two Dirac delta functions. The impact of measurement noise on the analysis is detailed more fully in Chapter 5. Using a change in variables, the marginalisation over the intrinsic size and magnitude can be carried out so that the posterior takes the form

$$\begin{aligned} p(\alpha|\theta, m) \propto \int \; & dz \mu^{-\frac{1}{2}} p_{[\theta_0, m_0|z]} \left(\mu^{-\frac{1}{2}} \theta, m + 2.5 \log_{10}\{\mu\}|z \right) \\ & \times \; p_{[z|m_0]}(z|m + 2.5 \log_{10}\{\mu\}), \end{aligned} \tag{4.10}$$

where notation $p_{[x]}(y)$ denotes the probability density function for x evaluated at $x = y$. The posterior on the lensing mass profile for each galaxy is then constructed by sampling the intrinsic size-magnitude distribution along a de-lensing line, which recovers the intrinsic size and magnitude for that source as a function of the lensing matter profile free parameter. The accuracy of the recovered posterior is strongly dependent on the accuracy with which the a-priori size-magnitude distribution can be recovered, and care must be taken to ensure that this distribution describes the selected source sample. With knowledge of the probability density functions for

the unlensed magnitude, redshift given intrinsic magnitude and intrinsic size given a luminosity, a posterior for the density profile of the lens can therefore be determined. In principle, these distributions can be measured directly using data taken over a blank field, or a large survey area, where only a small fraction of sources may be expected to be significantly lensed so that intrinsic variations in measured quantities dominate. The bias resulting from measuring the intrinsic-size-magnitude distribution on a field dominated by clusters is investigated more fully later in this chapter.

Where the joint size magnitude distribution may be taken from literature, it is convenient to refactor the intrinsic size-magnitude distribution, to the distribution of physical size given a luminosity or absolute magnitude, (M), as this is frequently quoted in studies. Rewriting this in these terms, the likelihood becomes

$$p(R, M|\alpha) = \int \mathrm{d}\theta \mathrm{d}m \; p(R, M|\alpha, \theta, m) p(\theta, m|\alpha) \tag{4.11}$$

The first term here is deterministic when the relationship between absolute and apparent magnitude is well known[3]. In this case, the likelihood reduces to

$$\begin{aligned} p(\alpha|\theta, m) = \int \; dz \; \mu^{-\frac{1}{2}} p_{[R|M]} \left(\frac{D_{\mathrm{A}}(z)\theta}{\mu^{\frac{1}{2}}[1+z]}, M_{|_{m+2.5\log_{10}\{\mu\}}}|z \right) \\ \times \; p_{[z|M]}(z, M|_{m+2.5\log_{10}\{\mu\}}). \end{aligned} \tag{4.12}$$

where $M_{|_{m_0,z}}$ denotes the absolute magnitude evaluated at intrinsic magnitude m_0 at redshift z.

4.2.2 Magnification-dependent normalisation of the likelihood

Survey dependent magnitude- and size- limits act on lensed quantities, with the result that a galaxy in a region with a local magnification that differs from unity may be lensed outwith these limits and therefore not observed as part of the survey. As the value of the magnification factor changes, the body of the underlying size-magnitude distribution moves in size-magnitude parameter space, equivalent to an effective change in size and magnitude limits, and changing the total probability within these limits (see Figure

[3]As with the deterministic relationship assumed between lensed and un-lensed quantities earlier, one can account for scatter in the relationship between absolute and apparent magnitude (e.g. due to K-corrections) by altering this Dirac delta relation to one with a finite width which represents this scatter, such as a Gaussian

2.7). As a result, the likelihood which feeds into the determined posterior for each galaxy will change as a function of the convergence value, and must be renormalised to avoid biasing the returned posterior.

For both the size-only and size-magnitude analysis, the likelihood should be renormalised such that

$$\int_{m_l}^{m_u} \mathrm{d}m \int_{\theta_l}^{\theta_u} \mathrm{d}\theta \; p(\theta, m|\alpha) = \int_{\theta_l}^{\theta_u} \mathrm{d}\theta \; p(\theta|\alpha) = 1 \tag{4.13}$$

implying

$$\begin{aligned}\int dz \; \mu^{-\frac{1}{2}} \int_{m_l}^{m_u} dm \int_{\theta_l}^{\theta_h} d\theta \; p_{[\theta_0,m_0|z]} \left(\mu^{\frac{1}{2}}\theta, m + 2.5\log_{10}\{\mu\}\right) p(z|m + 2.5\log_{10}\{\mu\}),\\ = \int dz \int_{m_l+2.5\log_{10}\{\mu\}}^{m_u+2.5\log_{10}\{\mu\}} dm_0 \int_{\mu^{-\frac{1}{2}}\theta_l}^{\mu^{-\frac{1}{2}}\theta_h} d\theta_0 \; p_{[\theta_0,m_0|z]} \left(\theta_0, m_0\right) p(z|m_0) = 1,\end{aligned}$$

where in the final step I assumed a deterministic relationship between the observed and intrinsic size and magnitude, due to lensing only and devoid of measurement error. The size and magnitude limits are understood to act on observed (lensed) quantities, and the limits themselves are understood to be redshift dependent through the local magnification in that patch of sky.

4.2.3 Surface mass density profile constraints using galaxy sizes only

In the above formalism, a full posterior for the surface mass density of the foreground lensing body can be determined with accurate knowledge of the unlensed size-magnitude distribution. In reality, we may be limited in the knowledge of this distribution, through uncertainties in the measurement of either source size or magnitude, or limitations in the data. In particular, where redshift information is not available for a large fraction of the sample, as is the case in the STAGES field analysed in chapter 5, one cannot easily determine the redshift dependence of the intrinsic size-magnitude distribution for the selected source sample. In this case, one may be motivated to assume redshift independence of the distribution, or model the redshift dependence of the distribution using measurements on other fields, however one must take care to ensure a consistent source selection between the data sample and

the sample which forms the a-priori distribution. In particular, I note that a median-redshift-magnitude dependence is expected, and I will use the measurement on the GOODS field in Schrabback et al. (2007) in the remainder of this work:

$$z_{\rm med} = 0.29(m_{\rm F606W} - 22) + 0.31. \tag{4.14}$$

Where the a-priori distribution is assumed to be redshift-independent, a bias is therefore likely to result if such a relation holds for the source sample considered, which can be minimised at the expense of larger statistical errors through the marginalisation of the source magnitude information.

The size-only posterior is determined by marginalising over the magnitude in the full joint size-magnitude posterior (equation 4.10), giving

$$\begin{aligned} p(\alpha|\theta) = \int dz\ \mu^{-\frac{1}{2}} \int_{m_l}^{m_u} dm\ p_{[\theta_0,m_0|\alpha,z]} \left(\mu^{-\frac{1}{2}}\theta, m + 2.5\log_{10}\{\mu\}\right) \\ \times\ p(z|m + 2.5\log_{10}\{\mu\}), \end{aligned} \tag{4.15}$$

where m_l and m_u denote the bright and faint limits of the survey respectively. Changing variables to integrate over the unlensed magnitude (assuming subdominant measurement error, as above), this becomes

$$p(\alpha|\theta) = \int dz\ \mu^{-\frac{1}{2}} \int_{m_l+2.5\log_{10}\{\mu\}}^{m_u+2.5\log_{10}\{\mu\}} dm_0\ p_{[\theta_0,m_0|z]} \left(\mu^{-\frac{1}{2}}\theta, m_0\right) p(z|m_0). \tag{4.16}$$

The redshift dependence of the survey limits for each galaxy considered is now explicit, and it is clear that the likelihood will vary as a function of convergence as the magnitude-size distribution is taken outside these observable limits, as illustrated in Figure 2.7. If the redshift is known, the redshift distribution is a Dirac delta centred on the measured redshift of the source, and the posterior reduces to

$$p(\alpha|\theta) \;=\; \mu^{-\frac{1}{2}} p_{[\theta_0|z]} \left(\mu^{-\frac{1}{2}}\theta\right), \tag{4.17}$$

where $p_{[\theta_0|\alpha,z]}$ is the projected intrinsic size distribution, projected over the magnification-factor-dependent magnitude limits of the survey:

$$p_{[\theta_0|z]} = \int_{m_l+2.5\log_{10}\{\mu\}}^{m_u+2.5\log_{10}\{\mu\}} {\rm d}m_0\ p_{[\theta_0,m_0|z]} \tag{4.18}$$

and correctly normalised as

$$\int_{\mu^{-1/2}\theta_l}^{\mu^{-1/2}\theta_u} \mathrm{d}\theta_0 \; p_{[\theta_0|z]} = 1. \tag{4.19}$$

4.2.4 Surface mass density profile constraints using galaxy magnitudes only

In the case where the sizes of the source sample have been accurately determined, the full size-magnitude method motivated in the section 4.2.1 can be expected to give the strongest constraints on the lensing matter profile. However, it is not always possible to achieve an accurate measurement of the galaxy size. In particular, galaxies whose intrinsic size is much smaller than the PSF for that observation are likely to have poorly measured galaxy size, even with accurate PSF deconvolution as the PSF will erase any small scale information. It is not possible to use the size measurement of such galaxies to determine the mass profile of the lens as the inclusion of a large number of such galaxies would bias the returned profile parameters and introduce noise to the sample.

Further, the method laid out in section 4.2.1 makes the assumption that the measurement error is subdominant to the intrinsic distribution of galaxy size. In actuality, the determination of the galaxy size would be subject to a measurement error which is a function of flux signal-to-noise and size. As a result, this assumption may be less applicable to the smallest galaxies in the sample. In the case where the galaxy's size information is unreliable, constraints may still be put on the lensing distribution using the magnitude information by marginalising over the galaxy size, and the likelihood given in equation 4.10 becomes

$$p(\alpha|m) \propto \int dz \; \mu^{-\frac{1}{2}} \int_{\theta_l}^{\theta_u} d\theta \; p_{[\theta_0,m_0|\alpha,z]} \left(\mu^{-\frac{1}{2}}\theta, m + 2.5\log_{10}\{\mu\}\right) \times \; p(z|m + 2.5\log_{10}\{\mu\}), \tag{4.20}$$

where θ_l and θ_u denote the size limits of the source sample. As with the size-only method, the likelihood in this case is constructed by marginalising over the *observed* size of the source, itself dependent on the lensing profile of the foreground matter distribution. Carrying out the integration, the posterior becomes

$$p(\alpha|m) \propto \int dz \; p_{[m_0]}(m + 2.5\log_{10}\{\mu\}) p(z|m + 2.5\log_{10}\{\mu\}), \tag{4.21}$$

where $p_{[m_0]}$ is understood to be the intrinsic magnitude distribution between the size limits of the sample

$$p_{[m_0]} = \int_{\mu^{-1/2}\theta_l}^{\mu^{-1/2}\theta_u} \mathrm{d}\theta_0 \; p_{[\theta_0, m_0]}, \tag{4.22}$$

and

$$\int_{m_l + 2.5\log_{10}\{\mu\}}^{m_u + 2.5\log_{10}\{\mu\}} \mathrm{d}m_0 \; p_{[m_0]} = 1 \tag{4.23}$$

where m_u and m_l represent the limits of the observed magnitude for the sample. Thus, the intrinsic magnitude distribution must be representative of the galaxy sample, and must account for intrinsic size-magnitude correlations where the sample used is size-limited.

Where the galaxy's redshift is known, the posterior reduces to

$$p(\alpha|m) \propto p_{[m_0]}(m + 2.5\log_{10}\{\mu\}), \tag{4.24}$$

so that the posterior on α for a given magnitude is just the distribution of intrinsic magnitudes for that sample of galaxies evaluated along a line which gives the respective intrinsic magnitude for that source or various values of the local magnification factor.

4.3 Application to mock catalogues

Having detailed the previous method, I wish to investigate its application to data. I therefore construct mock catalogues, which can be used to assess the accuracy and precision of the method. As I wish to evaluate the methods reliability when applied to the STAGES data-set in chapter 5, I briefly introduce the STAGES field here.

4.3.1 The Space Telescope A901/902 Galaxy Evolution Survey (STAGES)

The STAGES survey (Gray et al., 2009) utilised the F606W filter of the Advanced Camera for Surveys (*ACS*) of the Hubble Space Telescope (*HST*) to image a quarter square degree centred on the A901/2 supercluster. STAGES images are complimented by optical imaging using COMBO-17 (Wolf et al., 2003) with five broad bands and twelve narrow bands, and which provides high quality photometric redshifts, with the precision $\sigma_z \sim 0.02(1+z)$ for about $\sim 10\%$ of the brightest galaxies ($R_{\mathrm{Vega}} <$

$24)$ in the STAGES sample. The STAGES catalogue is publicly available[4], and contains $\sim 70,000$ extended sources observed over a short timescale on an unmasked footprint of ~ 0.22 square degrees, giving a global number density of sources of $\sim 85\ \mathrm{gal/arcminute}^2$. The Galaxy Evolution and Morphology Survey (GEMS) (Rix et al., 2004) (discussed further in Chapter 5) observed a blank field in the same passband using ACS, and provides complementary information to the STAGES dataset. This combination of a high number density of sources with high resolution imaging and complementary GEMS dataset from which intrinsic size and flux properties may be obtained provides a valuable opportunity to apply my Bayesian method of mass reconstruction. Further, the mass profiles of STAGES clusters determined using shear measurements in Heymans et al. (2008), allow for the direct comparison of the application of shear and magnification measurements and the investigation into how competitive each analysis is to each other, and how complementary the combination of both may be.

4.3.2 Construction of Mocks

Mock catalogues are constructed from the STAGES data using the following process

1. Galaxies are randomly positioned in the mock survey field.

2. Each mock galaxy is assigned a magnitude and size, both randomly sampled simultaneously from the STAGES catalogue. This ensures that each galaxy's magnitude and size are randomly sampled from the size and magnitude distributions in the STAGES field, whilst preserving any intrinsic size-magnitude relation.

3. Each galaxy is assigned a redshift randomly sampled from a redshift distribution given by equation 3.33 with median redshift given by the median-redshift-magnitude relation of Schrabback et al. (2007) measured on the GOODS field. This redshift relation returns a negative median redshift for galaxies with magnitude brighter than 21: for these galaxies, the redshift is left as unassigned, however as the pipeline implemented in chapter 5 considers only a sample of galaxies fainter than $m = 23$ in an effort to remove cluster members from the sample, these galaxies will automatically be removed from the sample when analysed and are not expected to affect the results.

[4]http://www.nottingham.ac.uk/astronomy/stages/index.html

4. Unlensed distributions are output, where all redshifts are discarded for the unlensed STAGES mock catalogue, and where a mock "COMBO" subset of galaxies is constructed by randomly sampling a sub-set of 10% of the full STAGES mock. The COMBO mocks will therefore vary qualitatively from the COMBO-17 sub-sample of STAGES galaxies with redshift information: in the observations, redshifts are obtained only for the brightest galaxies, whilst no magnitude cuts are applied in the construction of the COMBO mock catalogue; as such the mock will have an overall larger median redshift than the observations. The COMBO mock catalogues considered here are constructed with the purpose of testing the sensitivity of the method to the change in number counts and redshift knowledge that results from the application of the method to the sub-set of STAGES galaxies with COMBO-17 redshift information, and are not constructed to be fully representative of that sample. This choice is justified in the results of section 4.3.3.

5. Each galaxy has its size and magnitude altered according to the lensing relations given in equations 2.77 and 2.91. Each galaxy is assigned a local magnification due to a set of foreground clusters, modelled as NFW profiles, where the redshift information from the previous step is retained and used to evaluate $\Sigma_{\rm Crit}$ for each galaxy. Each lensing cluster is placed at a redshift of $z_{\rm lens} = 0.165$, which is the measured redshift of the four STAGES clusters. Where only a single mock cluster is considered, the cluster is placed with its centre on the BCG of the A901a cluster. In the case of multiple clusters, for ease of computation the magnification assigned to each mock galaxy is assumed to be linear and is determined by the sum of the convergences associated with each cluster, allowing for cluster overlap in the mocks where appropriate. The impact of assuming linearity is investigated in section 4.3.3, and found to be small provided the pipeline also enforces linearity. No limitation on the size of the magnification factor is enforced. Sources which lie within the caustic of the cluster, and therefore experience a negative magnification equivalent to a flip in parity, are removed from the sample. For the sizes of the clusters modelled in this section, the caustic ring is small and so only a small number of sources are removed for this reason (roughly 1 in 70,000).

Unless otherwise stated, the prior joint size-magnitude distribution is determined from the full STAGES catalogue, even when the subsample of galaxies with redshift

information is considered, to reduce the noise on the prior. The prior size-magnitude distribution is assumed to be redshift independent: this assumption is supported by the lack of redshift dependence of galaxy sizes measured in the COMBO data-set (Section 5.3), however the magnitude distribution shows a larger redshift dependence, and a magnitude-redshift dependence is assumed in the magnitude-median redshift relation used to model the unknown galaxy redshift distribution for the STAGES sample. The effect of this assumption is tested in section 4.3.3.

Clusters are modelled as spherically-symmetric NFW profiles, where the integrated surface mass density is constructed as given in equation 2.38. Following the analysis of Heymans et al. (2008), I use the Λ-CDM mass-concentration relation of Dolag et al. (2004)

$$c(M_{200}, z_{\rm lens}) = \frac{9.59}{1+z_{\rm lens}} \left(\frac{M_{200}}{10^{14} h^{-1} M_{\odot}} \right)^{-0.102} . \tag{4.25}$$

The NFW model used in the construction of the mocks and the posterior is a model with the virial radius (or equivalently virial mass) as the single free parameter.

4.3.3 Testing the method

In this section, I investigate the use of each analysis in determining the posterior for the NFW clusters modelled as part of the construction of the mock catalogue, detailed above. In doing so, I will present signal–to–noise results for each probe, and consider the biases resulting from simplifying assumptions enforced on the method due to limitations of the data, with the aim of discerning the accuracy of the method, and guiding the application to data.

The application of the method is chosen to match its use on the STAGES field in chapter 5. As such, for all results presented here, the size-magnitude distribution is constructed and smoothed using Kernel Density Estimation (KDE), using a bivariate-Gaussian smoothing window in size and magnitude, with covariance equal to 0.01 times the covariance of the data sample. KDE-smoothed apparent magnitude and size distributions constructed in this manner compare well to histograms of the same quantities. Error bars are calculated as the region which includes 68% of the probability on either side of the mode of the posterior on α, assuming a hard prior on $r_{200} \geq 0$. The total width of the error bars contain 68% of the probability along the full posterior, but the width of the error bar on either side of the mode point should not be interpreted as containing 32% of the total probability: instead, the lower error bar contains 68%

of the probability to the left of the posterior mode, whilst the upper error bar contains 68% of the probability to the right of the posterior mode.

All results are shown using a mask of $0.5'$ around each cluster BCG (which I will frequently refer to as a 'core cut'): whilst the use of a core mask is unnecessary for the idealised cases presented here, this masking of the cluster centre is the smallest of the core cuts used in the application to the STAGES field to remove cluster contaminants, and is included here for consistency. The pipeline evaluates only those galaxies fainter than $m_{\mathrm{F606W}} = 23$: this magnitude limit is imposed on the data to remove the cluster galaxies from the sample in the absence of redshifts, and whilst the simulations will not contain these cluster galaxies, the limit is imposed for consistency. As with the data, galaxies with $z < 0.21$ are not considered as part of the pipeline.

Figure 4.1 shows a comparison plot for four different analyses using mock STAGES data-sets, where single NFW clusters have been modelled. The plot considers four different data-sets for the analysis:

1. COMBO, Size-Mag: Posteriors are constructed using information on both galaxy size and magnitude. The data-set is limited to only those galaxies with redshift information.

2. STAGES, Size-Mag: As above, using the full STAGES data-set. Where no galaxy redshift information is present, the posterior is constructed by marginalising over a redshift distribution.

3. STAGES, Mag-Only: As above, using only magnitude information: galaxy size information is marginalised, as detailed in section 4.2.4.

4. STAGES, Size-Only: As STAGES, Size-Mag, using galaxy sizes only: magnitude information is marginalised, as detailed in section 4.2.3.

The top panel of Figure 4.1 shows example single runs for each analysis type for two different input masses. Whilst there is some expected statistical variation between runs, in all cases the input mass seems well reproduced. The bottom panel shows an estimate of the signal–to–noise, constructed as the mode point of the recovered mass posterior for the largest input mass divided by half the total error width, averaged over 10 independent realisations for each data-set considered. From this one can see two features: Firstly, one sees a significant increase in the signal–to–noise when the full STAGES data set is used, rather than the sub-set of sources with COMBO redshift

information. This is a result of the decrease in statistical noise as a consequence of the increase by a factor of ~ 10 in the number density of sources in the full STAGES dataset. Secondly, we find that using the STAGES data-set, there is a small increase in signal–to–noise as one moves from a magnitude- to size-only analysis, with a significant increase when both are used. This latter point is expected as both the size and magnitude information contain complementary information on the magnification field which results from the presence of the lensing cluster.

Figure 4.1 shows the idealised case where galaxy size and magnitude information is considered well known for the whole sample, so that the only limit on these quantities come from the survey limits, or the bright magnitude cut used to remove foreground contamination. The applicability of such an assumption is detailed in sections 4.2.4 and 4.2.3, and will be considered in more detail in chapter 5, however I note here that the application of size cuts, PSF confusion or measurement error may cause a decrease in the constraining power of the size-only or size-mag analyses. In such a case, one may also expect an increase in the relative signal–to–noise of the size-mag and size-only analyses, as the addition of magnitude information allows the measurement of the magnification for the smallest galaxies where size measurements are impossible. Even so, the combination of size and magnitude information is expected to give more information than either alone, and I will focus on the use of the joint size-magnitude analysis on the full STAGES data-set for the remainder of this section.

Figure 4.2 shows typical noise properties for a size-magnitude analysis using the full STAGES dataset, over 10 independent mock realisations, whilst Table 4.1 shows the average noise over 10 realisations for each experiment. The single halo fits from Table 1 of Heymans et al. (2008) show that the A901a and A901b clusters can be constrained with a signal–to–noise of ~ 4.2[5]. Comparison of the values quoted in Table 4.1 and given in Figure 4.1 for an $M = 2 \times 10^{14}\ h^{-1}M_{\odot}$ mock cluster to these shear measurements allow for a reasonable approximate comparison of the ability of the magnification and shear analyses in determining the properties of the foreground lensing cluster. We see that in the idealised case presented here, the magnification analysis is competitive to the shear, with a larger signal–to–noise for all three probes on the full STAGES data-set, and almost twice as large for the full joint size-magnitude magnification analysis. It is important to note that average values presented here only

[5]The constraints presented in Heymans et al. (2008) give the recovered masses of A901a and A901b as $(18.8 \pm 4.4) \times 10^{13}\ h^{-1}M_{\odot}$ and $(18.1 \pm 4.4) \times 10^{13}\ h^{-1}M_{\odot}$, where a single halo has been fit to each.

Table 4.1: The average width of 1σ error bars taken over 10 mock realisations, for each probe considered in Figure 4.1.

	$r_{200} = 1.2h^{-1}\mathrm{Mpc};\ M_{200} \sim 2 \times 10^{14}h^{-1}M_{\odot}$	
Experiment	$\bar{\sigma}_{r_{200}}[h^{-1}\mathrm{Mpc}]$	$\bar{\sigma}_{M_{200}}(\times 10^{13})[h^{-1}M_{\odot}]$
COMBO Size-Mag	0.14	6.6
STAGES Mag-Only	0.07	3.5
STAGES Size-Only	0.07	3.1
STAGES Size-Mag	0.05	2.4

partially account for the cuts that are required to ensure accuracy in the application to real data: for example, these results mask a core of $0.5'$ around each cluster, which is the least conservative core mask used on all four clusters in chapter 5, and does not include any cuts of measured galaxy size which would be required to remove the noisiest size measurements from the sample. Each of these effects would serve to increase the statistical noise of the analysis through the reduction of the size of the source sample, suggesting that the signal–to–noise presented here will be over-estimated.

I now turn my attention from the precision of the analysis to the accuracy of the analysis, and investigate the levels of bias coming from difference potential sources of bias in such an analysis. I identify three main potential sources of bias:

1. An 'analysis bias', which is a bias in recovered lensing mass parameters coming from simplifications or assumptions in the construction of the posterior. Most notable of these is the assumption of redshift-independence of the size-magnitude prior. This is justified through the analysis of the size and magnitude distributions in the STAGES and GEMS field in section 5.3. In the construction of the mock datasets, I impose a magnitude-dependent redshift distribution using the results of Schrabback et al. (2007), thus imposing an expected redshift dependence in the galaxy magnitude.

2. A 'lensed prior bias' due to the construction of the size-magnitude prior using a dataset in a field with a non-zero global convergence. In this case, the magnification field causes a shift in the underlying size and magnitude distribution, leading to a bias in the results if this distribution is interpreted and used as an unlensed prior. This problem is expected to be worse for smaller fields, dominated by foreground over-densities as a larger fraction of the total

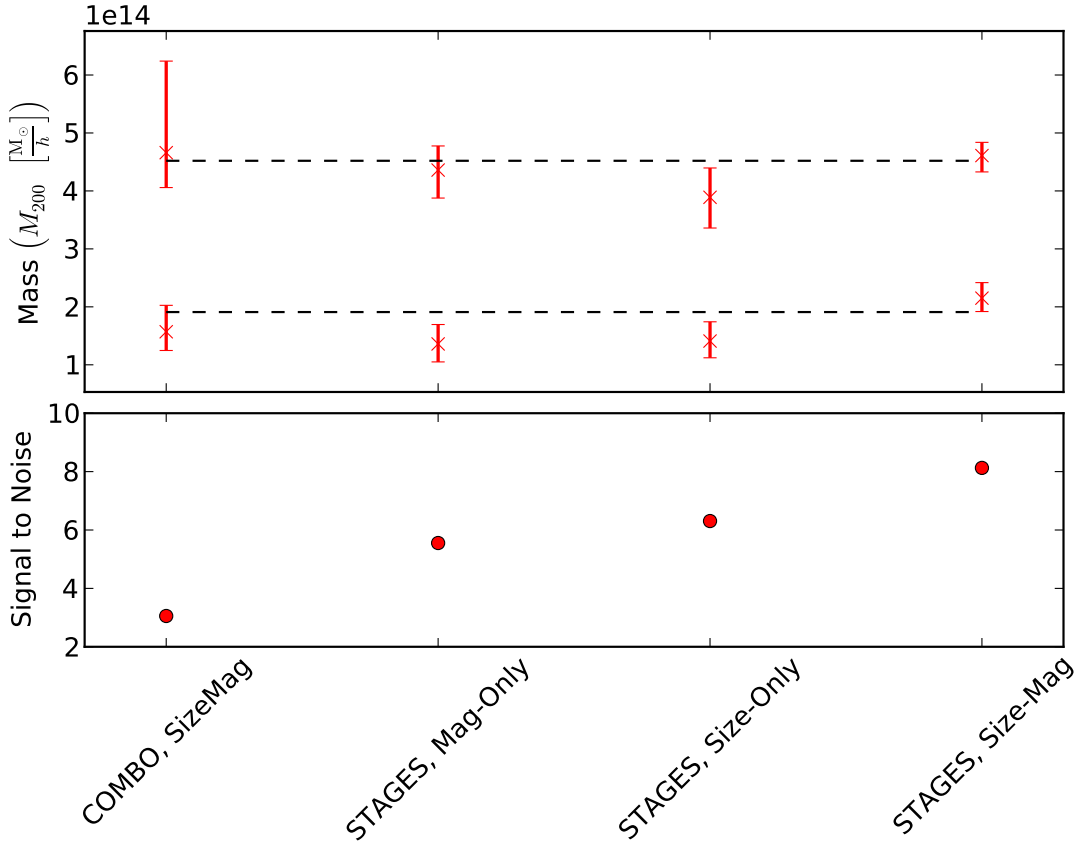

Figure 4.1: Comparison plot between the size-only, magnitude-only and size-magnitude analyses for both mock COMBO- and the mock STAGES-datasets for an example single run of the analysis. The *top* panel shows example runs for each case. In all cases, a single cluster was modelled on the field to avoid bias due to overlap between clusters, and the prior was constructed on the unlensed STAGES dataset. Errors are 68% confidence limits of the recovered posterior about the mode position. Dashed lines show the input mass for each case. The *bottom* panel shows signal-to-noise, calculated as the mode point divided by half the total error width for each comparison. One can see that the size-magnitude analysis with the full STAGES set gives the largest signal-to-noise of all four cases, motivating its use on the full STAGES dataset

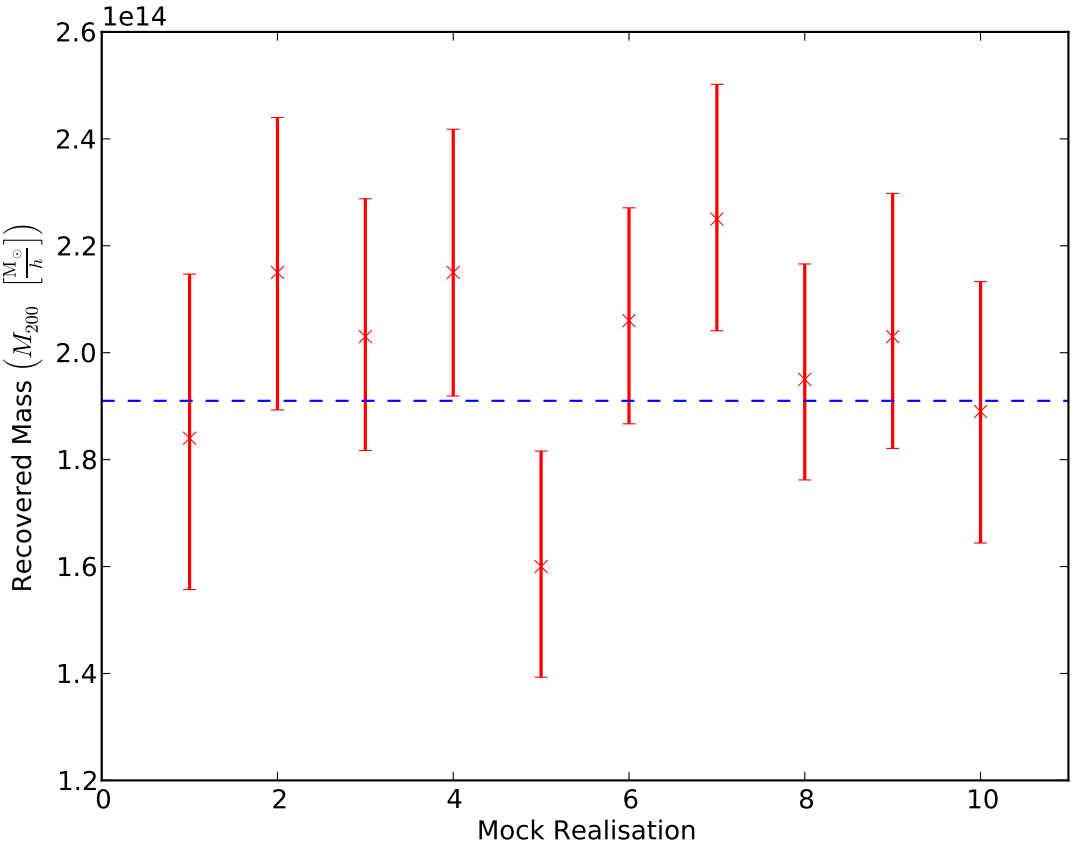

Figure 4.2: Plot showing the noise properties of 10 mock realisations of the STAGES+COMBO dataset, using the size-magnitude analysis. Errors are 68% confidence limits of the recovered posterior about the mode position. The dashed line shows the input mass of the cluster, where in this case a single cluster was modelled on the field, to remove bias due to cluster overlap, and the prior was constructed from the unlensed distributions.

sample would experience significant lensing by the foreground. Similarly, for a given field size, this bias would be expected to increase with the mass of the lensing foreground, as larger lensing masses would cause a larger shift in the size and magnitude of the background sources. Moreover, the presence of a non-zero magnification field will cause a broadening in the intrinsic size-magnitude distribution. In general the noise properties of such a field are non-trivial due to the non-linear relations between the observed- and intrinsic- size and magnitude, however the broadening of the size-magnitude distribution is expected to be small in the case where the magnification factor is close to one and has an uncertainty smaller than the uncertainty in size or magnitude.

3. An 'overlap bias' caused by the misinterpretation of part of the lensing signal due to another overlapping cluster. In this case sources close to one cluster will experience lensing due to the nearby cluster, causing a bias in the recovered dark matter profile parameters for the main cluster as the shift in these sources' size and magnitude is interpreted as a shift caused by the cluster being constrained. The strength of this effect is a function of the magnification field due to the neighbouring lensing masses in the region of the foreground being considered, and may be expected to be strongest for large mass neighbours, or those close in angular separation. This bias can be avoided by constraining all lensing masses on the field simultaneously.

Further, I will consider the importance of going beyond the weak lensing form of the magnification factor. I consider each of these in turn, with the aim of quantifying the significance of each on the application of this analysis on the STAGES field. All bias plots show the result from the combination of 10 independent mock realisations of the data. Unless otherwise stated, for each case a single cluster is modelled on the field to avoid overlap biases, and the redshift distribution is chosen to be as in equation 3.33 with median redshift of $z = 1$.

Figure 4.3 shows the fractional bias[6] for a "medium" lensing analysis (ML), where the magnification factor is defined as in equation 2.17, and a weak lensing analysis where the linear magnification factor (equation 2.18) is assumed in both the pipeline and simulations (WL). From both, we see that there is no evidence for bias, indicating that the method described above gives accurate recovery of the cluster profile over

[6]Defined as the difference between the mode of the combined posterior, over 10 mock realisations, and the input mass, as a fraction of the input mass

many independent runs. It should be noted that a number of simplifying assumptions have entered into this analysis, each of which will be explored further in this section. Blue crosses show the bias that results from incorrectly enforcing the weak lensing assumption in the pipeline for varying lensing halo mass ("ML Mocks, WL Pipeline"). As expected, the absolute value of the bias increases as a function of mass, as the weak lensing assumption becomes inaccurate for a larger fraction of the source sample.

We see that incorrectly assuming weak lensing as part of the analysis causes one to over-estimate the mass of the lensing cluster. The reason for this can be seen in Figure 4.4: $\mu_{\rm ML}$ represents the 'true' magnification factor for a distant source $\sim 0.24h^{-1}{\rm Mpc}$ from the cluster centre as a function of virial radius (or mass), whereas $\mu_{\rm WL}$ shows the equivalent magnification factor in the weak lensing approximation. For a given source which experiences a magnification by $\mu_{\rm ML}$, one must consider a larger virial radius to obtain the same magnification factor in the weak lensing approximation: consequently, assuming weak lensing in a magnification analysis will cause the cluster mass to be over-estimated.

Analysis Bias

Figure 4.5 shows the fractional bias when the analysis assumes redshift independence of the intrinsic size-magnitude distribution, when the data satisfies the magnitude-median-redshift relation given in Schrabback et al. (2007) (noted previously as 'analysis bias'). We see the expected variation of the combined posterior mode around a fractional bias of zero for all input masses, and therefore no evidence for significant bias, suggesting that the incorrect assumption of redshift independence of the intrinsic magnitude distribution does not lead to inaccuracies in the analysis. Together with the observed redshift independence of the size distribution (see section 5.3), I conclude that the assumption of a redshift-independent size-magnitude distribution is valid and should not lead to significant bias in the application to STAGES clusters if the evolution of the size distribution in the COMBO-17 sample is representative of the whole STAGES data-set.

Lensed Prior Bias

A difficulty in the use of the size- or flux-magnification signal as a probe of the convergence field is the necessity to know the global, unlensed properties of the field in order to extract the signal. In the case of probing the convergence field using a

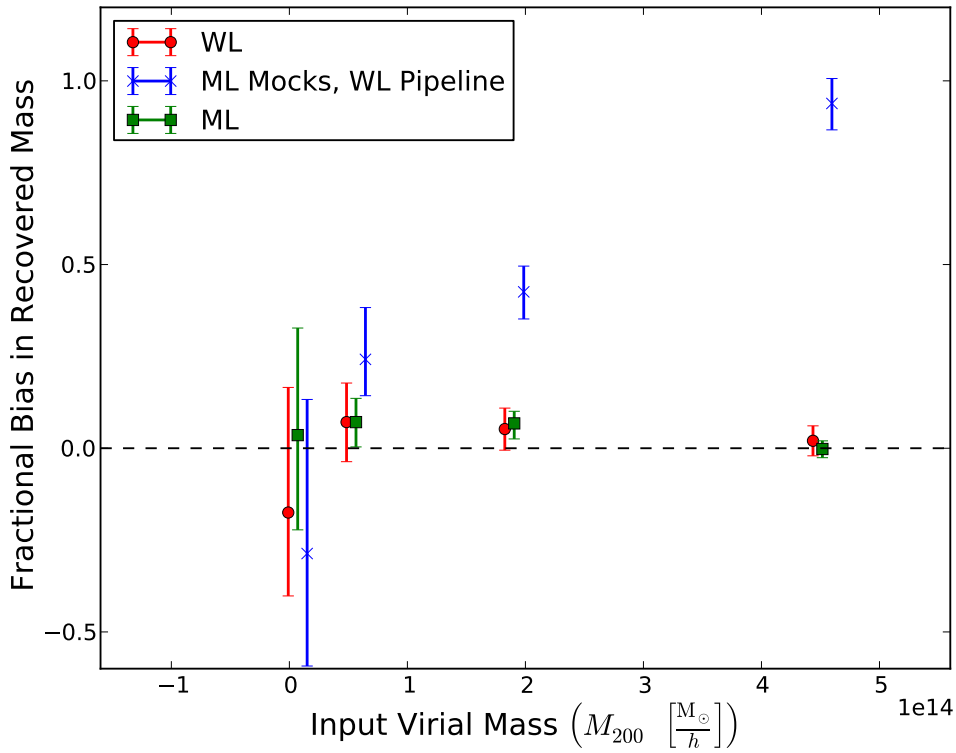

Figure 4.3: Fractional bias on the cluster virial mass for a size-magnitude analysis using a mock STAGES+COMBO-17 dataset, where weak lensing relations have been enforced on both mock catalogues and the pipeline (WL), and where the magnification factor takes the form of equation 2.17 (ML). A single cluster is modelled to avoid overlap bias, and the prior was constructed on the unlensed mock STAGES dataset. Recovered posteriors are unbiased in the virial radius and virial mass when the WL or ML lensing relations are applied to both the mocks and the pipeline. Blue crosses show the bias when the weak lensing assumption is used as part of the pipeline. Blue crosses and red circles have been offset from the true input mass to aid visualisation.

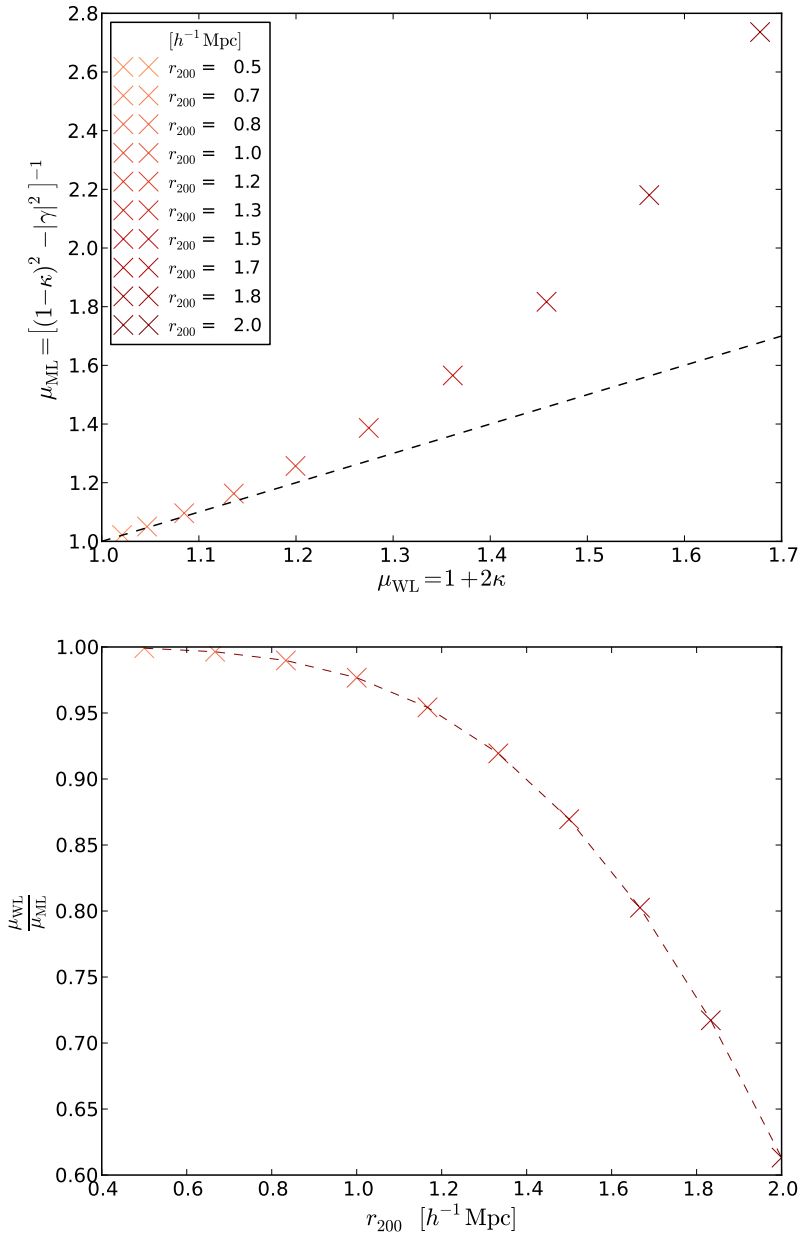

Figure 4.4: Diagram showing the variation of the "medium" lensing magnification factor and weak lensing magnification factor with increasing cluster virial radius (and mass). The *top* panel shows the magnification factor as a function of virial radius. In general, moving further right and up corresponds to larger cluster mass. The *bottom* panel shows ratio to weak lensing to "medium" lensing magnification factor as a function of virial radius.

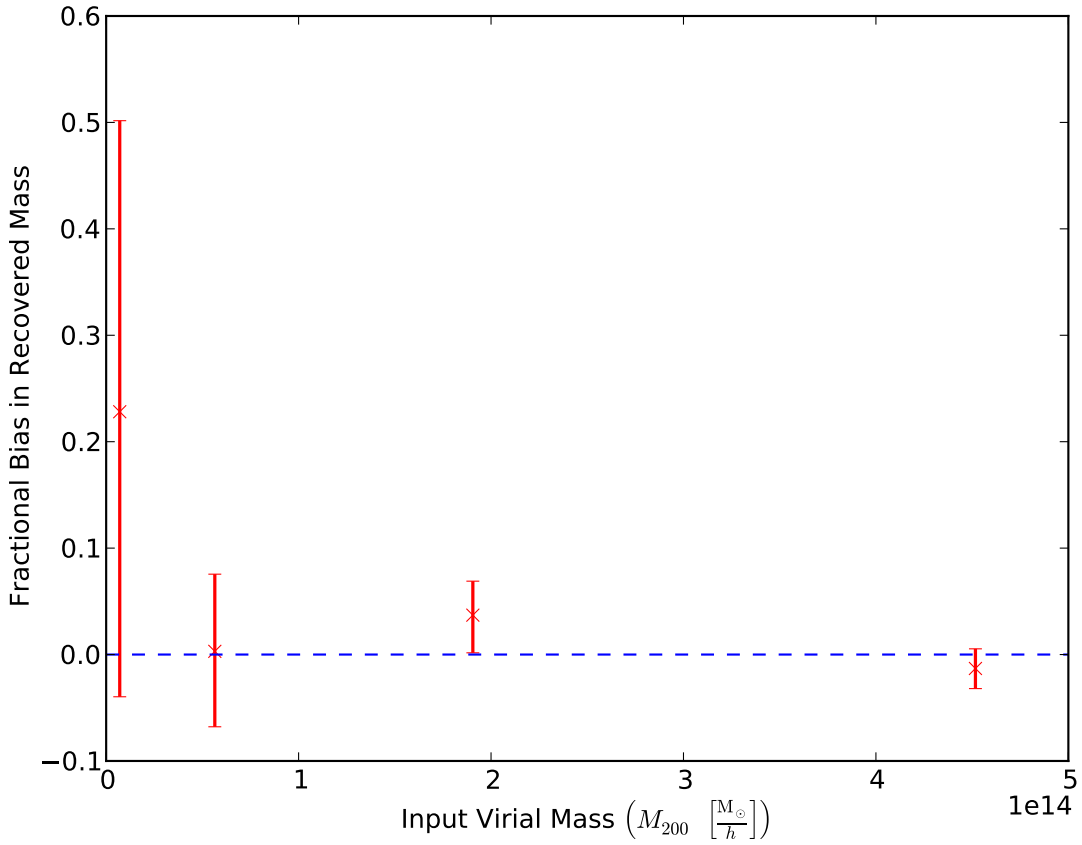

Figure 4.5: Plot showing the fractional bias in cluster mass, caused by the assumption that the prior size-magnitude distribution is redshift-independent, when the magnitude-median-redshift relation of Schrabback et al. (2007) is enforced in the construction of the mocks. In this case, galaxy redshifts are assigned using their magnitudes in the construction of the mock catalogues, but redshift independence of the magnitude distribution is assumed as part of the pipeline. A single cluster is modelled to avoid overlap bias, and the prior was constructed on the unlensed mock STAGES dataset.

local shift in the size or magnitude distribution, this issue can be understood thus: the presence of a foreground mass which dominates the field on which the sample is taken will cause a shift in the size- or magnitude- distribution from which a statistic such as the mean can be taken. The misinterpretation of this statistic as describing the unlensed field can therefore introduce a bias in the local recovery of the convergence field when using a convergence estimator which compares the local statistics to the global value, such as equation 2.81. The interpretation of the source of this bias is similar in the analysis considered here, but slightly nuanced. In the posterior reconstruction method described in section 4.2, accurate reconstruction of the lensing mass profile depends strongly on the accuracy of the a-priori unlensed size-magnitude distribution. The presence of a convergence field whose average is non-zero across the field will cause a shift in the size and magnitude of the background sources and thus shift and widen the observed size-magnitude distribution using the sample across the whole field. The recovered posterior for each galaxy in the sample will be inaccurate if this lensed distribution is misinterpreted as the prior distribution on the size-magnitude plane for that survey. As such, it is most natural to construct this prior on a blank field (such as the data-set provided by the GEMS survey), or using a sample which covers a large survey area so that the average of the convergence field across the survey area is zero and to first order as many sample sources experience a positive convergence as negative, where possible.

As the STAGES field is dominated by four large clusters, it is expected that the recovery of posteriors on the cluster mass profile may be biased if the prior distribution is also constructed using the STAGES data-set. Figure 4.6 shows the fractional bias as a function of input mass where the intrinsic size-magnitude distribution is constructed from the lensed catalogue, from the combination of 10 mock realisations of the STAGES field with a single lensing cluster. In this case, the intrinsic size-magnitude distribution is constructed from measurements on the lensed field, and incorrectly interpreted in the pipeline as an unlensed distribution. We see that the absolute fractional bias (and the absolute bias) becomes larger with an increase in the lensing mass: this is expected as a larger lensing mass causes greater shifts in the size-magnitude distribution, so the result less accurately describes the unlensed distribution. For the largest mass considered, the fractional bias is $\sim 10\%$ of the mass of the cluster. Using the results of Heymans et al. (2008) the total mass of all four clusters is $\sim 4 \times 10^{14} M_{\odot}/h$: it is therefore expected that this bias will be insignificant on the

application to STAGES data. Future work will circumvent this bias by constructing the a-priori intrinsic size-magnitude distribution through measurements on the GEMS field, which constitutes a blank field.

Overlap Bias

The final main source of bias I consider in this section is the bias caused by the overlap between neighbouring clusters. The motivation for this bias is clear: the magnification field at a particular point on the field is dependent on the total surface mass density at that point, which itself is a combination of contributions from all lenses. Thus, a galaxy located close to a given cluster will have a contribution to the magnification from a neighbouring cluster, which increases with a reduction of the distance to the neighbouring cluster and its mass. If each cluster is fitted individually with no consideration for close neighbours then the returned mass for that cluster will be expected to be biased due to the misinterpretation of the lensing signal for that galaxy.

Blue points on Figure 4.6 show the fractional bias for two equally massive clusters centred on A901a and A901b. We see that as the clusters increase in mass, the bias due to cluster overlap increases, as expected. For the largest masses considered here, we see that the fractional bias can be as large as $\sim 20\%$ of the input mass, giving a bias which is roughly as large as the statistical noise on a single run for that cluster suggesting this bias may be significant in the analysis of the STAGES field. For the STAGES field, where A901a and A901b are both measured to be $\sim 2 \times 10^{14}\ h^{-1} M_{\odot}$ (Heymans et al., 2008), the predicted bias is $\sim 10\%$ of the input mass, and smaller than predicted statistical noise on a single realisation. Future work will circumvent this bias by simultaneously fitting all four clusters.

4.4 Conclusions

In this chapter I have detailed a Bayesian method for determining the dark matter halo model properties of a foreground lens, using measurements of source size and magnitude, both of which are modified in the presence of a magnification field. This method starts from a-priori knowledge of the intrinsic size-magnitude distribution, which may be measured from data. As such, provided this distribution is accurately known, this method automatically accounts for intrinsic size-magnitude correlations,

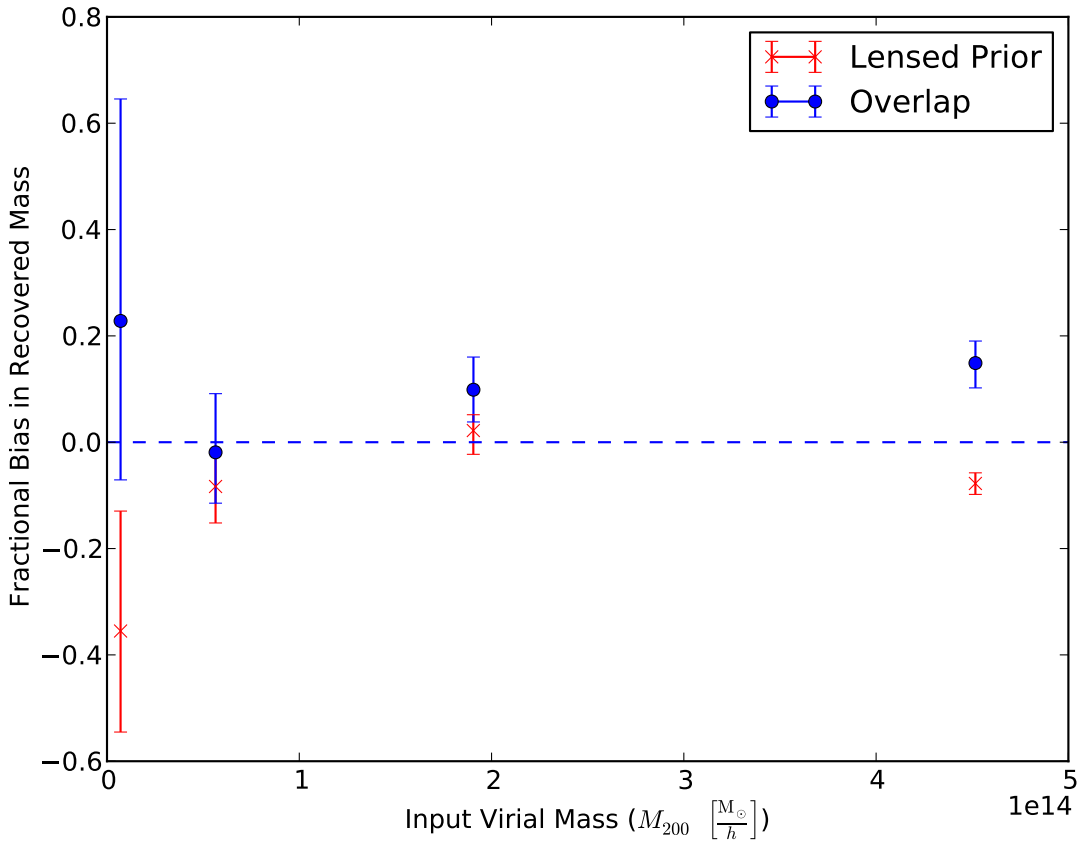

Figure 4.6: Plot showing the fractional bias in cluster mass (to mass of cluster modelled in the mock), when the prior is constructed from the lensed distribution (red crosses) and due to cluster overlap (blue points). Overlap bias is calculated using two equal mass clusters centred on A901a and A901b, where the source sample is taken within a $2'$ aperture centred on the cluster centre.

and therefore does not need correction for the bias caused by these correlations in a flux-limited sample, as discussed in section 2.3.3. A particular strength of the method lies in the fact that provided the size-magnitude distribution can be adequately measured using data, one does not need to make any simplifying assumptions about the distribution, as in Schmidt et al. (2012). The method was designed to allow for the marginalisation over the source redshift, where the redshift is not known, provided a form for the redshift distribution of the sample is known. As a result, this method automatically accounts for the error in parameter estimation that results from uncertainties in the redshift determination.

In its fullest form, the method is presented in a way that allows the measurement of lensing dark-matter halo properties using both sizes and magnitudes, however I have also presented equivalent results using either probe individually. Whilst the joint measurement of size and magnitude will provide better constraints, one may wish to consider size- or magnitude-only probes as a result of limitations on the data. For example, the smallest galaxies are most affected by uncertainties in their size-measurement: rather than discard the information from these sources, one may wish to construct posteriors with only the magnitude information for these sources whilst using the maximally constraining size-magnitude analysis for larger galaxies for whom the measurement of size is more exact.

The method was tested through the application to mock datasets sampled from the STAGES field. The method was found to be unbiased in the case where a single cluster was modelled, and the intrinsic size-magnitude distribution was known. I found that the simplifying assumption of redshift independence of the intrinsic-size-magnitude distribution did not cause notable bias in the recovered cluster virial mass when the magnitude-redshift relation of Schrabback et al. (2007) was enforced. Together with the increase in expected signal–to–noise from the addition of sources without redshift motivates the use of the full STAGES catalogue, rather than just the subset of sources with COMBO-17 redshift information. I found that in the idealised case where the size information for all galaxies is reliable, the use of galaxy-sizes-only gave larger signal–to–noise than the use of galaxy magnitudes, with a further significant increase when both are used.

Two further biases were tested, resulting from cluster overlap and the use of an intrinsic size-magnitude relation which has not been measured on a blank field. I found that cluster overlap gave a bias close to 10% of the input cluster mass for a

$\sim 2 \times 10^{14} M_{\rm Sun}/h$ cluster, which corresponds to the expected mass of the A901a/b clusters, as measured using shear measurements in Heymans et al. (2008). The effect of taking the a-priori intrinsic size-magnitude distribution on a lensed field was found to be small, with a sub-10% negative bias for the total mass of lensing matter on the STAGES field. This suggests that the intrinsic size-magnitude distribution could be measured on the field with only a small bias in the recovered cluster masses, within the expected statistical noise for a single run. I note that both these biases can be mitigated by either simultaneously constraining all clusters or measuring the a-priori distribution on a blank field such as that provided by the GEMS survey.

I therefore conclude that the use of the method described in this chapter can return accurate measurements of the cluster mass to a significant signal–to–noise for the STAGES clusters. In the next chapter, I develop and apply this method to the STAGES field, accounting for further limitations in the data.

Chapter 5

Mass Reconstruction using galaxy size and magnitudes in the STAGES field

5.1 Motivation for the use of the STAGES dataset

The STAGES survey, introduced in section 4.3.1, provides an excellent data-set on which to investigate the application of magnification measurements as a method of cluster mass reconstruction. To facilitate the aim of accurate mass reconstruction using weak lensing measurements, the survey was designed with the accurate measurement of galaxy shapes in mind: in particular, the survey provides deep ($m_{\mathrm{F606W}} \lesssim 27.5$), high resolution HST images from which a large sample set of robust galaxy shapes, sizes and fluxes can be obtained. Observations were taken within a small observational time frame, with greater than 50% of the tiles were observed in one five-day period, and over 90% within 21 days, whilst seven tiles were observed six months later. The mosaic of 80 ACS tiles which constitutes the STAGES field is shown in Figure 5.1, grouped in colour by observation period.

The STAGES dataset is complemented by high precision multi-band photometry from COMBO-17, which provides accurate photometric redshifts for the brightest $\sim 10\%$ of the STAGES sample. The availability of such information allows for the investigation into the accuracy and precision of the result when simplifying assumptions about the evolution of this distribution are made. Redshift information for the bright cluster galaxies allows for the removal of cluster contaminants from the source sample, improving the accuracy of the mass reconstruction. Further, source galaxies with redshifts do not require the marginalisation over an a-priori redshift

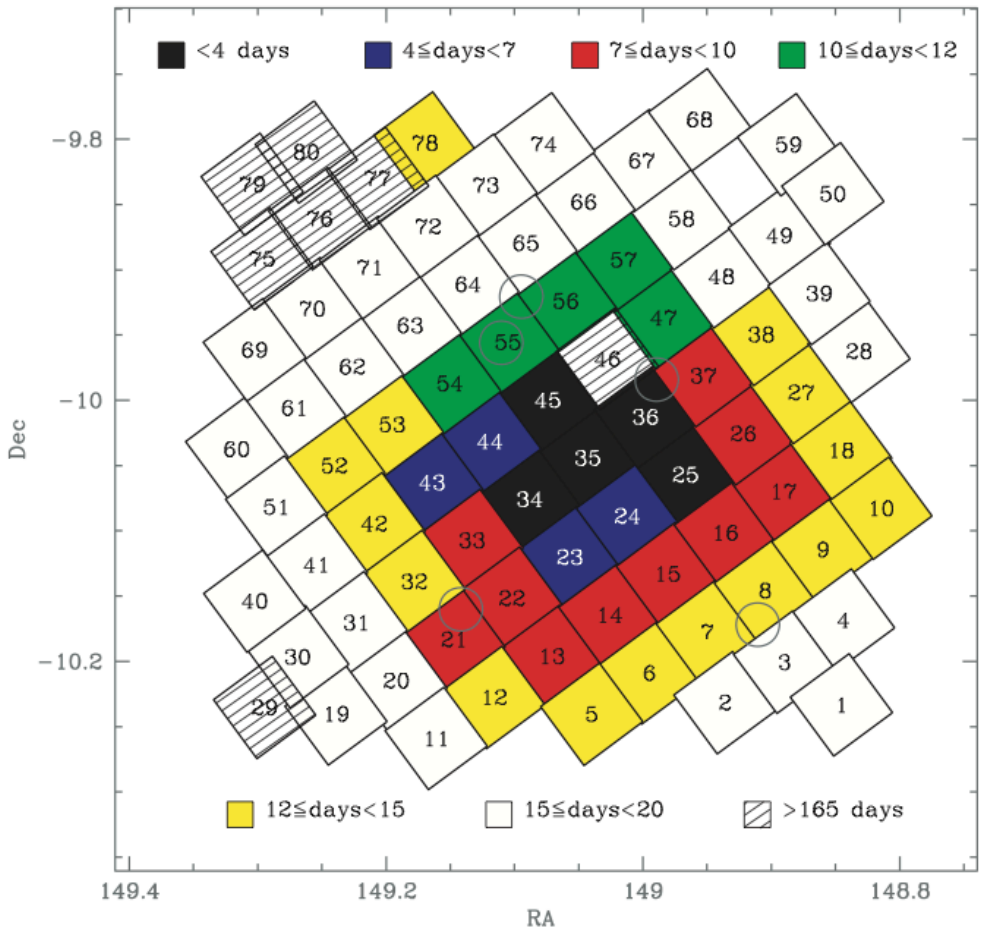

Figure 5.1: ACS tile pattern which constitutes the STAGES field. The colour scheme labels varying observational lengths, and details the grouping in which the PSF is measured. Circles, with radius of 1 arcminute, show the position of the four main clusters centred on the BCG: A901a (tile 55), A901b (36), A902 (21) and the South West (SW) group (8). The in-falling X-ray group A901α is also circled. Taken from Heymans et al. (2008).

distribution which would increase the width of the posterior on the cluster mass for that source.

Complementary measurements are available from the Galaxy Evolution from Morphology and SEDs (GEMS) survey (Rix et al., 2004), which imaged a quarter square degree area of the sky using the ACS of the HST, imaged in MF606W with 9 by 9 pointings. As with the STAGES field, HST images of the GEMS field are complemented by imaging from COMBO-17 for galaxies with $R < 24$, providing accurate redshifts for $\sim 10,000$ galaxies in the GEMS sample. The STAGES survey was designed to closely match that of the GEMS field, and both surveys were conducted in the same passbands (F606W), to allow for the investigation of the dependence of galaxy evolution in cluster and field environments respectively. The high-resolution, deep HST images and high number density (of ~ 90 galaxies per square arcminute) provided by both the STAGES and GEMS surveys provide an excellent dataset for a lensing analysis, and an investigation into the virial to stellar mass ratio using galaxy-galaxy shear measurements in the GEMS field were undertaken in Heymans et al. (2006), cosmological constraints in Heymans et al. (2005) and cluster mass profile fitting using shear measurements of the STAGES field in Heymans et al. (2008).

The similarity of the imaging between the two surveys provides a unique opportunity to investigate the use of galaxy size and magnitudes as a probe of lensing matter: in particular, measurements of field galaxies in the GEMS field can be used to form the a-priori size-magnitude distribution, utilised in the formalism of section 4.2, without contamination of the distribution due to the presence of cluster galaxies. Moreover, the GEMS dataset provides independent verification of measurements on the STAGES field, and can provide the means of determining the level of systematics in a magnification analysis through the application to a blank field where the signal is expected to be consistent with zero.

As noted, a variety of weak lensing analyses have already been undertaken using the STAGES dataset. Of particular interest is the mass reconstruction of the STAGES clusters using traditional shear measurements (Heymans et al., 2008). The availability of such information provides a unique opportunity for the comparison between a shear and size- and flux- magnification analysis, as well as a indicator for the complementarity of both analyses.

5.2 Galaxy size measurements

A weak lensing analysis using galaxy sizes or ellipticities must measure these quantities from images, which are distorted due to aberrations and optical distortions originating from the telescope and lens, and pixelisation due to the use of CCD's, as well as atmospheric distortions in the case of ground-based surveys. As a result, a great deal of effort within the lensing community has been devoted to the development of methods to accurately measure the shapes of noisy images (Bridle et al., 2009; Kitching et al., 2012), with the aim of disentangling the lensing effects from contamination. A consequence of this is that multiple methods of shape measurement exist, from second order quadrupole moments (described in the remainder of this Section) to Bayesian model fitting such as Lensfit (Miller et al., 2007) and im3shape (Zuntz et al., 2013), and galaxy-morphology fitting with Shapelets (Bernstein & Jarvis, 2002). Whilst each method has its own associated advantages and disadvantages, they differ only on the method of PSF correction and shape measurement: in general, all require as pre-requisites well-reduced data, good separation of galaxies and stars and the accurate measurement of the PSF, usually using stellar images as point sources.

In this section, I will describe briefly the measurement of galaxy morphology using the method of 2nd order brightness moments, and describe briefly the modelling of the point-spread-function (PSF), containing information on the distortion of observed source size and shape due to atmospheric distortion and telescope optics, using the Kaiser, Squires & Broadhurst (1995) (KSB) and Rhodes, Refregier & Groth (2000) (RRG) methods.

Consider a galaxy image, whose surface brightness profile (I) is described by the pixel brightness on a grid. The second order brightness moment along axes $i, j = \{1, 2\}$ is defined as

$$Q_{ij} = \int d^2\theta \; \theta_i \theta_j W[I(\boldsymbol{\theta})] I(\boldsymbol{\theta}) \tag{5.1}$$

where $W[I(\theta)]$ is a window function, normalised to unity over all space whose inclusion ensures convergence of the integral over noisy images, or where galaxies are not isolated on the image. For convenience of notation, I have defined the origin of the angle θ from the centroid of the image. The total flux contained within this window is then

$$Q = \int d^2\theta \; w(I(\theta)) I(\theta), \tag{5.2}$$

and following the notation of (RRG), I have defined the 'flux-renormalised' moment as

$J_{i,j} = Q_{ij}/Q$. When defined in this way, the brightness moments of a gravitationally lensed object are tensors related to the brightness moments of the unlensed source (superscript s) as

$$J^s = \mathcal{A} J \mathcal{A}^T, \tag{5.3}$$

where $\mathcal{A}$ is the lensing Jacobian, and superscript T here denotes the transpose (Bartelmann & Schneider, 2001).

The flux-renormalised second order brightness moment can be thought of, heuristically, in the following way: if the combination of the brightness profile of the image and the window function describe a probability density function, then the second order brightness moment describes the covariance of random variables θ_1 and θ_2. In this analogy, the auto-correlations J_{11} and J_{22} the define a width of the combination of brightness profile and window in the θ_1 and θ_2 parameter space respectively: since θ_1 and θ_2 describe spatial co-ordinates, this translates to widths of the brightness profile and window function in real space. Similarly, $J_{12} = J_{21}$ describe the covariance of the parameters, which translates to a width at 45 degrees to the orthogonal co-ordinate axes θ_1 and θ_2.

From this definition one may define the size of an image as

$$S_1 = \det(J)^{\frac{1}{4}} = (J_{11}J_{22} - J_{12}^2)^{\frac{1}{4}} \tag{5.4}$$

$$S_2 = (J_{11} + J_{22})^{\frac{1}{2}}, \tag{5.5}$$

so both definitions have the units of *length*. Transforming the brightness moment using Equation (5.3), both size measures can be related to their unlensed equivalents. The first measure, S_1 transforms as

$$S_1 = \frac{J_{11}^s J_{22}^s - [J_{12}^s]^2}{|\gamma|^2 - (1-\kappa)^2} = \mu^{\frac{1}{2}} S_1^s, \tag{5.6}$$

and thus transforms as a length, as required. The transformation for S_2 is more difficult. To linear order in the convergence and shear, S_2 transforms according to

$$S_2 = [(J_{11}^s + J_{22}^s)[1 + 2\kappa] + 2(J_{11}^s - J_{22}^s)\gamma_1 + 4J_{12}^s\gamma_2]^{\frac{1}{2}}. \tag{5.7}$$

Taking each term in turn, we can see that $(J_{11}^s + J_{22}^s)$ is increased by a factor of $\mu^{\frac{1}{2}}$, as expected for an isotropic magnification. The source 'ellipticity' components $(J_{11}^s - J_{22}^s)$ is coupled to γ_1, which describes the distortion along a given axis, whilst J_{12} is coupled

to γ_2 which describes the distortion at 45 degrees to that axis. Thus, the size measure S_2 depends to linear order on the intrinsic ellipticity of the source. Under the assumption that the intrinsic ellipticity is random, $\langle e_{\rm int}\rangle = 0$, the size reduces to $S_2 = \mu^{\frac{1}{2}} S_2^s$, as expected for an isotropic magnification. Of note here is the process by which this result is gained: the size measurement given by S_2 transforms as one would expect a length to, only under the assumption of the weak lensing limit, whilst S_1 is exact. Thus, the transformational properties of S_1 are simpler than that of S_2, however the construction of the size measure S_1 itself is non-linear and its use therefore comes with more complicated noise properties.

Similarly, one may also define two ellipticity measures as (Seitz & Schneider, 1995, 1997)

$$\chi = \frac{J_{11} - J_{22} + 2iJ_{12}}{J_{11} + J_{22}} \tag{5.8}$$

$$\epsilon = \frac{J_{11} - J_{22} + 2iJ_{12}}{J_{11} + J_{22} + 2[\det(J)]^{\frac{1}{2}}}. \tag{5.9}$$

In both cases, the denominator divides out the size measure and thus the isotropic magnification, whilst the numerator mimics the definition of the complex ellipticity, with $J_{11} - J_{22}$ the ellipticity along a given axis, and J_{12} along an axis at 45 degrees to this axis, justifying their interoperation in the transformation of S_2. Both definitions of the ellipticity transform according to (Seitz & Schneider, 1995, 1997)

$$\chi^s = \frac{\chi - 2g + g^2\chi^*}{1 + |g^2| - 2\mathcal{R}(g\chi^*)} \tag{5.10}$$

$$\epsilon^s = \begin{cases} \frac{\epsilon - g}{1 - g^*\epsilon} & |g| < 1 \\ \\ \frac{1 - g\epsilon^*}{\epsilon^* - g^*} & |g| > 1 \end{cases} \tag{5.11}$$

with inverse transformations given by replacing g with $-g$, and χ with χ^s or ϵ with ϵ^s respectively. In the weak lensing limit, these transformations reduce to

$$\epsilon \approx \epsilon^s + g \tag{5.12}$$

$$\chi \approx \chi^s + 2g - 2g|\chi^s|^2. \tag{5.13}$$

In both cases, it is noticeable that either transformation depends on the reduced shear

rather than the shear, such that it is only the reduced shear that is measurable. However, in the weak-lensing limit $g \approx \gamma$.

In the measurement methods of both KSB and RRG, the surface-brightness dependent weight function of Equation (5.1) is replaced with a position dependent weight $w(\theta)$ taken to be a Gaussian

$$W(\theta) = \frac{1}{2\pi w^2} e^{-\frac{\theta^2}{2w^2}} \tag{5.14}$$

with width (w) approximately that of the radius of the galaxy, usually set using external radius measures such as the half-light radius. Using this form for the weight function, the translations given above no longer hold, and KSB show that the act of shearing by foreground structure induces a shear on the ellipticity as

$$\epsilon_\alpha = \epsilon^s_\alpha + P^{\rm s}_{\alpha\beta}\gamma_\beta, \tag{5.15}$$

where the shear polarisability tensor, $P^{\rm s}$ is a product of the weighted moments, and determines the responsivity of the ellipticity measure to changes in the applied shear field[1]. KSB show that if the PSF can be modelled as a small anisotropic distortion convolved with a large, circularly symmetric Gaussian then the ellipticity can be corrected for the PSF as

$$\epsilon^{\rm cor}_\alpha = \epsilon^{\rm obs}_\alpha - P^{\rm Sm}_{\alpha\beta} p_\beta, \tag{5.16}$$

with $P^{\rm Sm}$ an isotropic 'smearing' of the image caused by the isotropic part of the PSF, and p a 'shearing' of the image caused by the anisotropic part of the PSF. Since the corrected stellar ellipticity must be zero, p can be determined from the measurement of stars as

$$p^*_\beta = [P^{*\rm Sm}]^{-1}_{\beta\alpha} \epsilon^{*\rm obs}_\alpha, \tag{5.17}$$

[1]In general, the shear responsivity accounts for the fact that a shear field acting on an image will induce an ellipticity which is dependent on the ellipticity of the source itself. This can be seen clearly with reference to the ellipticity as defined in Equation (5.10), which when expanded out without the assumption of small source ellipticity returns $\chi = \chi^s + 2g(1 - [\chi^s]^2)$. Under small source ellipticity, this reduces to the result given above, however in this form it is clear that the measured ellipticity is bounded from above: if the source ellipticity is close to one, then the measured ellipticity will be one, no matter how large and positive the shear field becomes. Thus, in this parameterisation, an object cannot become more elliptical than a straight line.

so that the PSF-corrected galaxy shear measurement is given as

$$\gamma_\beta = [P^{\rm s}]^{-1}_{\beta\alpha}[\epsilon^{\rm obs}_\alpha - P^{\rm Sm}_{\beta\alpha}[P^{*\rm Sm}]^{-1}_{\beta\alpha}\epsilon^{*\rm obs}_\alpha]. \tag{5.18}$$

Thus, an estimate of the shear on a galaxy can be determined from the PSF corrected ellipticity measure, where the PSF is measured from noisy quadrupole moments on non-saturated stellar images, and the shear polarisability P^s is measured on the non-PSF corrected galaxy image. Further, the PSF should be measured with the same weight function as the galaxy image, but in practice is measured using a weight function whose width is set to the seeing size.

With the PSF corrections above, KSB has been shown to be accurate to about 1%, on high signal-to-noise sources (Kitching et al., 2012), and is a computationally efficient method of obtaining the ellipticities of sources. Whilst the size can be calculated from quadrupole moments, and is indeed a direct by-product of the ellipticity measurement as the quadrupole-measured ellipticity is size-renormalised (Equation(5.8)), the application of the KSB method as described above allows no mechanism to correct the size measure for the PSF: the KSB method instead corrects the size-renormalised ellipticity. On the other hand, the methods presented in RRG correct for the PSF at the quadrupole level, ensuring that both ellipticities and sizes calculated from the PSF-corrected quadrupole moments using the RRG method will themselves be PSF-corrected.

In RRG the authors show that the second order brightness moments for a source with a PSF-convolved observed surface brightness profile

$$I'(\theta) = \int d^2\theta'\ p(\theta - \theta')I(\theta), \tag{5.19}$$

were p denotes the PSF across the image, can be corrected for a Gaussian, isotropic and an anisotropic PSF using

$$J^{\rm I}_{ij} = \left(\frac{g}{g_w}\right)(J'_{ij} - \delta_{ij}g^2); \quad J^{\rm a}_{ij} = J'_{ij} - C_{ijkl}(J)P_{kl}. \tag{5.20}$$

Here $J^{\rm I}$ and $J^{\rm a}$ is the isotropic- and anisotropic- PSF corrected moments respectively, P_{kl} is the unweighted second order moment of the PSF, which measures the anisotropic component of the PSF and can be calculated from stellar observations, $w_{\rm I}$ the width of the isotropic Gaussian PSF model, $g^2_w = (w^{-2}_{\rm I} + w^{-2})^{-1}$, and C_{ijkl} is the *convolution*

susceptibility tensor given as

$$C_{ijkl}(J) = \delta_{ik}\delta_{jl} - \frac{2}{w^2}J_{k[i}\delta_{j]l} + \frac{1}{2w^2}(J_{ijkl} - J_{ij}J_{kl}), \tag{5.21}$$

and where notation $A_{[i,j...k,l]} = 1/n! \sum_{\mathrm{perm\ i,j..k,l}} A_{i,j...k,l}$ labels the renormalised summation of all permutations of indices within brackets. The convolution susceptibility tensor requires the calculation of the fourth order moments, given as

$$Q_{ijkl} = \int d^2\theta\ \theta_i\theta_j\theta_k\theta_l w(\theta)I(\theta), \tag{5.22}$$

and renormalised as $J_{ijkl} = Q_{ijkl}/Q$ as before. Before the measured galaxy moments can be corrected for the PSF, the measured moments for the PSF itself must be corrected for the use of the weight function $w(\theta)$ as

$$P_{ij} = J^*_{ij} - \frac{1}{2w^2}(J^*_{ij}J^*_{kk} - J^*_{ijkk}), \tag{5.23}$$

with J^* the flux-renormalised brightness moment measured on stellar images.

Thus, the measured surface brightness moments can be corrected for the PSF in the following manner:

1. Separate a star and galaxy sample

2. Measure the PSF moments from the stellar images, correct for the weight function using 5.23, and fit a polynomial model for the 2nd and 4th order moments across the field to allow for interpolation across the image.

3. Measure the galaxy moments from the galaxy images and construct the convolution susceptibility tensor from these uncorrected moments, Equation 5.21

4. Correct the galaxy moments using the unweighted stellar moments measured in Step 1 and the convolution susceptibility tensor using the RHS of equation 5.20. Correct the galaxy moments for the isotropic PSF using LHS of equation 5.20.

The PSF- and weight-corrected size and ellipticity measurements can then be constructed in the usual way from the corrected galaxy quadrupole moments, however it must be noted that neither method corrects the measurement of the source size for the application of the weight function, which will typically cause an underestimation in the size of the source. Notably, both quadrupole-based measurements make the

assumption that the centroid of the image is known, or can be determined from first-order moments of the weighted intensity profile of the source. Errors in the determination of the centroid can lead to *centroid bias* (Bernstein & Jarvis, 2002; Kaiser, 2000).

I applied the above measurement methods to the STAGES field to produce size and ellipticity measurements for the STAGES galaxy sample. For KSB measurements, the correction for the PSF and the weighting function are applied only to the ellipticity measurements, whereas the RRG PSF correction corrects the quadrupole moments. As a result, quadrupole size measurements using the KSB method will not be corrected for the PSF or the choice of a weighting function. The PSF 2nd and 4th order moments is fitted using a polynomial fit across the field using stellar measurements, in groups according to time of observation. The grouping of HST tiles used for the PSF model is shown in Figure 5.1. The weight function is chosen to be a Gaussian, as given in equation 5.14, where the width w is taken to be the half-light radius of the sources surface brightness profile measured using SExtractor (Bertin & Arnouts, 1996). A flux signal-to-noise cut of $\sigma > 7$ is applied to the data to remove the noisiest galaxy images from the sample, where the flux and error on the flux were measured using SExtractor. RRG ellipticity measures are corrected using the signal-to-noise dependent responsivity correction of Leauthaud et al. (2007).

Figure 5.2 shows a comparison between the KSB and RRG measurements of galaxy size and ellipticity in the STAGES field. Quoted ellipticity measures are calculated using the χ estimator, given in equation 5.8. We see that the corrected KSB ellipticity and RRG ellipticity agree well, providing a good consistency check of the RRG PSF correction technique. However, galaxy size measurements using the RRG method are typically smaller than the KSB equivalent, with the difference between the two measures decreasing with increasing galaxy size. As the KSB size measurements are not corrected for either the PSF or weight function, this behaviour is expected: for smaller galaxies the effect of the PSF will be largest, causing an overestimation of the size using the KSB measurement. The difference due to the PSF correction may be expected to be largest for the "$\det(J)$" size estimator, as it contains a contribution from the J_{12} and J_{21} terms: this behaviour is observed in Figure 5.2.

Whilst the comparison of results presented here provides a good consistency check of the size measurement technique, a more comprehensive analysis would investigate the accuracy of the measured galaxy sizes using image simulations. For this thesis,

the comparison presented here is considered sufficient to indicate the accuracy of the technique, and the use of image simulations is deferred for future work.

5.3 Galaxy size and magnitude distributions in the STAGES and GEMS fields

To utilise the above formalism for the reconstruction of the lensing mass profile, it is important to understand the joint size-magnitude distribution of the underlying field. I therefore present here a summary of the size and magnitude distributions for the STAGES field, with an emphasis on how the measured distributions may be implemented into the above formalism. Since the size-magnitude distribution required for this analysis should describe the unlensed size and magnitude, one would wish to construct this distribution using a dataset taken over a blank field where the convergence is zero on average. In practice, I will construct this distribution from the STAGES data itself: the bias that would result from such a choice was considered in section 4.3.3 and I concluded that the effect would be smaller than statistical errors on the mass reconstruction of the STAGES clusters. Measurement of the galaxy size and magnitude distributions in the GEMS field provide independent verification of the results presented here for the STAGES dataset: whilst the analysis of the GEMS sample using the size measurement techniques described in section 5.2 is left for future work, I will utilise the size measurements from Galfit from the GEMS master catalogue to verify the use of the size-magnitude distribution constructed from the STAGES data in this analysis.

Results presented in this chapter are constructed using the public STAGES and GEMS catalogues. The former is supplemented by size measurements using the quadrupole measurement technique described in Section 5.2. Size measurements presented here use the size estimator given in equation 5.5. Unless otherwise stated, magnitudes taken from the public catalogues are measured in the HST F606W (v-band) filter, and are quoted in the AB system. As with the analysis presented in section 5.4, catalogues are clipped to exclude any galaxies with $m < 23$ to remove cluster contamination: these magnitude cut corresponds to a median redshift of $z \leq 0.6$ using the median-redshift-magnitude relation of Schrabback et al. (2007).

Because the STAGES data set will be used to construct the size-magnitude prior used in the analysis, we wish to understand the behaviour of the source sample as a

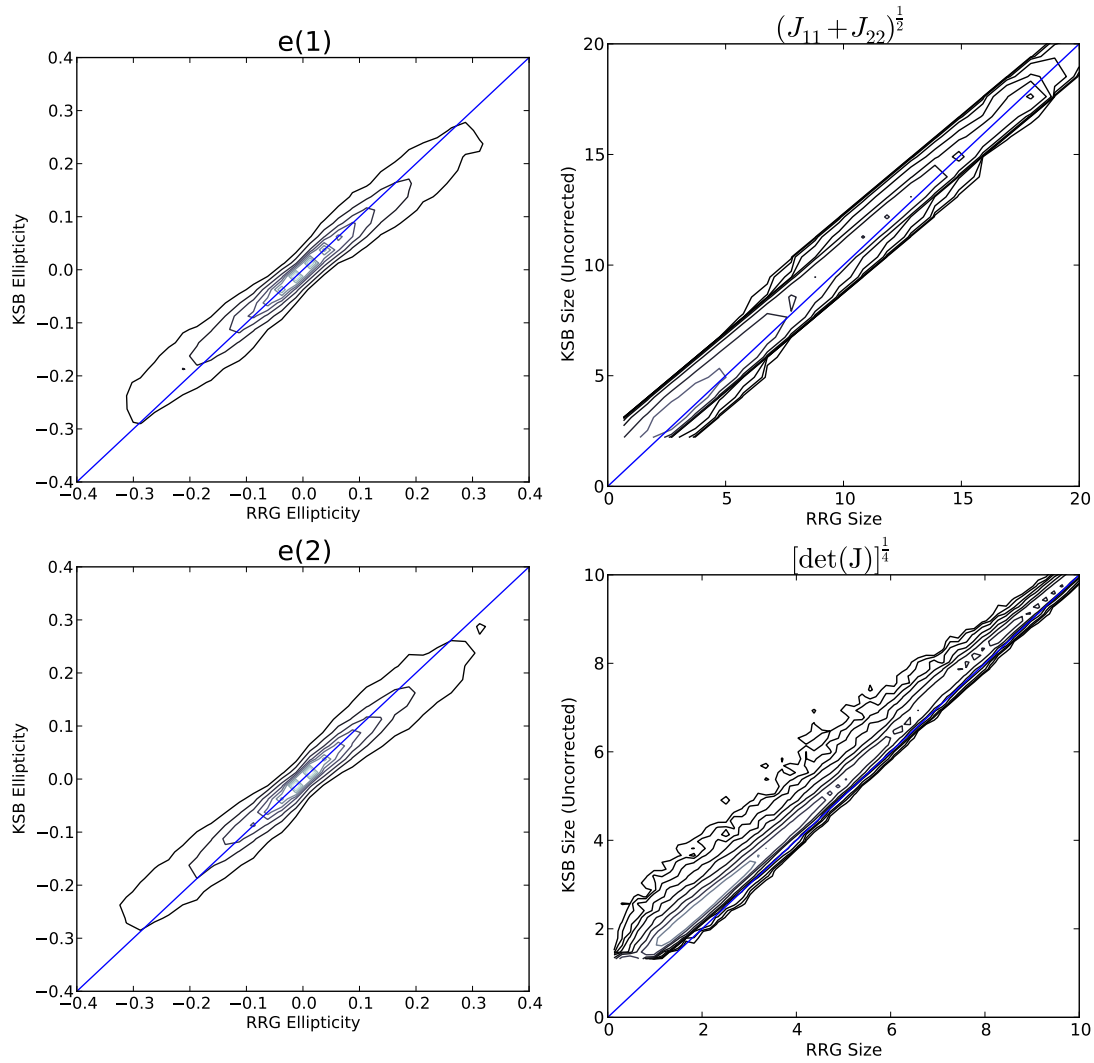

Figure 5.2: A number-density comparison of galaxy ellipticity (*left*) and size (*right*) measurements using the KSB and RRG methods on the STAGES field. KSB ellipticities have been corrected for the PSF (measured on stellar images) and weight function, however KSB size estimates have not. Both RRG ellipticities and size estimates are corrected for the PSF and weight function. Both size estimates are measured in pixels.

function of redshift. Figure 5.3 shows the magnitude (*bottom*) and log-pixel-size (*top*) distributions for STAGES sources with COMBO-17 redshift information, as a function of redshift bin. Bins were chosen such that approximately equal numbers of COMBO-17 sources lie in each bin. Right hand plots show the mean size or magnitude for each redshift bin. We see there is an overall decrease in the pixel size as with an increase in redshift, however this decrease is small in the redshift range of the COMBO subsample, with $\delta \ln(R) \sim 0.08$ at the points of largest difference. We also see that there is little variation in the width of the log-size distributions between redshift bins, with a typical r.m.s. variance in each bin of $\sigma_{\ln R} \sim 0.5$. This is in agreement with the measurement by Shen et al. (2003), who find $\sigma_{\ln R} \sim 0.5$ for the faintest galaxies in their sample, and less favourable[2] than the variance of $\sigma_{\ln R} = 0.2$ for the brightest galaxies in their sample, however the SDSS sample chosen is brighter than those considered here.

An equivalent plot for the GEMS COMBO-17 sample is shown in Figure 5.4, where the pixel size is the half-light radius measured using Galfit included in the public catalogue. The same trends are seen in the GEMS field as noted in the STAGES field, with an overall small decrease in the average size of the sample with increasing redshift. Similarly, there is no significant variation in the width of the log-size distribution with redshift, with typical r.m.s variance in each bin of $\sigma_{\ln R} \sim 0.7$. I note that the r.m.s. variance of log-sizes in the GEMS COMBO sample is larger than that of the STAGES sample, due to the presence of longer tails in the large log-size distributions of the GEMS sample. Whilst direct comparison between the STAGES and GEMS result is difficult due to the different size measurements used in either, this difference may be expected to result from the method by which the size in each case is obtained: in the RRG method of section 5.2, a maximum size is placed on the window function used in the determination of the surface brightness quadruple moments, removing the largest bodies from the sample. The RRG log-size distribution extends to a maximum size of close to 25 pixels, whilst the GEMS sample extends far beyond this, with some galaxy sizes in excess of 150 pixels. These galaxies are most likely outliers for whom the size measurement is least certain, and their removal is not expected to affect the results hereafter presented.

In the application of the mass reconstruction to the STAGES dataset, I enforce a bright magnitude cut of $m = 23$ to minimise cluster contamination where the galaxy redshift is not known. Figure 5.5 shows the size and magnitude distributions for the

[2]Using the estimator given in equation 2.79, one can see that the error on the convergence is proportional to the intrinsic variation in log-size for the source sample.

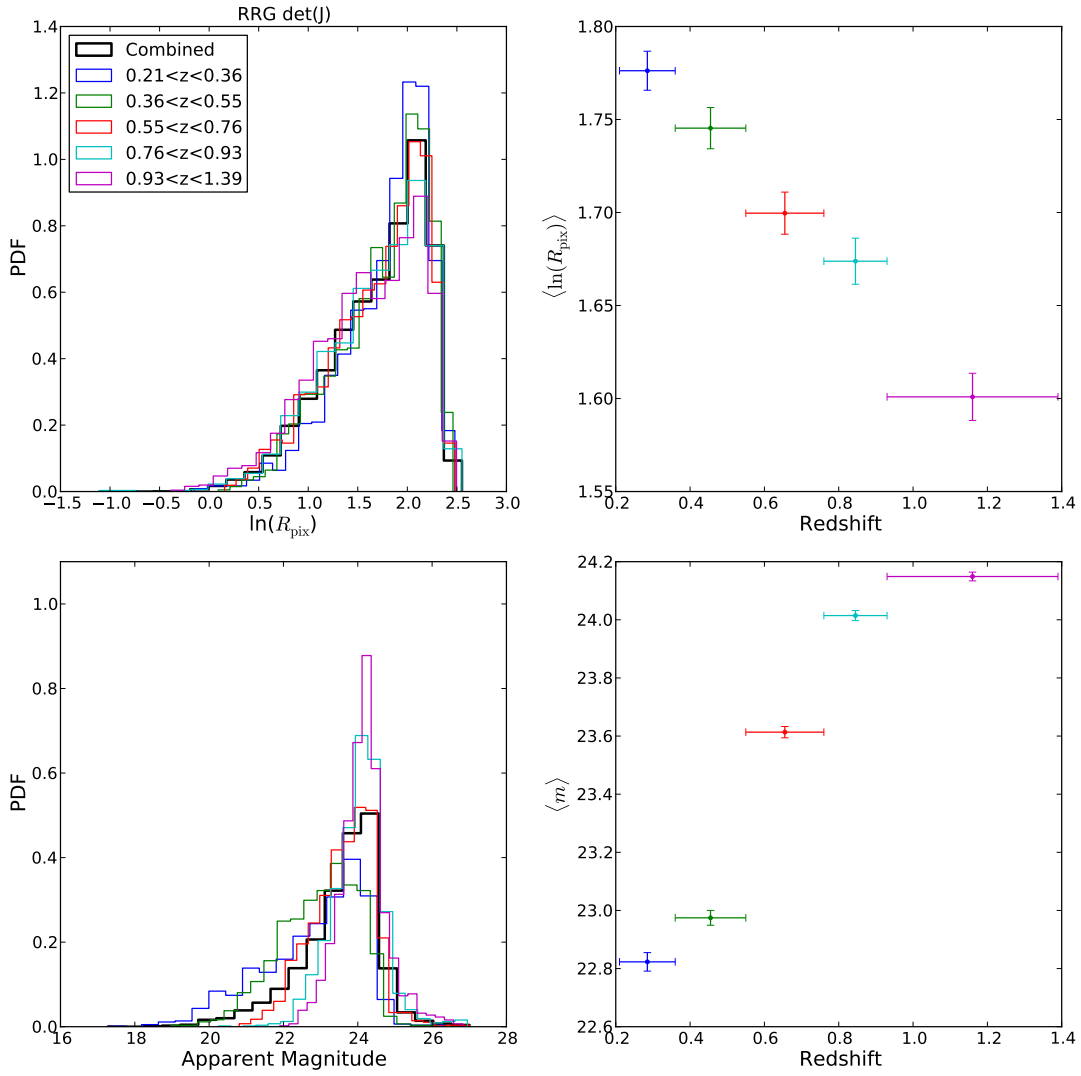

Figure 5.3: Pixel-size distribution (*top*) and apparent-magnitude distribution (*bottom*) for the STAGES source sample with COMBO-17 redshift information across five redshift bins, chosen so that each contains approximately equal number of galaxies in each bin. *Left* shows the distributions across redshift bins, whilst *right* plots the mean size and magnitude for each bin as a function of redshift. Error bars on x-values cover bin width, whilst y-errors show the error on the mean value for that bin. Pixel Size is measured using the RRG method described in Section 5.2, using the size estimate given in equation 5.4.

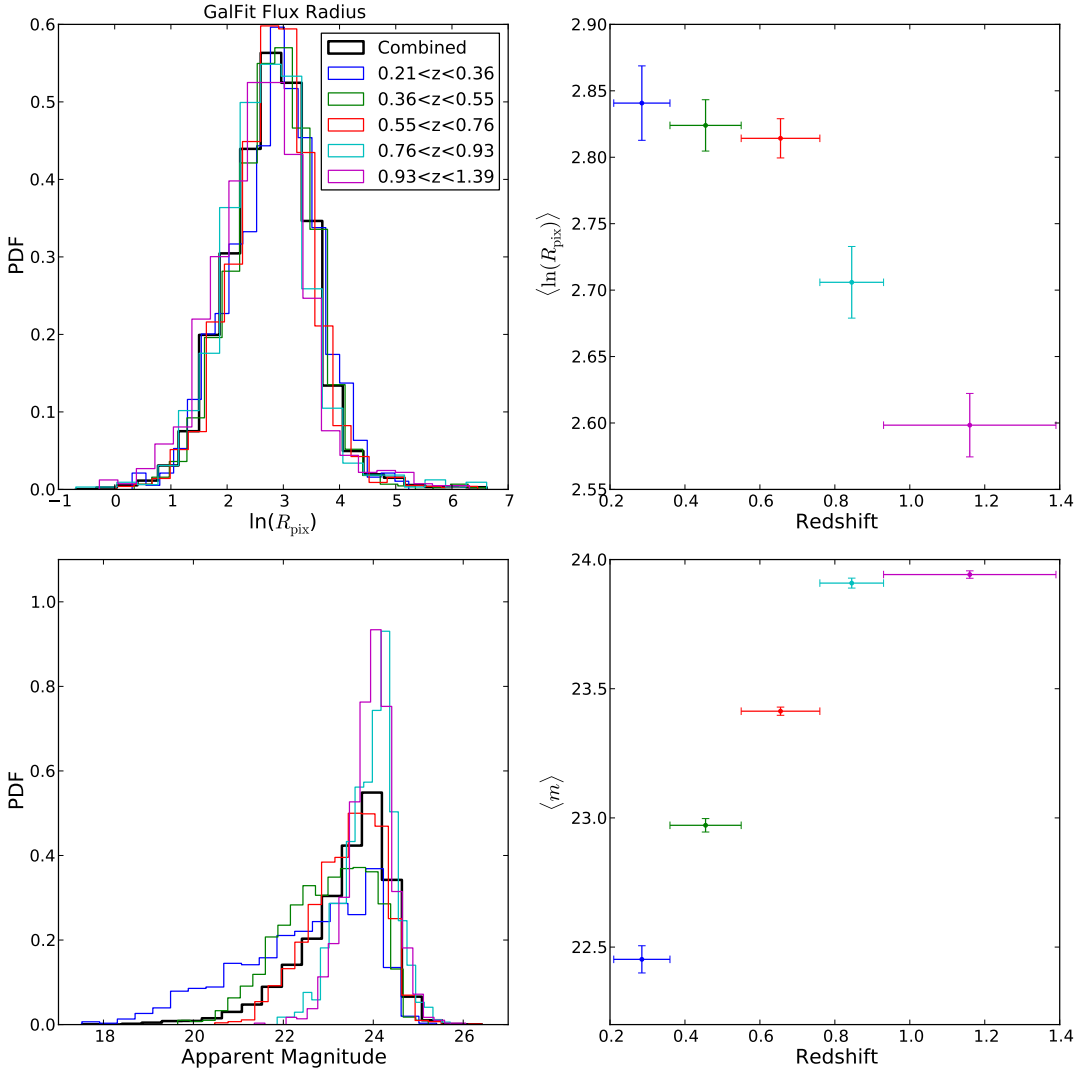

Figure 5.4: As Figure 5.3 for the GEMS field. Pixel Size is GalFit half-light radius.

COMBO sample when this bright cut is enforced. I note that the application of such a cut significantly reduces the number of galaxies in the sample from ~ 8800 to ~ 6500, as the sub-sample of STAGES sources with COMBO-17 redshift is limited to those with $R_{\rm Vega} < 24$. I note that as above, there is little variation in pixel size with redshift, and indeed smaller variation between the lower redshift bins. We see that the behaviour of the average size of the sample with redshift is different that the results presented in Figure 5.3 for the lower redshift bins. This results from the application of the bright magnitude cuts which predominantly removes the largest galaxies at lower redshift from the sample. As can be seen in the lower panel of Figure 5.5, the lower-redshift bins contain a larger fraction of brighter galaxies. In all cases the largest redshift bin might be expected to overestimate the average size of the sample, due to the faint limit of the survey which preferentially selects intrinsically brighter and larger, distant galaxies.

Based on these observations, I conclude that there is no evidence for evolution of the size distribution for the COMBO-17 data-set within the statistical noise of the analysis. I note that due to the independence of the width of the log-size distributions with redshift bin, subdividing the source sample by redshift will not improve the recovered mass profile of the foreground lensing cluster. This result suggests that knowledge of the redshift of the source is unimportant to the accuracy of the analysis, justifying the choice of analysing the larger STAGES sample at the expense of a larger posterior width for each individual galaxy which results from the need to marginalise over a postulated redshift distribution.

For both samples, a larger redshift dependence is observed for the mean magnitude for each sample, suggesting that the assumption of redshift-independence of the magnitude distribution in the size-magnitude prior distribution will be more misplaced than in the size distribution. The bias in the cluster profile reconstruction due to the assumption of redshift-independence of the prior when a magnitude-dependent redshift distribution was imposed on the mocks was investigated in section 4.3.3, and was shown to give a bias smaller than the statistical errors in the analysis. I therefore conclude that the simplifying assumption of redshift-independence should not significantly bias inferred parameter values for the lensing clusters in the STAGES field.

Using the absolute magnitude measurements of the COMBO subsample, I can measure the intrinsic size-luminosity relation of the sample of source galaxies. Figure

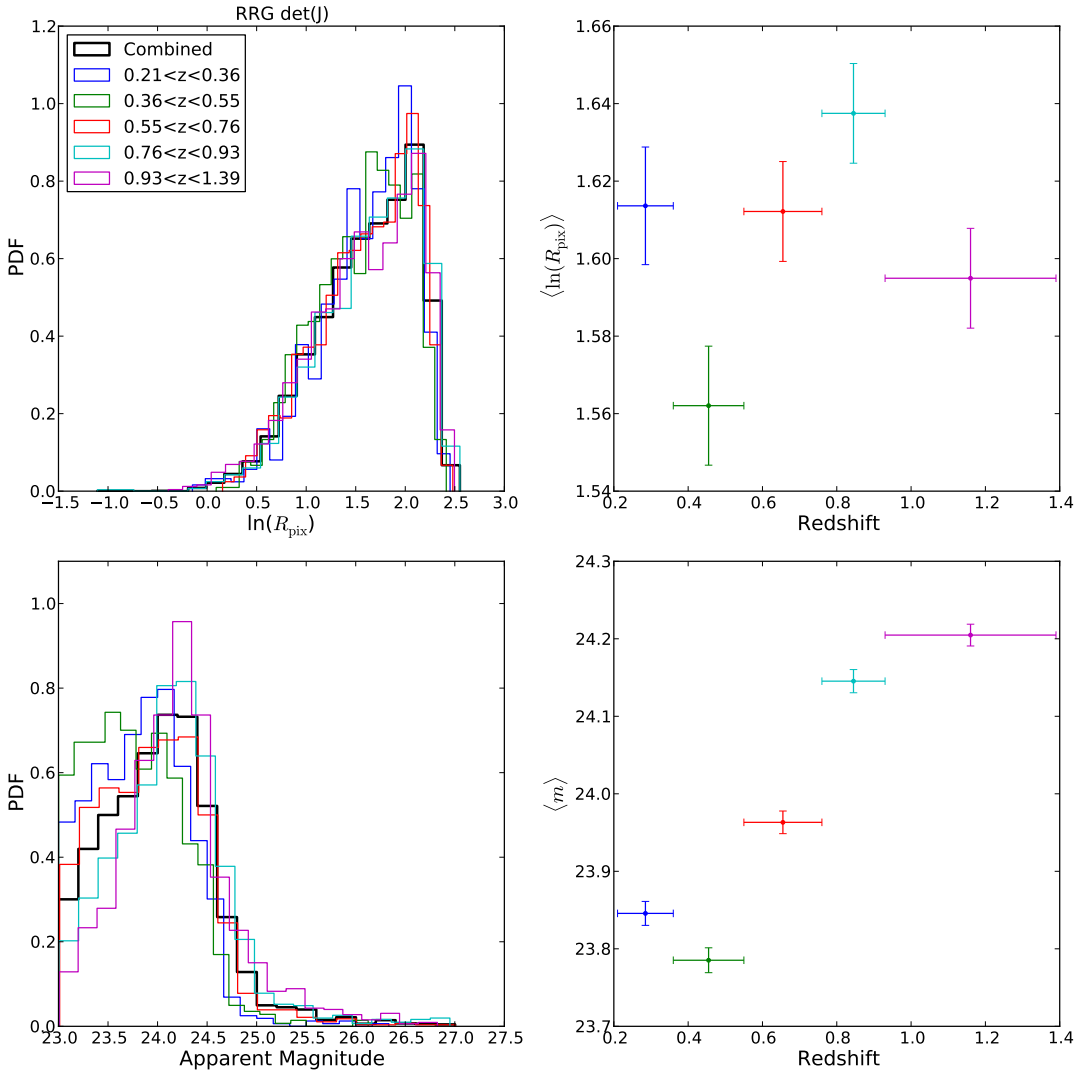

Figure 5.5: As Figure 5.3, with the implementation of a bright cut of $m \geq 23$, used to remove bright cluster galaxies.

5.6 shows the measurement of the exponent of the size-luminosity relation in the STAGES and GEMS fields. This measurement of β gives an indication of the possible bias on the recovered lens mass for a flux-selected sample, as detailed in section 2.3.3. However, the reader is encouraged to note that the correction for this bias is unnecessary in the method proposed in section 4.2, as the intrinsic size-luminosity relation is encoded into the intrinsic size-magnitude distribution that feeds into that method. This should be considered a particular strength of the method. Whilst the measurements of β are not required for the use of this method, I present them here for completeness. Using equation 2.88, these measurements suggest that a measurement of convergence which does not correct for the intrinsic size-luminosity relation may be expected to be biased low by $\sim 30\%$. We find a more favourable size-luminosity relation for convergence estimation with the COMBO-selected sample of galaxies in the STAGES and GEMS field over the measurements of Shen et al. (2003): this measurement of β is consistent with the faint late-type sample of Shen et al. (2003) who measure $\beta \sim 0.2$, but is noticeably smaller than their measurements on bright late-types or early-type galaxies ($\sim 0.5 - 0.6$ respectively). I reiterate that the SDSS samples used as part of the analysis of Shen et al. (2003) are brighter (and typically larger) than the samples used here.

Finally, I note that in Shen et al. (2003), the authors found a decrease in the width of the size distribution with increasing brightness of the sample, when split into absolute magnitude bins. In this case, a point-estimator analysis such as that discussed in section 2.3.3 would measure the convergence with smaller statistical errors in the brightest bin, suggesting that division of the sample by absolute magnitude may increase the signal–to–noise of the final result. In such a case, one may limit the analysis to only those galaxies with COMBO-17 information, and the correction of the measured convergence by the size-luminosity relation would be necessary to ensure an unbiased estimate of the convergence, however as can be seen in the errors on log-size in Figure 5.6, this is not seen in the sample considered here.

Figure 5.7 shows the joint size-magnitude distribution for the sources in the STAGES field, utilising the bright cut of $m = 23$ to be used in the analysis following. The distribution shows a weak size-magnitude dependence, with fainter galaxies found to be smaller. Figure 5.8 shows the marginal size-and magnitude- distributions for the STAGES source sample. Given the lack of redshift dependence in the size- and magnitude-distributions in the subsample of STAGES sources, these distributions form

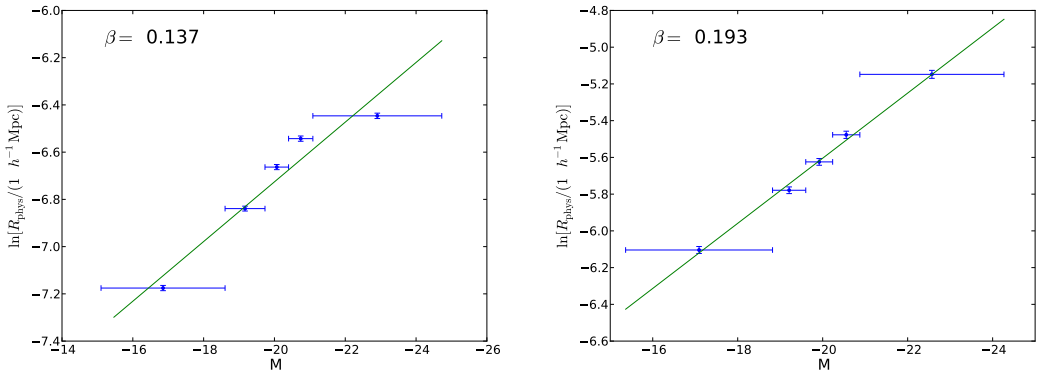

Figure 5.6: The inferred slope of the size-luminosity relation in the STAGES (*left*) and GEMS (*right*) source sample, where COMBO-17 information is available. The full source sample has been binned into absolute magnitude bins chosen to hold approximately equal numbers of galaxies in each bin. Plotted points show the mean log-size in each bins, horizontal bars span the bin width, and the error on log-size gives the error on the mean for each bin. No noticeable reduction in the width of the log-size distribution is evident in any of the magnitude bins.

the prior size-magnitude distribution used in the analysis of the cluster masses in the STAGES field in section 5.4. In doing so, I assume that the lack of redshift dependence in the measured source sizes and magnitudes continue to higher redshifts than the sources in the COMBO-17 subsamples, and that the change in the overall distribution due to the lensing of the STAGES clusters is small.

I note finally that the observed distribution in magnitude and log-sizes in Figure 5.7 show evidence of non-Guassianity, with a skew towards smaller sizes and a bright magnitude tail. Much of this non-Guassianity in the log-size distribution comes from the size cuts implemented as part of this analysis, and I note that this is not true for the Galfit sizes measured on the GEMS field, Figure 5.4. This suggests that the assumption of Gaussianity of the log-size-magnitude distribution as part of the analysis of Schmidt et al. (2012) to simplify the contraction of the maximum-likelihood point will not be accurate, and may introduce a bias in the recovered lensing mass. An advantage of the Bayesian method motivated in chapter 4 and implemented here-after lies in the fact that it does not require any simplifying assumptions on the form of the distribution, provided it can be accurately measured from data, as done in the remainder of this analysis.

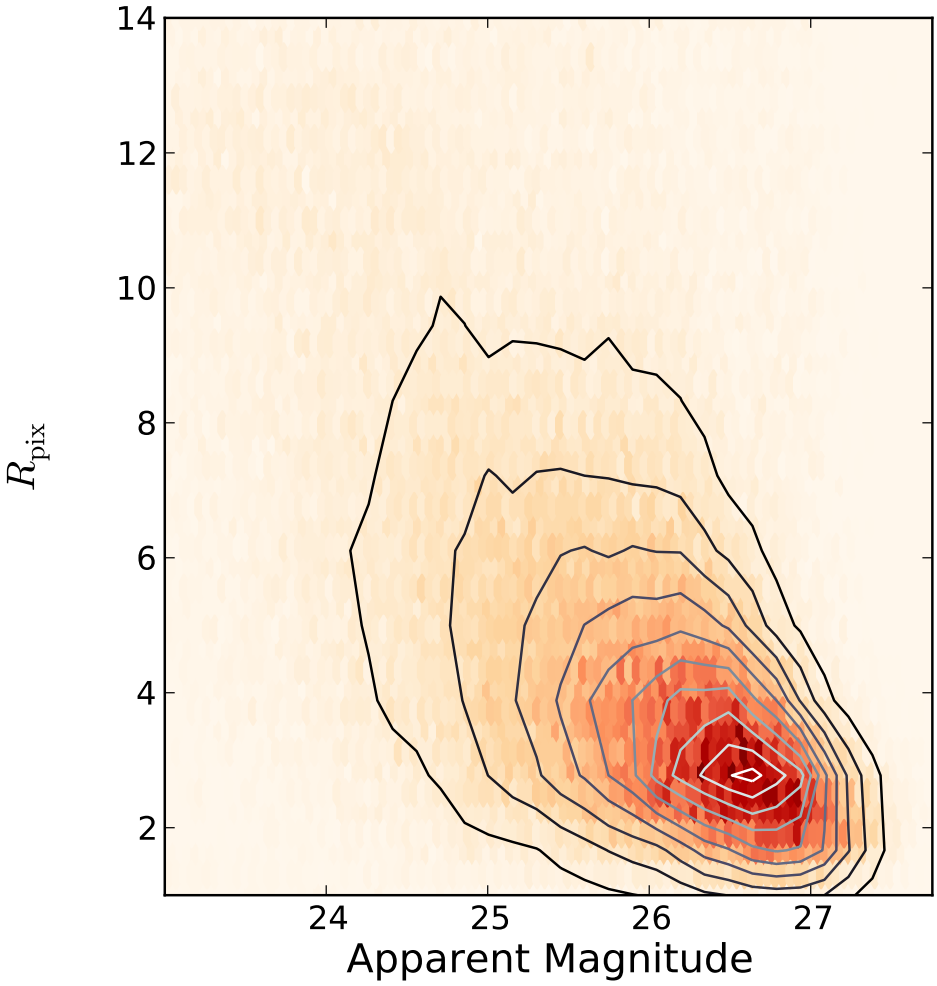

Figure 5.7: The pixel-size-apparent-magnitude distribution for galaxies in the STAGES catalogue. The colour of bins corresponds to the number density of sources in that are of size-magnitude parameter space, with darker, redder colours representing larger number of source galaxies in that bin. Cuts on the magnitude corresponding to $m > 23$ have been applied here to isolate the source sample and remove cluster contaminants. Pixel size is measured using the RRG method described in Section 5.2, using the size estimate given in equation 5.4. Pixel scale is $0.03''$.

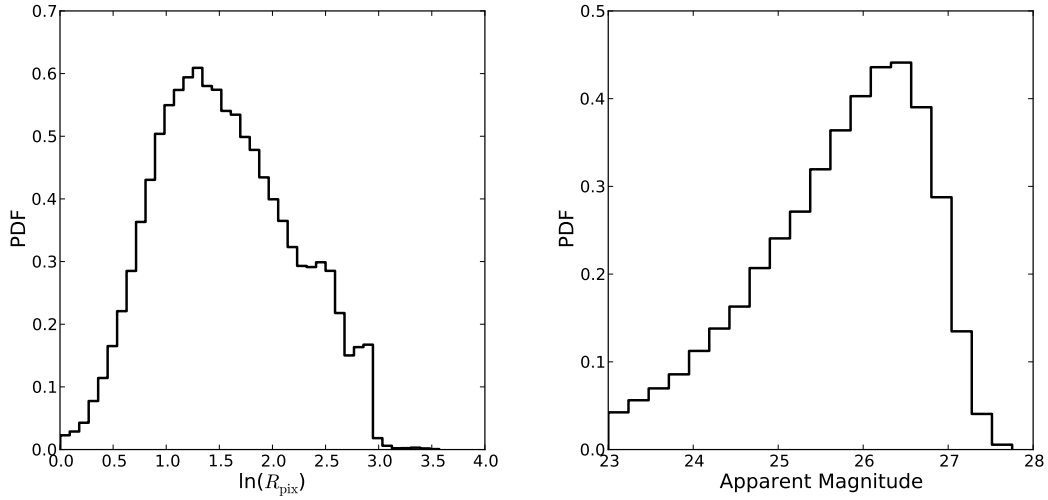

Figure 5.8: Marginal log-size (*left*) and apparent magnitude (*right*) distributions, corresponding to the joint size-magnitude distribution shown in Figure 5.7.

5.4 Mass reconstruction of the STAGES clusters

Previous weak lensing analyses of the A901/2 clusters by Gray et al. (2009) and Heymans et al. (2008) revealed three significant peaks in the mass distribution around the A901a, A901b and A902 clusters, and a low-significance peak around the south-west galaxy group (hereafter SW). Using COMBO-17 observations, Taylor et al. (2004) found a higher redshift cluster (CB1) which lies behind A902 at a redshift of $z = 0.46$. Heymans et al. (2008) found an extension of the dark matter distribution around A901a in the direction of the in-falling X-ray group A901α, and fit to this group separately.

In this section, I apply the method of mass reconstruction using galaxy sizes and magnitudes, detailed in section 4.2, to the public STAGES catalogue, with the aim of determining the precision of a size-magnitude mass reconstruction, its competitiveness to a traditional shear analysis as well as its strengths or weaknesses, and the prospects of increased statistical significance using a combined shear and magnification analysis in mass reconstruction. In section 5.4.1 I detail the method in which posteriors are constructed, including model determination, source selection, and the construction of the underlying size-magnitude distribution. Results are presented in section 5.4.2.

5.4.1 Method

Source Selection

A challenge with the use of the STAGES field lies in the separation of the foreground, and the isolation of the background sample. The presence of cluster members in the source sample can cause biases in the recovered mass profile constraints. As these galaxies are not lensed by the cluster, any individual galaxy posteriors for cluster members will not accurately represent the local magnification field. Moreover, weak lensing measurements such as shear or size suffer from systematics beyond those induced by observational limits imposed by the telescopes optics or seeing. The existence of astrophysical correlations between galaxy size and mass, due to physical processes in high density environments such as tidal stripping or galaxy formation processes, can cause a misinterpretation of the magnification for a source that lies close to the cluster or is a cluster member. Additionally, the clustering due to local environment, coupled with a positive size-density correlation could cause a misinterpretation of cluster members as magnified source. Such correlations are still subject of current research and remain open issues, with recent literature suggesting that the process shows a complicated dependence on galaxy type and mass. Lani et al. (2013) detects a positive size-density correlation between galaxy size and density in large quiescent galaxies between $1 < z < 2$ in the UKIDDS Ultra Deep Survey, with a weaker correlation for star-forming galaxies in the same range, and a weakening of the size-density relation to lower redshifts. Similarly, positive size-density correlations are observed in CANDELS cluster galaxies (Papovich et al., 2012) and massive early-type galaxies in DEEP2 and DEEP3 (Cooper et al., 2012). Maltby et al. (2010) conducted study using the cluster members of the STAGES field and field galaxies separated by redshift found a small anti-correlation between galaxy size and environment, with cluster galaxies typically $\sim 15\%$ smaller than field galaxies.

Further, intra-cluster light could cause inaccuracies in the source photometry and size estimation. If it is erroneously removed by background subtraction during data reduction, there would be a decrease in the measured flux and size of the source as the background is over subtracted in the region, raising the local magnitude zero-point. Extinction of sources, for example due to the dust content of cluster members, can cause a reduction in the observed flux of the source, causing the measurement of magnitude for sources which lie close to the cluster centre in projection to be fainter than the true source magnitude and leading to a possible low bias in the recovered

cluster mass. A possible solution lies through measuring the magnitude shift in multiple bands, since the magnification effect as achromatic whilst extinction is not. Moreover, the presence of a large, bright foreground can mask the background source sample, removing (preferentially fainter) sources close to the lens centre.

As a first step, for the subsample of galaxies with redshift information, any galaxies with a COMBO-17 redshift less than $z = 0.21$ are removed from the sample. For the remaining galaxies without redshift information, I select galaxies with $m_{\mathrm{F606W}} > 23$, corresponding to a median redshift of $z_{\mathrm{med}} > 0.6$ using equation 4.14. A small pixel-size cut of $\theta > 2.2$ pix, similar to the size limit used in Schmidt et al. (2012), is applied to the source sample used in the size-magnitude analysis to limit contamination by small galaxies most affected by the PSF and measurement noise.

Figure 5.9 shows the number density of catalogue objects around each cluster BCG, plotted against the global mean number density for that analysis, given as the number of sources in the sample after cuts divided by the survey area, accounting for masking. A902 shows an increase in the number density of sources towards the centre of the cluster, indicative of contamination of the source sample by cluster members. A901a shows a decrease in number density toward the cluster centre, indicative of foreground masking. The SW group shows an increase in number density towards small angular scales followed by a decrease. A901b shows an increase in number density over the global value on all scales, suggesting that cluster contamination for A901b persists to large angular scales, and potentially outwith the size of the aperture within which the source sample is selected. From this, I choose to mask an area around the cluster center, using an aperture of radius $1.5'$ around A901a, $1.5'$ around A901b, $0.5'$ around A902 and $0.9'$ around SW to remove cluster members from the sample. Since the source sample is chosen to be those galaxies within $2'$ of the cluster BCG, constraints on A901a and A901b are limited to a sample set within a $0.5'$ strip, and would be expected to significantly improve with the larger source sample that would result from increasing the aperture size in which the source sample is selected beyond $2'$.

A stricter core mask should improve the removal of cluster contaminants at the expense of statistical errors, potentially improving the accuracy of recovered posteriors. This in turn can be mitigated by the use of source galaxies to larger radii than that considered here, provided all clusters may be fit simultaneously to limit overlap bias. Moreover, as the cluster contamination persists to larger radii than the core masking area for A901b, it can be expected that the effects of cluster

contamination will persist for this cluster unless a much stricter core mask is applied. Thus, the potential benefits in increasing the sample selection aperture would be expected to be largest for A901b, where the most accurate constraints on the cluster mass may result only from the simultaneous fitting of sources far from the cluster centre.

In the case where the removal of the foreground is not possible through observations alone, I note that the effect of the foreground could potentially be minimised by weighting the source according to its radial distance. For example, in Velander, Kuijken & Schrabback (2010) close lens-source pairs are weighted according to their assigned lensing efficiency, taken as the mean for that source sampled from a expected redshift distribution. Such a weighting would reduce the contribution from sources expected to be radially close to the lens.

A more natural method to include the presence of un-lensed cluster members is the sample would be to edit the a-priori redshift distribution to include the presence of a fraction of cluster contaminants. The redshift distribution chosen in this application is expected to accurately represent the distribution of field galaxies, but does not account for the local over-density of galaxies at a certain angular position and redshift due the presence of a cluster at that position. In this case, a bias may result from the use of a redshift distribution which is not representative of the sample if cluster member are not adequately removed. The redshift distribution could be made to more accurately represent by the addition of a spike in the redshift distribution, centred on the mean redshift of the cluster members and with width representative of the uncertainty in the photometric redshifts at that redshift. Such a modification would only account for cluster contamination of this type provided the size-magnitude distribution for the cluster members is accurately described by that measured for the field sample, and provided any size- or magnitude-density correlations were small. If the former assumption does not hold, the a-priori size-magnitude distribution would need to account for whether the source is a field galaxy or a cluster member: since such a distinction is not possible in this case, such a situation could not be easily rectified. If the latter assumption did not hold, the method could be generalised to include a magnitude- or size-density correlation through a modification to the relationship between the observed and intrinsic sizes and magnitudes, given in equation 4.9 where the relation presented is assumed to be due to the magnification effect only. The use of such techniques may allow for the use of less stringent core cuts, consequently

minimising the statistical noise of the analysis, and the investigation of this is left to future work.

The resulting source catalogue used for the magnitude-only analysis consists of $74,421$ galaxies, corresponding to a number density of $\sim 90\mathrm{gal}/\mathrm{arcminute}^2$. With the subtraction of the core of each cluster, the source sample in each 2 arcminute aperture centred around the cluster BCG consists of 528 (A901a), 605 (A901b), 1118 (A902), and 871 (SW) galaxies. The size-cut source catalogue used for the joint size-magnitude analysis consists of $65,395$ galaxies, with a number density of $\sim 80\mathrm{gal}/\mathrm{arcminute}^2$. With core-cuts, the number of sources in each $2'$ aperture is 375 (A901a), 397 (A901b), 773 (A902), and 571 (SW).

Cluster Profile Model

To determine the mass profiles of the STAGES clusters, I follow the analysis of Heymans et al. (2008) (*hereafter CH08*) and fit an NFW profile (section 2.2.3) around each cluster centre. The centre of each cluster is set to be the brightest-central-galaxy (BCG) of each cluster, values for which are taken directly from the result of CH08. The NFW model is a two-parameter model, and is determined by the virial radius (or equivalently the viral mass) and concentration of the cluster. For this analysis, the concentration is related to the virial mass using fits to numerical simulations from Dolag et al. (2004) (equation 4.25). The concentration is therefore uniquely determined by the virial radius of the cluster, and the resulting NFW model has only the virial radius as a free parameter.

The magnification factor for each NFW halo is calculated according to equation 2.17, where the convergence and shear resulting from an NFW lens are calculated from the analytical results of Wright & Brainerd (1999), detailed in section 2.2.3. The convergence and shear are a function of both the lens redshift (through the redshift dependence of the NFW surface mass profile) and the source redshift. All four clusters are taken to have a redshift of $z = 0.165$. The STAGES catalogue is limited in accurate COMBO-17 redshift information, for only $\sim 10\%$ of the brightest galaxies in the sample. As a result, I have access to redshift information for a large fraction of the cluster galaxies, but no redshift information for the majority of source galaxies which were too faint to obtain COMBO-17 redshifts. Where the redshift is not known, the posterior is calculated by marginalising over a redshift distribution whose form is given by equation 3.33, where the median redshift is determined using the median-redshift-

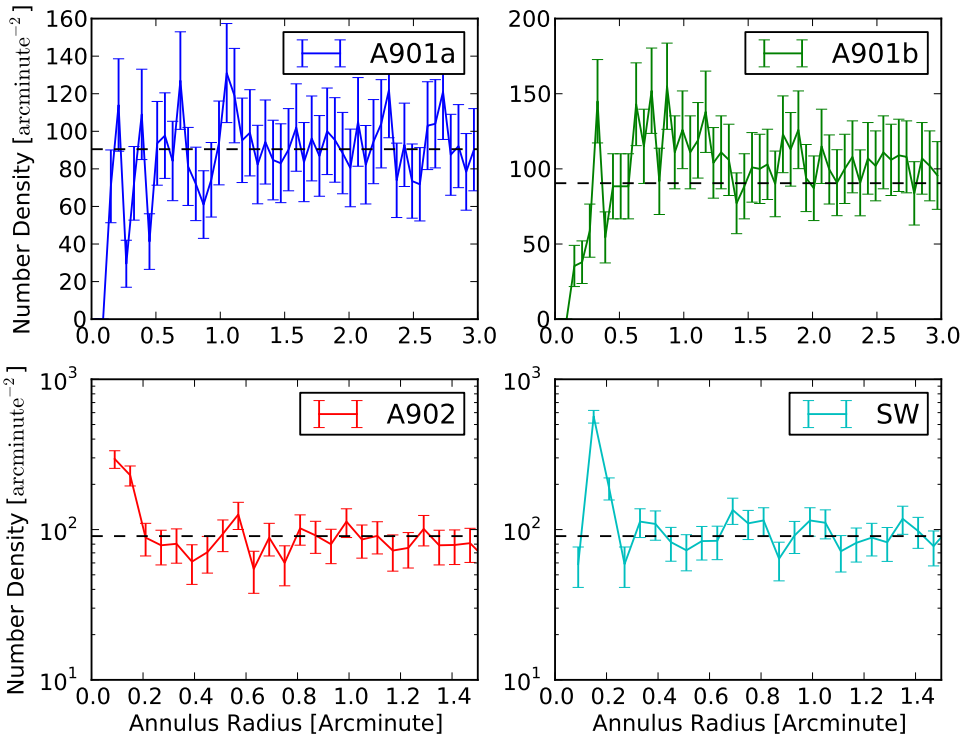

Figure 5.9: Number density of STAGES galaxies in annuli around the cluster BCG for the magnitude-only source catalogue. The equivalent plot for the size-magnitude analysis is indistinguishable and not shown. Galaxies have been selected to have $m_{\mathrm{F606W}} > 23$ and $z > 0.21$ where redshift information is available. Dashed lines show the global number density of galaxies in the source catalogue, after redshift, apparent magnitude and size (where applicable) cuts. The resulting catalogue contains $74,421$ galaxies respectively, over an unmasked survey area of ~ 822 square arc minutes. A901b shows evidence for an over density of sources on all scales considered, with a decrease at small scales consistent with masking. A902 and SW both show large increase at small scales due to cluster contamination. To emphasise small-scale behaviour, lower panels are shown for half the angular width of the upper panels, and use a log-scale on the ordinate axis to prevent large number densities at small scales washing detail on larger angular scales.

magnitude relation of Schrabback et al. (2007) (see Equation 4.14).

A single NFW profile is fit to each cluster, and constraints are obtained for each cluster individually: cluster overlap and substructure are therefore ignored in this analysis. To ensure the bias that results from ignoring cluster overlap is minimised, I restrict the source sample around each cluster centre to be only those sources that lie with a 2 arcminute aperture of the BCG. The bias in inferred parameter values that results from ignoring cluster overlap was investigated in section 4.3.3. A fuller analysis, which fits all four clusters simultaneously, would allow for the whole source sample to be used in the construction of each cluster profile, minimising bias and statistical error, and is left for future work.

In CH08 constraints were placed on the mass profile for the in falling X-ray group A901α and CB1 by simultaneously fitting an NFW to both as well as the larger A901a/b, A902 clusters and the SW group. Since both these mass distributions lie close to the larger A901a and A902 clusters, constraints cannot be placed on either without simultaneously fitting NFW profiles to these larger clusters. By fitting to A901a and A902 individually, this analysis will measure the combined magnification of these clusters and the A901α and CB1 peaks. Similarly, the dark matter reconstruction of CH08 found evidence for the existence of two halos, and an underestimation of the reduced shear close to the centre of the SW group with good agreement to a single halo model at larger radii. This suggests that fitting a single NFW profile is a poor approximation of the SW group close to the cluster centre, however the effect will be mitigated by the use of a core cut on the data, which will remove sources from the sample for which the effect is expected to be largest: core cuts are applied in the application to data to remove cluster contamination, and detailed in section 5.4.1.

Construction of the a-priori size-magnitude distribution

The application of the method detailed in section 4.2 requires accurate determination of the intrinsic size-magnitude distribution. In this analysis, I construct this distribution directly from the STAGES catalogue. The removal of cluster members in the construction of this distribution is similar to the process detailed in section 5.4.1, however I employ a more conservative mask of 2' around each cluster center to remove cluster contamination. Since the prior is constructed over the whole field, rather than in a small aperture around the cluster centre, the removal of a larger core around each cluster is expected to have only a small effect on the noise in the construction of the

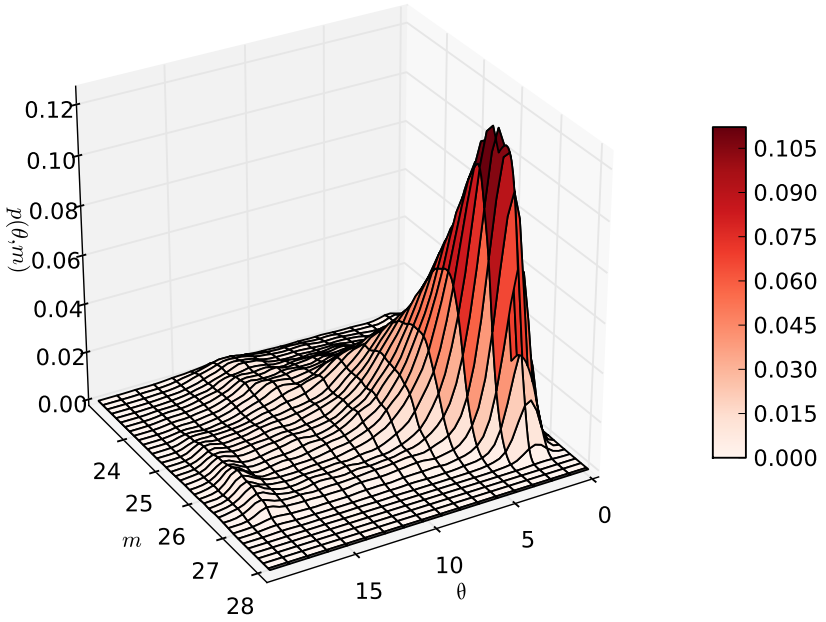

Figure 5.10: Pixel-size-apparent-magnitude distribution measured on the STAGES field, using source galaxies between $m = (23, 27.5)$, and with the removal of a 2' aperture centred on the BCG of each cluster to remove foreground contamination.

distribution. Since the STAGES field contains large matter over densities, it may be expected that the use of a size-magnitude distribution from this field will introduce a bias to the recovered mass profile constraints. The size of this bias was investigated in section 4.3.3, and found to be small for the size of clusters in the STAGES field. Further, the use of stricter cluster core subtraction, as used here, is expected to further reduce this bias.

The size-magnitude distribution is constructed using a kernel-density-estimate using a multivariate-Gaussian smoothing window function, whose covariance is 0.01 times the measured covariance of the data in size-magnitude parameter space. The resulting distribution is shown in Figure 5.10 .

5.4.2 Results

Using galaxy magnitude measurements only

Using the method of prior construction and source selection described above, I apply the method of NFW profile fitting for the four large over-densities on the STAGES field, using measurements of galaxy magnitude and size. Figure 5.11 shows the recovered posteriors on cluster virial radius using measurements of galaxy magnitude, taken directly from the STAGES catalogue. We see that for the A901a, A902 clusters and the SW group, the virial radius measured from galaxy magnitudes is consistent with the results of CH08 (shown here as vertical dotted lines), with no obvious significant bias.

The recovered posterior for the A901b cluster is consistent with no cluster[3] and is inconsistent with the measured virial radius from CH08. I suggest that the measurement of A901b is a clear anomaly, for which the measurement presented here suffers from systematic errors and contamination of the sample. With reference to Figure 5.9, we see that A901b shows an excess in the number density in annuli up to large angular separation, which persists in excess of the angular range considered in the plot. In producing both the magnitude-only and size-magnitude analyses presented here, a core subtraction of $1.5'$ was used for A902, which is noticeably smaller than the scales on which this excess is seen. This suggests that the subtraction of the foreground was not adequately done, and contamination of the source sample by cluster members persists.

Whilst section 5.4.1 shows that the contamination due to the presence of unlensed cluster galaxies in the sample gives only a small negative bias for A901b using this core masking, that analysis does not take into account intrinsic size-density correlations or errors in the measurement of galaxy size and magnitude due to cluster contamination. For example, A901b presents a crowded field, from which inaccurate magnitude or size measurements could result if images are not sufficiently de-blended as part of the application of SExtractor. Figure 5.12 shows X-ray images of the STAGES field, and shows the presence of a strong peak in X-ray emissions around the A901b cluster. If the presence of intra-cluster gas is correlated to intra-cluster light, galaxy size

[3]It should be noted that the posterior is constructed to a lower limit of $r_{200} = 0.05\mathrm{Mpc}/h$. Thus, for the A901b cluster we cannot rule out the possibility that the combined posterior will peak at or below $r_{200} = 0.$, consistent with no cluster. This application, however does place an upper limit on the cluster mass using the method, however contamination of the source sample may result in this limit not being a realistic representation of the true value.

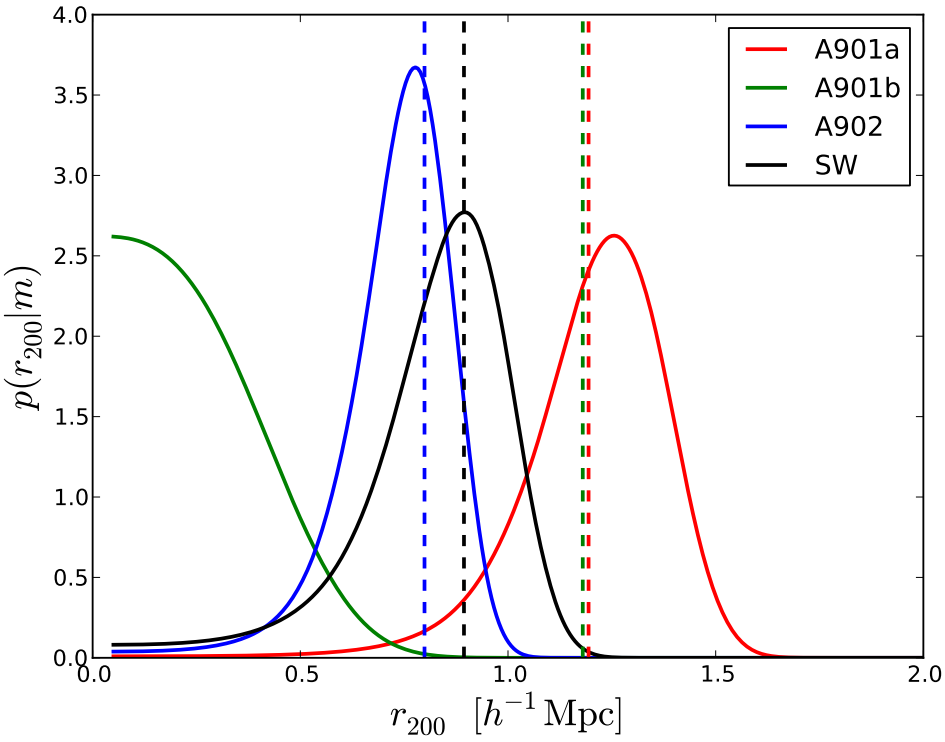

Figure 5.11: Recovered posteriors on NFW cluster virial radius for the A901a, A901b, A902 clusters and the south-west group, using measurements of source magnitude. The source sample was constructed as detailed in section 5.4.1, no cuts on galaxy size were used, and cluster core subtraction was applied. The dashed lines show results from a shear-only analysis (from CH08), where a single profile NFW profile was fit to each cluster.

and magnitude may be underestimated in the vicinity of A901b due to the necessary subtraction of the larger background, causing a low bias in the measurement of the magnification effect close to the cluster.

I note that the results of CH08 suggest that A901b shows an extended and non-circular mass distribution: as a result, the subtraction of sources within a circular aperture may not sufficiently remove the cluster members in the direction in which the light distribution is most extended, and a more sophisticated core subtraction routine which matches the subtraction region to the light distribution of the cluster may help to address this issue. Further, I note that the model fitting method used here fits a circularly symmetric NFW profile to the lensing clusters, and may be expected to be least accurate on extended distribution such as A901b, however the results presented for the shear case in CH08 also fit a circularly symmetric mass model, and thus one may expect that therefore the shear result would be similarly affected if this was an issue. The effects of cluster contamination in the A901b measurement could be mitigated by the use of more stringent core cuts at the expense of sample size. I reiterate that in this analysis the source sample was chosen within a $2'$ aperture around the cluster centre to minimise the effect of cluster overlap: this provides an upper limit on the size of the core subtraction region, however the simultaneous fitting of all clusters would mean that each profile could be constrained using the full field as the source sample. Thus, one might expect that a measurement of A901b may be possible in this case using more stringent core subtraction: this is left for future work.

The results presented here are summarised Figure 5.13, which shows a comparison between the measured virial radius using galaxy magnitudes and shear, where the latter results were taken from Table 1 of CH08. For the reasons discussed below I have opted to remove A901b from the comparison, and leave the comparison of results using galaxy size until further investigation into the accuracy of the size measurement has been undertaken. We see that the recovered posterior values from the magnitude-only analysis shows excellent agreement with shear measurements. Whilst the errors on the virial radius coming from the magnitude magnification are larger than those from the shear analysis, errors from the magnitude-magnification are comparable to the shear. These results are summarised in Table 5.1.

I note that the determination of the virial radius using shear measurements use the whole field as a sample, whilst for reasons discussed previously the magnification limits its sample to a small aperture centered on each cluster. Thus, one might

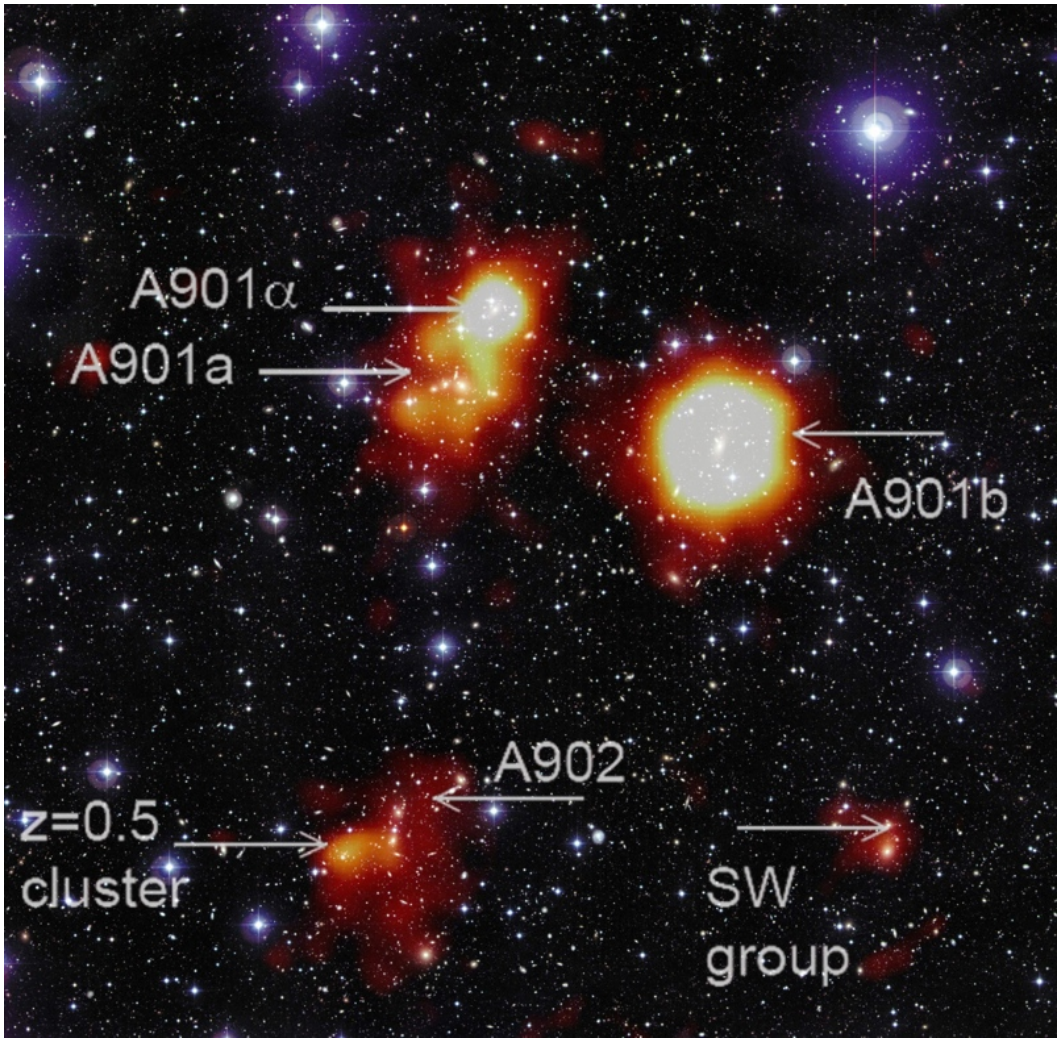

Figure 5.12: X-Ray imaging of the STAGES field, with the major STAGES structure labelled. Of particular note is the large region of X-ray emission close to A901b, indicative of a large quantity of hot X-ray gas in the vicinity of the cluster. Courtesy of Meghan Gray, (STAGES PI).

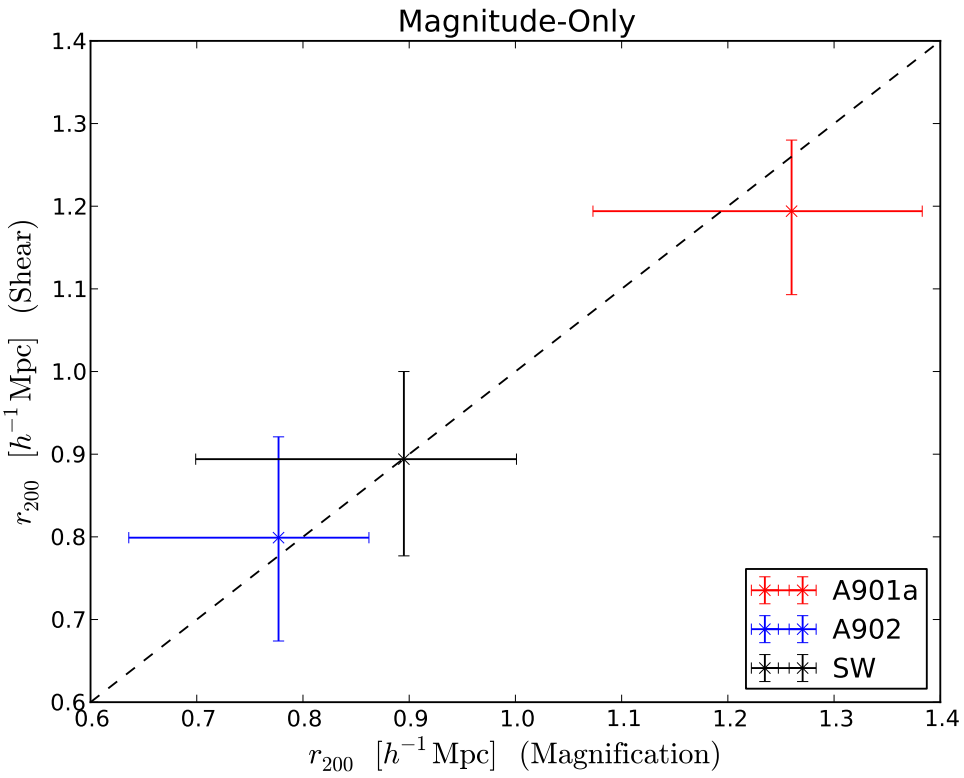

Figure 5.13: Comparison of the recovered cluster virial radius using the magnitude-only analysis against the one halo results of CH08. Magnification results correspond to the posteriors presented in Figure 5.11 with a hard flat prior on $r_{200} \geq 0$. Shear results are taken from Table 1 of CH08, correspond to the single halo fit for each cluster, and quoted errors are statistical errors only. The dashed line shows a one-to-one relation.

Table 5.1: Signal–to–noise for a magnitude-only measurement of the cluster virial radius, corresponding to the result shown in Figure 5.11.

Cluster	r_{200} $[h^{-1}\mathrm{Mpc}]$	Signal–to–noise
A901a	$1.26^{+0.12}_{-0.19}$	6.72
A902	$0.777^{+0.085}_{0.14}$	5.53
SW	$0.895^{+0.11}_{-0.2}$	4.56

expect a significant increase in the significance of the magnification detection with the simultaneous fitting of the clusters, which would allow the use of a much greater sample size, and the addition of a well-measured size-magnification component[4].

Further reduction in the statistical noise could be expected from the combination of shear and magnification measures, with potential self-calibration of the systematics inherent in either analysis. Figure 5.13 shows only statistical noise in either the shear or magnification measurement, however the systematic noise is quantified through the measurement of B-Modes in CH08. The measurement of systematics in an magnification analysis are harder to quantify, however the level of systematic in this analysis could potentially be quantified through the application of the method to a blank field such as GEMS.

A joint size-magnitude analysis

Figure 5.14 shows the equivalent posteriors using joint measurements of size and magnitude. Measurements using sizes and magnitude jointly are clearly more problematic than the magnitude-only analysis: in this case, the posteriors on A901a and A902 peak at values significantly lower than the shear measurements in CH08, with a significant tail to small virial radius values, whilst the posteriors on A901b and SW are consistent with zero. In each case, the shear measurements lie in the tails of the distributions, suggesting that they are disfavoured by this analysis. Further, the posteriors in the size-magnitude case are less constraining than the magnitude-only case, which is in part a result of the reduced number density due to the application of size cuts on the data. However, the shift in the maximum likelihood cluster mass for all clusters points to the presence of systematics in the size measurement.

There are a variety of potential contaminants that could account for this shift. A bias may be introduced if the lack of size evolution observed in the COMBO size distributions does not extend across the full redshift range of the STAGES sample. Most likely, the size measurement itself is biased by a signal–to–noise dependent measurement error (see for example Casaponsa et al. (2013) for an example using Lensfit) which will enter the method through the source sample and widening of the a-priori size-magnitude distribution. I note that the method applied in the measurement of cluster profile parameters presented here does not account for measurement error,

[4]Recall that Figure 4.1 predicts an increase of $\sim 33\%$ with the addition of size information where no size cuts are required.

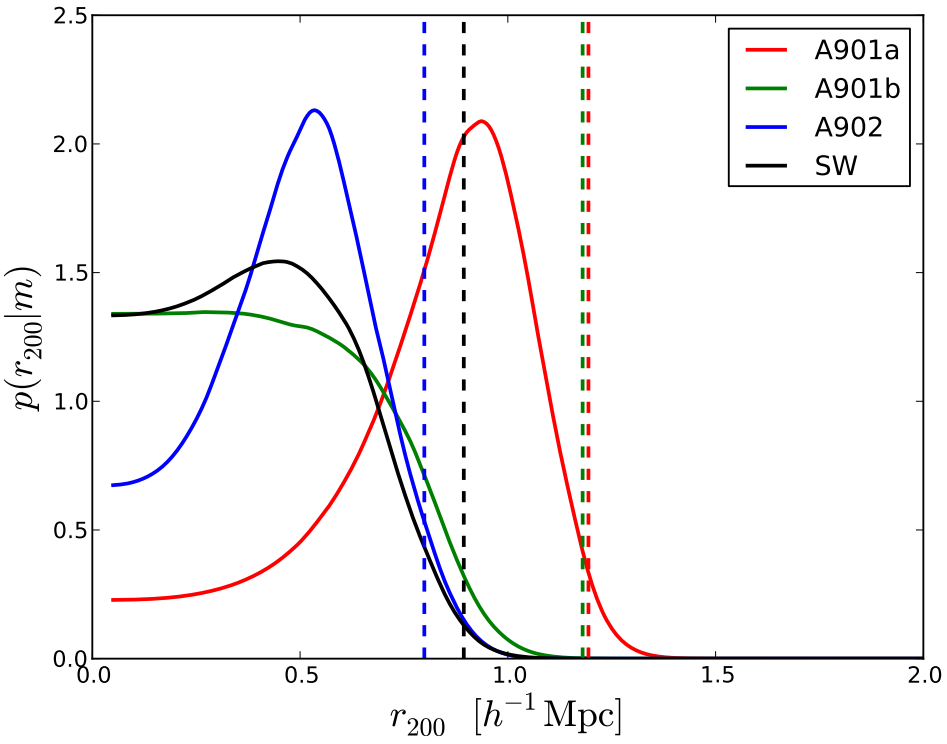

Figure 5.14: Recovered posteriors on NFW cluster virial radius for the A901a, A901b, A902 clusters and the south-west group, using measurements of source magnitude and size. The source sample was constructed as detailed in section 5.4.1, a lower cut of $\theta = 2.2$ was taken on galaxy size, and cluster core subtraction was applied. Dashed lines indicate best-fit virial radii from a shear analysis (from CH08), where a single NFW profile was fit whilst

however as noted in section 4.2 the method can be modified to accommodate a model of the size measurement error in the determination of the observed galaxy size. Such a model would require the measurement of the measurement noise as a function of galaxy size for the sample being considered, and as such would require the use of image simulations to quantify this for the size measurement method being used here. As such, a vital next step in the measurement of cluster model parameter values on the STAGES field using galaxy sizes would require a thorough investigation into the accuracy of the size measurement routine, beyond the consistency checks presented in section 5.2. Until this further work is completed, I consider the result including size measurement to be uncertain.

A further source of contamination is through contamination by the presence of the foreground cluster itself. I consider this source of contamination further in the next section, with the aim of understanding the size of its effect on a joint size-magnitude analysis of cluster mass.

The effect of cluster contamination on recovered posteriors using galaxy sizes and magnitudes

A potential source of bias in the reconstruction of a cluster mass profile is the contamination of the source sample by cluster members. This contamination can be split into two separate groups: the first considers physical contaminants, through systematic measurement errors in source size and magnitude due to physical effects within the cluster such as tidal stripping and intrinsic size- or magnitude- density correlations; the second considers the contamination of the signal that results from the inclusion of a subsection of the source sample that for whom the lensing is negligible due to the radial proximity of the source to the lensing cluster. In the latter, inaccuracies in the application of the method result from inaccuracies in the a-priori redshift and size-magnitude distributions, which are measured from a sample of field galaxies and are therefore not representative of the source sample contaminated by cluster members. I only consider this final contaminant in this section, and the investigation into the effect of physical contaminants such as those described in the first group is left to future work.

The posterior reconstruction method is applied to mock catalogues, where a single NFW cluster is modelled at the position of A901a. The construction of the mocks proceeds as in section 4.3.2, with an addition to the method: a separate catalogue,

containing mock cluster members is constructed before the output of 'unlensed' catalogues (point 4). This cluster catalogue is constructed according to the magnitude-only cluster contamination profile shown in Figure 5.9, where each annulus bin is assigned a number of cluster contaminants given by

$$N_{\rm Contaminant} = f n^{\rm mock}_{\rm global} \Omega - N^{\rm Poisson}_{\rm annulus}, \tag{5.24}$$

where $f = n_{\rm annulus}/n^{\rm data}_{\rm global}$ as measured from Figure 5.9, $n^{\rm mock}_{\rm global}$ is the global number density of sources in the un-contaminated mock catalogue, Ω labels the area of the annulus, $N^{\rm Poisson}_{\rm annulus}$ the number of sources in that annulus in the un-contaminated mock catalogue. Where $f \leq 0$, no cluster members are added to the catalogue. Thus, the cluster catalogue is constructed such that the contamination fraction of the mock is equal to that measured in the data where $f \geq 0$. The cluster members are randomly placed within the annulus, with a size and magnitude jointly randomly sampled from the reference data catalogue with $m \geq 23$ (to mimic the data cuts used in the construction of the contamination profile of Figure 5.9), and assigned a redshift of $z = 0.165$. This cluster catalogue is concatenated with the original source catalogue after the source catalogue has been lensed by a model NFW profile (point 5).

For each cluster considered, the cluster catalogue is constructed according to the measured contamination fraction profile for that cluster, given in Figure 5.9. Each cluster is modelled individually to avoid overlap bias, and a core aperture mask of $1.5'$ around A901a, $1.5'$ around A901b, $0.5'$ around A902 and $0.9'$ around SW is applied to mimic the application to data.

Figure 5.15 shows the average signal–to–noise and fractional bias on recovered virial radius using a joint size-magnitude analysis over 10 mock realisations using the above method of mock construction. In each case, the cluster is modelled individually to avoid overlap bias, and is positioned on the measured BCG of A901a. Cluster contaminants are added in annuli up to $3'$ from the centre of the cluster. Typically, A901a contains 140 contaminants ($\sim 7\%$ of total sources within $3'$), A901b contains ~ 300 ($\sim 16\%$), A902 ~ 60 ($\sim 3\%$) and SW ~ 80 ($\sim 4.5\%$) when core masking is not used. The top panel shows the fractional bias for each modelled cluster as a function of input cluster virial radius, where the fractional bias is defined as in section 4.3.3. We see that in the presence of cluster contaminants, there is no strong evidence for bias amongst all modelled clusters, with the possible exception of A901b which shows evidence of a small negative bias of a few percent, particularly at larger virial radius

where the statistical noise is smallest. The bottom panel shows the average signal–to–noise on the virial radius for each cluster, where A901a and A901b are modelled as clusters with $r_{200} = 1.2h^{-1}\mathrm{Mpc}$, and A902 and SW with $r_{200} = 0.8h^{-1}\mathrm{Mpc}$. Errors are the variance of the mean signal–to–noise across these realisations. The control sample takes 10 realisations where the catalogues are constructed without a contamination sample; as the core masking and choice of input virial radius for A901a and A901b are identical, the control signal–to–noise for these clusters are taken to be identical. The reduction in signal–to–noise in the A902 control sample over A901a and A901b is due to the reduction in the input virial radius (and consequently viral mass) of that cluster, and the further reduction in SW is a result of the stricter core masking used in that case. We see no evidence for a significant change in the signal–to–noise in any of the clusters when cluster contamination is added: the difference between the control and cluster contamination points for A901a can be explained by a slight high bias in the control run, combined with a slight low bias in the contaminated run, both within statistical uncertainties of the input virial radius.

Figure 5.15 indicates that the choice of core masking aperture applied to the data is sufficient to remove any bias caused by cluster contamination of the sort considered here, with only a small bias in A901b. Consequently, these results suggest that cluster contamination of the sort described above cannot account for the low recovered values for the joint size-magnitude analysis, and the A901b cluster in the application to the data. I note, however that these results consider a particular simplified form of cluster contamination, with the inclusion of a contaminant sample which has not been lensed, and does not account for intrinsic magnitude- or size-density correlations due to physical processes during galaxy formation, nor inaccurate size measurement due to photometric errors. Such contamination may be included in the method as described in chapter 4. The investigation of such effects are an important next step in the understanding of the results presented here.

5.5 Conclusions

In this chapter, I have applied the Bayesian posterior reconstruction method for mass profile model fitting, detailed in section 4.2, to the STAGES data-set. In doing so, I have detailed the construction of the a-priori size-magnitude distribution, measured on the STAGES field and assumed to be a sufficiently accurate description of the intrinsic

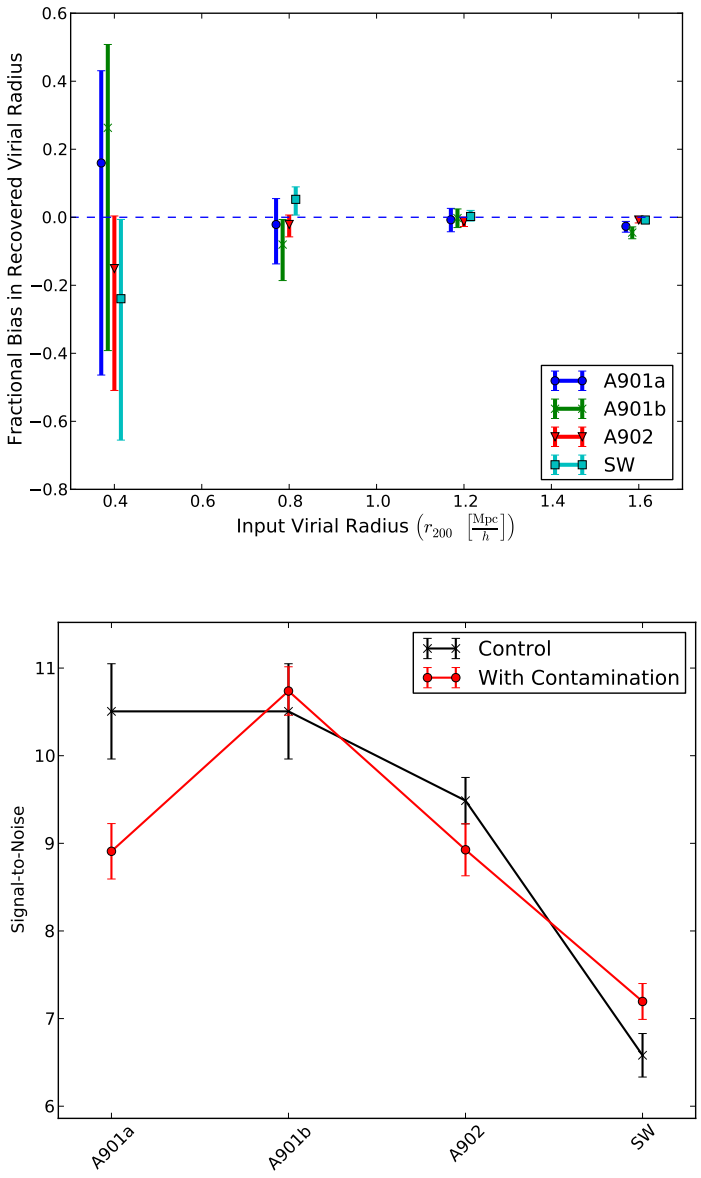

Figure 5.15: Figure showing the effect of a sample of cluster contaminants on the recovered posterior on the cluster virial radius. The *top* panel shows the fractional bias in virial radius for the contaminated catalogue as a function on modelled virial radius. Data points are slightly offset in the x-value to aid visualisation. The *bottom* panel shows average signal–to–noise for each cluster, where A901a and A901b are modelled using $r_{200} = 1.2h^{-1}\mathrm{Mpc}$, and A902 and SW using $r_{200} = 0.8h^{-1}\mathrm{Mpc}$. All values are calculated over 10 mock realisations of the catalogue, where each cluster is modelled individually to avoid overlap bias. The posterior is calculated for each cluster using the core masking for that cluster detailed in section 5.4.1, with number of contaminant clusters chosen to match the profile of Figure 5.9 where an over-density is observed.

size-magnitude distribution of the source samples. Sizes were measured using the PSF and weight function correction of Rhodes, Refregier & Groth (2000), and consistency checks against KSB measurements of the size and ellipticity were presented. I investigated the evolution of the size and magnitude distributions in the STAGES and GEMS data-sets, and justified the assumption of redshift-independence of the size-magnitude distribution which feeds into the posterior construction. I presented measurements of the variance of log-sizes and size-luminosity relation, required for a point-estimate measure of the convergence not considered here, and this was compared to literature.

Posteriors on the virial radius for the four main structures in the STAGES field (the clusters A901a, A901b, A902 and the South-West group) were produced using measurements of the galaxy magnitude, and a joint size-magnitude analysis.

The virial radius constraints from magnitude measurements only are consistent with the shear measurements for all structures considered, except the A901b cluster, and provide a detection of a non-zero virial radius to $\sim 7\sigma, 5.5\sigma$, and 4.5σ in A901a, A902 and SW respectively. The statistical noise in each measurement is larger, but comparable to those taken from Heymans et al. (2008). Measurements using galaxy sizes did not provide lower limits on the cluster virial radius, and seemed to be inconsistent with the shear only results of CH08. As these measurements were in disagreement with the magnitude-only magnification results and the shear results of CH08, I conclude that this is indicative of insufficient removal of size contaminants or systematics in the size measurements. Such contaminants may include

1. Contamination of the source sample by un-lensed cluster members
2. Errors in size determination due to photometric errors resulting from intra-cluster light
3. Intrinsic size-density correlations which are unaccounted for in the analysis
4. Inaccurate assumptions about trends in the evolution of galaxy size with redshift for the source sample.
5. Systematics in the application of the size measurement routine

Of these, point 5 is the most likely source of contamination, therefore the investigation into the accuracy of the size measurement method using image simulations, beyond the consistency checks presented, is of vital importance as part of this

investigation. Such an investigation can also determine the measurement noise in the application of the measurement method used here, which can be naturally folded into this analysis. Further investigation into the remaining points is worthwhile: I note that points 2 and 3 should be mitigated with the use of sufficient core masking, and Points 3 and can be naturally integrated into the analysis given accurate models (as discussed in chapter 4). Point 1 was considered in section 5.4.2 and I found that the bias from such contamination was small for the contamination profiles measured as part of the analysis (Figure 5.9) , and therefore could not account for low recovered cluster mass from the joint size-magnitude analysis.

In both measurements the A901b cluster is not well recovered, and is inconsistent with the measurement from shear taken in CH08. I conclude that this results from systematics in the photometry which results from intra-cluster light or insufficient deblending of the sources close to the cluster. I note that for A901b we see an excess in number density of sources with persists to scales larger than the applied core mask, and indeed larger than the size of aperture in which the source sample was selected, and X-Ray images show extended emission around this cluster. The mass reconstruction of CH08 indicates that the A901b cluster is particularly elongated, suggesting that the subtraction of sources within a circular aperture may not sufficiently remove cluster members in the direction of elongation and the fit of a circular NFW profile will be least accurate for this cluster. The analysis of A901b could potentially be improved by the use of a core subtraction region which matches the shape of the light distribution of the cluster, and the use of a larger core subtraction region. As noted previously, the use of simultaneous fitting may allow the use of sources further from the cluster centre which are less likely to be affected by some of the issues discussed above.

The measurement of virial radii using galaxy magnitudes that are consistent and comparable with shear results is promising, and it is expected that a reduction of the statistical errors in the magnification analysis will result from the inclusion of an accurate size-magnification measurement. Whilst the accurate measurement of galaxy size is difficult for ground-based surveys with larger PSF (Casaponsa et al., 2013), the use of magnitude-magnification contains valuable information on the local magnification field. Thus, I conclude that the use of magnification measurements show promise as a means of mass determination in comparison to shear measurements. Further, they may be an excellent complement to shear measurements as the combination of shear and magnification measurements can be expected to reduce

statistical noise further, provide a means of internal calibration of each method's systematics, and will naturally break the mass-sheet degeneracy.

Chapter 6

Conclusions

The aim of this thesis was to lead an investigation into the use of the oft-neglected magnification signal, as a competitive or complementary probe to the more traditional cosmic shear analysis. The magnification effect causes two effects on observations of distant lensed bodies. The first is an isotropic expansion of the image due to the tidal bending of light by foreground matter, causing an increase or decrease in size due to a foreground over- or under-density respectively, and is a counterpoint to the change in measured ellipticity of a lensed source by the shearing of images. As gravitational lensing conserves surface brightness (a consequence of Liouville's theorem), this change in source size corresponds to a change in the observed flux of the source, with an amplification or de-amplification behind foreground over- and under-densities.

From both these effects, one can construct a number of ways to measure the magnification effect through observations taken as part of existing surveys. One of these is the measurement of changes in the statistics of a size distribution of sources directly. As with the measurement of ellipticities, such an analysis requires techniques to accurately measure galaxy size from images in the presence of observational systematics such as the telescope optics or atmospheric seeing. However, the gains of such an analysis are potentially significant in lifting degeneracies in combination with an existing shear measurement (Heavens, Alsing & Jaffe, 2013; Eifler et al., 2013), particularly using space-based observations with small PSF where the size can be accurately measured (Casaponsa et al., 2013). In a similar vein, one may use the change in statistics of the source magnitude distribution to probe the magnification field through the source (de-)amplification effect. Such a measurement is likely to

be sensitive to extinction by a dusty foreground, which can be circumvented through multiple-band measurements of the statistics of the source magnitude distribution (Ménard et al., 2010). A further means of measuring the magnification field is through number count fluctuations, frequently termed "magnification bias". Such a measurement uses the fact that the observed number counts of sources is affected by magnification of a foreground through its change in position, and change in flux which may bring a body of sources into or out of flux limits of the survey. As with the other measurement methods mentioned here, such a measurement requires data already obtained as part of standard clustering and lensing analyses, and thus represents an untapped source of information which can be used with little further expense.

In chapter 3, I presented the results of an investigation into the use of number counts using photometric redshifts, as a means of constraining cosmological parameters. The motivation for this work was to investigate the information contained in this data, and evaluate its use as a cosmological probe as an individual analysis and in combination with source ellipticity measurements, and to guide the application to data in order to obtain the best cosmological constraints from large-scale redshift surveys. To do so, I presented theoretical models for three separate lensing observables which could be constructed from correlations between number density and ellipticity: namely photometric clustering, cosmic shear and galaxy-galaxy lensing (GGL) power spectra, the projected Fourier-space correlations between number counts, ellipticities and between number counts and ellipticities respectively. Both the clustering and galaxy-galaxy lensing terms contained contributions due to the number count fluctuations caused by the magnification of the source sample by the foreground large-scale structure. Each term was constructed using sources binned in tomographic redshift bins, and photometric redshift errors were modelled for each bin.

The strength of the magnification contribution to the clustering and GGL signals could be set through the parameter α, whose interpretation is the slope of the number counts at the faint magnitude limit of the survey. The value of α was measured across six redshift bins, and using source samples split into late- and early-type galaxies by SED value, using public CFHTLenS catalogues. Using a signal-to–noise estimator for the flux magnification contribution to the clustering signal, I concluded that the best strategy to maximise the magnification signal was to consider the source sample down to the faint limit of the survey. Selecting the sources in this way did not maximise the value of α, but provided improved signal–to–noise over brighter magnitude cuts due to

decreased statistical noise from the increased source sample size. I found that although the behaviour of α with limiting apparent magnitude varied between redshift bins, the value of α at the faint limit of the survey did not vary appreciably at the faint magnitude limit of the CFHTLenS dataset. The data suggested that a magnification analysis using number counts fluctuations in CFHTLenS should use the whole dataset of the survey to maximise signal–to–noise, and would measure a value of $\alpha \sim 0.7$ which did not change with redshift. These measurements were used to justify the choice of α in the succeeding analysis.

Using a Fisher matrix analysis, I found that the cosmological parameter constraints from a photometric clustering analysis were not competitive to cosmic shear measurements for the majority of cosmological parameters considered. However, I found that the combination of clustering with shear serves to lift parameter degeneracies from each individual probe, and results in significant improvements over the shear-only parameter constraints. The further addition of the GGL signal give even more significant improvement. These results are summarised in Table 3.2, however the most important results for a Stage-IV space based survey are as follows: the addition of a photometric clustering signal, using correlations between all redshift bins, to a shear analysis gives an improvement to a dark-energy figure-of-merit (defined as inversely proportional to the area contained in an ellipse covering a 68% confidence interval in w, Ω_Λ parameter space) by a factor of ~ 1.5; the combination of a shear and GGL signal gives an improvement by a factor of ~ 2; and the full combination of clustering, GGL and shear a factor of ~ 3.6 when all redshift bin correlations are considered, and ~ 2.81 when only auto-correlations of the clustering signal are considered. In all of these results, the galaxy bias is unknown and allowed to vary independently across all redshift bins. When the galaxy bias is well-known the improvement over shear-only for the full combined analysis increases to a factor of ~ 12: thus, whilst though we see significant improvement through the combination of probes even when the galaxy bias must be simultaneously constrained using the data, knowledge of the galaxy bias could offer more significant improvement to cosmological constraints.

As stated, both the clustering and GGL signals contain a contribution from the magnification, through the fluctuation in number counts due to lensing by the large-scale-structure. Further to the information gain from the combination of probes, I investigated the dependance of each analysis on the magnification contribution, specifically with respect to the accuracy to which α must be determined to ensure

a precise and accurate result. I found that the precision[1] of photometric clustering analysis showed a strong dependence on the strength of the magnification signal when all redshift bins correlations were included, but only a very weak dependence when only auto-correlations in redshift were considered. This is to be expected as the magnification contribution to the clustering signal becomes dominant to the intrinsic clustering for a widely separated foreground and background sample. When all probes were combined, I found that the precision of the result varied by $\sim 1\%$ when α was set by the CFHTLenS measurement to the case where the magnification signal was artificially set to zero. This is because both the clustering and GGL signals are significantly less constraining than the cosmic shear only case, and improvements in parameter constraints from the combination of these probes comes primarily from parameter degeneracy lifting. I therefore conclude that the precision of a combined analysis is only weakly dependent on the flux magnification contribution.

By investigating the shift in maximum-likelihood point with variations on the modelled magnification strength, I found that the accuracy of the full combined analysis was strongly dependent on the value of α. This effect was worst when either the GGL signal, or clustering with all redshift bins were included as part of an analysis. By contrast, biases in model parameters were subdominant to statistical uncertainty in those parameters in the case where the clustering auto-correlations were combined with the cosmic shear. I found that the combination of all probes required knowledge of α to an uncertainty of $\lesssim 10\%$ for a Stage-III ground-based survey (such as CFHTLenS) and $\lesssim 3\%$ for a Stage-IV space-based survey (such as Euclid) to ensure accuracy of recovered parameter values. I therefore conclude that, although the precision of results is only weakly dependent on the magnification signal, the magnification contribution must be accurately measured and modelled when fitting a cosmology-dependent model to the data to ensure the accuracy of the result.

In conclusion, I find that the addition of number density information to existing ellipticity measurements for a large-scale photometric galaxy redshift survey, through the inclusion of clustering and galaxy-galaxy lensing signals, gives substantial improvement to cosmological parameter constraints. The biggest gains are made by including all the clustering information rather than isolating only the intrinsic clustering (through auto correlations) or magnification (widely separated redshift bins) signals, due to the decrease in statistical uncertainty that results from the increase in

[1]The statistical uncertainty on model parameters.

source number density through the inclusion of all redshift bins. Such improvement in the precision of the result comes with the increased complexity of the analysis, as the magnification signal must be precisely measured and modelled to ensure the accuracy of inferred parameter values. For example, I noted that a ground based survey such as CFHTLenS must know α to $\lesssim 10\%$ to ensure unbiased results. As I measured α at the faint limit of the CFHTLenS data with a statistical uncertainty of $\sim 1\%$, one may conclude that such a combined analysis could accurately recover cosmological parameter constraints with CFHTLenS. One must be aware, however, that the accurate determination of α depends on more than just the statistical uncertainty inherent in the dataset, but may also be affected by observational effects such as sample incompleteness, local variations in survey depth and dust extinction (covered in more detail in section 3.5).

The importance of these results lies in their ability to guide the application to data. In particular, with the wealth of data from forthcoming large-scale surveys, one is motivated to utilise to its full extent the complete range of data available to each survey. Doing so not only reduces the inherent statistical uncertainty of the measurement, but also provides a means of internally self-calibrating systematics between probes. From this, one can hope to infer knowledge of the Universe to the highest level of precision and accuracy, validating current theories or pointing to new, interesting physics.

From the results presented in this thesis, we know that the combination of shear with photometric clustering auto-correlations is expected to be insensitive to the correct modelling of the flux magnification signal. Thus, these results suggest that as a first step, a joint ellipticity-number-density analysis should consider only the combination with clustering auto-correlations. From this, a path to the full joint analysis using all redshift bins and including GGL could be constructed, and the measurement of the magnification undertaken in each step.

Further to the understanding that the accuracy of a combined analysis is sensitive to the strength of the flux magnification, the results presented hear suggest that many other systematics which can mimic a magnification signal may be significant effects in a joint analysis. These were listed above, and would need to be investigated on the path to carrying out such an analysis.

Whilst the path to obtaining accurate cosmological parameter constraints from such a joint analysis requires more work, the benefits of doing so are evident from the results presented here, with significant decrease in statistical errors and evidence of internal

self-calibration. Strict science requirements, and the desire to constrain interesting cosmological models, with current and upcoming surveys such as LSST, Euclid, DES, KiDS and others suggest that such work would be profitable. Further, the addition of a spectroscopic sample is expected to give further significant improvement (Gaztañaga et al., 2012; Cai & Bernstein, 2012; Kirk et al., 2013). As a result, the combination of an overlapping bright spectroscopic and faint photometric sample, such as that provided by the overlapping footprints provided by surveys such as KiDS with GAMA or HSC and PFS show particular promise in probing cosmology.

In chapter 4, I presented a fully Bayesian method of dark matter mass reconstruction using measurements of the sizes and magnitudes of a sample of lensed bodies. This method produces posterior distributions on a set of free parameters which describe the form of a foreground lensing mass profile. As such, this measurement requires the use of a mass model, and the use of such a method to produce posterior distributions for model free parameters which set the virial mass of the lens using both SIS and NFW profiles was discussed. The method of posterior construction was presented in three forms:

1. Posterior construction using both measured galaxy sizes and magnitudes, both altered by the presence of a magnification field. This joint analysis is expected to be the most constraining of the three presented in the idealised case where no cuts on the sample are required, but also most susceptible to bias due to inaccuracies in the measurement of either quantity.

2. Posterior construction using galaxy sizes only. In this case the magnitude information of the source sample is marginalised, resulting in larger statistical uncertainty in the model free parameters than the full joint analysis. However, such a measurement is less sensitive to inaccuracies in the measurement of the source magnitude, or the determination of an intrinsic magnitude distribution which must be known a-priori, such as the redshift evolution of the magnitude distribution of the source sample.

3. Posterior construction using observed galaxy magnitudes only. In this case, galaxy size information is marginalised. As with the size-only analysis, this comes at the expense of increased statistical uncertainty over the joint analysis, but is less sensitive to inaccuracies in the measurement of galaxy size (e.g. for small of faint galaxies) or accurate determination of the intrinsic size

distribution.

In all forms, the posterior is constructed using a-priori knowledge of the intrinsic size-magnitude distribution, using well-defined lensing relations for the flux- and size-magnification effects. As a result, the method presented does not require any assumptions on the form of the intrinsic size-magnitude distribution to be made prior to use, if the distribution can be well measured. This lends the method a greater degree of flexibility than equivalent estimator based methods, such as the analysis undertaken in Schmidt et al. (2012). Such a distribution could be measured from the data itself, however one must note that doing so may introduce a bias in the recovered posterior if the average over-density across the field is non-zero.

The magnification which acts on a distant source is a function not only of the redshift of the lensing matter, but also of the source redshift. Where the source galaxy redshift is not known, the method presented provides a means of marginalising over an a-priori magnitude-dependent redshift distribution. Such a distribution can be motivated from a separate analysis, provided it is expected to accurately describe the redshift distribution and redshift-magnitude relation of the selected source sample. As with the size-magnitude distribution, such knowledge must be motivated a-priori, and must accurately describe the distribution of the *intrinsic* quantities of the source sample. Thus, ideally such relations must be inferred from measurements on a blank field. Marginalising over such a source redshift distribution will result in less-constraining posterior distributions over the case where the redshift of the source is well-known, however the use of such an a-prior redshift distribution allows for the inclusion in the source sample of a set of galaxies for whom no redshift information is available, thus reducing statistical noise for the whole sample due to an increase in the sample size.

I investigated the distribution of sizes and magnitudes in the STAGES (Space Telescope A901/902 Galaxy Evolution Survey) data-set using Hubble Space Telescope Advanced Camera for Surveys images. Sizes were determined using quadrupole moments, with a correction for the measured PSF using the method of Rhodes, Refregier & Groth (2000). Using the subsample of the STAGES data-set with COMBO-17 redshift information, I found no evidence for significant evolution of the galaxy size in pixels with redshift, and a shallower intrinsic-size-luminosity relation than measurements on SDSS (Shen et al., 2003). I found that the galaxy size distribution is well-described by a log-normal, but that deviations from Gaussianity

in log-sizes were evident when cuts on the data were implemented. The apparent magnitude distribution was significantly non-Gaussian, with a large tail that extends to brighter magnitudes. This suggests that the simplifying assumption of Gaussianity in log-size and magnitude undertaken by Schmidt et al. (2012) would not be an accurate description of the intrinsic distributions, which could potentially lead to a bias in the inferred lensing mass.

The method was tested by application to mock catalogues, with galaxy sizes and magnitudes randomly sampled from the STAGES data-set. The mocks were constructed to allow for the addition of a contaminant sample of cluster members, and contained redshift information for 10% of the full catalogue. From this, I was able to test some simplifying assumptions which would be made in the application of the method to the actual STAGES data-set. I investigated three main sources of bias in the analysis: namely an 'analysis bias' which resulted from the assumption of redshift-independence of the a-priori size-magnitude distribution in the presence of an actual median-redshift-magnitude relation such as that measured on the GOODS field in Schrabback et al. (2007); an 'overlap bias' which results from fitting foreground lenses on the field individually, in the case where individual galaxies reside in a non-zero magnification field due to neighbouring clusters; and a 'lensed prior' bias that results from measuring the a-priori size-magnitude distribution on a field with non-zero average over-density. I found that the method returns unbiased results in the simplified case where one lensing cluster is modelled, and the a-priori distribution is measured from a catalogue of unlensed sizes and magnitudes. This indicates that the assumption of redshift-independence in the intrinsic magnitude distribution does not significantly affect the accuracy of the returned posteriors. I find that the 'lensed prior' bias increases with increasing average over-density of the field, but results in only a small bias which is smaller than statistical uncertainties for a single realisation for expected total mass of the STAGES clusters. I found that cluster overlap is a potentially larger effect, with a predicted bias for the STAGES field of $\sim 10\%$ of the input mass. All biases investigated were found to be smaller than the statistical uncertainty for a single run in the idealised case where only a small core mask was used and no size cuts were taken, and indicates that the method will return accurate mass estimates of the STAGES clusters in application to data. The 'lensed prior' and overlap bias can be avoided by minor alterations to the application of the method, by measuring the a-priori size-magnitude distribution on the blank GEMS field and with simultaneous

fitting of the clusters, and will be implemented in the application to the STAGES field in future work.

In chapter 5 the method was applied to the full STAGESs data-set, and posteriors were constructed on the virial radius for A901a, A90b, A902 and the south-west group (SW) using galaxy magnitudes, and a joint analysis of galaxy sizes and magnitudes. Using source magnitudes only, I obtained maximum-likelihood values for the virial radius consistent with results from a shear analysis on the same field undertaken in Heymans et al. (2008) for A901a, A902 and the SW group, with a signal–to–noise of 6.7, 5.5 and 4.6 respectively, equivalent to 52%, 81% and 58% of the equivalent signal–to–noise for the shear-only analysis. The measurement of A901b using galaxy magnitudes was consistent with a virial radius close to zero, and is inconsistent with equivalent measurements from a shear-only analysis. Through consideration of the number density of sources in annuli around the cluster BCG, I found that contamination of the source sample around A901b by cluster members persists to angular scales larger than the aperture within which sources were taken. X-Ray images show extended emission around A901b, and consideration of optical images suggest that A901b is a particularly crowded field. I therefore conclude that the failure of the method in constraining the A901b cluster may be a result of systematics in the determination of the source magnitude due to insufficient de-blending of sources or the presence of intra-cluster light affecting the photometry of sources in the vicinity of the cluster.

A joint size-magnitude analysis of the STAGES clusters gave results that produced no lower bound on the cluster virial radius and were inconsistent with shear-only results for all clusters, and also with magnitude-only results for A901a, A902 and SW. The disagreement is indicative of potential systematics in the application to galaxy size measurements. Such systematics could result from the assumption of sub-dominant measurement noise in the determination of galaxy sizes, physical effects such as tidal stripping or intrinsic size-density relations, or biases in the implementation of the galaxy size measurement method. Size-density relations have been measured with various different data-sets with differing behaviour (Lani et al., 2013; Cooper et al., 2012; Papovich et al., 2012) and on the STAGES field in Maltby et al. (2010). With knowledge of any size-density relation, a model for such a relation could be naturally folded into the method presented in chapter 4. Systematics in the size measurement and measurement of the measurement noise can be investigated through the use of image

simulations. Measurement noise can be implemented into the method, as discussed in chapter 4. The investigation of these effects is an important next step in the application of the method to the STAGES data-set, and I consider the reconstruction of the cluster mass profile of STAGES clusters with this technique uncertain until this investigation has been completed.

Whilst the measurement of cluster mass on the STAGES field using galaxy sizes requires further investigation, I note that the signal–to–noise for the measurement of A901a, A902 and SW using galaxy magnitudes is comparable to that using traditional shear techniques. The addition of an accurate size measurement will further reduce the statistical uncertainty in a magnification analysis and will further increase the signal–to–noise presented here. Further improvement will result in the use of sources with lie further from the BCG than those with a $2'$ aperture considered here. Such a development will result from a minor alteration to the method to simultaneously fit all over-densities on the field. I therefore conclude that the measurement presented here is limited mainly by source selection and removal of contaminants, and that given adequate investigation into the accurate measurement of galaxy sizes, the measurement of cluster mass using the magnification effect will provide results that are competitive to traditional shear analyses.

The work in this thesis has focussed on the application of the size and flux magnification to measure the mass of clusters on the STAGES field, however such techniques could be easily extended to the measurement of galaxy halo profiles with galaxy-galaxy-size-lensing (GGSL). Rather than modelling mass profiles around cluster centres, the GGSL application would model mass profiles around each foreground galaxy. Whilst the accurate measurement of galaxy size may be difficult for small, faint high-redshift sources, as with shape measurements, the flux magnification may allow the use of higher redshift sources than a shear analysis for whom shape measurement would not be possible. The magnification measurement around each foreground can then be stacked to achieve constraints for a foreground sample. Such an application would avoid many of the potential contaminants of this analysis: for example, given accurate redshifts the foreground is clearly identifiable and easily removed from the source sample; further, one can expect the contamination due to foreground light or source masking to be much smaller, so that accurate size and magnitude measurement close to the foreground may be more easily achievable. Conversely, further idiosyncratic systematics such as dust extinction would need

investigated, however I note that measurements in multiple bands may allow the effect of dust extinction to be measured (e.g. Ménard et al., 2010; Bauer et al., 2013).

In the next decade, the astrophysical community is due to receive a glut of data from many upcoming large scale galaxy surveys. In this time, Euclid will be launched and LSST will see first light. Driven by the desire to utilise these surveys to their maximum potential, it has become more important than ever to understand the full range of cosmological probes at our disposal, and how these probes can be combined to produce the most accurate and precise constraints on cosmological models. In doing so, we can aim to test and improvement cosmological models (potentially beyond the standard model) and discover new and interesting physics.

In this thesis I have shown that significant improvements to measurements from traditional lensing analyses can be expected with the addition of measurements already taken as part of a galaxy survey. I have focussed on the various magnification analyses that can be undertaken, and how these can be used to gain information, in an effort to obtain optimal cosmological constraints from a given survey in an inexpensive way. I have shown that the addition of number density measurements, including a flux magnification contribution, can provide significant improvement to the precision of inferred cosmological parameters, motivating the use of such a combination in any of the surveys mentioned above. However, I have shown that such a combination comes with a price, with the extra complexity which results from the need to accurately measure and model the flux magnification to avoid biasing results. Such a result implies that the combination of such probes is evidently profitable, but brings in a new range of systematics which must be understood.

I have presented the first observational analysis using combined measurements of size- and magnitude- magnification around massive clusters in the STAGES field. To do so I have presented a new method of producing probability density functions on free parameters which describe a foreground mass model, which avoids many of the simplifying assumptions made in earlier measurements around galaxy groups, and can be extended to measure galaxy mass profiles in a similar way to traditional galaxy-galaxy lensing. I found results using measurements of source magnitude that were consistent and comparable to shear measurements of the same clusters. The disagreement between the magnitude-only results and those with the application of size indicates that use of size measurements is more difficult, and care must be taken to ensure that the size measurement is accurate free from contamination. My investigation

using mock catalogues suggests that where the measurements are accurate and the source sample is free from contamination, magnification measurements may provide tighter constraints on foreground mass profiles than shear analyses. Further, as was found with the combination of shear and clustering, one can expect that the addition of such as measurement may help to provide not only more precise measurements, but also more accurate measurements through internal self-calibration. My conclusion is therefore that in order to benefit from this extra information, size measurement needs to become part of the lensing measurement challenges of the future. If this is the case, then we gain important inexpensive information that otherwise would not be used.

We see therefore that there is valuable cosmological information to be gleaned from the oft-neglected magnification signal. With little extra expense, and the investment of time in the community, such information can be utilised to provide the most accurate and precise constraints possible from a lensing analysis with a given survey.

Appendix A

A.1 Liouville's Theorem, and its application to flux magnification

Liouville's Theorem states that the density of points representing particles in six dimensional phase phase is invariant as the points propagate, provided that any forces that act on them are both conservative and differentiable. These conditions require that the force be smooth, and must not change the total energy of the system. More formally, we require that any force on the particles is divergence free in momentum space, $\nabla_p F = 0$, as we shall see later. We closely follow Bradt (2008).

Define the number density of particles in phase space as $f(\boldsymbol{x}, \boldsymbol{p}, t)$, such that the number of particles within a given volume element in phase space is given as $N = \int f(\boldsymbol{x}, \boldsymbol{p}, t) d^3x d^3p$, where each vector $\boldsymbol{x}, \boldsymbol{p}$ represent the particles position and momentum in 3 dimensional basis coordinates, $x_1, x_2, x_3, p_1, p_2, p_3$. Liouville's theorem (hereafter LT) requires the distribution function of particles f is constant at positions that follow a group of particles as time progresses. Thus, the condition

$$\frac{df(x,p,t)}{dt} = \frac{\partial f}{\partial t} + \sum_i \frac{\partial f}{\partial x_i}\frac{\partial x_i}{\partial t} + \sum_j \frac{\partial f}{\partial p_j}\frac{\partial p_j}{\partial t} = 0 \tag{A.1}$$

is sufficient to show LT.

Starting from the continuity equation for the number density in physical space

$$\frac{\partial f}{\partial t} = -\nabla_x \cdot (f\boldsymbol{v}) \tag{A.2}$$

which can be shown by considering the rate of flow through an element surface area dS as a function of the particles' flow velocity v and integrating over a closed surface S.

This gives the conservation equation for number density in physical space only. The corresponding continuity equation in phase space can be derived by noting that the force on a given particle F takes on the same meaning in phase space as the velocity v in physical space (i.e. $v = dx/dt$ and $F = dp/dt$). Thus the rate of flow of particles in momentum space can be represented by the force acting on those particles.

Provided that any external force acting on the particles is differentiable, the conservation equation for number density in momentum space is then

$$\frac{\partial f}{\partial t} = -\nabla_p \cdot (f\boldsymbol{F}) \tag{A.3}$$

giving the continuity equation in full phase space as

$$\begin{aligned} \frac{\partial f}{\partial t} &= -\nabla_x \cdot (f\boldsymbol{v}) - \nabla_p \cdot (f\boldsymbol{F}) \\ &= -f\nabla_x \cdot \boldsymbol{v} - \boldsymbol{v} \cdot \nabla_x f - f\nabla_p \cdot \boldsymbol{F} - \boldsymbol{F} \cdot \nabla_p f. \end{aligned} \tag{A.4}$$

Requiring $\nabla_x \cdot \boldsymbol{v} + \nabla_p \cdot \boldsymbol{F} = 0$, this reduces to the Boltmann equation without collisions, also known as the Vlasov equation:

$$\frac{\partial f}{\partial t} + \boldsymbol{v} \cdot \nabla_x f + \boldsymbol{F} \cdot \nabla_p f = \frac{df}{dt} = 0 \tag{A.5}$$

where the left hand side has been identified as Equation (A.1). Under the conditions of a conservative and differentiable force, Liouville's Theorem holds.

I have shown under certain conditions the phase space density of representative particles is invariant in time as we follow the particles. I now wish to relate that to the physical process of emission and propagation of photons from a source, and thus aim to relate the phase space density f with the specific intensity $I(\nu)$ or specific brightness B.

Consider a number intensity J to be the number of particles with energy in range U to $U + dU$ passing through unit surface area, per unit solid angle per unit time. The number of particles passing perpendicular through a surface dA within solid angle $d\Omega$ in time dt is then

$$N = JdUdAd\Omega dt \tag{A.6}$$

Similarly, the number of representative particles in a given phase volume is given as

$$N = \int\int f\ d^3x d^3p = fvdtdAp^2dpd\Omega_p \tag{A.7}$$

Where v is the velocity in of the particles in real space. Equating these two we see that the phase space density is related to J by

$$JdU = fvp^2dp \tag{A.8}$$

provided the real and momentum space axes are co-aligned so that $d\Omega = d\Omega_p$. Special Relativity gives $U^2 = p^2c^2 + (mc^2)^2$ so that $UdU = c^2pdp$. Similarly, $p = \gamma mv$ with $U = \gamma/mc^2$ so that $UdU = c^2pdp = vdpU$ giving $dU = vdp$. Thus, (A.8) gives

$$J = fp^2 \tag{A.9}$$

We wish to relate this to the specific intensity per unit frequency, defined as the energy flow through unit surface area dA, per unit solid angle per unit frequency. Thus the energy flow per unit surface area, per unit solid angle in frequency interval $\nu \rightarrow \nu + d\nu$ is given by $I(\nu)d\nu$. Similarly, the particle flow per unit surface area, per unit solid angle with energy interval $U \rightarrow U + dU$ is given as JdU so that the energy flow per unit surface area, per unit solid angle with in the same energy interval is approximately $UJdU$ to lowest order. For photons, $U = h\nu$ so that $dU = hd\nu$, thus we find

$$\begin{aligned} I(\nu)d\nu &= UJdU = h^2\nu Jd\nu \\ &\rightarrow I(\nu) = h^2\nu J \end{aligned} \tag{A.10}$$

Using (A.9) with photon momentum given as $p = h\nu/c^2$ we find

$$I(\nu) = \frac{h^4\nu^3}{c^4} f(\boldsymbol{x}, \boldsymbol{p}, t) \tag{A.11}$$

As LT requires $df/dt = 0$, the above indicates that provided the conditions for LT are satisfied, and provided the frequency of emitted photons are constant, specific intensity is also conserved.

Specific Intensity is frequently used to denote the energy flow per unit area, per unit solid angle per unit frequency of radiation received by some observer, such as a telescope, whilst surface brightness (B_ν) is used to describe the energy flow per unit

area, per unit solid angle per unit frequency of radiation emitted by some source. In the absence of some intervening method of absorption or emission of photons, the surface brightness is equal to the specific intensity, so that $B_\nu = I_\nu$. Thus, in the case where Liouville's theorem are applicable and the phase space density are conserved, the conservation of surface brightness is also expected, $dB/dt = 0$.

As gravity is conservative and there exists no means to absorb/emit photons in gravitational lensing, it is clear therefore clear that lensing conserves surface brightness. Thus magnification due to weak lensing will change the total flux of the source, and consequently its observed magnitude due to its change in size.

A.2 The Galaxy Bias Prior – Normalising the Likelihood

We define the covariance matrix for the prior on N_z linear galaxy bias parameters as in Equation (3.28). The covariance matrix then takes the form $\boldsymbol{C} = \sigma_\nu^2 \boldsymbol{R}$, where $\boldsymbol{R}$ is the matrix of correlation parameters (ν) in Toeplitz form. Assuming the full likelihood for the bias parameters is Gaussian, it then follows that

$$\frac{p(\boldsymbol{b})}{p(\boldsymbol{0})} = e^{-\frac{1}{2}\chi^2}, \tag{A.12}$$

where $\boldsymbol{b}$ labels the set of galaxy bias nuisance parameters, we have renormalised to the likelihood when $\boldsymbol{b} = \boldsymbol{0}$ to remove any pre-factors, and where

$$\chi^2 = \boldsymbol{b}\boldsymbol{C}^{-1}\boldsymbol{b}^T = \sum_{ij}^{N_z} b^2 (\boldsymbol{C}^{-1})_{ij}, \tag{A.13}$$

along the line $b_1 = b_2 = \cdots = b_{N_z} \equiv b$. From the definition of the covariance matrix in Equation (3.28) it follows that

$$\begin{aligned}
\chi^2 &= \frac{b^2}{\sigma_\nu^2}\sum_{ij}^{n}(\boldsymbol{R}^{-1})_{ij} = \frac{b^2}{\sigma_\nu^2}\sum_{ij}^{N_z}\left[\frac{\boldsymbol{Adj}(\boldsymbol{R})}{\det(\boldsymbol{R})}\right]_{ij}, \\
&= \frac{b^2}{\sigma_\nu^2\det(\boldsymbol{R})}\sum_{ij}^{N_z}[\boldsymbol{Co}(\boldsymbol{R})^{\mathrm{T}}]_{ij}, \\
&= \frac{b^2}{\sigma_\nu^2\det(\boldsymbol{R})}\sum_{ij}^{N_z}[\boldsymbol{Co}(\boldsymbol{R})]_{ij}, \qquad \text{(A.14)}
\end{aligned}$$

where $\boldsymbol{Adj}(\boldsymbol{R})$ denotes the adjoint matrix of $\boldsymbol{R}$, $\boldsymbol{Co}(\boldsymbol{R})$ the matrix of cofactors, defined as $\mathrm{Co(R)}_{ij} = (-1)^{i+j}\mathrm{M}_{ij}$, $\boldsymbol{M}$ the minor matrix of determinants, and we have used the symmetry of R to note that $\boldsymbol{Co}(\boldsymbol{R})^{\mathrm{T}} = \boldsymbol{Co}(\boldsymbol{R})$.

By the symmetry of $\boldsymbol{R}$, and the definition of the minor matrix of determinants, the matrix of cofactors $\boldsymbol{Co}(\boldsymbol{R})$ satisfies

$$\boldsymbol{Co}(\boldsymbol{R}) = \begin{pmatrix} x_1 & x_2 & 0 & 0 & \cdots & 0 \\ x_2 & x_3 & x_2 & 0 & \cdots & 0 \\ 0 & x_2 & x_3 & x_2 & \cdots & 0 \\ \vdots & & \ddots & & & \vdots \\ 0 & \cdots & 0 & 0 & x_2 & x_1 \end{pmatrix}, \qquad \text{(A.15)}$$

so that

$$\sum_{ij}^{n}\boldsymbol{Co}(\boldsymbol{R})_{ij} = 2x_1 + 2(N_z - 1)x_2 + (N_z - 2)x_3, \qquad \text{(A.16)}$$

and $\det(\boldsymbol{R}) = (1-\nu^2)^{N_z-1}$. Variable x_1 is the determinant of the $N_z - 1$ case of the matrix $\boldsymbol{R}$, which we denote as $\det(\boldsymbol{R}^{(N_z-1)})$. The remaining factors can be calculated by noting that

$$\sum_{j}^{N_z}\boldsymbol{R}_{ij}\boldsymbol{Co}(\boldsymbol{R})_{ij} = \det(\boldsymbol{R}), \qquad \text{(A.17)}$$

so that

$$\begin{aligned}
x_2 &= \frac{1}{\nu}[\det(\boldsymbol{R}^{(N_z)}) - \det(\boldsymbol{R}^{(N_z-1)})], \qquad \text{(A.18)} \\
x_3 &= 2\det(\boldsymbol{R}^{(N_z-1)}) - \det(\boldsymbol{R}^{(N_z)}). \qquad \text{(A.19)}
\end{aligned}$$

Using Equations (A.16) and (A.14), we find that

$$\chi^2 = \frac{b^2}{\sigma_\nu^2}\left[\frac{N_z - (N_z-2)\nu}{1+\nu}\right]. \tag{A.20}$$

It is clear then that if we keep σ_ν constant as we change ν, χ^2 at a given point along the $b_1 = b_2 = \cdots = b_{N_z} = b$ line will vary with ν causing a change in the volume of galaxy bias parameter space probed by 1σ contours to also vary with the correlation strength. We therefore normalise χ^2 along $b_i = b$ by choosing σ_ν such that $\chi^2_\nu = \chi^2_{\nu=0}$ for all values of ν. Noting that by Pythagoras' theorem $b = \sigma_0/\sqrt{N_z}$ and requiring that $\sigma_\nu(\nu = 0) = \sigma_0$, we find that

$$\sigma_\nu = \sigma_0\left[\frac{N_z - (N_z-2)\nu}{N_z(1+\nu)}\right]^{\frac{1}{2}}, \tag{A.21}$$

as stated in Equation (3.29).

A.3 The Fisher Matrix

Consider a finite set of observations which for a data vector $\mathbf{x}$, and we wish to understand how well a set of model parameters can be constrained from this data set. An answer to this question can be determined through the use of the Fisher Information Matrix. For the purposes of this discussion I closely follow the results presented in Tegmark, Taylor & Heavens (1997) with a few digressions.

Baye's theorem [1] states that the probability distribution of the model parameters given a set of measurements can be related to the likelihood of those measurements as

$$p(\boldsymbol{\Theta}|\boldsymbol{x}) = \frac{p(\boldsymbol{x}|\boldsymbol{\Theta})p(\boldsymbol{\Theta})}{p(\boldsymbol{x})} \propto p(\boldsymbol{x}|\boldsymbol{\Theta}). \tag{A.22}$$

In Bayesian nomenclature, $p(\Theta|x)$ denotes the *posterior* distribution on which we would like to define our statistics on model parameters, $p(x|\Theta)$ the *likelihood*, $p(\Theta)$ the *prior* which sets a-priori knowledge on the model parameters, and $p(x)$ the *evidence* which serves to normalise the posteriors. The final approximation assumes the application of a flat prior, where no a-priori knowledge on model parameter values

[1] Used extensively throughout this thesis, implicitly through the use of the Fisher matrix in Chapter 3, and explicitly in determining halo profile parameters in Chapters 4 and 5

has been set. Thus, we can see that under this assumption the posterior can be related to the likelihood up to some scaling factor.

Let $\mathcal{L} = \ln L(\boldsymbol{x}|\boldsymbol{\Theta})$. The Taylor expansion of the log-likelihood around the maximum likelihood (ML) value in parameter space, chosen as a BUE [2] and denoted as $\Theta_{\rm ML}$ gives

$$\begin{aligned}\mathcal{L}(\boldsymbol{x}|\boldsymbol{\Theta}) &= \mathcal{L}(\boldsymbol{x}, \boldsymbol{\Theta_{ML}}) + \Delta\Theta_\alpha \mathcal{L}_{,\alpha}|_{\rm ML} + \frac{1}{2}\Delta\Theta_\alpha \mathcal{L}_{,\alpha\beta}|_{\rm ML}\Delta\Theta_\beta + {\rm O}(\Delta\Theta^3) \\ &= \mathcal{L}(\boldsymbol{x}, \boldsymbol{\Theta_{ML}}) + \frac{1}{2}\Delta\Theta_\alpha \mathcal{L}_{,\alpha\beta}|_{\rm ML}\Delta\Theta_\beta + {\rm O}(\Delta\Theta^3), \end{aligned} \tag{A.23}$$

where $\Delta\Theta = \boldsymbol{\Theta} - \boldsymbol{\Theta_{\rm ML}}$, subscript $_{,\alpha}$ denotes the partial derivative with respect to the model parameter Θ_α, $|_{\rm ML}$ denotes evaluation as the model parameter ML point $\boldsymbol{\Theta_{\rm ML}}$ and Einstein summation is implied. In the final equality $\mathcal{L}_{,\alpha} = 0$ has been applied since the slope of the likelihood is zero at the ML point in parameter space, and higher order terms have been neglected. This final point requires that the likelihood is sufficiently sharply peaked around the maximum likelihood point that the curvature $\mathcal{L}_{,\alpha\beta}$ is large and the quadratic terms are dominant. Under these assumptions, one can see that the likelihood is approximately Gaussian close to the ML point, and takes the form

$$L(\boldsymbol{x}|\boldsymbol{\Theta}) = L(\boldsymbol{x}|\boldsymbol{\Theta_{\rm ML}}) \exp\left[-\frac{1}{2}(\boldsymbol{\Theta} - \boldsymbol{\Theta_{ML}})_\alpha H^{-1}_{\alpha\beta}(\boldsymbol{\Theta} - \boldsymbol{\Theta_{ML}})_\beta\right] \propto L(\boldsymbol{\Theta}|\boldsymbol{x}), \tag{A.24}$$

where I have defined the Hessian as $H^{-1}_{\alpha\beta} = -\mathcal{L}_{,\alpha\beta}(\boldsymbol{x}|\boldsymbol{\Theta})$ and Baye's Theorem has been applied in the last step. The Fisher matrix, defined as the average of the inverse Hessian

$$F_{\alpha\beta} = \langle H^{-1}_{\alpha\beta}\rangle = -\langle \mathcal{L}_{,\alpha\beta}(\boldsymbol{x}|\boldsymbol{\Theta})\rangle \tag{A.25}$$

can then be identified as the covariance of model parameters around their true values, provided that the ML is a BUE and thus returns the true value on average. The marginal errors on model parameters then satisfy $\sigma_{\Theta_\alpha} \geq \sqrt{(F^{-1})_{\alpha\alpha}}$, a statement of the Cramér-Rao inequality. Thus, the Fisher matrix provides a means of determining the best-case error bars on model parameters given a data vector.

In the above derivation, I assumed a flat prior on the model parameters to simplify the analysis, however since the Fisher matrix is determined through the derivatives of the log-likelihood it is easy to show that a prior on model parameters can be added as

[2] Best Unbiased Estimator: an estimator whose average returns the true parameter value with minimum variance.

$\boldsymbol{F}_{\alpha\beta} \rightarrow \boldsymbol{F}_{\alpha\beta} + (\boldsymbol{C}^{-1}_{\rm prior})_{\alpha\beta}$, where $C_{\rm prior}$ defines the covariance of the prior distribution in parameter space.

From the derivation presented here, it is clear that the Fisher matrix gives the local curvature of the likelihood close to the maximum-likelihood point, assumed to give the true parameter value on average. As such, the Fisher matrix itself is a local statistic, and does not contain information on the likelihood far from the ML point where the reduction to second order in the log-likelihood (and Gaussianisation of the likelihood) holds. Since the Fisher matrix is by definition local, one must be careful to evaluate the curvature of the likelihood close to the global maximum of the distribution, and not in a local maximum. Further, this brings up two important points: firstly, the Fisher matrix can lead to the spurious lifting of degeneracies between parameters which may be largely or infinity degenerate; secondly, the Fisher matrix is likely to be inaccurate when the likelihood is in reality non-Gaussian. In both cases, the Fisher matrix may be expected to be too optimistic, and under-estimate the best errors for a given data set. In such a situation, one would be better served using a method which samples the full likelihood distribution [3]. However, the Fisher matrix is quick to calculate in contrast to methods which sample the full posterior space, and is therefore frequently used in forecasts on cosmological parameters for a given analysis.

A.4 An alternative Fisher matrix analysis for the shear-only, clustering and combined analyses

For the cases where we wish to use the full information for a given probe, such as using ellipticity information, number over-density or a combination of both over all redshift bins, we can alternatively take the data vector to contain either ellipticity, number density contrast, or both. By definition, the data then have zero mean, and the Fisher matrix elements for parameters labelled by η and τ, takes the form Tegmark, Taylor & Heavens (1997) as

$$\boldsymbol{F}_{\eta\tau} = \sum_{\boldsymbol{\ell}_r} \frac{\boldsymbol{\ell}_r \Delta\boldsymbol{\ell}_r \Delta\Omega}{4\pi} Tr[\boldsymbol{C}^{-1}(\boldsymbol{\ell}_r)\boldsymbol{C}_{,\eta}(\boldsymbol{\ell}_r)\boldsymbol{C}^{-1}(\boldsymbol{\ell}_r)\boldsymbol{C}_{,\tau}(\boldsymbol{\ell}_r)], \tag{A.26}$$

[3] For a discussion on this, see Wolz et al. (2012), where the authors undertook a comparison between Fisher matrix forecasts and MCMC analyses on cosmological parameter errors for a variety of probes, including gravitational lensing.

where $\boldsymbol{C}$ is a matrix containing the covariance between all 1-point estimators entering the data vector.

Using this formalism, the covariance matrix takes a simpler form than for the formalism detailed in Section 3.2.2 . For example, for the combination of a shear analysis with information from clustering and magnification over all redshift bins, and including galaxy-galaxy lensing (Sh+AllCl+GGL), the data vector takes the form $\boldsymbol{D}(\boldsymbol{\ell}) = \{\epsilon^{(1)}(\boldsymbol{\ell}), \ldots, \epsilon^{(N_z)}(\boldsymbol{\ell}), \delta n^{(1)}(\boldsymbol{\ell}), \ldots, \delta n^{(N_z)}(\boldsymbol{\ell})\}$ so that the covariance matrix takes block form

$$\boldsymbol{C}(\boldsymbol{\ell}) = \left(\begin{array}{c|c} P_{\epsilon\epsilon}(\boldsymbol{\ell}) & P_{\epsilon\delta n}(\boldsymbol{\ell}) \\ \hline P_{\delta n\epsilon}(\boldsymbol{\ell}) & P_{\delta n\delta n}(\boldsymbol{\ell}) \end{array} \right), \tag{A.27}$$

with power spectra as defined in Equations (3.5 through 3.7).

The equivalence of both the above prescription and the prescription set out in Section 3.2.2 is detailed in Joachimi, Taylor & Kiessling (2011) when assuming Gaussian statistics. Results for the Sh, AllCl and Sh+AllCl+GGL analyses were verified using both methods for this paper.

Bibliography

Anderson L. et al., 2012, Monthly Notices of the Royal Astronomical Society, 427, 3435

Balaguera-Antolínez A., Sánchez A. G., Böhringer H., Collins C., Guzzo L., Phleps S., 2011, Monthly Notices of the Royal Astronomical Society, 413, 386

Bardeen J. M., Bond J. R., Kaiser N., Szalay A. S., 1986, Astrophysical Journal, 304, 15

Bartelmann M., Schneider P., 2001, Physics Reports, 340, 291

Bauer A. H., Gaztañaga E., Martí P., Miquel R., 2013, eprint arXiv, 1312, 2458

Benjamin J. et al., 2013, MNRAS, 431, 1547

Bernstein G. M., 2009, The Astrophysical Journal, 695, 652, submitted to ApJ

Bernstein G. M., Cai Y.-C., 2011, arXiv, astro-ph.CO

Bernstein G. M., Jarvis M., 2002, The Astronomical Journal, 123, 583

Bertin E., Arnouts S., 1996, Astronomy and Astrophysics Supplement, 117, 393

Bertin G., Lombardi M., 2006, The Astrophysical Journal, 648, L17

Beutler F. et al., 2011, Monthly Notices of the Royal Astronomical Society, 416, 3017

Blake C., Bacon D., Fluke C., Kitching T., Miller L., Power C., Wilman R., 2014, Proposal for an SKA weak lensing survey

Blake C. et al., 2013, Monthly Notices of the Royal Astronomical Society, 436, 3089

Blake C. et al., 2010, Monthly Notices of the Royal Astronomical Society, 406, 803

Blake C. et al., 2011, Monthly Notices of the Royal Astronomical Society, 415, 2892

Bond J. R., Efstathiou G., 1984, Astrophysical Journal, 285, L45

Bradač M., Allen S. W., Treu T., Ebeling H., Massey R., Morris R. G., von der Linden A., Applegate D., 2008, The Astrophysical Journal, 687, 959

Bradt H., 2008, Astrophysical Processes

Brainerd T. G., Blandford R. D., Smail I., 1996, Astrophysical Journal v.466, 466, 623

Bridle S., King L., 2007, New Journal of Physics, 9, 444

Bridle S. et al., 2009, Annals of Applied Statistics, 3, 6

Brown M. L., Battye R. A., 2011, Monthly Notices of the Royal Astronomical Society, 410, 2057

Brown M. L., Taylor A. N., Hambly N. C., Dye S., 2002, Monthly Notices of the Royal Astronomical Society, 333, 501

Cai Y.-C., Bernstein G., 2012, Monthly Notices of the Royal Astronomical Society, 422, 1045

Casaponsa B., Heavens A. F., Kitching T. D., Miller L., Barreiro R. B., Martínez-González E., 2013, Monthly Notices of the Royal Astronomical Society, 741

Castro P. G., Heavens A. F., Kitching T. D., 2005, Physical Review D, 72, 23516

Choi A., Tyson J. A., Morrison C. B., Jee M. J., Schmidt S. J., Margoniner V. E., Wittman D. M., 2012, ApJ, 759, 101

Clowe D., Bradač M., Gonzalez A. H., Markevitch M., Randall S. W., Jones C., Zaritsky D., 2006, The Astrophysical Journal, 648, L109

Collaboration P. et al., 2013a, arXiv, astro-ph.CO

Collaboration P. et al., 2014, Astronomy & Astrophysics, 571, A20

Collaboration P. et al., 2013b, arXiv, astro-ph.CO

Collaboration P. et al., 2013c, eprint arXiv, 1303, 5075

Cooper M. C. et al., 2012, Monthly Notices of the Royal Astronomical Society, 419, 3018

de Jong J. T. A. et al., 2013, The Messenger, 154, 44

Dolag K., Bartelmann M., Perrotta F., Baccigalupi C., Moscardini L., Meneghetti M., Tormen G., 2004, A&A, 416, 853

Eifler T., Krause E., Schneider P., Honscheid K., 2013, eprint arXiv, 1302, 2401

Eisenstein D. J., Hu W., 1998, Astrophysical Journal v.496, 496, 605

Erben T., Hildebrand H., Miller L., Waerbeke L. V., Heymans C., Hoekstra H., Kitching T. D., et al., 2012, arXiv, 1210, 8156, submitted to MNRAS

Ettori S., Fabian A. C., 1999, Monthly Notices of the Royal Astronomical Society, 305, 834

Ettori S., Morandi A., Tozzi P., Balestra I., Borgani S., Rosati P., Lovisari L., Terenziani F., 2009, A&A, 501, 61

Fedeli C., Bartelmann M., Meneghetti M., Moscardini L., 2008, A&A, 486, 35

Ford J., Hildebrandt H., van Waerbeke L., Erben T., Laigle C., Milkeraitis M., Morrison C. B., 2014, Monthly Notices of the Royal Astronomical Society, 439, 3755

Gaztañaga E., Eriksen M., Crocce M., Castander F. J., Fosalba P., Marti P., Miquel R., Cabré A., 2012, MNRAS, 2931

Gray M. E. et al., 2009, Monthly Notices of the Royal Astronomical Society, 393, 1275

Grego L., Carlstrom J. E., Reese E. D., Holder G. P., Holzapfel W. L., Joy M. K., Mohr J. J., Patel S., 2001, The Astrophysical Journal, 552, 2

Harvey D., Massey R., Kitching T., Taylor A., Jullo E., Kneib J.-P., Tittley E., Marshall P. J., 2013, Monthly Notices of the Royal Astronomical Society, 433, 1517

Harvey D. et al., 2014, Monthly Notices of the Royal Astronomical Society, 441, 404

Heavens A., Alsing J., Jaffe A. H., 2013, Monthly Notices of the Royal Astronomical Society: Letters, L98

Heavens A. F., Joachimi B., 2011, Monthly Notices of the Royal Astronomical Society, 415, 1681, 11 pages, 6 figures

Heavens A. F., Kitching T. D., Taylor A. N., 2006, arXiv, astro-ph

Heymans C. et al., 2006, Monthly Notices of the Royal Astronomical Society: Letters, 371, L60

Heymans C. et al., 2005, Monthly Notices of the Royal Astronomical Society, 361, 160

Heymans C. et al., 2008, Monthly Notices of the Royal Astronomical Society, 385, 1431

Heymans C. et al., 2013, Monthly Notices of the Royal Astronomical Society, 1297

Hildebrandt H. et al., 2012, MNRAS, 421, 2355

Hildebrandt H. et al., 2011, The Astrophysical Journal Letters, 733, L30

Hildebrandt H., Waerbeke L. V., Erben T., 2009, Astronomy and Astrophysics, 507, 683

Hildebrandt H. et al., 2013, Monthly Notices of the Royal Astronomical Society, 429, 3230

Hirata C. M., Mandelbaum R., Ishak M., Seljak U., Nichol R., Pimbblet K. A., Ross N. P., Wake D., 2007, Monthly Notices of the Royal Astronomical Society, 381, 1197

Hirata C. M., Seljak U., 2004, arXiv, astro-ph

Hoekstra H., Franx M., Kuijken K., 2000, The Astrophysical Journal, 532, 88

Hoekstra H., Franx M., Kuijken K., Carlberg R. G., Yee H. K. C., 2003, Monthly Notice of the Royal Astronomical Society, 340, 609

Hu W., 1999, arXiv, astro-ph

Huff E. M., Graves G. J., 2011, eprint arXiv, 1111, 1070, 6 pages, 4 Figures. Submitted to ApJL

J.A.Peacock, 1999, Cosmological Physics. Cambridge University Press

Joachimi B., Bridle S. L., 2010, Astronomy and Astrophysics, 523, 1

Joachimi B., Mandelbaum R., Abdalla F. B., Bridle S. L., 2011, A&A, 527, 26

Joachimi B., Schneider P., 2008, Astronomy and Astrophysics, 488, 829

Joachimi B., Schneider P., 2009, Astronomy and Astrophysics, 507, 105

Joachimi B., Taylor A. N., Kiessling A., 2011, MNRAS, 418, 145

Kaiser N., 2000, The Astrophysical Journal, 537, 555

Kaiser N., Squires G., 1993, Astrophysical Journal, 404, 441

Kaiser N., Squires G., Broadhurst T., 1995, Astrophysical Journal v.449, 449, 460

Kilbinger M. et al., 2013, Monthly Notices of the Royal Astronomical Society, 430, 2200

Kirk D., Bridle S., Schneider M., 2010, Monthly Notices of the Royal Astronomical Society, 408, 1502

Kirk D., Lahav O., Bridle S., Jouvel S., Abdalla F. B., Frieman J. A., 2013, eprint arXiv, 1307, 8062, 22 pages, 8 figures

Kitching T. D. et al., 2012, MNRAS, 423, 3163

Kitching T. D. et al., 2014, arXiv, astro-ph.CO

Kronberg P. P., Dyer C. C., Burbidge E. M., Junkkarinen V. T., 1991, Astrophysical Journal, 367, L1

Lani C. et al., 2013, Monthly Notices of the Royal Astronomical Society, 435, 207

Laureijs R. et al., 2011, eprint arXiv, 1110, 3193

Leauthaud A. et al., 2007, The Astrophysical Journal Supplement Series, 172, 219

Maltby D. T. et al., 2010, Monthly Notices of the Royal Astronomical Society, 402, 282

Mandelbaum R. et al., 2011, Monthly Notices of the Royal Astronomical Society, 410, 844

Mandelbaum R., Hirata C. M., Ishak M., Seljak U., Brinkmann J., 2006, Monthly Notices of the Royal Astronomical Society, 367, 611

Mandelbaum R., Slosar A., Baldauf T., Seljak U., Hirata C. M., Nakajima R., Reyes R., Smith R. E., 2013, Monthly Notices of the Royal Astronomical Society, 432, 1544

Mantz A., Allen S. W., Ebeling H., Rapetti D., 2008, Monthly Notices of the Royal Astronomical Society, 387, 1179

Markevitch M., Gonzalez A. H., Clowe D., Vikhlinin A., Forman W., Jones C., Murray S., Tucker W., 2004, The Astrophysical Journal, 606, 819

McDonald P., Seljak U., 2009, Journal of Cosmology and Astroparticle Physics, 10, 007

Melchior P. et al., 2014, arXiv, astro-ph.CO

Menard B., Bartelmann M., 2002, A&A, 386, 784

Ménard B., Scranton R., Fukugita M., Richards G., 2010, Monthly Notices of the Royal Astronomical Society, 405, 1025

Miller L., Kitching T. D., Heymans C., Heavens A. F., Waerbeke L. V., 2007, Monthly Notices of the Royal Astronomical Society, 382, 315

Morrison C. B., Scranton R., Ménard B., Schmidt S. J., Tyson J. A., Ryan R., Choi A., Wittman D., 2012, arXiv, astro-ph.CO

Myers A. D., Outram P. J., Shanks T., Boyle B. J., Croom S. M., Loaring N. S., Miller L., Smith R. J., 2003, Monthly Notice of the Royal Astronomical Society, 342, 467

Navarro J. F., Frenk C. S., White S. D. M., 1997, Astrophysical Journal v.490, 490, 493

Papovich C. et al., 2012, ApJ, 750, 93

Peacock J. A., Dodds S. J., 1996, Monthly Notices of the Royal Astronomical Society, 280, L19

Peacock J. A., Smith R. E., 2000, Monthly Notices of the Royal Astronomical Society, 318, 1144

Percival W. J. et al., 2010, Monthly Notices of the Royal Astronomical Society, 401, 2148

Perlmutter S. et al., 1999, The Astrophysical Journal, 517, 565

Rassat A. et al., 2008, eprint arXiv, 0810, 3, submitted to MNRAS

Reiprich T. H., Böhringer H., 2002, The Astrophysical Journal, 567, 716

Rhodes J., Refregier A., Groth E. J., 2000, The Astrophysical Journal, 536, 79

Riess A. G. et al., 2011, The Astrophysical Journal, 730, 119

Rix H.-W. et al., 2004, The Astrophysical Journal Supplement Series, 152, 163

Rozo E., Schmidt F., 2010, arXiv, astro-ph.CO

Schmidt B. P. et al., 1998, The Astrophysical Journal, 507, 46

Schmidt F., Leauthaud A., Massey R., Rhodes J., George M. R., Koekemoer A. M., Finoguenov A., Tanaka M., 2012, The Astrophysical Journal Letters, 744, L22

Schmidt F., Rozo E., Dodelson S., Hui L., Sheldon E., 2009a, ApJ, 702, 593

Schmidt F., Rozo E., Dodelson S., Hui L., Sheldon E., 2009b, arXiv, astro-ph.CO

Schneider M. D., 2014, arXiv, astro-ph.CO

Schneider P., Ehlers J., Falco E. E., 1992, Gravitational Lenses

Schrabback T. et al., 2007, Astronomy and Astrophysics, 468, 823

Scranton R. et al., 2005, The Astrophysical Journal, 633, 589

Seitz C., Schneider P., 1995, Astronomy and Astrophysics, 297, 287

Seitz C., Schneider P., 1997, Astronomy and Astrophysics, 318, 687

Seljak U., 2000, Monthly Notices of the Royal Astronomical Society, 318, 203

Semboloni E., Hoekstra H., Schaye J., Daalen M. P. V., Mccarthy I. G., 2011, Monthly Notices of the Royal Astronomical Society, 417, 2020

Shen S., Mo H. J., White S. D. M., Blanton M. R., Kauffmann G., Voges W., Brinkmann J., Csabai I., 2003, Monthly Notice of the Royal Astronomical Society, 343, 978

Simpson F. et al., 2013, Monthly Notices of the Royal Astronomical Society, 429, 2249

Smail I., Ellis R. S., Fitchett M. J., 1994, MNRAS, 270, 245

Smith R. E. et al., 2003, Monthly Notice of the Royal Astronomical Society, 341, 1311

Stil J. M., Krause M., Beck R., Taylor A. R., 2009, ApJ, 693, 1392

Sugiyama N., 1995, Astrophysical Journal Supplement v.100, 100, 281

Sullivan M. et al., 2011, ApJ, 737, 102

Surpi G. C., Harari D. D., 1999, The Astrophysical Journal, 515, 455

Suyu S. H. et al., 2013, ApJ, 766, 70

Takahashi R., Sato M., Nishimichi T., Taruya A., Oguri M., 2012, ApJ, 761, 152

Taylor A. N. et al., 2004, Monthly Notices of the Royal Astronomical Society, 353, 1176

Taylor A. N., Kitching T. D., Bacon D. J., Heavens A. F., 2007, MNRAS, 374, 1377

Tegmark M., Taylor A. N., Heavens A. F., 1997, ApJ, 480, 22

Umetsu K. et al., 2014, arXiv, astro-ph.CO

van Waerbeke L., 2010, MNRAS, 401, 2093

Velander M., Kuijken K., Schrabback T., 2010, arXiv, astro-ph.CO

Velander M. et al., 2014, Monthly Notices of the Royal Astronomical Society, 437, 2111

Voit G. M., 2005, Reviews of Modern Physics, 77, 207

Wolf C., Meisenheimer K., Rix H.-W., Borch A., Dye S., Kleinheinrich M., 2003, Astronomy and Astrophysics, 401, 73

Wolz L., Kilbinger M., Weller J., Giannantonio T., 2012, arXiv, astro-ph.CO

Wright C. O., Brainerd T. G., 1999, arXiv, astro-ph

Wyman M., Rudd D. H., Vanderveld R. A., 2013, arXiv, astro-ph.CO

Zuntz J., Kacprzak T., Voigt L., Hirsch M., Rowe B., Bridle S., 2013, Monthly Notices of the Royal Astronomical Society, 434, 1604

Bibliography

Anderson L. et al., 2012, Monthly Notices of the Royal Astronomical Society, 427, 3435

Balaguera-Antolínez A., Sánchez A. G., Böhringer H., Collins C., Guzzo L., Phleps S., 2011, Monthly Notices of the Royal Astronomical Society, 413, 386

Bardeen J. M., Bond J. R., Kaiser N., Szalay A. S., 1986, Astrophysical Journal, 304, 15

Bartelmann M., Schneider P., 2001, Physics Reports, 340, 291

Bauer A. H., Gaztañaga E., Martí P., Miquel R., 2013, eprint arXiv, 1312, 2458

Benjamin J. et al., 2013, MNRAS, 431, 1547

Bernstein G. M., 2009, The Astrophysical Journal, 695, 652, submitted to ApJ

Bernstein G. M., Cai Y.-C., 2011, arXiv, astro-ph.CO

Bernstein G. M., Jarvis M., 2002, The Astronomical Journal, 123, 583

Bertin E., Arnouts S., 1996, Astronomy and Astrophysics Supplement, 117, 393

Bertin G., Lombardi M., 2006, The Astrophysical Journal, 648, L17

Beutler F. et al., 2011, Monthly Notices of the Royal Astronomical Society, 416, 3017

Blake C., Bacon D., Fluke C., Kitching T., Miller L., Power C., Wilman R., 2014, Proposal for an SKA weak lensing survey

Blake C. et al., 2013, Monthly Notices of the Royal Astronomical Society, 436, 3089

Blake C. et al., 2010, Monthly Notices of the Royal Astronomical Society, 406, 803

Blake C. et al., 2011, Monthly Notices of the Royal Astronomical Society, 415, 2892

Bond J. R., Efstathiou G., 1984, Astrophysical Journal, 285, L45

Bradač M., Allen S. W., Treu T., Ebeling H., Massey R., Morris R. G., von der Linden A., Applegate D., 2008, The Astrophysical Journal, 687, 959

Bradt H., 2008, Astrophysical Processes

Brainerd T. G., Blandford R. D., Smail I., 1996, Astrophysical Journal v.466, 466, 623

Bridle S., King L., 2007, New Journal of Physics, 9, 444

Bridle S. et al., 2009, Annals of Applied Statistics, 3, 6

Brown M. L., Battye R. A., 2011, Monthly Notices of the Royal Astronomical Society, 410, 2057

Brown M. L., Taylor A. N., Hambly N. C., Dye S., 2002, Monthly Notices of the Royal Astronomical Society, 333, 501

Cai Y.-C., Bernstein G., 2012, Monthly Notices of the Royal Astronomical Society, 422, 1045

Casaponsa B., Heavens A. F., Kitching T. D., Miller L., Barreiro R. B., Martínez-González E., 2013, Monthly Notices of the Royal Astronomical Society, 741

Castro P. G., Heavens A. F., Kitching T. D., 2005, Physical Review D, 72, 23516

Choi A., Tyson J. A., Morrison C. B., Jee M. J., Schmidt S. J., Margoniner V. E., Wittman D. M., 2012, ApJ, 759, 101

Clowe D., Bradač M., Gonzalez A. H., Markevitch M., Randall S. W., Jones C., Zaritsky D., 2006, The Astrophysical Journal, 648, L109

Collaboration P. et al., 2013a, arXiv, astro-ph.CO

Collaboration P. et al., 2014, Astronomy & Astrophysics, 571, A20

Collaboration P. et al., 2013b, arXiv, astro-ph.CO

Collaboration P. et al., 2013c, eprint arXiv, 1303, 5075

Cooper M. C. et al., 2012, Monthly Notices of the Royal Astronomical Society, 419, 3018

de Jong J. T. A. et al., 2013, The Messenger, 154, 44

Dolag K., Bartelmann M., Perrotta F., Baccigalupi C., Moscardini L., Meneghetti M., Tormen G., 2004, A&A, 416, 853

Eifler T., Krause E., Schneider P., Honscheid K., 2013, eprint arXiv, 1302, 2401

Eisenstein D. J., Hu W., 1998, Astrophysical Journal v.496, 496, 605

Erben T., Hildebrand H., Miller L., Waerbeke L. V., Heymans C., Hoekstra H., Kitching T. D., et al., 2012, arXiv, 1210, 8156, submitted to MNRAS

Ettori S., Fabian A. C., 1999, Monthly Notices of the Royal Astronomical Society, 305, 834

Ettori S., Morandi A., Tozzi P., Balestra I., Borgani S., Rosati P., Lovisari L., Terenziani F., 2009, A&A, 501, 61

Fedeli C., Bartelmann M., Meneghetti M., Moscardini L., 2008, A&A, 486, 35

Ford J., Hildebrandt H., van Waerbeke L., Erben T., Laigle C., Milkeraitis M., Morrison C. B., 2014, Monthly Notices of the Royal Astronomical Society, 439, 3755

Gaztañaga E., Eriksen M., Crocce M., Castander F. J., Fosalba P., Marti P., Miquel R., Cabré A., 2012, MNRAS, 2931

Gray M. E. et al., 2009, Monthly Notices of the Royal Astronomical Society, 393, 1275

Grego L., Carlstrom J. E., Reese E. D., Holder G. P., Holzapfel W. L., Joy M. K., Mohr J. J., Patel S., 2001, The Astrophysical Journal, 552, 2

Harvey D., Massey R., Kitching T., Taylor A., Jullo E., Kneib J.-P., Tittley E., Marshall P. J., 2013, Monthly Notices of the Royal Astronomical Society, 433, 1517

Harvey D. et al., 2014, Monthly Notices of the Royal Astronomical Society, 441, 404

Heavens A., Alsing J., Jaffe A. H., 2013, Monthly Notices of the Royal Astronomical Society: Letters, L98

Heavens A. F., Joachimi B., 2011, Monthly Notices of the Royal Astronomical Society, 415, 1681, 11 pages, 6 figures

Heavens A. F., Kitching T. D., Taylor A. N., 2006, arXiv, astro-ph

Heymans C. et al., 2006, Monthly Notices of the Royal Astronomical Society: Letters, 371, L60

Heymans C. et al., 2005, Monthly Notices of the Royal Astronomical Society, 361, 160

Heymans C. et al., 2008, Monthly Notices of the Royal Astronomical Society, 385, 1431

Heymans C. et al., 2013, Monthly Notices of the Royal Astronomical Society, 1297

Hildebrandt H. et al., 2012, MNRAS, 421, 2355

Hildebrandt H. et al., 2011, The Astrophysical Journal Letters, 733, L30

Hildebrandt H., Waerbeke L. V., Erben T., 2009, Astronomy and Astrophysics, 507, 683

Hildebrandt H. et al., 2013, Monthly Notices of the Royal Astronomical Society, 429, 3230

Hirata C. M., Mandelbaum R., Ishak M., Seljak U., Nichol R., Pimbblet K. A., Ross N. P., Wake D., 2007, Monthly Notices of the Royal Astronomical Society, 381, 1197

Hirata C. M., Seljak U., 2004, arXiv, astro-ph

Hoekstra H., Franx M., Kuijken K., 2000, The Astrophysical Journal, 532, 88

Hoekstra H., Franx M., Kuijken K., Carlberg R. G., Yee H. K. C., 2003, Monthly Notice of the Royal Astronomical Society, 340, 609

Hu W., 1999, arXiv, astro-ph

Huff E. M., Graves G. J., 2011, eprint arXiv, 1111, 1070, 6 pages, 4 Figures. Submitted to ApJL

J.A.Peacock, 1999, Cosmological Physics. Cambridge University Press

Joachimi B., Bridle S. L., 2010, Astronomy and Astrophysics, 523, 1

Joachimi B., Mandelbaum R., Abdalla F. B., Bridle S. L., 2011, A&A, 527, 26

Joachimi B., Schneider P., 2008, Astronomy and Astrophysics, 488, 829

Joachimi B., Schneider P., 2009, Astronomy and Astrophysics, 507, 105

Joachimi B., Taylor A. N., Kiessling A., 2011, MNRAS, 418, 145

Kaiser N., 2000, The Astrophysical Journal, 537, 555

Kaiser N., Squires G., 1993, Astrophysical Journal, 404, 441

Kaiser N., Squires G., Broadhurst T., 1995, Astrophysical Journal v.449, 449, 460

Kilbinger M. et al., 2013, Monthly Notices of the Royal Astronomical Society, 430, 2200

Kirk D., Bridle S., Schneider M., 2010, Monthly Notices of the Royal Astronomical Society, 408, 1502

Kirk D., Lahav O., Bridle S., Jouvel S., Abdalla F. B., Frieman J. A., 2013, eprint arXiv, 1307, 8062, 22 pages, 8 figures

Kitching T. D. et al., 2012, MNRAS, 423, 3163

Kitching T. D. et al., 2014, arXiv, astro-ph.CO

Kronberg P. P., Dyer C. C., Burbidge E. M., Junkkarinen V. T., 1991, Astrophysical Journal, 367, L1

Lani C. et al., 2013, Monthly Notices of the Royal Astronomical Society, 435, 207

Laureijs R. et al., 2011, eprint arXiv, 1110, 3193

Leauthaud A. et al., 2007, The Astrophysical Journal Supplement Series, 172, 219

Maltby D. T. et al., 2010, Monthly Notices of the Royal Astronomical Society, 402, 282

Mandelbaum R. et al., 2011, Monthly Notices of the Royal Astronomical Society, 410, 844

Mandelbaum R., Hirata C. M., Ishak M., Seljak U., Brinkmann J., 2006, Monthly Notices of the Royal Astronomical Society, 367, 611

Mandelbaum R., Slosar A., Baldauf T., Seljak U., Hirata C. M., Nakajima R., Reyes R., Smith R. E., 2013, Monthly Notices of the Royal Astronomical Society, 432, 1544

Mantz A., Allen S. W., Ebeling H., Rapetti D., 2008, Monthly Notices of the Royal Astronomical Society, 387, 1179

Markevitch M., Gonzalez A. H., Clowe D., Vikhlinin A., Forman W., Jones C., Murray S., Tucker W., 2004, The Astrophysical Journal, 606, 819

McDonald P., Seljak U., 2009, Journal of Cosmology and Astroparticle Physics, 10, 007

Melchior P. et al., 2014, arXiv, astro-ph.CO

Menard B., Bartelmann M., 2002, A&A, 386, 784

Ménard B., Scranton R., Fukugita M., Richards G., 2010, Monthly Notices of the Royal Astronomical Society, 405, 1025

Miller L., Kitching T. D., Heymans C., Heavens A. F., Waerbeke L. V., 2007, Monthly Notices of the Royal Astronomical Society, 382, 315

Morrison C. B., Scranton R., Ménard B., Schmidt S. J., Tyson J. A., Ryan R., Choi A., Wittman D., 2012, arXiv, astro-ph.CO

Myers A. D., Outram P. J., Shanks T., Boyle B. J., Croom S. M., Loaring N. S., Miller L., Smith R. J., 2003, Monthly Notice of the Royal Astronomical Society, 342, 467

Navarro J. F., Frenk C. S., White S. D. M., 1997, Astrophysical Journal v.490, 490, 493

Papovich C. et al., 2012, ApJ, 750, 93

Peacock J. A., Dodds S. J., 1996, Monthly Notices of the Royal Astronomical Society, 280, L19

Peacock J. A., Smith R. E., 2000, Monthly Notices of the Royal Astronomical Society, 318, 1144

Percival W. J. et al., 2010, Monthly Notices of the Royal Astronomical Society, 401, 2148

Perlmutter S. et al., 1999, The Astrophysical Journal, 517, 565

Rassat A. et al., 2008, eprint arXiv, 0810, 3, submitted to MNRAS

Reiprich T. H., Böhringer H., 2002, The Astrophysical Journal, 567, 716

Rhodes J., Refregier A., Groth E. J., 2000, The Astrophysical Journal, 536, 79

Riess A. G. et al., 2011, The Astrophysical Journal, 730, 119

Rix H.-W. et al., 2004, The Astrophysical Journal Supplement Series, 152, 163

Rozo E., Schmidt F., 2010, arXiv, astro-ph.CO

Schmidt B. P. et al., 1998, The Astrophysical Journal, 507, 46

Schmidt F., Leauthaud A., Massey R., Rhodes J., George M. R., Koekemoer A. M., Finoguenov A., Tanaka M., 2012, The Astrophysical Journal Letters, 744, L22

Schmidt F., Rozo E., Dodelson S., Hui L., Sheldon E., 2009a, ApJ, 702, 593

Schmidt F., Rozo E., Dodelson S., Hui L., Sheldon E., 2009b, arXiv, astro-ph.CO

Schneider M. D., 2014, arXiv, astro-ph.CO

Schneider P., Ehlers J., Falco E. E., 1992, Gravitational Lenses

Schrabback T. et al., 2007, Astronomy and Astrophysics, 468, 823

Scranton R. et al., 2005, The Astrophysical Journal, 633, 589

Seitz C., Schneider P., 1995, Astronomy and Astrophysics, 297, 287

Seitz C., Schneider P., 1997, Astronomy and Astrophysics, 318, 687

Seljak U., 2000, Monthly Notices of the Royal Astronomical Society, 318, 203

Semboloni E., Hoekstra H., Schaye J., Daalen M. P. V., Mccarthy I. G., 2011, Monthly Notices of the Royal Astronomical Society, 417, 2020

Shen S., Mo H. J., White S. D. M., Blanton M. R., Kauffmann G., Voges W., Brinkmann J., Csabai I., 2003, Monthly Notice of the Royal Astronomical Society, 343, 978

Simpson F. et al., 2013, Monthly Notices of the Royal Astronomical Society, 429, 2249

Smail I., Ellis R. S., Fitchett M. J., 1994, MNRAS, 270, 245

Smith R. E. et al., 2003, Monthly Notice of the Royal Astronomical Society, 341, 1311

Stil J. M., Krause M., Beck R., Taylor A. R., 2009, ApJ, 693, 1392

Sugiyama N., 1995, Astrophysical Journal Supplement v.100, 100, 281

Sullivan M. et al., 2011, ApJ, 737, 102

Surpi G. C., Harari D. D., 1999, The Astrophysical Journal, 515, 455

Suyu S. H. et al., 2013, ApJ, 766, 70

Takahashi R., Sato M., Nishimichi T., Taruya A., Oguri M., 2012, ApJ, 761, 152

Taylor A. N. et al., 2004, Monthly Notices of the Royal Astronomical Society, 353, 1176

Taylor A. N., Kitching T. D., Bacon D. J., Heavens A. F., 2007, MNRAS, 374, 1377

Tegmark M., Taylor A. N., Heavens A. F., 1997, ApJ, 480, 22

Umetsu K. et al., 2014, arXiv, astro-ph.CO

van Waerbeke L., 2010, MNRAS, 401, 2093

Velander M., Kuijken K., Schrabback T., 2010, arXiv, astro-ph.CO

Velander M. et al., 2014, Monthly Notices of the Royal Astronomical Society, 437, 2111

Voit G. M., 2005, Reviews of Modern Physics, 77, 207

Wolf C., Meisenheimer K., Rix H.-W., Borch A., Dye S., Kleinheinrich M., 2003, Astronomy and Astrophysics, 401, 73

Wolz L., Kilbinger M., Weller J., Giannantonio T., 2012, arXiv, astro-ph.CO

Wright C. O., Brainerd T. G., 1999, arXiv, astro-ph

Wyman M., Rudd D. H., Vanderveld R. A., 2013, arXiv, astro-ph.CO

Zuntz J., Kacprzak T., Voigt L., Hirsch M., Rowe B., Bridle S., 2013, Monthly Notices of the Royal Astronomical Society, 434, 1604

Publications

Duncan, Christopher A. J.; Joachimi, Benjamin; Heavens, Alan F.; Heymans, Catherine; Hildebrandt, Hendrik. "On the complementarity of galaxy clustering with cosmic shear and flux magnification". In Monthly Notices of the Royal Astronomical Society, Volume 437, Issue 3, p.2471-2487. 2014.
Url: http://adsabs.harvard.edu/abs/2014MNRAS.437.2471D